Electrical effects in winding of large electrical ac machines application to advanced large size DFIM

Thèse N° 8101

Frédéric Michael MAURER

Acceptée sur proposition du jury

Prof. M. Paolone, président du jury
Dr B. Kawkabani, Dr J. Haldemann, directeurs de thèse
Prof. J. K. Nøland, rapporteur
Prof. M. Radulescu, rapporteur
Prof. A. Rufer, rapporteur

2019

ÉCOLE POLYTECHNIQUE
FÉDÉRALE DE LAUSANNE

In the end, you're
measured not by how much
you undertake, but by what
you finally accomplish.
— Donald Trump

We know the truth, not
only by the reason, but also
by the heart.
— Blaise Pascal

To the one and only . . .

Remerciements

Par ces quelques lignes je souhaite remercier certaines personnes qui m'ont aidé sur mon chemin.

Je souhaite remercier en premier lieu l'EPFL comme institution pour son accueil, et les moyens qu'elle a mis à ma disposition. Sans vouloir épiloguer sur le sujet du "traitement des doctorants dans les hautes écoles", j'aimerais juste dire que je n'ai jamais ressenti ni vécu de tels problèmes dans cette école, pire j'ai plutôt senti une pression positive pour finir plus rapidement. Je suis finalement extrêmement reconnaissant de ne pas avoir eu à connaître de telles situations et remercie ici encore une fois l'EPFL pour l'excellent encadrement qu'elle propose.

Je tiens aussi à remercier Peter Brühlmeier, Roland Dupuis Manuel Leitos et Pierre-André Despont des ateliers de fabrications ACI, AFA et ATMX. Leur précieux savoir-faire m'a grandement aidé lors de la finalisation des expériences. Grâce à leurs pièces, j'ai pu mener à bien les expériences dans de bonnes conditions, car mes compétences de pliage / découpes, etc... ont largement été dépassées lors de la réalisation pratique de l'expérience. Je remercie aussi le SCITAS pour leur aide lors des simulations numériques sur leurs clusters de calculs. J'aimerai aussi remercier Roland Wetter, Stéphane Burri et Sylvain Robert pour leur soutien très apprécié, notamment lors de la réalisation des expériences. Je remercie aussi André Hodder pour les nombreux échanges techniques que j'ai grandement apprécié ainsi que Prof. Mario Paolone de m'avoir accueilli dans son unité le DESL.
Je tiens aussi à profondément remercier la société ALSTOM Hydro qui a lancé ce projet de thèse ainsi que la société GE Renewables Energy qui a continué ce projet en assurant son financement en des temps incertains. La collaboration avec ALSTOM Hydro fut un franc succès. Finalement je remercie les Dr. Basile Kawkabani et Johann Haldemann d'avoir accepté la direction de cette thèse tout en conservant leurs mandats bien qu'ils aient pris une retraite bien méritée.

Je tiens à remercier ma femme de m'avoir accompagné sur mon chemin et de m'avoir motivé lorsque j'ai connu des moments difficiles ainsi que toutes les personnes que j'ai malheureusement omises jusqu'à présent. Merci mille fois pour votre aide aussi faible soit-elle. Ce sont les petites gouttes qui forment les grandes rivières.

Lausanne, 26 Août 2018   F. Maurer.

Abstract

In the context of global warming, renewable energies will play a more and more important and global role. The main drawback of "classical" renewable energies, namely Wind and Solar energy, lies in their unpredictability. The electrical grid needs high energy storage to ensure its stable operation. Today's most powerful energy storage is hydro pump storage. To meet the electrical grid's demand on pump power variation, GE Renewable Energy develops since 10 years variable speed machines (also called Doubly Fed Induction Generators or DFIG). Within turbogenerators, the phenomenon of circulating currents in Roebel bars is well known, while is it has not yet been studied for DFIGs. The main goal of this study is to calculate the circulating currents in the stator and rotor bars of DFIG under different operating points with a theoretical and practical precision of around 1%.

This study starts with an overview of the current situation in circulating current calculation and presentation of the characteristic circulating current curves for a hydrogenerator, study that led to a patent application. After a presentation of the possible calculation methods and models based on a deep and broad literature review, this study performs with a deep review of the slot inductance model analysing its precision and limitations. Based on these finds, two novel analytical models are proposed to enhance the taking into account of the strand dimensions. Only the last slot inductance model developed, based on a slot differential inductance model, permits to take the strand dimensions and the saturation into account. This model is validated experimentally using a small-scale slot/strand-model, while all slots models are compared to each other to highlight their differences.

The winding overhang model and novel analytical expressions are presented in a later chapter as well as the analytical treatment of the rotor overhang made of non-linear steel. The winding overhang model uses analytical expressions to determine the magnetic field and vector potential in the winding overhang, which have the advantage of additional knowledge compared to the results of a finite-element computation.

In another chapter, novel exact transient current and torques expressions are derived for a DFIG experiencing a 3-phase and a 2-phase short-circuit. Then the winding overhang force computation and the circulating current calculation results are presented in two crowing chapters. In these chapters, the influence of the approximation and boundary on the end winding forces as well as the origin of the end winding forces are shown. The last result chapter

is dedicated to the circulating current calculation, where several original results are presented to detail the circulating current losses reduction potential and the impact of well-known classical special transitions on the circulating currents in the case of a DFIG. The influence of the operating point and the boundary are also shown for the stator and the rotor.

This study presents many original contributions on several domains. It presented a novel slot inductance model, which was validated using a specially designed small-scale model of a slot. This small-scale model concept can certainly be extended to other parts of an electrical machine, which could help to study these effects in a laboratory instead of a power plant. This study could quantify the circulating current losses in the stator winding of a DFIG, losses that can easily be reduced to increase the efficiency of this machine. This study also presented several original fundamental contributions in the field of analytical expressions for the transient expression of current and torque in the case of a 3-phase and 2-phase short-circuit. More importantly, this study presented novel exact expression for the magnetic field and vector potential for several magnetic bodies and current carrying conductor, which are very important results that can also be used in other fields of research where very high magnetic field precision is required.

These expressions led to the most important achievement of this study namely the winding overhang model, which has been implemented in the form of a general purpose 3D integral magnetic field and vector potential calculation tool. This highly parallelised hpc-compatible tool can be used for an arbitrary geometry, can take the rotation of a body into account, can take any current into account and deal with non-linear iron as well as permanent magnets. This tool is ready-to-use and have a direct impact in many industrial applications such as computation of the end winding forces, the winding overhang inductances or the overhang induced voltages.

Résumé

Dans le contexte du réchauffement climatique, les énergies renouvelables vont jouer un rôle global de plus en plus important. Le principal défaut des énergies renouvelables "classiques", que sont les énergies éoliennes et solaires, se situe dans leur non-prédictabilité. Afin d'assurer la stabilité des réseaux électriques, il faut disposer de solutions pour stocker cette grande quantité d'énergie. Aujourd'hui le pompage-turbinage constitue la plus grande forme de stockage énergétique. Pour pouvoir satisfaire la demande des réseaux électriques en terme de variation de puissance en mode pompe, GE Renewables Energy développe depuis 10 ans des machines à vitesse variable (appelées aussi Doubly Fed Induction Generators ou DFIG). Dans les turbo-générateurs, le phénomène des courants de circulation dans les barres roebel est bien connue depuis de longues années, tandis qu'il est inconnu dans les DFIG. Le but majeur de cette thèse est donc le calcul des courants de circulation dans les barres roebel statoriques et rotoriques d'un DFIG opérant sous différents points de fonctionnement avec une précision théorique et pratique de l'ordre de 1%.

Cette étude débute par un état de la situation au niveau du calcul des courants de circulations ainsi qu'une présentation des courbes caractéristiques des courants de circulation appliqués au cas d'un générateur synchrone à pôles saillants. Les résultats de cette étude ont permis de déposer un brevet. Après une présentation des méthodes de calcul et des modèles possibles basés sur une étude détaillée de la littérature publiée, cette étude effectue une revue détaillée et approfondie du modèle de l'inductance dans l'encoche tout en mettant en évidence sa précision et ses limitations. En se basant sur ces faits, deux modèles analytiques originaux sont développés afin d'améliorer la prise en compte de la dimension des conducteurs. Uniquement le dernier modèle, basé sur la méthode des inductances différentielles, permet de tenir compte de la saturation. Ce modèle est validé expérimentalement sur un modèle-réduit, de plus tous les modèles d'inductance dans l'encoche sont comparés entre eux afin de mettre en évidence leur différences.

Le modèle des têtes de bobines ainsi que les nouvelles expressions analytiques développées pour ce modèle sont présentées dans le chapitre suivant de même que le traitement analytique de l'acier non-linéaire situé axialement dans les têtes de bobines rotoriques. Le modèle des têtes de bobines utilise des expressions analytiques pour déterminer le champ magnétique et le potentiel vecteur dans ces têtes de bobine, ce qui a l'avantage d'apporter des connaissances supplémentaires comparativement aux résultats d'un calcul par éléments finis.

Résumé

Dans le chapitre suivant, les nouvelles expressions analytiques pour le courant et couple transitoire d'une DFIG sont présentées et démontrées pour un court-circuit biphasé et triphasé. Ensuite, la force dans les têtes de bobine et le calcul des courants de court-circuit sont également présentés dans les deux derniers chapitres. Dans ces chapitres, l'influence de l'approximation et des conditions aux limites sur la force dans les têtes de bobine ainsi que l'origine des forces sont présentés. Le dernier chapitre est dédié aux courants de circulation où plusieurs résultats originaux sont présentés afin de détailler le potentiel de réduction des pertes par courant de circulation dans l'enroulement rotorique ainsi que l'impact de transpositions classiques et connues sur les courants de circulation dans le cas d'un DFIG. L'influence du point de fonctionnement et des conditions aux limites sont aussi présentés aussi bien pour le rotor que pour le stator.

Cette thèse présente bien des contributions originales dans plusieurs domaines. Elle présente un nouveau modèle d'inductance dans l'encoche qui a été validé expérimentalement en utilisant un modèle-réduit spécialement construit à cet effet. Ce concept de modèle-réduit peut certainement être étendu à d'autres parties des machines électriques, afin d'étudier certains effects en détail dans un laboratoire en lieu et place d'une centrale électrique. Cette étude a permis de quantifier les pertes par courant de circulation dans l'enroulement statorique d'une DFIG, pertes qui peuvent être réduites afin d'augmenter le rendement de cette machine. Cette étude a aussi présenté quelques contributions fondamentales dans le domaine des expressions analytiques pour le calcul des courants de court-circuit triphasés mais surtout biphasés. Plus important encore, cette étude a présenté une nouvelle expression exacte du champ magnétique et du potentiel vectoriel pour plusieurs corps magnétiques et conducteurs porteurs de courant. Ces résultats très importants peuvent également être utilisés dans d'autres domaines de recherche nécessitant une très grande précision du champ magnétique.

Ces expressions mènent à la réalisation la plus importante de cette étude, à savoir le modèle des têtes de bobines, qui a été mis en oeuvre sous la forme d'un outil de calcul tridimensionnel intégral générique de champ magnétique et de potentiel vectoriel à usage général. Cet outil hautement parallélisé et compatible avec un serveur de calcul peut être utilisé pour une géométrie quelconque et peut prendre en compte la rotation d'un corps, n'importe quel courant et prendre en charge le fer non linéaire ainsi que les aimants permanents. Cet outil est prêt à l'emploi et a un impact direct sur de nombreuses applications industrielles telles que le calcul des forces dans les têtes de bobines, les inductances ou les tensions induites dans les têtes de bobine.

Contents

Contents

Contents

List of Figures

List of Tables

1 Introduction

Global warming is more than ever a current topic for humankind. More and more people around the world are convinced that the main root cause of the actual global warming is manmade and is due to the large scale emission of greenhouse gases produced by the burning of fossil fuels. On the 11th December 1997, 84 nations signed the Kyoto Protocol to reduce their carbon dioxide emissions. Some countries have already achieved their goals while others still struggle to achieve theirs or did not even sign this protocol. In the meantime, the scientific community agreed on a maximal 2°C-target for global warming. This target was the base for the discussions that took place in 2015 in Paris at the COP21 UN Climate Change Conference. The countries agreed on an even lower target for the global warming, namely 1.5°C. To achieve that target, some scientists argue that it will require a reduction to zero emissions sometime between 2030 and 2050[1].

These very challenging targets will impact the society and the life of the next generations and will be the main driver for the current generation. There is no doubt that a global and multilateral approach will lead to the achievement of these very challenging goals. There is no other option than to achieve them, since the human beings are lenders of that planet and it is their duty to hand it over to the next generation in a same or a better state than they received it from their ancestors. For the current generation, this statement implies to hand it over in a much better state than it received it from its ancestors.

Growing economies need more and more energy which is until now mostly supplied by fossil fuels as coal, natural gas and oil. Depending on the country this increase is more or less pronounced. China and Africa have an increase of around 180 Mtoe/$trn GDP (million tonne oil equivalent per trillion $ GDP at purchase power parity) while the European union and the USA are around 30 Mtoe/$trn GDP transposing differences in the economy as well as energy efficiency [3]. The share of hydroelectricity and renewable electricity is growing but still below 10% of the world annual consumption [19]. Figure 1.1 shows the development of the world

---

[1]https://en.wikipedia.org/wiki/2015_United_Nations_Climate_Change_Conference

energy consumption from 1991 to 2016. The consumption has increased from around 8'000 to a little bit more than 13'000 Mtoe, whereas only the huge economic crisis of 2009 temporarily damped this growth, followed by a slightly lower growth as before.
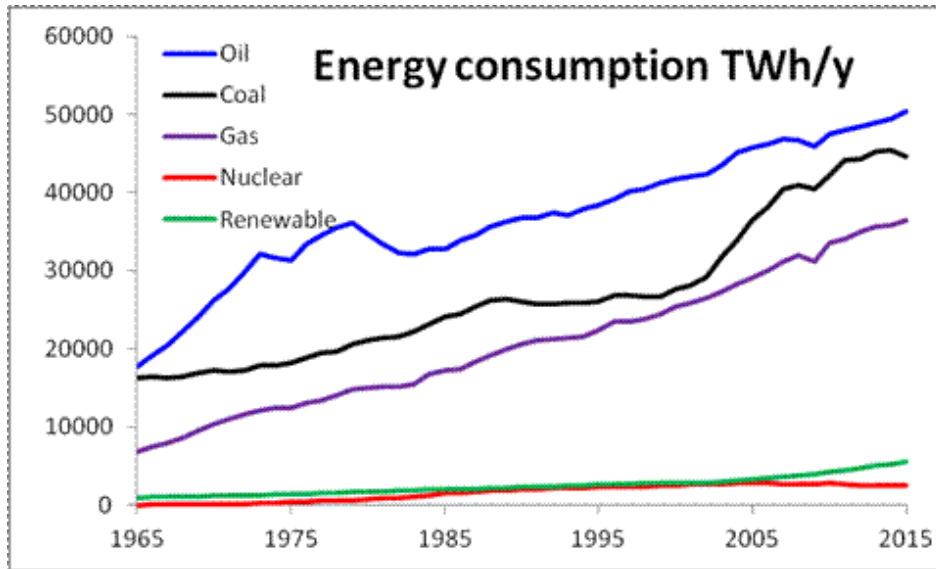
Figure 1.1 – World energy consumption from 1965 to 2014, taken from https://en.wikipedia.org/wiki/World_energy_consumption with data from [19].

As one may directly see from this figure, there is a long way to go and around not a lot of time, around 20-30 years, to achieve the goals of the COP21. To reduce drastically the fossil fuel consumption, people argue that electricity should be expanded as for example in electrical cars as an electrical motor has an efficiency around 90% while its combustion engine counter-part has a maximal efficiency below 33%. For sure, electricity will have a more and more bigger share of the world energy sources but electricity will certainly not fuel planes in a near future despite the incredible performance of Solar Impulse. There is a need for other renewable resources like for example biomass, fusion or even hydrogen, which fuelled the Apollo missions.

The main advantage of electricity regarding other energy sources is that its conversion to mechanical or thermal energy can be done at very high efficiency, typically higher than 90%. It main drawback lies in its impossibility to be stored in form of electric energy. Electricity can be stored chemically in batteries or in hydrogen, magnetically in supra-conductive coils, potentially in hydro pump-storage plants and electrostatically in capacitances. The digitalisation of our society will also increase our dependance to electricity making that energy source more and more demanded around the world. The increase of energy consumption should follow as much as possible sustainable growth principle keeping in mind that energy has always be a very important geo-political instrument where countries try to rely on national energy sources

rather than using renewables sources abroad.

2012 (13 361 Mtoe)   **2040 (18 290 Mtoe)**
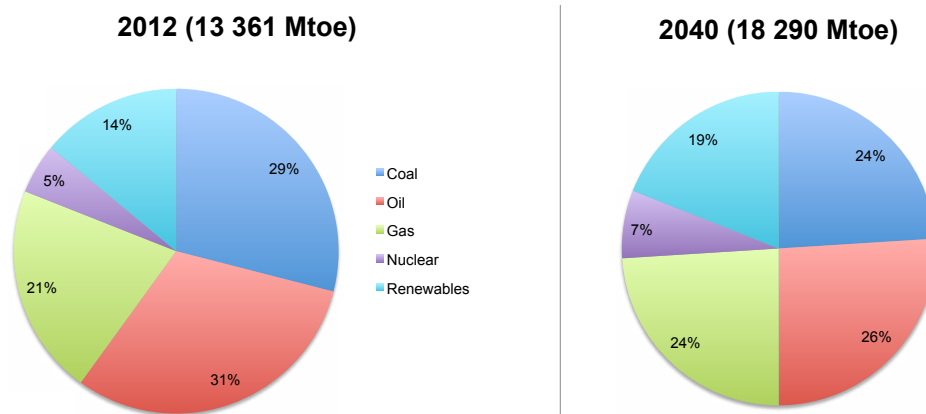
Figure 1.2 – Fuel shares in world primary energy demand according the "New Policies Scenario", source of the data [3].

In 2014, the International Energy Agency IAE published its "New Policies Scenario" which fuel shares are depicted in figure 1.2. This scenario sees an increase of the renewable and nuclear energy from 19% of fuel share to 28% the rest being still held by fossil fuels, while the overall world energy consumption rises from 13'361 Mtoe to 18'290 Mtoe [3]. In this scenario, electricity will account for 23% of the world energy sources in 2040, while it accounted only 18% in 2012, which represents a multiplication by 2 of the electricity generated in the world. This scenario doesn't take into account the goals of the COP21 Climate conference.

Since 2015, many countries have implemented the goals of the COP 21 in their national energy policy, trying among other policies or instruments to increase the share of renewable energy in their energy mix. For electricity it means increasing hydroelectricity, wind farms or solar panels citing only the actual most important renewable sources. Economically speaking renewable energy sources like the sun and the wind are very promising as they are free of charges until now so that their marginal cost is very low compared to gas power plants. But they are intermittent (refer to figures 1.3 and 1.4) and seldom at their maximal power, which reduces their return on investment. In 2012, the installed capacity was 30.81GW[2] while the maximal power produced did not exceed 25GW.

This intermittence as well as the increase of electricity demand is very challenging for the electrical grids. Smart grids try to overcome these challenges with the smallest economical impact mainly by shifting the production and consumption time as the load of the power lines lied between 30% and 40% in Switzerland in 2009[3]. Practically speaking it could mean that

---

[2]https://www.energy-charts.de/power_inst.htm?year=2012&period=annual&type=power_inst
[3]https://de.wikipedia.org/wiki/Intelligentes_Stromnetz
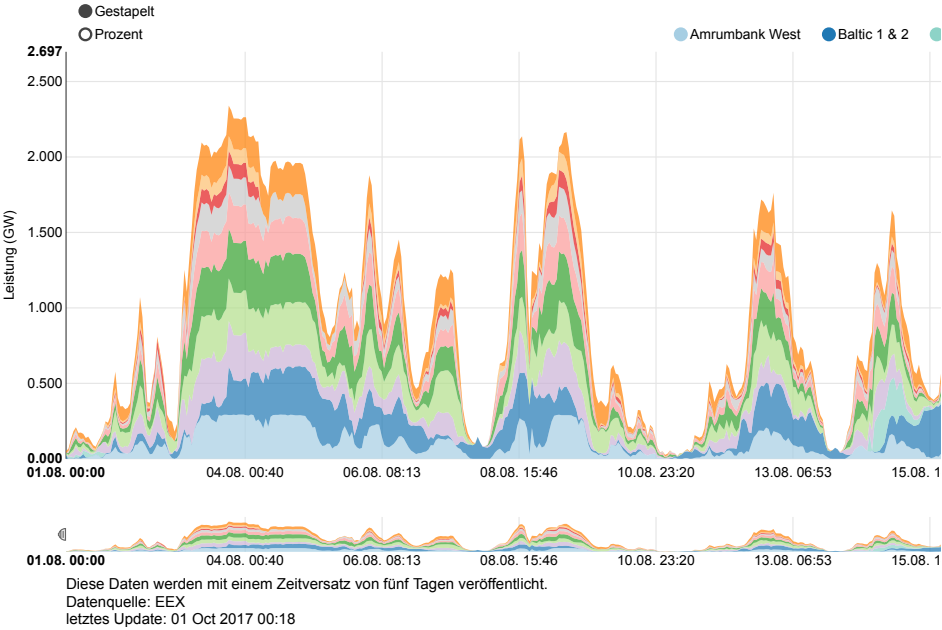
Figure 1.3 – Monthly german wind energy production in august 2017, source of the data and figure https://www.energy-charts.de.
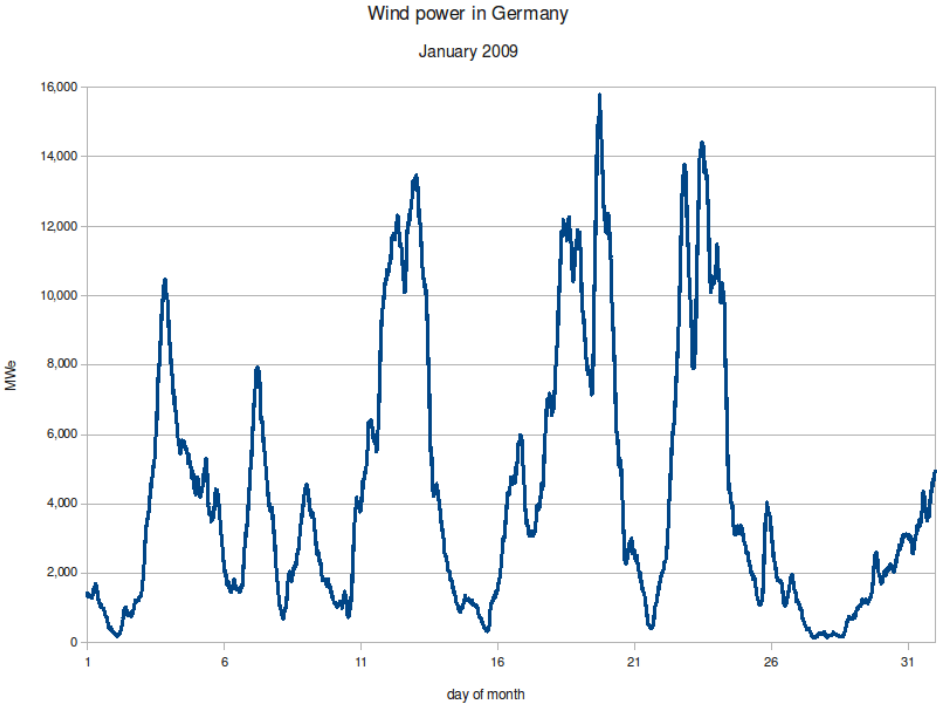
Figure 1.4 – Monthly german wind and solar energy production in february 2017, source of the data and figure https://www.energy-charts.de.

washing machines can only be operated during the night as well as charging of the electrical car batteries. Another important parameter to be taken into account in the electrical grid management is the decentralised power generation. In traditional electrical grids, the power is generated through centralised power generation units with ratings far above 10MW. The energy is then transferred to the consumers via electrical grids whereas the electrical generation must always follow the electrical consumption to keep the frequency of the electrical grid stabilised. Nowadays every single household can produce its own energy using solar panels on the roof top reducing its dependence of centralised power generating units. This house producers can also feed their production into the grid which somehow must also absorb these multiple small scale producers. Small scale producers sometimes also store their production in at-home batteries with the idea of getting self-sufficient in an electrical point of view. This could be possible for householder in villages or small cities but is certainly not very realistic for blocks in cities. Consumption hotspots concentrated in cities are therefore unavoidable.

To counter-balance this more and more growing intermittent power generation over a couple of days or more, bigger storage capacities with single capacities above 100MWh are required. Today, pump-storage hydro power plants provide the largest storage capacities ever achieved. The flexibility required by the grid demands to be able to regulate the power not only in the generating mode turbining water but also in the consumption mode pumping water into the upper reservoir. This pump power regulation is the most important asset of a modern pump storage power plant as it permits to balance the excess of injected intermittent renewable energy into the grid as good as possible. The regulation of the pump power can be achieved using a hydraulic short-circuit which needs at least two units connected to the same upper and lower reservoir or a ternary unit. Both options are quite cost intensive. More economical solutions are the double-fed-induction machine (DFIG), which is an induction machine with a stator-like winding on the rotor with brushes to feed the rotor with the appropriate three-phase current, and the double-fed salient pole machine (DFSM), which is a salient pole synchronous machine fed by a converter. From a grid perspective, both types of machines are equivalent up to the point that a DFIG has construction-conditioned a significant higher inertia than its equivalent DFSM. The choice between both technologies is therefore mainly economically driven.

Figure 1.5 shows a 3D view of a DFIG. The rotor is composed of a stacked rotor core. The rotor winding is located in the rotor slots. There is a rotor overhang, which provides a holding structure for the rotor winding in the overhang. The stator is identical to a stator of a salient pole synchronous machine. This rotor is very similar to the rotor of a turbogenerator with much more smaller air-gaps than for a turbogenerator.

Figure 1.6 shows a 3D view of a salient pole synchronous machine. The rotor is smaller than the stator and the field winding is a concentric winding wounded around the pole core.
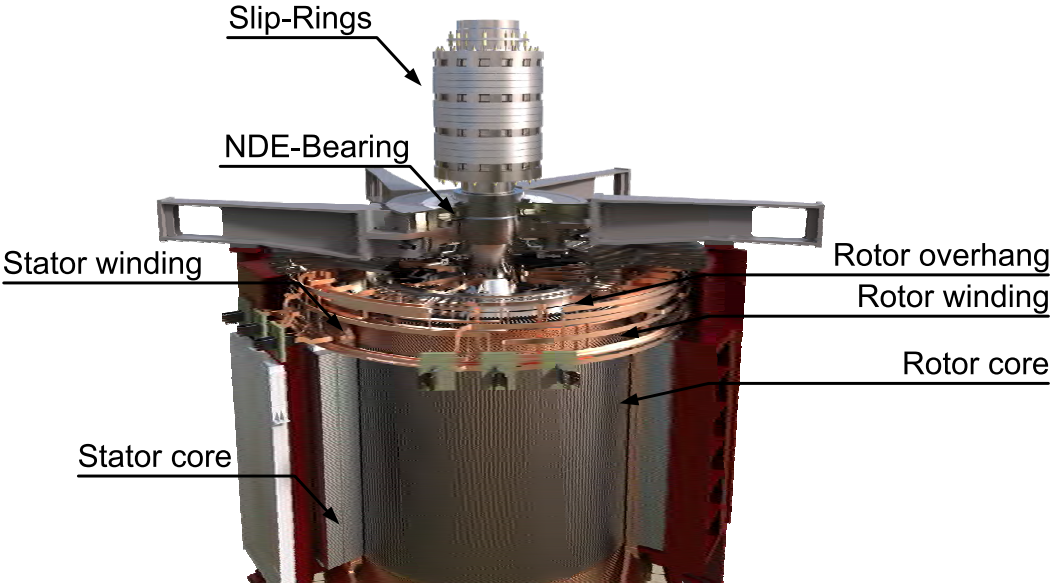
Figure 1.5 – 3D-view of a DFIG, courtesy of GE Renewable Energy reproduced with the autorisation of the right-holder.
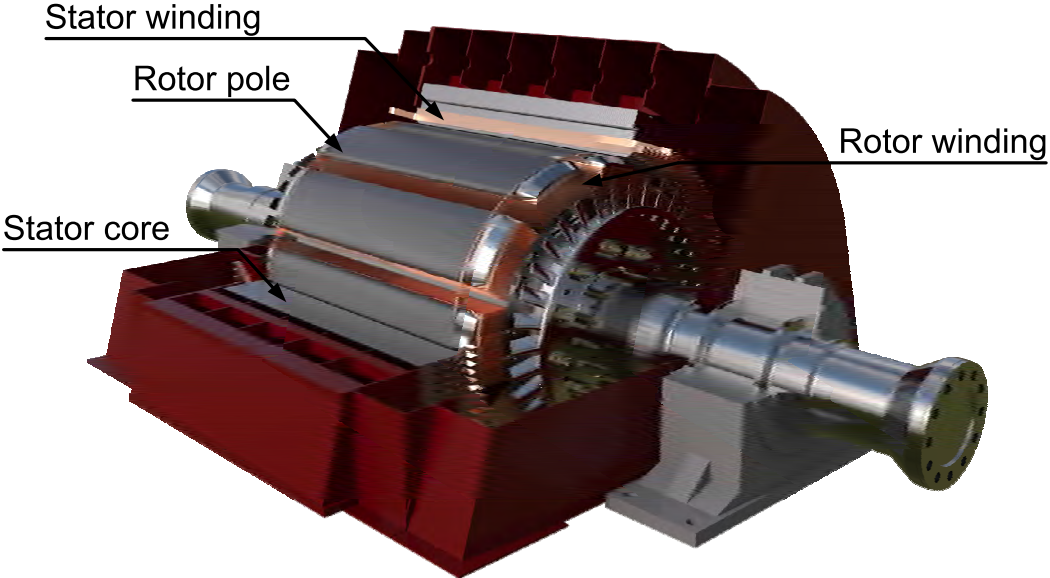
Figure 1.6 – 3D-view of a salient pole synchronous machine, courtesy of GE Renewable Energy reproduced with the autorisation of the right-holder.

Historically speaking the DFIG is the oldest way to regulate the pump power as the rated power of the converter used to be in the range of tens of MVA. In the same time as the rated power on the converter rose, the DFSM were installed. The maximal rated power of the converter and its volume are the main limiting factors for the use of large DFSM. Today, there are around 20 power plants totalising more than 30 units in operation or construction using the DFIG technology while there is only one power plant with one unit using the DFSM technology. The DFIG remains until today the leading technology to regulate the pump power in hydro pump-storage plants.

Even if the design of DFIG machine is already quite advanced and common, based on the more than 30 units installed around the world, there is still a huge potential for design optimisations. The optimal cooling of the rotor remains, as well as for salient pole machines, one of the main focus of interest in recent developments of electrical machines. A possible way to reduce the need of cooling in the rotor overhangs is to reduce the additional copper losses of the rotor winding which are caused by circulating currents in the rotor roebel bars among other sources of additional losses.
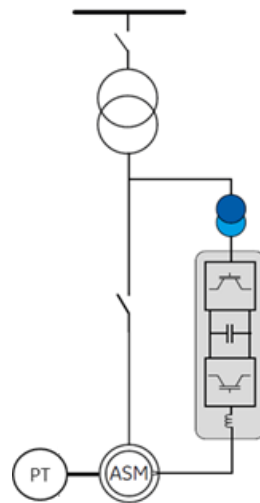
Figure 1.7 – Schematic representation of the DFIG (ASM) coupled with the pump-turbine (PT), where the rotor is feeded by a 3-level VSI converter.

Figure 1.7 presents a schematic representation of a DFIG coupled with its pump-turbine with the rotor fed by a 3-level VSI converter. The 3-level converter is PWM-modulated producing a quasi-sinusoidal current with very low harmonic content. The rotor voltage shape is typical for a 3-level converter. Measurements done on a 250MW machine shows the quasi-sinusoidal rotor and stator current shape and a typical 3-level converter rotor voltage shape. In this work, the currents will therefore be considered as sinusoidal.

Before entering into the details of the roebel bars, their circulating currents and their optimisation, let us start with their history as documented by Johann Haldemann in an unpublished paper. The following two paragraphs have been copied and slightly adjusted from his unpublished publication [69].

"In the last decade of the 19th century, a so-called "battle of current" took place between Thomas Alva Edison in favour of the DC-current on one side and George Westinghouse together with Nicola Tesla in favour of the AC-current on the other side. Both current systems were competing for the so-called current supremacy. The advantages of the AC-current lied in their capacity to be transformed into higher voltages while the DC-current could only be transported over small distances due to the voltage drop along the low-voltage transmission lines. This "battle" ended 1895 with the construction of the Niagara Falls power plant (3.7MW, 25Hz). From this point on, the pioneers of electrical machines started to build more and more powerful AC-current electrical machines. The maximal rated power stacked until 1912 around 10MW-20MW because of the increasing eddy current losses in the massive stator conductors.

Ludwig Roebel with its invention of the "Roebel bar" made the necessary breakthrough which enabled to skyrocket the rated power. Nowadays, the stator winding of big high voltage electrical machines is composed of bars inserted in a straight slot. These "Roebel bars" are the backbone of the high power electrical machines. In the original design of 1912, which is still current today, each bar is composed of multiple strands transposed over 360° (this means that every strand has the same distance in height in the active part) in the active length. This transposition enables to fully compensate the induced voltage between each strand in the active part, neglecting the effect of the ventilation slits, because their effect can be neglected in the case of equally spaced ventilation slits. With this full compensation, the roebel bar reduces its circulating currents towards zero. Only the strand eddy currents remain. This bar topology is called "Roebel bar" from the name of its inventor Ludwig Roebel. Other people have also created similar transposition methods or different ways to transpose the bar (for example Punga) mainly to get around Roebel's patent, but none of them has made a breakthrough in the industry as the "Roebel bar"[4]."[5]

Figure 1.8 presents a 3D view of the transposition of a Roebel bar, number 1 shows a strand of a roebel bar. This figure shows the "travel" done by every strand in active part, also showing that every strand spends the same "time" at every height of the bar. The action of the column change of a strand is called transposition. The distance between two transpositions is called "roebel-step". When comparing the roebel-step to the active length of the machine, some people may use the term "roebel-factor" which relates the active length to the number of

---

[4]In this work, the word "roebel bar" is also used.

[5]These two paragraphs have been copied and slightly adapted from an unpublished publication from Johann Haldemann [69].
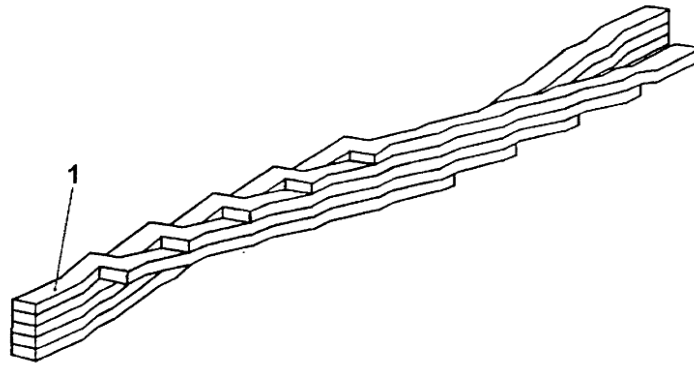
Figure 1.8 – 3D view of the transposition of a Roebel bar in the active part, source US Patent 5'777'417 reproduced with the autorisation of the right-holder.

transpositions and to the "roebel-step". The term "roebelisation" is also used when speaking of transpositions in a more general context.
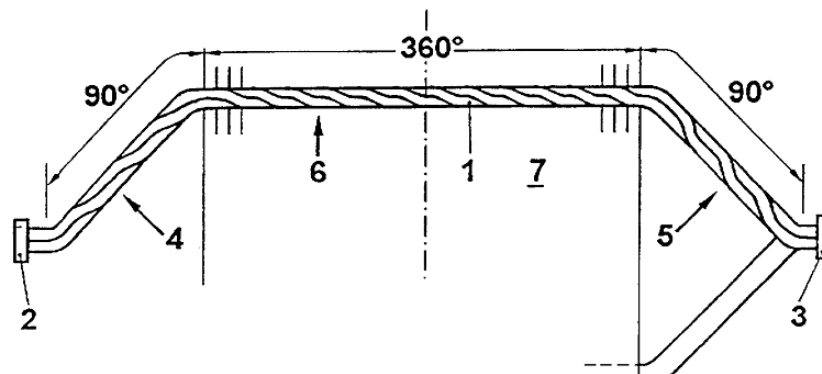
Figure 1.9 – View of the transposition of a Roebel bar with transposition in the overhang (90°) and in the active part (360°), source US Patent 5'777'417 reproduced with the autorisation of the right-holder.

Figure 1.9 presents a view of the Roebel bar in the $z - \phi$-plane of the electrical machine, the z-Axis being the rotation axis of the machine. 1 represents a strand of the bar, 2 and 3 are the brazing lugs short-circuiting the strands together at both ends of the bar. 4 and 5 show transpositions in the overhang while 6 represents the transpositions in active part. The transposition angle of the active part is 360° and is written just around the symmetry axis in the figure. 7 is the stator core. The overhang transposition angle is 90°. This figure shows the geometry of the bar, one can see the complex 3D-geometry in the overhang region, making the field calculation very challenging. In the overhang, there will be some induced voltages due to the parasitic field in this region causing circulation of currents between the strands of the bar.
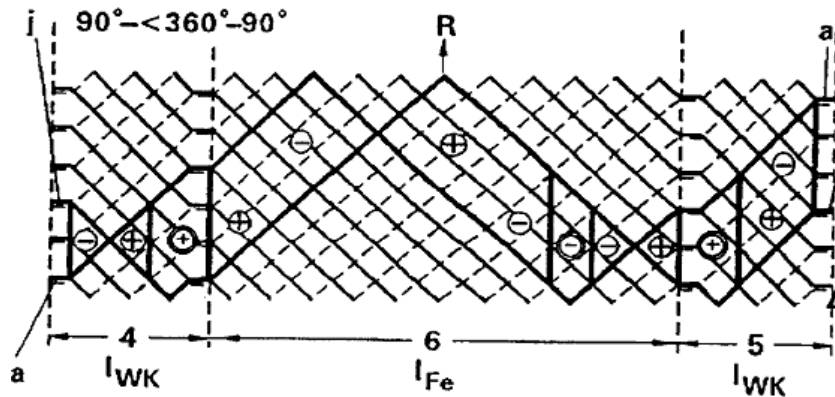
Figure 1.10 – View of the transposition scheme of a Roebel bar, source US Patent 5'777'417 reproduced with the autorisation of the right-holder.

Figure 1.10 shows a roebel bar in the $r - z$-plane. This scheme shows the "travel-plan" of the strands inside the roebel bar. Using this representation, one can understand and analyse the impact on the circulating currents in case of change in the transposition. This representation only gives qualitative information about the compensation of "internal" and "external" fields (which will be defined in chapter 3). In this figure, 6 represents the active part (l_{Fe}) while the overhang is given by 4 and 5 (l_{Wk}). The reference strands used for the analysis are highlighted using bold lines. One can see that the "+"-surface is not perfectly compensating the "-"-surface in the active part, meaning that there will be a small circulating current due to the active part. In the overhang, the compensation is incomplete, leading to induced voltage and finally circulating currents between the strands. Using this qualitative analysis concept, one can easily have an overview about the compensation status of a particular transposition in the active part as well as in the overhang.

1.1 Description of this work

1.1.1 Purpose

The topic of circulating current calculation has been comprehensively studied for more than 40 years mainly for turbogenerators, where the circulating current losses are significantly higher than for hydrogenerators (refer to figure 3.2 and other from chapter 3). First studies were conducted in the field of turbogenerators as they experienced damaged stator bars due to the excessive circulating current losses. At least three PhD-thesis have been written in this topic with the main goal to model the circulating losses within a computer program and to enhance and validate this model with field measurements [104], [77], [66], [67] and [68]. Some studies have also been done to compute the circulating current losses for several hydrogenerators [65]. This study concluded that there was no significant potential for circulating current loss reduction within hydrogenerators so there have been no further studies for a certain time. The

market evolution of the last years embossed by a strong competition in price and efficiency competition revived the interest in circulating current losses and calculation. Several studies showed that in some cases the circulating current losses could account for up to 20% of the DC-current copper losses (refer to f_s-factor minus one in figure 3.2). This interest is also motivated by the development of the DFIG machine which could have a significant amount of compensable circulating current losses.

An original study of the sensitivity, presented in chapter 3, of the parameters performed with the software developed originally for turbogenerators and adapted for the modelling of hydrogenerators showed that the calculation of circulating currents in hydrogenerators is much more demanding than its counter-part for turbogenerators due to several parameters: short winding overhang, small copper cross-section compared to a turbogenerator, small air-distances between the stator bars and short rotor compared to a turbogenerator. This leads to very high precision requirements on the novel calculation method: the precision of the circulating current should be around 1%. The novel calculation method must also take into account the magnetic rotor overhang of the DFIG. This is also quite challenging considering the numerical problems to adequately handle the non linear iron for all magnetic states as shown in section 5.3.

To achieve these challenging goals, an analysis of the precision and range of the existing models is performed. Based on the findings, the existing models are used, adapted or extended where applicable.

1.1.2 Methodology

Chapter 3 presents an original and detailed current situation of the circulating current calculation in hydrogenerators. This chapter can be seen as the extension of the introduction, as its goal is the present the current circulating current situation within hydrogenerators and to present the characteristic circulating current curves and the classical special transpositions applied to hydrogenerators. Due to the span of this current situation, it has been decided to present it in a separated chapter, as this current situation also presents original contributions. After a large and detailed literature review, the calculation method is chosen and this choice is duly motivated. For each constituent model of the fundamental calculation method a specific literature review is carried out, from which possible options are chosen. The option's choice favours analytical methods as they provide additional information regarding purely numerical methods, from which only the result can be obtained. Then they are analysed in detail focusing on their precision, hypothesis and fundamental drawbacks. Their precision is evaluated using comparison with finite element simulation as well as analytical formulas whenever possible. Depending on the result of the comparison, the evaluated part is changed or enhanced depending on the features of the possible alternatives.

The used constituent models are then validated using ever finite-element simulations, analytical formulas or comparison with published literature whenever possible. The comparison with literature is only of third priority as many publications show their results in form of figures from which it is very hard to obtain the raw data. A validation using published literature is therefore often only possible in form of a visual comparison of curves, resulting in a poor comparison quality and justifies its low ranking. The validation is mainly carried out on simple geometries to limit the computational effort especially for the 3D-finite-element simulations while keeping the mesh quality as high as possible. Measurements give additional validation for some constituent models. They could not be extended to all constituent models or to similar conditions as the calculation method, or even better to the complete calculation method. The validation is done for all parts separately and not on the complete calculation method as no DFIG is available for field measurements within the timeframe of this work. Whenever possible the calculation method is compared to already used programs validated for other applications. This comparison is rather a qualitative than a quantitative comparison as the used programs have also their hypotheses, precision and drawbacks, making an exact comparison with the same models, geometry and hypothesis impossible.

1.1.3   Notations used

The plasma physics notation is used. This means that the vectors are written underlined instead of with an arrow. The vectors are given for a particular time, so that the simulation performed is magneto-static. Instead of writing

$$\frac{\partial B_x}{\partial x} = \partial_x B_x \tag{1.1}$$

the simplified notation $\partial_x B_x$ is used. In addition, the integrals are written

$$\int_0^1 dx \int_{-1}^2 dy\, x^2 y \tag{1.2}$$

instead of

$$\int_0^1 \int_{-1}^2 x^2 y\, dx\, dy \tag{1.3}$$

in order not to confuse the integration limits of x and y, using the fact that the integration operator commutes.

The surface of the volume V is denoted ∂V and so on for surfaces (which will be denoted Σ) and lines (denoted Γ). When changing the integration variable, for example from ϕ to α, the limits are kept from ϕ_1 to ϕ_2 to keep a link to the geometry of the model. In chapter 6 the underlined quantities refer to phasors. The characters have been chosen uniquely and distinguishable to prevent confusion with vectors used elsewhere in this study.

1.1.4 Structure of this document

Two paragraphs from the author. Before entering in the details of this document, I would like to warn the reader that I deliberately took some style liberties while writing this document. I decided to use a simple and active english to enhance the understanding of the document as my goal is to propagate science and in my opinion scientific literature should be written in a as simple as possible english as the "difficulty" lies in the facts that are presented and not in the text. I therefore avoid as much as possible heavy passive sentences as well as very complicated phrases. In recent years, I have also seen that some authors have the tendency to bring the scientific results "in the mouth" of the reader, which is very positive in the sense that the author tries to makes a big step in the direction for the reader, but I believe that the scientific community made a too big step and one should leave more place for the reflection as well as the critical reflection about the achieved results. I therefore decided to leave an as big as possible place for reflection in this document. For me, science starts with observation of the nature and reflection to transpose its behaviour into equations, so that I tried to bring that fact into the document placing some "reflection points" (normally in separated sections) at some places, where the reader shall not only read the text but also ask himself some questions about the presented facts and results. As I believe that the legitimacy of the results I present in this work are not only based on the expected very good comparison results (which are normally the only one that are presented...) but also on the consented agreement of the reader that he approves my reflection on that topic. This is the main reason, why I also published some details about the reflection that have been made about this topic. Another reason lies that I think that the scientific debate is today too much reduced on the method and its results forgetting the "why-question". Why are we doing this ? Why ... ?

In addition, I have made some method choices, which are based on judgement of values more than a judgement of facts and I decided to keep as they are and I did not try to hide as I think that also in science we sometimes have to make some judgement of value rather than a judgement of facts as for example the choice between Finite-elements calculation or integral field calculation done in chapter 2.

In order to keep the document lean, some of the in-depth-calculations as well as additional figures have been moved into the appendix. The appendix itself is structured again along the chapters of this document.

Figure 1.11 presents an overview about the calculation of the circulating currents. The calculation is a two-level calculation. The first level is the "inductance calculation method", which is a macro-model level also called "method". This level can be understood as a working frame work. The choice of this framework is explained and detailed in chapter 2. The second level of the calculation are the calculation model itself. They are detailed in chapters 4 and 5. Following this introductory chapter this document is divided into the following chapters following a simple structure: theory, current situation, details on models, transient analytical equations and main results.
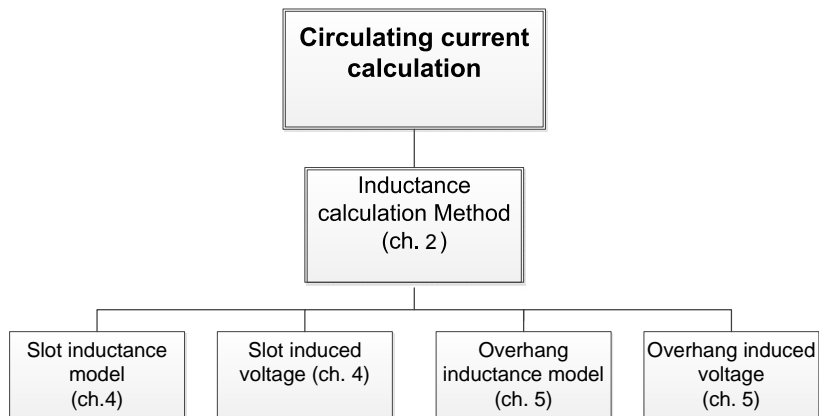
Figure 1.11 – Overview of the circulating current calculation.

Chapter 2

The chapter is dedicated to the description of the published calculation methods and the choice of the calculation method used in this work, namely the inductance calculation method. Each constitutive part, namely the strand inductance and induced voltage in the active part and in the overhang, of this method is analysed afterwards based on the published results. This analysis serves as a base to choose the constitutive parts that will be analysed, improved and used in this work. Finally, the equation system to be solved is presented.

Chapter 3

This chapter must be understood as the continuation of the introductory chapter, as it presents the characteristic curves in the circulating current domain. As this chapter covers a significant number of pages, it have been decided to place this current situation into a separated chapter. In addition, the current situation presents not only an actual state of the art in the circulating current calculation, but it also shows original contributions of this work, so that a placement of this study in the introductory chapter is not appropriate. This chapter presents an original overview of the circulating currents in salient pole hydro-generators. The main and most important transpositions are introduced and their effect is explained in a qualitative way by showing original applications of the known transposition to hydro-generators. The overview gives some ideas about the amplitude and the form the phenomenas which are the focus of this work.

Chapter 4

The slot inductance model is analysed in detail in this chapter starting from the well-known strand inductance model (1.0). Its limitations and precision are shown. The limitations lie in the in account taking of the saturation of the slot, the strand width and position of the strand

in the slot. From these limitations 3 novel models (2.0, 3.0 and 4.0) are proposed to reduce the unwanted effect of the limitations. Model 2.0 takes the strand width into account while it can't cope with two strands in the slot side-by-side and has a bigger error than Model 1.0 used for small strand height. Model 3.0 uses the mirror method to take the real strand geometry into account as well as the 4 boundaries of the ideal slot. This leads to multiple mirrors and double infinite summation. The convergence of this algorithm is asymptotic but its computational cost is too huge for this purpose. Further this model does not cope with the saturation of the slot. Model 4.0 takes all the limitations of the mainly used model into account and is based on the differential inductance calculation. The differential inductance calculation is based on multiple finite element calculation to determine the inductance matrix at a given time step. The results of this model are comprehensively detailed and discussed in section 4.6 and this model is also validated using measurement on a small-scale model.

Two sections, namely sections 4.2 and 4.5, are dedicated to reflections on the calculation of self and mutual inductance taking the conductor dimensions into account and to the use of an exact versus approximated field calculation method. These reflection sections have been place in a such way that the reflection point come directly after the raise of the reflected problem.

Chapter 5

The overhang magnetic field calculation is presented and detailed in this chapter. Novel analytical equations and the equations taken from publications are presented and derived for current conducting elements without cross-section and with a rectangular cross-section. The analytical equations for the magnetic field ($\underline{H}$) as well as for the vector potential ($\underline{A}$) are a novel contribution of this work. The analytical equations for magnetised bodies in cartesian coordinates as well as in cylindrical coordinates are presented afterwards and are composed of a mix of novel equations and equation taken from publication. The publication based algorithm for non-linear iron is described. Some hints, about the numerical calculation of elliptic integrals using known results and a novel approach to deal with the singularities induced by the integral equations, are given. The hypothesis of the 3D computational model used for the magnetic field calculation in the winding overhang is described and justified. Finally the equations developed in this chapter are validated using 3D-finite element simulation and experiments, while the comparison with published literature is kept in a small scale mainly due to the lack of raw data used in the published figures.

Chapter 6

This chapter deals with transient analytical equations for the induction machine (IM) as well as for the double-fed induction motor-generator (DFIG), which are the base for the end-winding magnetic force and mechanical stress computation, as the winding overhang force is maximal during a severe transient like a short-circuit or false synchronisation. In addition, the analytical equations provide a frequency information, which is used to ensure that no

mechanical eigenmodes can be triggered by a severe transient in the complete operating range of a DFIG. Starting with a literature review, the discussion is afterwards continued by the presentation of the novel developed analytical equations: the transient current and electromagnetic torque equations for an induction motor as well as for a DFIG during a severe transient as a two or three-phase short-circuit. The original transient current and torque equations are presented and compared to simulation performed using SIMSEN.

Chapter 7

The knowledge of these forces are very important as any high power electrical machine must withstand short-circuit stresses without any damages. In addition, the winding overhang is the weakest part of an electrical machine compared to other parts, as the winding overhang is only composed by copper and insulation material which are both very weak materials. It is very difficult and expensive to build reinforcement in the overhang, so that it is very interesting to compute and optimise the winding overhang force. Many authors published results on the force calculation in the end-winding of electrical machines, as for example [45].

After starting with a comparison of the calculated forces using the equation developed in this work with an in-use integral force calculation tool, this chapter presents some original contributions to the end-winding force calculation, namely the contribution of each bar to the force, the influence of the active part boundary to the force in the case of a DFIG and the influence of the approximation (refer to section 4.5) to the end-winding force.

Chapter 8

This chapter is dedicated to the presentation of the original results of the circulating current calculation in the rotor and stator roebel bars of a DFIG under different operating conditions and applying different boundaries.

It starts with the explanation of the model used for each part of the circulating current calculation according to figure 1.11 to close the loop started in chapter 2. The composition of the chain-matrix in the active part is detailed afterwards. Some pictures of the induced flux in the winding overhang are shown to explain the origin of the induced voltage in the overhang.

After the practical description of the calculation method and models, this chapter continues then with the presentation of the circulating current calculation presenting a lot of cases for both stator and rotor applying different boundaries of the active part, showing the impact of the stator and rotor winding on the circulating currents and detailing the impact of the operating point on the circulating currents. Then some results using special transpositions are shown and an optimisation of the transposition is presented and its loss impact. Finally, the impact of the ventilation slits on the circulating currents is presented. All the results presented in this chapter are original contributions of this work.

Regarding the influence of the boundary, this study must be seen as an exploratory study where first results are obtained, which must be studied more in details to derive more general rules.

2 Fundamentals on circulating current calculation: methods and models

This chapter starts with the presentation of the two main circulating current calculation methods used in the scientific community. The chosen calculation method is duly motivated, without going too deep in mathematical equations. This proposal is underpinned using reference to the corresponding section or to published work. The discussion level is held on a conceptual level only, as the used models will be analysed in details in the following chapters. The elements of the used method are presented afterwards starting with a literature review followed by a motivation of the choice made. Finally, the equation system used to calculate the circulating currents as well as the way to take in account the transpositions are described.

2.1 Circulating current calculation methods

Up to now, there have been two majors methods to calculate the circulating currents.
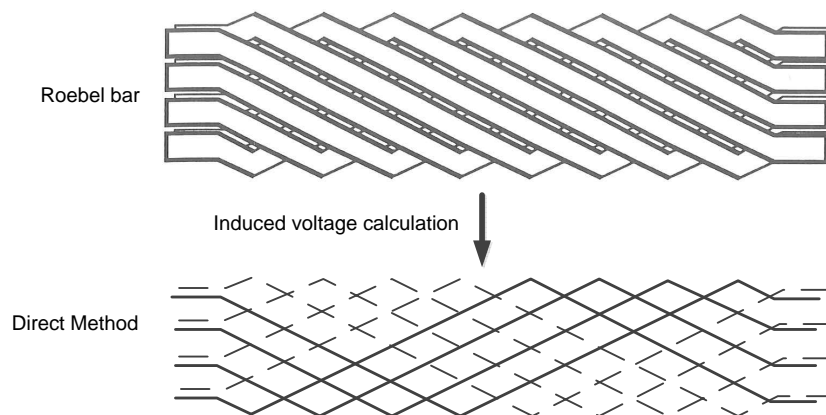
Figure 2.1 – Direct calculation method, the upper part of this figure is taken from [77].

The first one, called "direct calculation", was presented by [104]. The direct calculation uses a 3-dimensional non-linear finite-difference (FD) calculation scheme to obtain the

magnetic field at a given time. The finite-difference calculation is performed on a non-linear 3-dimensional model of the machine, where the calculation domain is adapted taking the periodicity along the θ-axis into account. With the results from this calculation the fundamental magnetic field is obtained from which the electric field is directly deduced applying Maxwell's equations. Integrating the electrical field over one strand leads to the induced voltage. The circulating currents are obtained solving a damper-bar like circuit composed of voltage sources and resistances only. The calculated currents are inserted back into the numerical simulation. This step is repeated upto convergence of the global scheme. This step is mandatory to achieve convergence, as no inductances are considered in the direct calculation there is no feedback from the calculated current to the magnetic field. The transpositions are taken into account, by adapting the integration path to the actual transposition path.
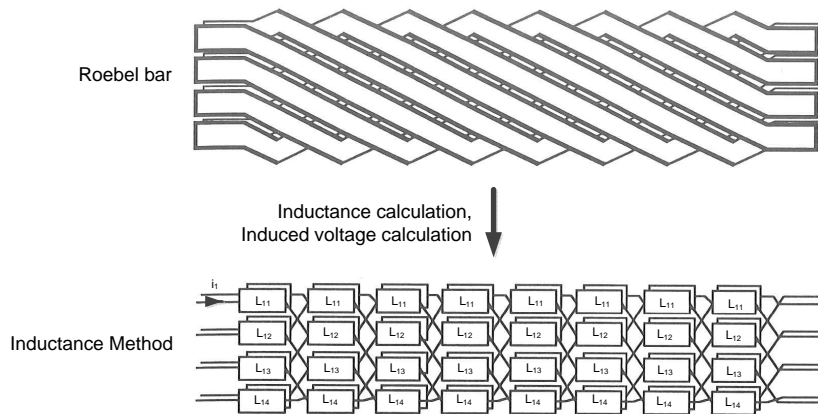
Figure 2.2 – Inductance calculation method, the upper part of this figure is taken from [77].

The second method, called "inductance calculation" can be found in many publications as for example [42], [77] and [68] and seems to be widely accepted and used to solve the problem of circulating current calculation. The inductance calculation uses an analytical or numerical integration of Biot-Savart's law or other numerical schemes (FEM, FD or integral methods) to obtain the induced voltage in the overhang. The strand inductances are normally calculated analytically for the slot portion as well as for the overhang portion using a filament approximation or a round conductor with a given radius. The circulating currents are computed solving a damper-bar like circuit composed by voltage sources, inductances and resistances. There is a priori no iteration with this method. "A priori" because there is an iterative process to obtain the magnetic state of saturable iron or if one would like to take into account the impact from circulating currents in strands of neighbouring bars. To avoid this particular iterative process, the neighbouring strands could be included in the circulating current calculation. In this case, the number of inductances to be calculated will increase quadratically. At some point, one will need to make a trade-off between an iterative algorithm and the complete integration of all strands in the inductance calculation. The transpositions are taken into account via the

so-called "transposition matrix" or "permutation matrix" (refer to [77] and section 2.4).

There are also analytical methods ([93], [94] and [132]) to obtain the circulating currents, their main drawback is that they require an hypothesis on the circulating current distribution. This fact makes them not very interesting for this work where the precision of the calculation methods is one of the major goals. In [94], the authors propose a very interesting decomposition of the strand current into two terms, one in phase with the stator current and one in quadrature to the stator current. The author of [42] uses the same theory as presented in [77] with the only difference that the induced voltage in the overhang is obtained via a finite element calculation.

In this work, the method "inductance calculation" is used. But both methods must give the same results. Forcing the inductance calculation provides a lot of knowledge about the magnetic field as well as of the coupling of the magnetic fields in the overhang. This additional knowledge is a very important additional value of this work and is the key advantage of the chosen method. At any rate, one has to keep in mind that this value-based choice is mainly motivated by the additional knowledge given by the inductance calculation and may be challenged if the expectation regarding computing precision could not be met.

The attentive reader has certainly already noticed that the direct calculation and the inductance calculation are very similar and share a lot of common points. Their main and major difference lie in the usage of the concept of "inductance" or not.

Fundamentally, an inductance is nothing else than a metric, giving an information about the coupling of two circuits / strands, while an induced voltage can be seen as the influence of an external field[1] / circuit without any feedback from the external field / circuit to the circuit / strand. Here lies the single difference between induced voltage and inductance: taking into account the flux feedback or not. Normally, the inductance is defined given one closed circuit (self-inductance calculation) or two closed circuits (self-inductance or mutual inductance calculation). Working with damper bars or the strands of a roebel-bar, one needs to rethink this definition, which implies using the concept of "partial inductances" (refer to section 4.2.2 for the definition of this concept and the associated literature review) to get rid of the "closing" of the circuits. In [77] and in [68] the authors define an arbitrary return conductor to calculate the induced voltage as well as the inductances over "closed" circuits, where the "closing" of the circuit is realised using an arbitrary placed return conductor. This is a valuable option, but not the only one. There are always discussions about the "right" choice of its location as well as a possible offset in the induced voltage. It can be proven that the choice is arbitrary and does not influence the results at all.

---

[1]Whereas "external field" respectively "external circuit" must be understood as an external field source having no coupling to the circuit where the voltage is induced.

An offset in the induced voltages and in the inductances can occur due to different definitions of the return conductor. Depending on its size and location, the inductances respectively the induced voltages will depend of the definition of the return conductor. As long, as the definition of the return conductor is the same for all strands, then the impact of the definition of the return conductor is null as the offset is the same for all strands. An offset can also be induced when the different models are added together in the inductance calculation method. In this method, the strand inductances and mutual inductances as well as the induced voltages are added along one strand. To avoid any offset "between" the models, one must ensure that 1V is 1V for all models and that 1H is 1H for all models. To guaranty that this condition is fulfilled is a little bit tricky, especially as the active part of the electrical machine is modelled using a 2-dimensional approximation, while the winding overhang is modelled using an incomplete 3-dimensional model.

For example, in [77] the author defines a current sheet of slot width (b_N) located at $y = h_N$ (refer to figure 2.4) as return conductor for the slot model. The overhang inductances use a cylindrical current sheet return conductor placed at a radius R from the center of the machine. As the radius is constant, the position of the return conductor changes for every strand. To avoid any offset, the current sheet should stay at the same position for all strands. This implies that the inductances may have an offset that will impact the calculated circulating currents. For the induced voltage calculation in the overhang, the return conductor is a filament conductor placed at one extremity of the roebel bar. This leads to different definitions of 1V between the strand inductances and the strand induced voltage, as one considers only differences the impact of the different definition is cancelled. The non-continuity of the return conductor will also produce errors in the circulating current calculation. To overcome the presented issues, [68] proposed modifications of the inductance calculation in the winding overhang.

As a conclusion of the discussion about a possible offset in the inductance and induced voltage calculation, one can state the following recommendations based on my reflection on this topic inspired by the results of [68] and [77]: the return conductor must be continuous in and between the different models, the return conductor must be the same for all strands and the same return conductor must be used for the inductance as well as the induced voltage calculation. If one of this three conditions is not met, then an offset will remain and will impact the calculation of the circulating currents. It is very difficult to quantity this effect, so that one should avoid the creation of any calculation offset. When using a 2-dimensional approximation of the magnetic field to calculate the inductances and induced voltages, then the magnetic field should be 2-dimensional. But this condition is obvious and straightforward.

As it will be shown in detail in section 5.5, the calculation can be divided in a 2-dimensional calculation for the active part and a 3-dimensional calculation for the overhangs without generating any loss of precision or return conductor problem. There is an interaction between the active part and the overhang, which takes place in the last stacking of the stator and /

or rotor where the magnetic field along the z-axis is not null. The z-axis component of the magnetic field is very small, so that its overall impact of the magnetisation that is a function of the magnitude of the magnetic field is negligible. This is the key fact that allows the decomposition of the calculation domain in two parts. So that, as long as the conditions stated in the previous paragraph are all met, then no offset will be generated by the domain decomposition and the inductances and induced voltages represent the "real" values in the complete roebel bar.

Thinking about the topology of a Roebel bar, one can realise that a roebel bar has ($N_{strands}-$1)! possible loops as the brazing lugs short-circuit all the strands together at both ends of the bar. Using that fact and the concept of "partial inductance" there is no need for an explicit return conductor anymore. There is also no need to define an arbitrary return path. It is sufficient to calculate the induced voltage and inductance over one strand and let the closing of the loops be self-defined by the short-circuits at both ends. The unnecessary discussion about the return conductor, its need, its shape or its location can simply be left out. The only drawback of this choice, is that the inductance must then be calculated using the vector potential instead of the flux passing through the loop as there are no more physical loops defined. The field calculation must therefore also provide the vector potential and not only the magnetic field as it is the case in the work published until now. Adding the vector potential in the magnetic field calculation formulation also brings the possibility to easily couple the developed magnetic field calculation to external sources and vice-versa, which generates another positive outcome of this work and transforming that drawback into a very attractive advantage. This work uses therefore the concept of partial inductance, calculated knowing the vector potential, and don't define explicitly any return conductor.

2.2 Chain-matrix model - "inductance calculation" method

This section details the chain-matrix model, also called "inductance calculation" method and presents how the different elements needed by this method are calculated. The different options and methods published until now will be resumed and discussed, while the final choice will be explained and motivated. The proposed method for this work is based on the methodology described in [68] and the theory presented in [77]. The method is divided into the following parts (refer to figure 1.11)

- Strand inductance in the slot;

- Strand induced voltage in the slot;

- Strand inductance in the overhang;

- Strand induced voltage in the overhang;

- Taking into account the transpositions (Permutation matrix or Transposition matrix);

- Obtaining the circulating currents (circulating currents only or strand currents);

In terms of amplitude of the contribution, which must be understood as the numerical value of the term's amplitude expressed in Volts or Henry, the following ranking can be established considering a complete 360°-transposition in the active part:

1. Strand inductance in the slot;

2. Strand induced voltage in the overhang;

3. Strand inductance in the overhang;

4. Strand induced voltage in the slot.

This ranking is derived from the results of figures 4.62, 4.48, 4.46, 4.46, 8.2 and 8.4. Using this ranking one can consider, which terms should be calculated with the highest possible precision, while dividing the different parts in first order contributions (inductance in the slot and induced voltage in the overhang), second order contributions (inductance in the overhang, inductance in the ventilation slits and induced voltage in the slot) and third order contributions (slope of the strands in the transposed part, taking into account the strand column change [refer to figure 1.8]). In practice, first and second order contributions will be evaluated with the same precision as they are both obtained using the same numerical calculation.

The calculation of the strand inductance in the ventilation slits is presented in [77], while the impact of none even distributed ventilation slits is explained and discussed in [52] and [51]. The strand inductance in the ventilation slits only contributes significantly to the circulating current calculation in the case of an incomplete 360°-transposition and in the active part with non-uniformly distributed ventilation slits. In all other cases, the strand inductance in the ventilation has only a marginal impact to the circulating current calculation as the inductance is one to two orders of magnitude smaller than the slot inductance, calculated considering the effect of the surrounding iron, and because the complete transposition in the active part equalises the strand inductances.

The 3D-component of the roebelisation can be decomposed into two parts as depicted in figure 2.3. The first part is the strand-slope. In figure 1.8 the strand has a partly vertical slope to move from the bottom to the top of the bar. This slope is not considered in the permutation-matrix, which only considers permutation of strands located at the same vertical position [77]. The permutation-matrix can be seen as a step-function on a slope point of view. Taking the slope of the strand into account leads to a much smoother approximation of the roebelisation than with the permutation-matrix. The second part is the column change. When the strand arrives at the lowest row of the roebel bar, it changes the column and moves up again. This part is neglected by the permutation-matrix. Fully taking into account the 3D-component of
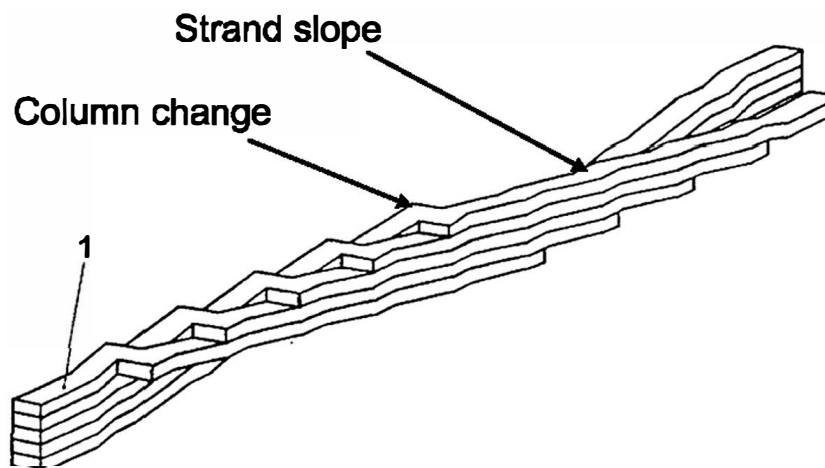
Figure 2.3 – 3D-components of the roebelisation, source US Patent 5'777'417 reproduced with the autorisation of the right-holder.

the roebelisation leads to the suppression of the permutation-matrix in the circulating current calculation which is replaced by a continuous inductance function of the strand position. The method proposed in [104] already uses this concept and does not use the permutation-matrix.

The main focus of this work is the first and second order contributions, nevertheless the methodology developed here makes it possible to take also these third order effects into account in the circulating current calculation using the differential inductance model.

2.2.1 Strand inductance in the slot

Figure 2.4 shows a schematic representation of 2 strands in an ideal slot. There are many publications about the calculation of the strand inductance in the slot (refer for example to [77], [68], [80], [132], [42], [34] and [26]). They all use the infinite iron permeability hypothesis. As shown in chapter 4, this hypothesis leads to errors in the inductance which is not in-line with the precision expectations stated in section 1.1. Based on several attempts, leading to the novel models 2.0 and 3.0, to extend the ideal slot model taking into account the exact geometry and location of the strands as well as attempts to take into account the non-linearity, the novel model 4.0 is proposed and validated experimentally. This model is based on the concept of "differential inductances" (presented by [84] and also used in [12]), to overcome this loss of precision and taking into account the different magnetic states of the machine with a very high fidelity (refer to section 4.6). This method can be extended to take the third order contributions into account such as the slope of the bar, but this is outside of the scope of this study.
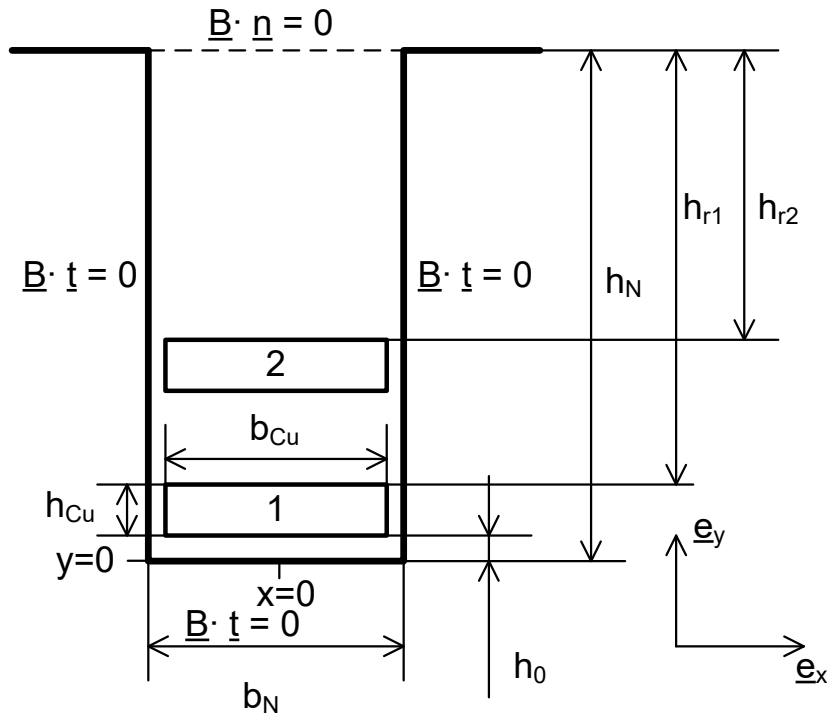
Figure 2.4 – Schematic representation of an ideal slot with 2 strands (copy of figure 4.3, refer to sections 4.1.1 and 4.1.2 and figure 4.3 for explanations about the geometric parameters.)

2.2.2 Strand induced voltage in the slot

[5], [63], [90] and [100] present the notion of "winding function" describing not only the magnetic field in the air-gap but also the induced voltage in slot. Up to now, the induced voltage in the slot, based on the infinite iron permeability hypothesis is very simple: for the bottom bar no induced voltage is considered while a constant induced voltage produced by the bottom bar is considered for the top bar. As shown in section 4.6, no induced voltage in the slot will be considered in this work, the coupling between the top and bottom bars is taken into account in the differential inductance matrix.

2.2.3 Strand inductance in the overhang

[77] developed a strand inductance model for the overhang based on a filament approach for the strand and a thin circular ring $R \gg 1$ for the return conductor. This approach is suitable for a "first shot" calculation, but has a drawback regarding the dimensions and geometry of the strands conductor considering the fact that the position of the return conductor is different for every strand. The bigger the radius R is, the less this position change will impact numerically the calculation. Nevertheless, this approach is questionable on a physical point of view, especially as the loop seems not to be closed in this formulation. [68] eliminated the drawback of the position change of the return conductor by placing it between the two

or more columns of strands and used a filament with a non-zero radius and with a fixed return conductor (with zero radius), identical for all strands belonging to the same roebel bar. This approach eliminates the physically questionable part of the work of [77] and should provide a higher precision in the inductance calculation as the problem of the non-closure of the loop is also solved, but still doesn't fully take into account the geometry of the strands and the exact geometry of the roebel bar in the overhang, taking into account the bending of the bar. In addition as one can see in figure 4.32, the choice of the equivalent radius can lead to overlapping conductors in some cases, which is non-physical. To eliminate this last inconvenience and in order to take into account the ferro-magnetic iron near the rotor bars in the overhang, a similar approach namely using the differential inductance method as for the strand inductance in the slots is adopted. It has the major difference that the inductance calculation will be provided by the 3D-integral calculation in the overhang and not anymore from a FE-calculation, but the basic relations underpinning the method can be kept.

The application of the differential strand inductance calculation to the overhang strand calculation is an original contribution of this work. The precision of the strand inductance calculation in the overhang is showed and discussed in section 5.12, where the newly developed model is compared to the results obtained in [68] and to field measurements. This gives not only an idea of the precision of the calculation, but also on which method, namely this work or [68], should be the most precise.

2.2.4 Strand induced voltage in the overhang

The main drivers for the decision of the constitutive parts of the 3-dimensionnal magnetostatic model are:

- taking the geometry of the roebel bar and the strand dimensions as much as possible into account;

- adding the non-linear ferro-magnetic rotor overhang in the magnetic field calculation;

- trying to remove the mirror-technique of the active part and to add a more accurate contribution of the active part to the overhang magnetic field.

After the slot inductance, the induced voltage in the overhang is in terms of amplitude of the phenomena the second major contributor in the method. The induced voltage calculation is based on the analytical or numerical integration of the Biot-Savart law over the winding overhang or using other methods ([41], [129], [70], [13], [83], [131], [1], [38], [40] and [130]). [105], [91] and [144] also calculate the 3D magnetic field but for linear motors. The winding overhang is divided into several pieces of straight conductors (with zero or non-zero cross-section), where the magnetic field calculation is carried on. [95] presents a 3D-finite element calculation to obtain the eddy-currents in the winding overhang, which could be used as a base

to obtain the magnetic field respectively vector potential in the winding overhang. Analytical or numerical integration provides the required quantity (magnetic field or vector potential). The active part of the electrical machine is modelled using the mirror method ([24], [71] and [39]). A so-called "air-gap conductor" takes into account the magnetic potential difference between stator and rotor ([24], [71] and [39]). The rotor winding is also modelled using Biot-Savart law ([77]). In [45], there is an attempt to take into account the ferro-magnetic iron in the rotor, decomposing the H-field with the Helmholz decomposition. Iterating over a piece-wise linear approximation of the non-linear saturation curve of the iron, decomposing the iron domain in pieces and using a Gramm-matrix like principle to obtain the magnetisation in each iron element ([78], [127]) and Pasciak ([110]). Then the total magnetic field is obtained using Helmholtz's decomposition. Depending on the author, the Biot-Savart law is integrated over filament conductors, or conductors with a given small radius larger than zero.

The integration of Biot-Savart law using straight elements to represent a curved conductor shows that the winding overhang must be divided into many items to obtain a reasonable numerical precision of the magnetic field ([77]). This fact makes this method unattractive as the conductor must be divided into many elements to achieve a reasonable numerical precision. Another drawback of the division of the roebel bar into straight elements, as performed by [77] and by [68], is that the exact bar geometry can not be represented in the field calculation: in roebel bars of hydro-generators, the roebel bar is bent radially and tangentially over radii, so that the 3-dimensional model of the roebel bar must cope with straight elements and curved elements.

Literature research in the domain of the magnets for particle accelerators showed very promising integral solutions for the filament conductor ([133]) and for the rectangular shape conductor ([134]) or for a curved conductor with axial current distribution ([8]). With this integral solution, the number of elements is drastically reduced and is equal to the number of bendings and straight parts in the bar. In different papers ([29], [30], [31], [32] and [145]) the authors show that the magnetic field can also be obtained using "magnetic sources" in the case of known current density. This approach is very promising, but the publication lacks results for the geometry needed for this work, namely arc-elements. As a result the magnetic field calculation of this work is based on the work of Urankar, where the roebel bar geometry can be represented in a quasi exact way, except for the geometry changes due to variation of the manufacturing tolerances, in the overhang taking the bar geometry and cross-section into account.

RADIA[2] and WISE[3] are reference softwares for magnetic field calculation for high precision supra-conducting coils used in accelerators. They can be considered as a precision target for this work, even if the magnetic field calculation for electrical machines does not require such precision levels. The magnetic field calculation developed in this work is not only intended to be used in electrical machines but also in any high precision application like supra-

---

[2]www.esrf.eu/Accelerators/groups/InsertionDevice/Software/Radia/Documentation/Introduction
[3]:wise.web.cern.ch

conductive coils, MRI's devices and so on. RADIA and WISE don't use curved rectangular cross-section elements, so that the analytical magnetic field calculation presented in section 5.1 for the rectangular cross-section is a very important breakthrough in high precision analytical magnetic field calculation and an important and original contribution of this work.

The total magnetic field is computed summing up the contributions coming from the current sources and the magnetic sources applying Helmholz's decomposition. A similar approach is used for the vector potential, which is the base vector field for the inductance calculation.

In [15], [14], [16], [73], [76], [78] and [89] the authors present different ways to take into account boundary conditions in integral formulations. These topics will be discussed in detail in sections 5.2, 5.3 and 5.5. In addition, the ferromagnetic iron of the rotor as well as the active part can be taken into account using integral formulation initially developed for the design of permanent magnet applications ([113], [115] and [140] among others).

Finally, the non-linearity of the iron can be dealt with in a very elegant way using formulations of Simkin ([78], [127]) and Pasciak ([110]). This new feature, which is integrated in the 3D-magnetostatic calculation model, enables to enhance the field calculation capacities of the software developed in this work: taking into account (iron) and in the calculation precision (conductors) while keeping the integral approach.

2.3 Analytical integral field calculation versus finite-element field calculation

Finite-element field calculation versus analytical or numerical integral field calculations is an old and well known opposition. A finite element field calculation has the main advantage of a relative simple system of equations to be solved, while the integral field calculation is based on very complex equations, whose calculation can be time-consuming. In a finite-element calculation the results are dependent on the used calculation mesh, whereas local mesh refinements can be considered but in an a-posteriori way. The integral calculation is mesh-independent, and only the magnetic bodies need to be discretised. The field quantities are only evaluated where they are needed and not everywhere in the calculation domain as for a finite-element calculation. Depending on the needed precision and development time, one or the other method can be chosen. Both should provide very similar results. In this work, it has been decided to stick as long as possible to the integral method because of its very interesting advantages, which are listed here after:

- Exact calculations (refer to section 5.9);

- Smooth results (refer to figure 7.8);

- Calculation on-demand (refer to figure 7.8);

- Taking into account perfectly the geometry of the stator bar (refer to section 5.5.1) and quasi-perfectly the geometry of the rotor bar (refer to section 5.5.1)

- Knowledge of the field origin (refer to section 7.5);

- Mesh independance: the calculation mesh can differ from the model mesh;

- Novel concept of moving mesh (refer to section 5.10);

- Small memory requirement (the complete machine depicted in figure 5.27 without iron takes approx. 650MB of memory);

- Fast calculation using Fukushima's calculation algorithm for elliptic integrals;

- Easy parallelisation of the calculation, considering that the code has been programmed using functional programming.

The concept of "moving mesh" is used mainly for visualisation purposes. The integral field calculation is made to be computed on GPU-based computers and builds therefore a very promising calculation method for the futur. Nevertheless, the choice of the computational method is value-based more than fact-based.

2.4   Taking into account the transpositions (Permutation matrix)

The obtaining of the permutation matrix, also called transposition matrix by some authors, reposes on the multi-pole network theory ([103]). As it can be seen in figures 1.8 and 2.2, the roebel bar is divided in sections spreading over one roebel step. The idea behind the permutation matrix is to keep the inductance, while changing the current passing through these inductances. As one may see in figures 1.8 and 2.2, the current i_1 is located at the top of the column in the first element. Then this current drops down to the second column in the second element and so on until reaching the last column, after that the current i_1 moves up to reaching again its initial position at the end of the bar. The permutation matrix transposes the movement of the current in mathematical terms. For a right-handed permutation, the permutation matrix is

$$
\boldsymbol{P_r} = \begin{pmatrix} 0 & 1 & 0 & 0 & \dots & 0 \\ 0 & 0 & 1 & 0 & \dots & 0 \\ \vdots & \vdots & & \vdots & \vdots & \vdots \\ 0 & 0 & 0 & 0 & \dots & 1 \\ 1 & 0 & 0 & 0 & \dots & 0 \end{pmatrix}
\tag{2.1}
$$

and for a left-handed this matrix becomes

$$
\boldsymbol{P_l} = \begin{pmatrix}
0 & 0 & 0 & \ldots & 0 & 1 \\
1 & 0 & 0 & \ldots & 0 & 0 \\
0 & 1 & 0 & \ldots & 0 & 0 \\
\vdots & \vdots & \vdots & \vdots & \vdots & \vdots \\
0 & 0 & 0 & \ldots & 1 & 0
\end{pmatrix}. \tag{2.2}
$$

A right-handed transposition is a counter-clock-wise rotation of the strands bringing the strand 1 in the position of the strand n (refer to figure 3.1) while a left-handed transposition is a clock-wise rotation of the strands bringing strand 1 to the position of strand 2. Like in the telegrapher's equation ([62]) the $\partial x'$-term must be converted in a Δx-term which is fixed. In this work, the Δx-term represents one transposition length also called roebel step in the 2D step wise approximation of the 3-dimensional transpositions. To avoid the use of the permutation matrix one could also simply add the Δx inductance pieces along the strand path, which is a practicable but not very elegant option to obtain the inductance matrix.

The inductance matrix in the slot as well as in the overhang part is assembled taking into account the transpositions by applying the permutation matrix. The methodology of assembly is the same as used in [77].

2.5 Obtaining the circulating currents (circulating currents only or total strand currents)

Up to now, the circulating currents are obtained solving the following complex equation written considering a two column roebel bar, (refer to [68] for the extension of the equation system to multiple column roebel bars and special column connections)

$$
\begin{pmatrix}
Z_{11} & \ldots & Z_{1m} & \ldots & Z_{1n} & -1 \\
\vdots & \vdots & \vdots & \vdots & \vdots & -1 \\
Z_{1m} & \ldots & Z_{mm} & \ldots & Z_{mn} & -1 \\
\vdots & \vdots & \vdots & \vdots & \vdots & -1 \\
Z_{n1} & \ldots & Z_{nm} & \ldots & Z_{nn} & -1 \\
-1 & \ldots & -1 & \ldots & -1 & 0
\end{pmatrix} \cdot
\begin{pmatrix}
\underline{I}_{c1} \\
\vdots \\
\underline{I}_{cm} \\
\vdots \\
\underline{I}_{cn} \\
u
\end{pmatrix} =
\begin{pmatrix}
\underline{U}_{f1} \\
\vdots \\
\underline{U}_{fn} \\
\vdots \\
-\underline{I}
\end{pmatrix} \tag{2.3}
$$

where $Z_{ii} = R_i + j\omega L_{ii}$ with R_i being the strand (DC or AC[4]) ohmic resistance and L_{ii} being the strand i self inductance, $Z_{ij} = Z_{ji} = j\omega L_{ij}$ is the mutual inductance between the strand i and

---

[4]In the slot, the eddy current losses causes a dramatic increase of the strand ohmic resistance, $\underline{I}$ is the bar current, u the branch voltage ([77]) and $\underline{U}_{f1}$ is a so-called "calibrating voltage" which changes when the return conductor is moved. This voltage has no impact on the calculation result. The biggest increase can be found near the air-gap. [43], [101] and [102] present calculation methods to obtain the eddy current losses for an ideal slot with equalised strand currents.

j, u the induced voltage in the strands and $\underline{I}_{ci}$ the strand circulating current (refer to figure 3.1 for the strand numbering). The last equation of (2.3) states that the sum of the circulating currents must be equal to zero, as the brazing lugs are short-circuiting the strand at both ends of the considered two-column roebel bar. This equation must be adapted when considering multiple column roebel bars and/or special connections of multiple roebel bars. In this case, it may be necessary to write multiple current conservation equations to take into account the multiple brazing lugs or special connections from one roebel bar to another roebel bar. The current in the strand i is then given by

$$\underline{I}_i = \underline{I}/n + \underline{I}_{ci} \tag{2.4}$$

where $\underline{I}$ is the bar current which is uniformly distributed over all strands. In [77], the equation system is written in terms of total current, which makes the inductance calculation more complicated as one needs to use the total bar current while in [68] the equation system is written in terms of circulating currents only. As this work uses differential inductance calculation, the equation system must be written in terms of total strand current, as the differential inductances are obtained for "small" strand current variations around the "DC-value"[5] of the strand current ($\underline{I}/n$).

Taking into account the non-linear iron leads to the following options: the first one is to make a hypothesis on the sinusoidal distribution of the magnetic field or the H-field (refer to Flux 2D). The advantage of this hypothesis is that the resolution of the circulating current equation is simplified to a matrix inversion problem while the overhang field calculation can be obtained in one simulation step. The drawback of this method lies in the fact that one must choose to set the magnetic field or the H-field as sinusoidally varying, which is a priori not an easy task and that the circulating currents are supposed to have a sinusoidal time-variation. The second option is to make a time-stepping simulation. This means that the differential inductances as well as the winding overhang induced voltage are calculated for each time step as well as the winding overhang inductances. The advantage of this option is that there is no need for a sinusoidal approximation of the magnetic field and of the circulating currents. The main drawback is the increase of the simulation time.

Simulation time is an important factor in the design of an electrical machine, but the calculation of the circulating current is performed only once per machine design. Therefore, the simulation time becomes a secondary parameter of choice. The second option has the advantage of its capability to be easily simplified to perform the first option. Using the second option, it is possible to see if the circulating current has higher harmonic contents, which is

---

[5] The strand current "DC-value" is defined by $\underline{I}/n$ where $\underline{I}$ is the bar current and n is the number of strands in this bar. In fact, it is an abuse of language, as the bar current has a time variation. The word "DC-value" refers here to the homogenous component of the current, where the "AC-value" of the current can be understood as the circulating current component of the strand current. This decomposition follows the losses decomposition where the so-called "DC windage losses" are defined by $P_{DC} = R_{DC} \cdot (\underline{I} \cdot \underline{I}^*)$ with the *-operator representing the complex conjugate. In this decomposition, the circulating current losses are accounted as "AC losses". From this point of view, it makes sense to divide also the strand current in an AC- respectively DC-component.

2.5. Obtaining the circulating currents (circulating currents only or total strand currents)

not possible with the first option.

Taking all these considerations into account leads to the choice of the second option for this work, keeping in mind that adding the feature of the first option can be easily implemented after. The circulating current equation becomes then the matrix-form of the following equation

$$u = R \cdot i + \frac{d}{dt} \psi \tag{2.5}$$

where ψ can be even an external flux (if there is no influence of the circulating current on the induced flux) or $\psi = L \cdot i$ if one should expect some influence of the circulating current on the induced flux. Equation 2.5 is nothing else than the time-dependant form of equation 2.3. In matrix-form one obtains

$$A \frac{d}{dt} i(t) + B i(t) = C(t). \tag{2.6}$$

The equation given by relation 2.6 cannot be solved directly in this form as it lacks the current conservation. The current conservation equation is given by

$$\sum_{i=1}^{n} i_i(t) = i(t) \tag{2.7}$$

where $i(t)$ is the known bar current, which can be zero depending on the calculated operating point. $i_i(t)$ is the total strand current, composed by its DC-value and its circulating current component and n is the total number of strands per bar. If more than one bar is considered in the equation system, then a current conservation equation per bar must be considered. The following development is made considering only one bar, where as its extension to multiple bars is straightforward and will be therefore omitted. The voltage equations must be changed as the additional equation, namely the current conservation equation, would lead to a zero-line and a zero-column in the matrix A. One voltage equation must be dropped to solve this issue. Proceeding in a similar way as in [84], this leads to the following branch-voltage equations

$$u_i(t) + r_i i_i(t) + \frac{d}{dt} \psi_i(t) = u_i(t) + r_i i_i(t) + \frac{d}{dt} \sum_{k=1}^{n} L_{ik} i_k(t) \tag{2.8}$$

$$u_j(t) + r_j i_j(t) + \frac{d}{dt} \psi_j(t) = u_j(t) + r_j i_j(t) + \frac{d}{dt} \sum_{k=1}^{n} L_{jk} i_k(t) \tag{2.9}$$

where i and j are the index of two strands, $u_i(t)$ respectively $u_j(t)$ their induced voltage, r_i and r_j their resistance and $\psi_i(t)$ and $\psi_j(t)$ their fluxes expressed in form of a linear combinaison of time invariant inductances time the corresponding current. The voltage equation is obtained performing the subtraction $u_i(t) - u_j(t)$. The loops are chosen in a way that $j = i + 1$ and the

last strand current i_n is replaced by

$$i_n = i(t) - \sum_{i=1}^{n-1} i_i(t). \tag{2.10}$$

In terms of return conductor, one could see the replaced strand as the return conductor. The replacement choice is arbitrary and any other current could be used for this replacement. This leads to

$$u_i(t) - u_{i+1}(t) + r_i i_i(t) - r_{i+1} i_{i+1}(t) + \frac{d}{dt} \sum_{k=1}^{n} L_{ik} i_k(t) - \frac{d}{dt} \sum_{k=1}^{n} L_{(i+1)k} i_k(t) = 0$$

$$u_i(t) - u_{i+1}(t) + r_i i_i(t) - r_{i+1} i_{i+1}(t) + \frac{d}{dt} \sum_{k=1}^{n-1} L_{ik} i_k(t) +$$

$$L_{in} \frac{d}{dt}(i(t) - \sum_{i=1}^{n-1} i_i(t)) - \frac{d}{dt} \sum_{k=1}^{n-1} L_{(i+1)k} i_k(t) - L_{(i+1)n} \frac{d}{dt}(i(t) - \sum_{i=1}^{n-1} i_i(t)) = 0$$

$$\frac{d}{dt} \sum_{k=1}^{n-1} (L_{ik} - L_{in}) i_k(t) + \frac{d}{dt} \sum_{k=1}^{n-1} (L_{(i+1)n} - L_{(i+1)k}) i_k(t) + u_i(t) - u_{i+1}(t) +$$

$$r_i i_i(t) - r_{i+1} i_{i+1}(t) + (L_{in} - L_{(i+1)n}) \frac{d}{dt} i = 0. \tag{2.11}$$

This equation is valid for all i expect for $i = n - 1$ where it gets

$$\frac{d}{dt} \sum_{k=1}^{n-1} (L_{(n-1)k} - L_{(n-1)n}) i_k(t) + \frac{d}{dt} \sum_{k=1}^{n-1} (L_{nn} - L_{nk}) i_k(t) + u_{n-1}(t) - u_n(t) +$$

$$r_{(n-1)} i_{(n-1)}(t) + r_n \sum_{k=1}^{n-1} i_k - r_n i + (L_{(n-1)n} - L_{nn}) \frac{d}{dt} i = 0. \tag{2.12}$$

The equations can be written in a matrix-form similar to the one of equation 2.6 where $\boldsymbol{A}$ is given by

$$\boldsymbol{A} = \begin{pmatrix} \sum_{k=1}^{n-1}(L_{1k} - L_{1n}) + \sum_{k=1}^{n-1}(L_{2n} - L_{2k}) \\ \vdots \\ \sum_{k=1}^{n-1}(L_{mk} - L_{mn}) + \sum_{k=1}^{n-1}(L_{(m+1)n} - L_{(m+1)k}) \\ \vdots \\ \sum_{k=1}^{n-1}(L_{(n-1)k} - L_{(n-1)n}) + \sum_{k=1}^{n-1}(L_{nn} - L_{nk}) \end{pmatrix} \tag{2.13}$$

the partial differential strand self and mutual inductance matrix, $\boldsymbol{B}$ is defined by

$$\boldsymbol{B} = \begin{pmatrix} r_1 & r_2 & \dots & \dots & 0 \\ \vdots & \vdots & \vdots & \vdots & \vdots \\ 0 & \dots & r_m & r_{m+1} & 0 \\ \vdots & \vdots & \vdots & \vdots & \vdots \\ r_1 & r_2 & \dots & 2r_{n-1} & -r_n \end{pmatrix} \tag{2.14}$$

the diagonal DC or AC strand resistance matrix and C is given by

$$C = \begin{pmatrix} u_2 - u_1 - (L_{1n} - L_{2n})\frac{d}{dt}i \\ \vdots \\ u_{i+1} - u_i - (L_{in} - L_{(i+1)n})\frac{d}{dt}i \\ \vdots \\ u_n(t) - u_{n-1}(t) - (L_{(n-1)n} - L_{nn})\frac{d}{dt}i \end{pmatrix}. \tag{2.15}$$

The induced voltages u_i and u_j are obtained using a first order numerical approximation of the time-derivative of the external flux. The equation is solved using the common and widely used explicit fourth order Runge-Kutta scheme. Numerical experiments show that a second order Heun scheme is also sufficient to achieve convergence. The integration time step lies around $10\mu s$ as the inductances are small quantities around $10\mu H$. When the inductance is not time independent, the equation of C must integrate an $i\frac{d}{dt}L_{ij}$-term to reflect the saturation of the inductance.

The division of the flux in the external flux (taken into account in C of equation 2.6) and the inductance flux (taken into account in A of equation 2.6) is detailed and justified in section 8.1. Depending of the flux division made, n can refer to the total number of strands on one roebel bar or to the total number of considered strands.

The global equation system is composed of as much partial contributions as there are transpositions in the calculated roebel bar. The equation system must be written for a strand current numeration, so that the contributions of the other parts must be projected in the chosen strand current numeration framework. The choice of the strand current numeration is arbitrary and is set considering the strand numeration following figure 3.1 valid for the first part of the roebel bar on the non-connection-side. Starting with this choice, the other contributions are added to the corresponding matrix using the following "detransposition" equation

$$L_{di} = P^{-i} L_i P^i \tag{2.16}$$

where L_i is the inductance matrix of the i-th element, L_{di} its detransposed form and P is the permutation matrix. The right-side multiplication takes into account the current transposition of the i-th element (refer to figure 2.2), while the left-side multiplication places the resulting voltage equation to the corresponding detransposed strand. For the induced voltage, the right-side multiplication can be omitted.

2.6 Conclusion

The inductance calculation method is used in this work as this method provides a lot of knowledge around the magnetic field as well as of the coupling of the magnetic fields in the

overhang. This additional knowledge is a very important additional value of this work and is the key advantage of the chosen method.

In a second step, the part of this method based on the decomposition done in [77] is presented. A ranking of the contribution of each part to the circulating current calculation is done by separating first order components with second order components and finally third order components. This original part helps to focus on which parts should be calculated with the highest precision to reach the precision goal fixed in section 1.1. For each part, the conducted analysis leads to the choice of the calculation method used in this work, whereas original contributions of this work are emphasised. The 3-dimensional winding overhang field calculation methodology is also detailed and the main advantages of the integral method are presented. Finally the circuit equations used for the calculation of the total strand current are presented and some practical aspects of the numerical integration of the circuit equation system have been highlighted.

3 Current situation and impact of the circulating currents in synchronous hydrogenerators

The aim of this chapter is to present a brief overview of the current situation in the circulating current calculation based on a case study on hydrogenerators, to make a brief review of the well-known characteristic curves in circulating current calculation and to set a common vocabulary for this work starting from the methodology and vocabulary defined in [65]. To shorten the text, it have been decided to mix the review of the well-known characteristic curves and the current situation with hydrogenerators. This current review is an original contribution of this work. This chapter is the continuation and finishing of the introduction to this study. It has been decided to present the current situation in a separate chapter as the current situation covers many pages, which would have increased too much the size of the introduction chapter. In addition, this chapter presents also original contribution of this work that shall not be included in the introduction chapter.

The topic of circulating current calculation has been comprehensively studied for more than 40 years mainly for turbogenerators, where the circulating current losses are significantly higher than for hydrogenerators (refer to figure 3.2 and other from chapter 3). First studies were conducted in the field of turbogenerators as they experienced damaged stator bars due to the excessive circulating current losses. At least three PhD-thesis have been written in this topic with the main goal to model the circulating losses within a computer program and to enhance and validate this model with field measurements [104], [77], [66], [67] and [68]. Some studies have also been done to compute the circulating current losses for several hydrogenerators [65]. This study concluded that there was no significant potential for circulating current loss reduction within hydrogenerators so there have been no further studies for a certain time.

The presented transpositions have already been widely analysed and published (refer to [65], [68] and its bibliography and [77] and its bibliography), whereas their application and study applied to hydrogenerators (salient pole machines) has not been studied in details or

published until now. The current situation starts with the "classical" transpositions 0/360/0[1], 0/450/0 and 0/540/0 and highlight their effect on hydrogenerators. After that, the impact of special active part roebelisation is shown. Finally the study moves to optimisation of the transpositions in hydrogenerators, combining a special active part transposition with an additional transposition in the winding overhang. This case study has been conducted using a software originally developed for turbogenerators. It is obvious that the modelling of the rotor will significantly differ from a turbogenerator to a hydrogenerator. This fact doesn't reduce the validity of this study as the rotor has only a small impact on the curves (refer to figure 3.5) which is mainly explainable by the fact that the rotor overhang is constructively much more shorter in hydrogenerators than in turbogenerators. Therefore, the model used for the rotor, which is certainly perfectible, has only a marginal impact on the obtained results leading to a very small reduction of the validity of these results. As this calculation has not been validated for hydrogenerators, the results should also be appreciated with some caution, but as the model is always the same regardless of the transposition angle one can state that the difference between two results should be correct, while their absolute value may present some errors.

The original contribution of this work lies in an exploratory study of the impact of the well-known different transpositions applied to hydrogenerators as well the optimisation of the circulating current losses in roebel bars of hydrogenenrators using incomplete active part transposition and / or overhang transpositions. The results of this study permitted to file a patent [64].

3.1   0/360/0-Transposition

The strands are numbered according to the following scheme (refer to figure 3.1) and follow the notation presented by [68]. The strand current is the peak-value of the calculated strand current at nominal grid frequency. It can be expressed in Amps or in pu, where 1pu is defined by the division of the nominal bar current by the number of strands which can also be called the "DC-strand current".

Figure 3.2 presents the circulating current in a Turbogenerator and in five salient-pole synchronous hydrogenerators. One can see that the turbogenerator exhibits, as expected, the highest circulating currents with a circulating current loss factor (fs) of 1.5022. This means that the circulating current losses represents a 50.22% mark-up on the DC winding losses. Hydrogenerators have a non negligible but smaller amount of circulating current losses. Speaking in kW, it may happen that a "Large" machine has more additional losses due to circulating current as a "Small" or "Medium" unit, because a "Large" machine has normally 1400-1500 stator bars, while a "Small" or "Medium" unit has only a few hundreds of it. This transposition

---

[1]0/360/0 means 0deg transposition in the NDE-Overhang, 360deg transposition in the active part and DE-Overhang.
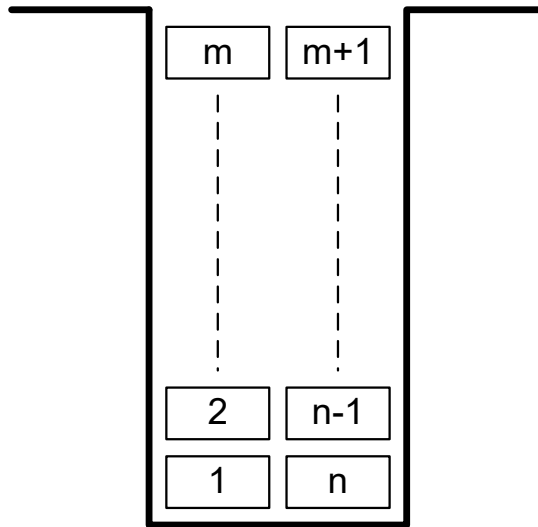
Figure 3.1 – Strand numeration in the slot. The strand numeration is the same for top bars and bottom bars. The top bar is the nearest to the air-gap bar, while the bottom bar lies at the bottom of the slot. n is the total number of strands per bar and m is the number of strands per column. Normally the top and bottom bars have the same number of strands.
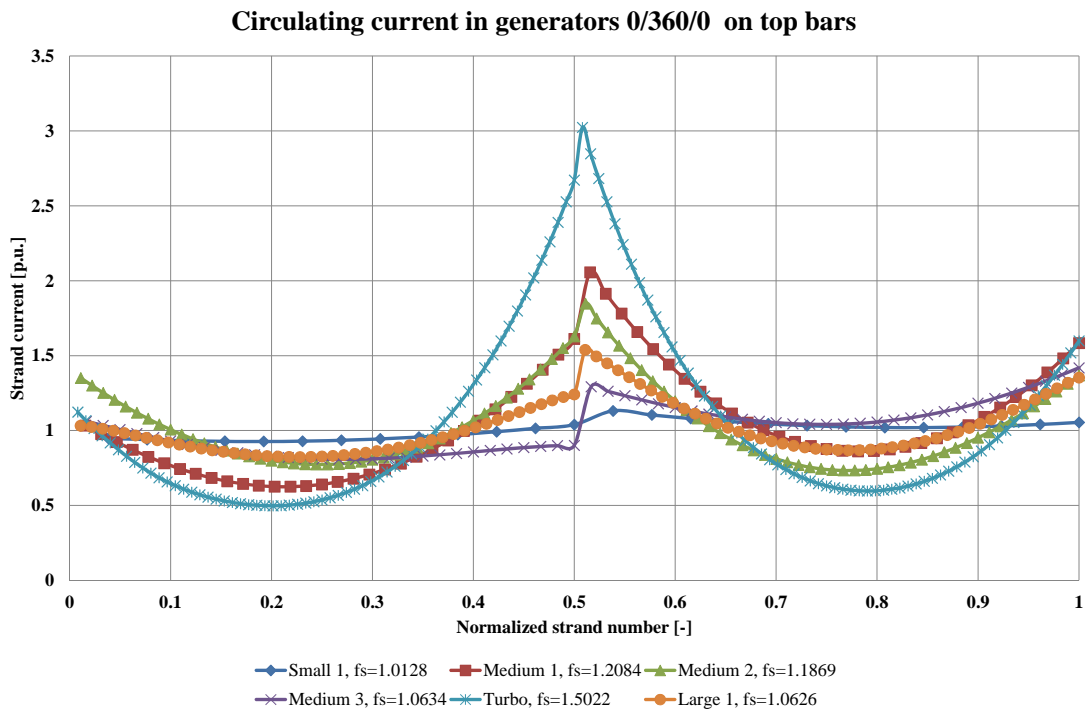
Figure 3.2 – Circulating currents in top bars of generators with a 0/360/0 transposition.

exhibits the most interesting effects caused by the parasitic field in the overhang due to the fact that the overhang has no transpositions. This is the reason why this case study starts with this transposition and its impact on the circulating currents. Table 3.1 shows some parameters of the chosen electrical machine.

Table 3.1 – Parameters of the chosen electrical machines.

Name of the machine	Apparent power (MVA)	Rated voltage (kV)	Rated frequency (Hz)	Rated speed (rpm)
Small 1	25	5.5	50	1500
Medium 1	200	13	50	300
Medium 2	106	15.75	50	333.33
Medium 3	100	12.5	50	500
Large 1	1111.11	24	50	130.43
Turbo 1	700	24	50	3000

The plotted current distribution is composed of an odd and even component. These two components counter-act to the parasitic field in the winding overhang. The even current component reacts to an odd parasitic field, while the odd current component reacts to an even parasitic field. According to the work of [77] and [68], the odd magnetic field is the so-called "internal" field of the bar itself (also called "skin effect" in some publications), while the even magnetic field is produced by the rotor or by surrounding bars also called "external" field (also called "proximity effect" in some publications). The fact that the current and the magnetic field have this odd/even behaviour is due to Ampere's law and to the fact that the rotational operator is an even operator. Figures 3.3 and 3.4 help to explain why the circulating currents have odd and even components.
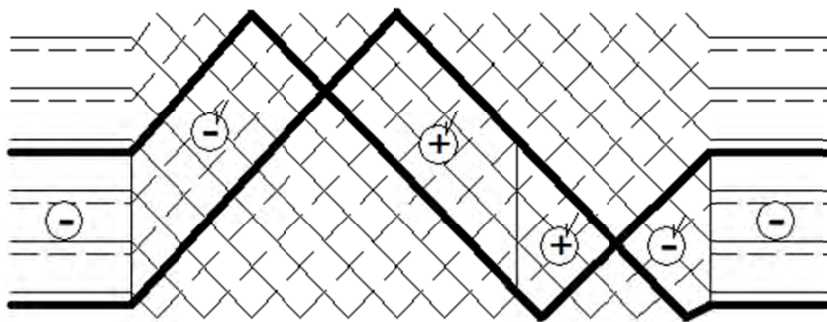
Figure 3.3 – External field compensation in a 0/360/0-transposition of a roebel bar, based on an original scheme from [68] reproduced with the autorisation of the right-holder.

Figure 3.3 shows the external field compensation in a 0/360/0-transposition roebel bar. The sign convention originates from the sign of a magnetic field generated by a circulating current

in the bolded lines. Keep in mind that the brazing lugs, which short-circuit the strands at both ends of the roebel bar, have been omitted in this drawing. Starting from a minus-sign, the sign of the magnetic field generated changes as soon as the strands cross each other. One can therefore deduce that as expected the external magnetic field is fully compensated in the slot, while the overhang component of the magnetic field remains. The slot external field can be seen as the magnetic field produced by the bottom bar in the case of an ideal slot or the radial magnetic field produced by the rotor and the other stator bars.
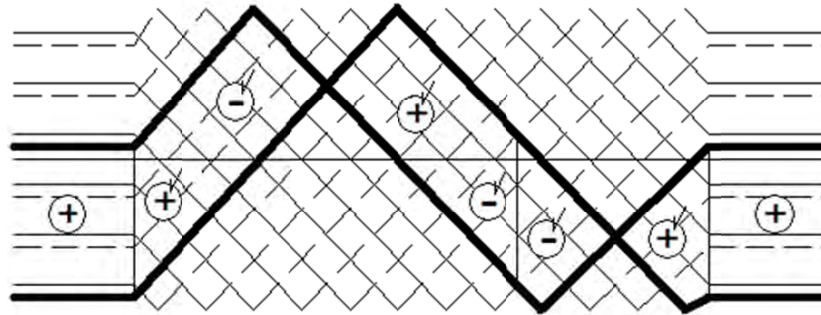
Figure 3.4 – Internal field compensation in a 0/360/0-transposition of a roebel bar, based on an original scheme from [68] reproduced with the autorisation of the right-holder.

The internal field compensation in a 0/360/0-transposition roebel bar is shown in figure 3.4. The line in the middle of figure 3.4 symbolises the median line of the magnetic field. The magnetic field is positive above this line and is negative below it (one can use the right-hand rule on the median line). The sign convention is governed by the following considerations: starting from a plus-sign (the starting sign can be arbitrarily chosen), the sign changes at every crossing of the middle line. When two strands cross each other, there is also a change of sign. As well as for the external field, one can state that the internal field of the roebel bar is fully compensated in the active part and therefore only the overhang component remains.

In hydrogenerators, both the parasitic field due to the bar itself as well as the parasitic field due to external fields are smaller than for a turbogenerator. Nevertheless, an increase in the stator bar height will generate higher circulating currents.

3.2   0/360/0-Transposition, impact of rotor current
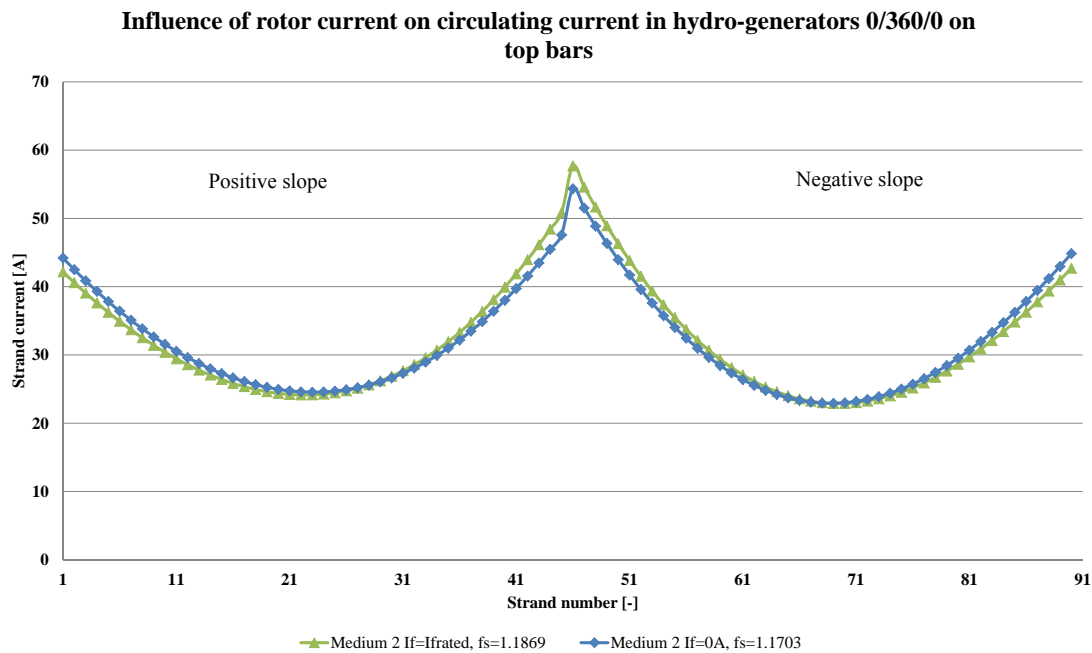
Figure 3.5 – Circulating current in hydrogenerators 0/360/0 on top bars, impact of rotor current.

Figure 3.5 shows the influence of the rotor current on the circulating currents. Its influence is rather low, mainly due to the fact that the rotor is constructively shorter than the stator and that the rotor winding is a concentric winding with a small overhang compared to the one of a turbogenerator. In hydrogenerators, the field winding exceeds the stator by approximately only the half of the width of the conductors composing the field winding. In turbogenerators, the overhang of the field winding, also called rotor overhang, will be constructively much longer and of a completely different construction than the one of a hydrogenerator. On the other hand the rather small influence of the rotor makes its modelling much more difficult, because one needs to be very precise in order to get reliable calculation results. Comparing both curves shows that the rotor induces currents that are oddly distributed regarding the center of one column. For reasons of definition of the strand number, the slope of this curve is greater than zero for the left column and smaller than zero for the right column. The odd current distribution is the main sign for the response to an "external field" [68]. Analysing the curve with no field current but with the nominal stator current shows a similar behaviour, with the difference that the odd distribution in the circulating currents is due to the "external field" produced by the stator winding itself (all bars except the one under analysis). The even current distribution is due to the bar itself ("internal field"), more precisely is due to the winding overhang (DE-side and NDE-side) of this bar, as the active part will not create any circulation current because this part is theoretically fully compensated.

To summarise, the rotor produces only a small amount of circulating current losses, while the

rest of the external field is due to the neighbouring stator winding bars. The main component of the circulating current comes from the bar itself.

3.3 0/540/0-Transposition
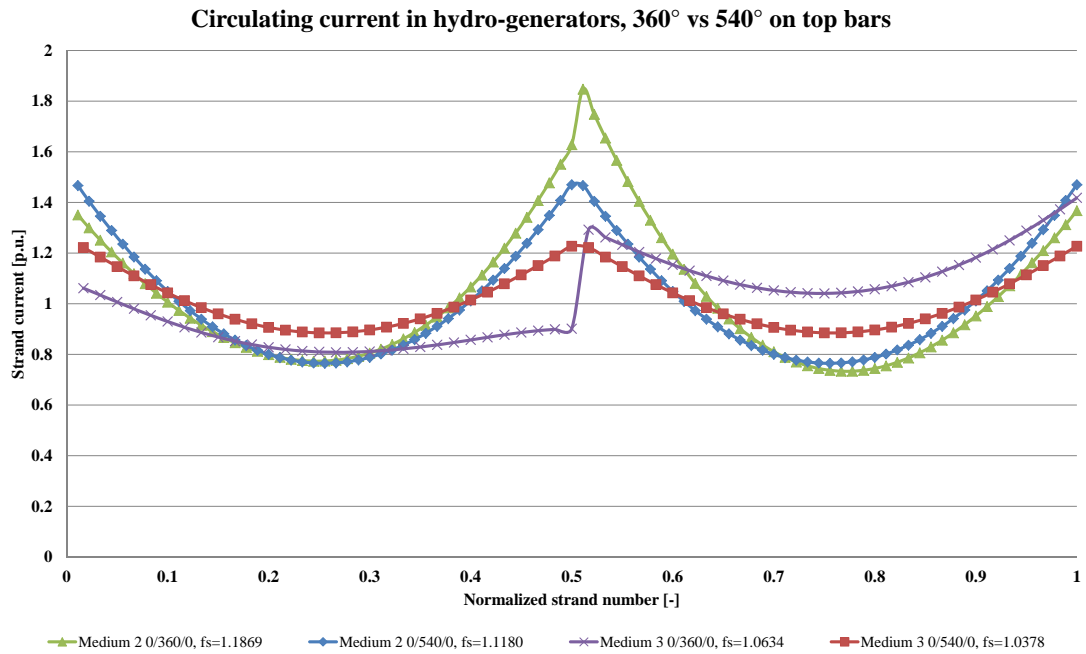
Figure 3.6 – Circulating current in hydrogenerators 0/540/0 on top bars.

Figure 3.6 shows the impact of an 540°-roebelisation in the active part. The major impact of such roebelisation is that the induced voltage of the DE-overhang and the NDE-overhang have a phase shift of 180°. As one may see on the curves, all odd circulating currents are compensated, meaning that the "external field" is nearly fully compensated. The circulating currents have a quasi-pure even current distribution, transposing the fact that only the "internal field" remains and produces circulating currents. Please note that these two machines have a lap winding meaning that the DE-overhang and the NDE-overhang are bent in the same direction and have more or less the same overhang length[2]. This helps massively to obtain a qualitatively good field compensation in the overhang. This situation may be different in wave windings, where one overhang (preferably on DE-side) is not only constructively significantly longer than the other one but also bended in the other direction. On a thermal point of view, the 540°-Roebelisation reduced the thermal hotspot value by 57%, which is not negligible. The main practical hurdle of this roebelisation is the iron length of the machine and the roebel-step. Due to manufacturing processes, the distance between two transposition can't be decreased towards zero, therefore there is a minimal iron length such that 540°-transposition

---

[2]In fact, the winding pitch is reduced by one slot step on the non-connection side, but numerically speaking the length difference between the two overhang is small.

can be done. In practice, there are only a few cases where the iron length is large enough to place a 540°-transposition in the active part of an hydrogenerator.
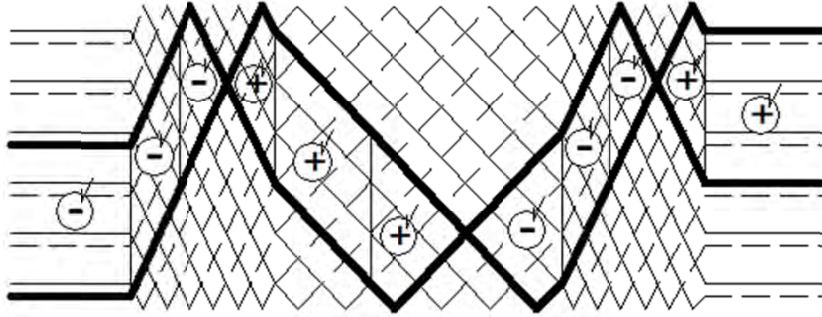
Figure 3.7 – External field compensation in a 0/540/0-transposition of a roebel bar, based on an original scheme from [68] reproduced with the autorisation of the right-holder.

Figure 3.7 shows the compensation of the external field. The 540° transposition induces a change of sign of the induced voltage in the overhang leading to the remarkable fact that the DE-side induced voltage and the NDE-side induced voltage cancel down themselves. The transposition step is divided by two over half of the active length so that this transposition keeps the features of the 360°-transposition in the active part. As it can be seen in figure 3.8, the internal field is not impacted by this transposition.
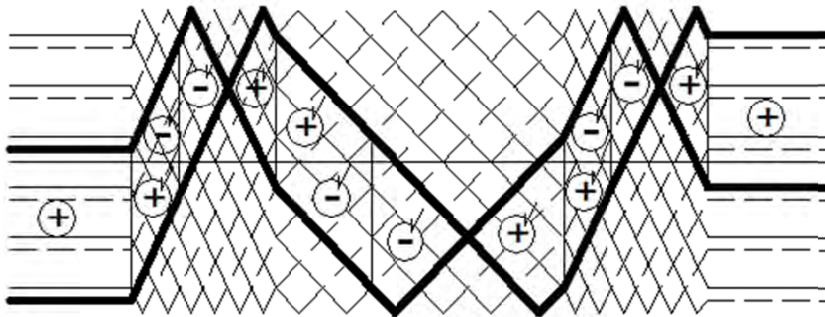
Figure 3.8 – Internal field compensation in a 0/540/0-transposition of a roebel bar, based on an original scheme from [68] reproduced with the autorisation of the right-holder.

To sum up, the 540°-transposition compensates the external field, only the "internal field" remains. The hotspot can be reduced by 57%. Its practical integration in hydrogenerators is not possible in every case due to relatively short active length compared to the minimum roebel step.

3.4   0/450/0-Transposition
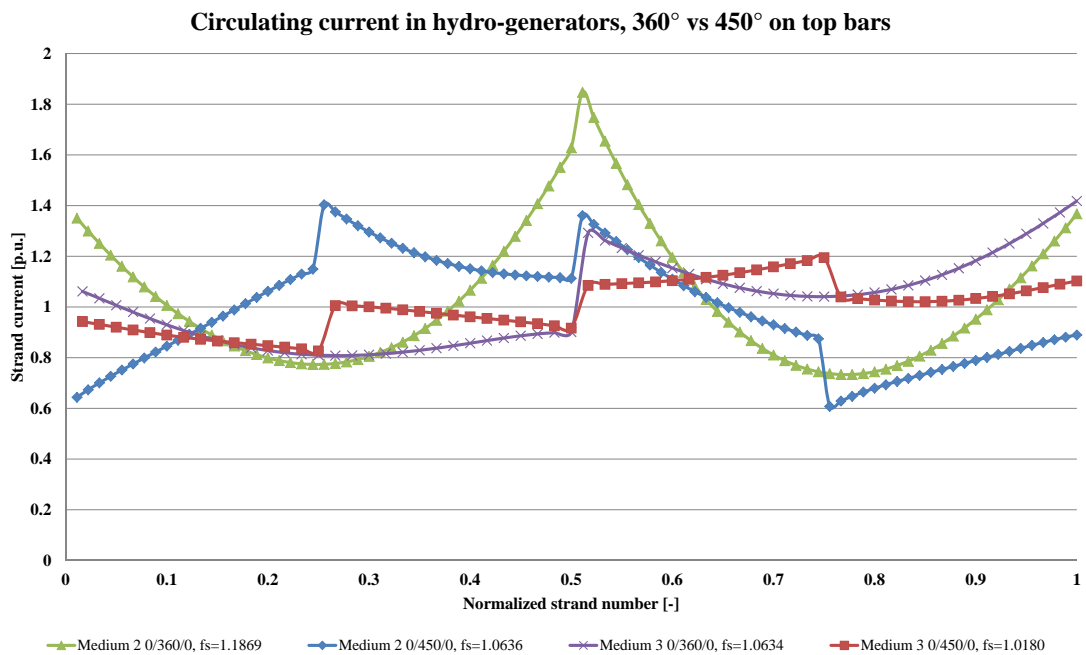
Figure 3.9 – Circulating current in hydrogenerators 0/450/0 on top bars.

Figure 3.9 shows the impact of a 450°-roebelisation in the active part. As one can see, the currents are more or less composed by straight lines, showing clearly that the 0/450/0 transposition compensates quasi perfectly the "internal field". For the machine "Medium 2", the transposition angle equals 452°, while for "Medium 3", the transposition angle equals 450°. This 2° angle difference makes a significant difference on the calculated curves and on the compensation of the "external fields", mainly due to the comparatively short length of the overhangs. The integer number of strands limits the number of possible angles so that this transposition is not always the best practical solution. In addition, this transposition also suffers from the same manufacturing problem as the 540°-roebelisation. Thermally speaking, the reduction of the hotspot is 65%, which is better than for the 0/540/0 transposition, as the main cause of circulating currents in hydrogenerators is the "internal field" and not the "external field".
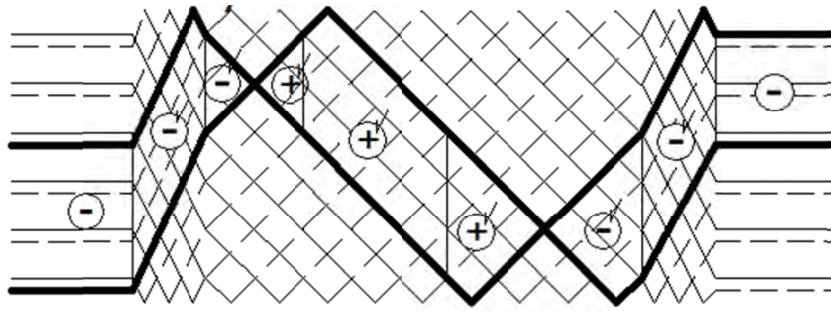
Figure 3.10 – External field compensation in a 0/450/0-transposition of a roebel bar, based on an original scheme from [68] reproduced with the autorisation of the right-holder.
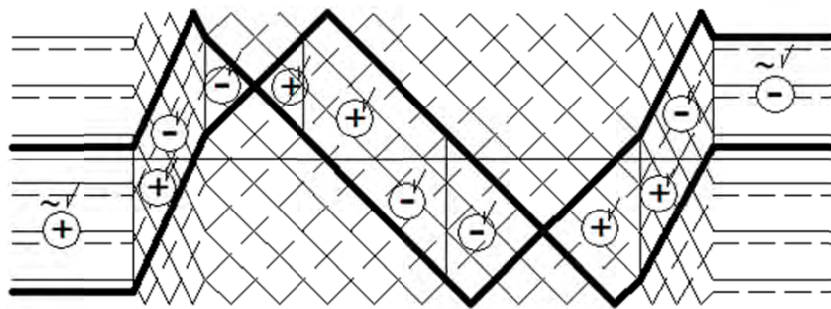
Figure 3.11 – Internal field compensation in a 0/450/0-transposition of a roebel bar, based on an original scheme from [68] reproduced with the autorisation of the right-holder.

Analysing figures 3.10 and 3.11 leads directly to the following conclusion : this transposition cancels the internal field, keeping the external field unchanged.

3.5   Influence of overhang roebelisation - medium size units

Figure 3.12 shows the impact of an overhang roebelisation on a 360°- and 540°-transposition in the active part. In the 540°-transposition, the current distribution is only depending on the internal field. The induction surface reduction in the overhang is particularly remarkable for this transposition as the "external field" is nearby fully compensated by the 540°-roebelisation in the active part. The reduction of the circulating current is more than 10% of the DC copper losses. For the 360°-transposition, the impact is even higher, because the reduction of the surface impacts not only the "internal field", but also the "external field" leading to a loss reduction of 13%. The 540°-transposition produces a very homogenous temperature distribution (as the circulating current factor is near to 1) in the bar, which is very interesting from a cooling point of view.

Figure 3.13 shows the impact of an overhang transposition on the external field compensation. The main impact of this transposition is located in a reduction of the induction surface, which
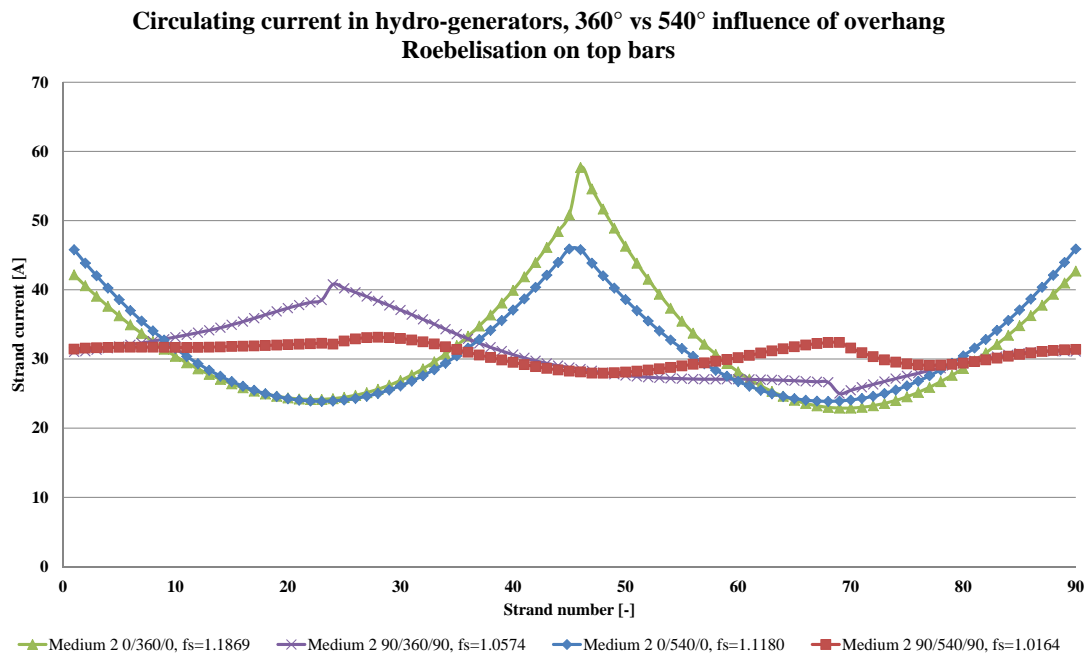
Figure 3.12 – Circulating current in hydrogenerators influence of overhang roebelisation - medium size units.
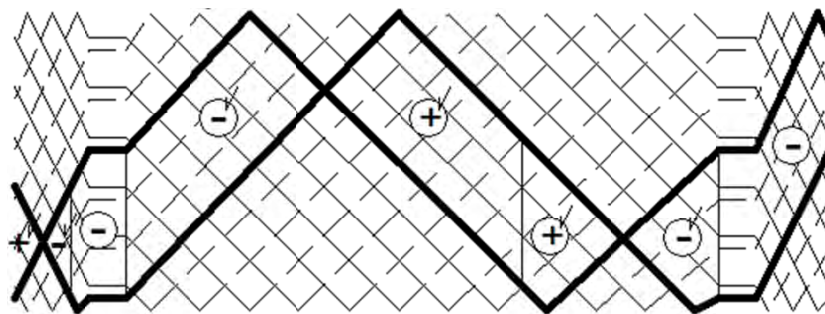
Figure 3.13 – External field compensation in a 90/360/90-transposition of a roebel bar, based on an original scheme from [68] reproduced with the autorisation of the right-holder.
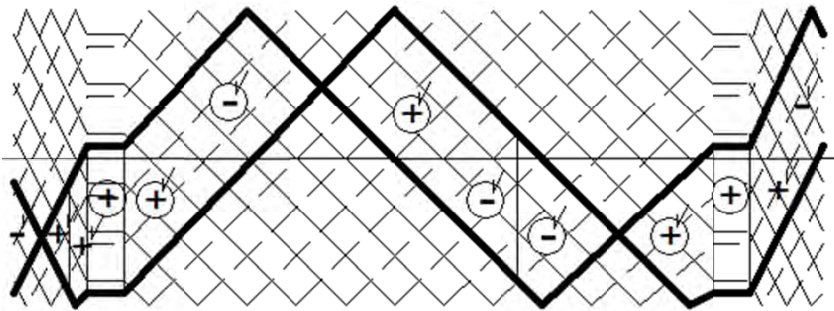
Figure 3.14 – Internal field compensation in a 90/360/90-transposition of a roebel bar, based on an original scheme from [68] reproduced with the autorisation of the right-holder.

implies a reduction of the induced voltage and therefore circulating currents. The perfect overhang compensation would be achieved for a transposition angle of 180° [37], but the overhang is too short in hydrogenerators, so that this solution can never be applied in practice. The same effect can also be seen on the internal field compensation, as depicted in figure 3.14.

3.6 Influence of special transposition in the active part - medium size units
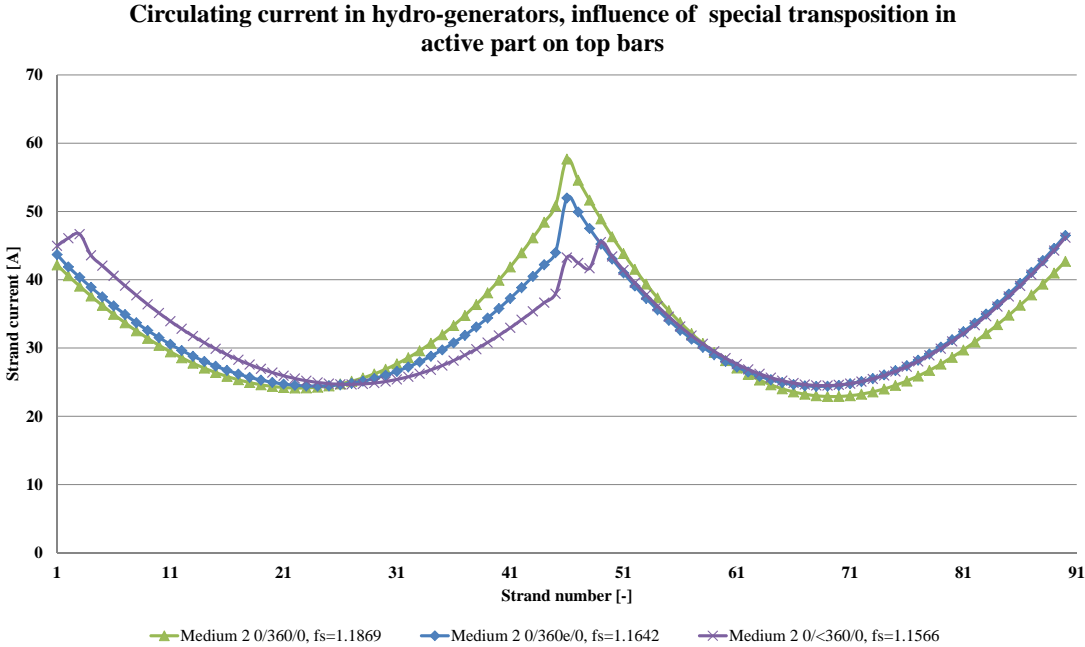
Figure 3.15 – Circulating current in hydrogenerators, influence of special transposition in the active part - medium size units.

Figure 3.15 presents the influence of a so-called special transposition in the active part.

0/360e/0 means that the transposition zone is extended outside of the stator core in the straight part of the stator bar. 0/<360/0 means that the roebel bar does not have a 360°-roebelisation, in the case of figure 3.15 the transposition angle equals 348°, in the active part. The idea behind these special transpositions is to use an extended transposition or an incomplete transposition in the active part to produce an induced voltage which compensates the induced voltage in the overhang. The active part has the largest contribution to the induced voltage as well as to the inductances mainly due to the slot iron. The contribution of the winding overhang is about one order of magnitude smaller than the active part contribution. Keep in mind that this comparison does not take into account the fact that for a 360°-roebelisation in the active part its contribution is zero. To obtain a reliable compensation using the special transpositions, one should use very precise calculation tools as the goal is to sum up two contributions and subtracting them afterwards one from the other.

The incomplete or extended transpositions do not affect every strand, but focuses on the strands with the highest current. The hotspot reduction is much less than for the 540°-roebelisation.
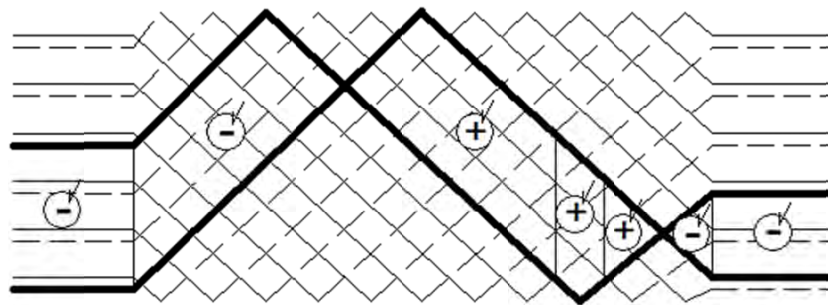
Figure 3.16 – External field compensation in a 0/<360/0-transposition of a roebel bar, based on an original scheme from [68] reproduced with the autorisation of the right-holder.
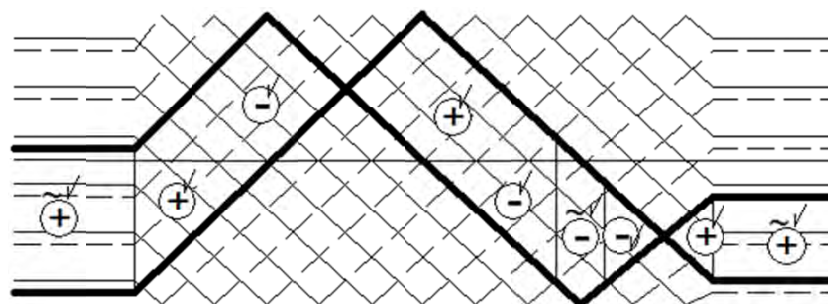
Figure 3.17 – Internal field compensation in a 0/<360/0-transposition of a roebel bar, based on an original scheme from [68] reproduced with the autorisation of the right-holder.

Figures 3.16 and 3.17 show the field compensation in the case of an incomplete active part

transposition. In both figures an excess of "plus surface" (in the case of the external field and minus for the internal field) remains in the active part, which is used to compensate "as good as possible" the excess of "minus surface" (respectively "plus surface" for the internal field) in the winding overhang. As already mentioned, the amplitude of the induced voltage is much higher in the active part as in the overhang part and one also needs to consider the phase angle of the induced voltage. These two facts make the field compensation very tricky and sensitive in practice and this compensation should be applied with caution. As shown in [53] it is also possible to do an incomplete 540°-transposition in the active part to compensate the effect of the winding overhang, this transposition suffering from the same problems as the special 360° transpositions.

3.7 Optimisation of the circulating current losses in hydrogenerators
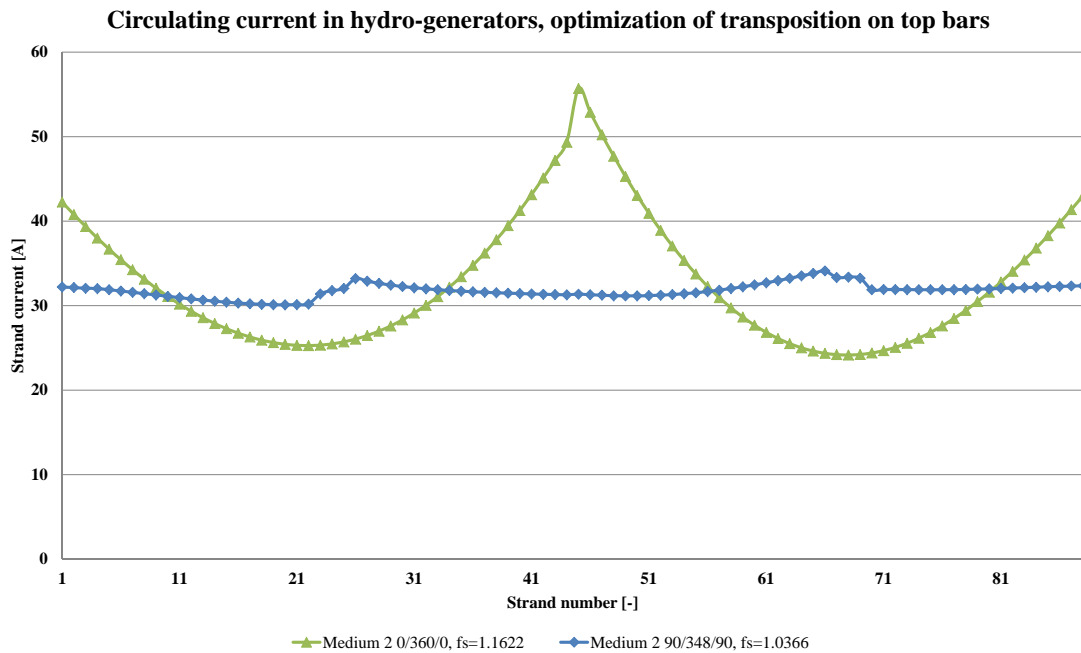
Figure 3.18 – Optimisation of the circulating current losses in hydrogenerators - strand current.

Figure 3.18 shows the result of the optimisation of the transposition on the circulating currents. The circulation current losses have been reduced by nearly 13% of the DC copper losses. The hotspot is also reduced by a factor 2.7 as it can be seen on figure 3.19. The circulating current factor is different than the one presented in figure 3.15 as the design of the machine is not exactly the same: the overhang has different geometry, the bore diameter is slightly different as well as the slot filling. This difference highlights the impact of small design changes on the circulating current losses.

The hotspot is reduced from 3.18 to 1.19 (refer to figure 3.19), so that the stator bar will
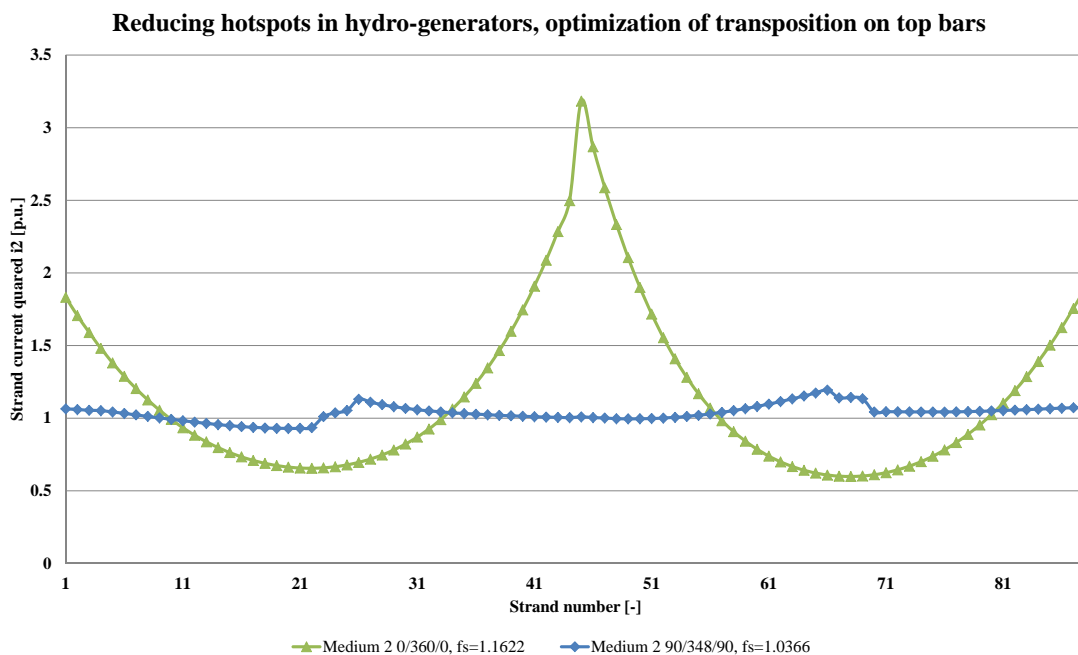
Figure 3.19 – Optimisation of the circulating current losses in hydrogenerators - strand current squared.

thermally speaking react like being fed with DC-current, whereas the eddy current losses have been neglected in the winding overhang as the conductor is surrounded by air. This is a very important parameter regarding the lifetime of the stator insulation as well as its efficient cooling.

3.8 Influence of overhang roebelisation - large size units

Figure 3.20 shows the impact of the overhang transposition on large machines. The impact is very similar to the impact seen on figure 3.12 for medium machines. The machine "Large 1" has a wave winding. The particularity of a wave winding is that the overhangs are not bent in the same direction, leading to a phase shift of more than one pole between the DE-side overhang and the NDE-side overhang. The case -90° on DE-side is added to the study to analyse if this overhang transposition could lead to some advantages regarding a possible circulating current reduction. Unfortunately it is not the case. The losses are bigger than in the 90/360/90 case. It seems that, using this transposition, one overhang is maybe somehow decompensating the other.
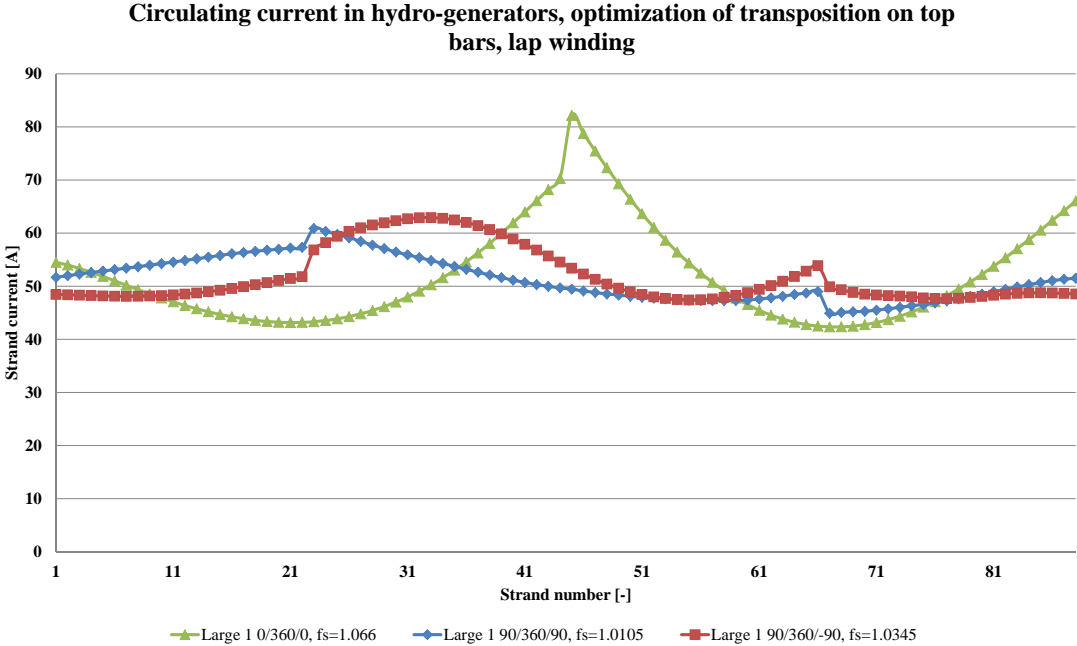
Figure 3.20 – Circulating current in hydrogenerators influence of overhang roebelisation - large size units.
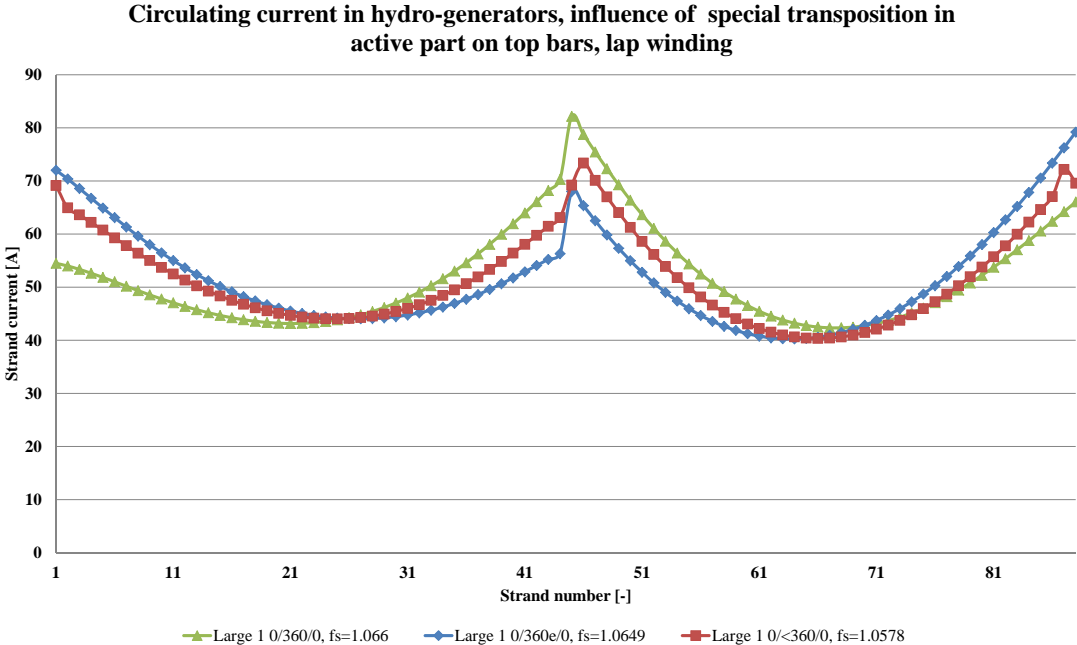
Figure 3.21 – Circulating current in hydrogenerators influence of special transposition in the active part - large size units.

3.9 Influence of special transposition in the active part - large size units

Figure 3.21 shows the impact of special transpositions in the active part. The impact is similar to the impact depicted in figure 3.15. The incomplete transposition case is done removing just one transposition. Once again, the main impact of this special transposition is a reduction of amplitude of the maximal strand current value.

3.10 Conclusion

This case study shows the impact of the "classical" transpositions on hydrogenerators of different sizes, which is an original contribution of this study. As hydrogenerators cover ranges from 4 poles to more than 100 poles it is very difficult to draw precise and unique conclusions regarding the impact of each design parameter on the circulating currents. The rotor has a small impact on the circulating currents. Circulating currents increase with increasing bar height and overhang length. It could not be identified why "Medium 3" has much less circulating currents than "Medium 2" and "Medium 1". Maybe the power criteria used to define the classes "Small", "Medium" and "Large" is not suitable to classify the circulating currents occurring in the stator winding.

The main source of parasitic fields in the overhang is the "internal field" of the bar itself. Special transpositions in the active part do not bring a significant contribution to the reduction of the circulating currents, as they can be seen as a 360-degree transposition from a total bar perspective, while the overhang is much shorter on hydrogenerators than on turbogenerators. The 0/450/0 transposition as well as the 0/540/0 transpositions are not very practicable for hydrogenerators due to their relative short active length. The best way to optimise the circulating current is therefore to make as many transpositions as possible in the overhang [64][3] and eventually to add another contribution emerging from a special transposition of the active part to get the lowest possible circulating current factor. Regarding the precision of the calculation algorithms, one can see that the effects (for example the impact of the rotor) have a smaller amplitude as for a turbogenerator. The computations tools must be very precise to produce reliable results.

The circulating current loss factor is significantly lower compared to a turbogenerator. Nevertheless it is very interesting to chase for an optimal transposition to reduce the circulating currents. The thermal hotspots can be reduced, leading to a reduction of the volume flow needed to cool the electrical machine. This effect is very interesting when thinking about the cooling of the winding overhang, which is always very tricky. In addition, the reduction of

---

[3]The short length of the winding overhang makes it sometimes impossible to manufacture a stator bar with 90° transposition in the overhang.

losses is also very important when designing high efficiency units where one needs not only to consider the additional losses reduction but also the reduction of the ventilation losses due to the better thermal properties of the optimised roebel bar creating a multiplier effect on the efficiency increase.

4 Strand inductance in the slot

This chapter details the slot inductance model used to calculate the strand circulating currents. This chapter strictly follows the methodology described in section 1.1.2: the equations of the tested model are shown as well as some characteristic curves of the model. Then a comparison between the analytical equation and a finite-element simulation is made to highlight the precision of the model and determine its limitations.

This comparison is the base of the decision whether the model is precise enough to be used for further calculation or if it needs to be enhanced by taking into account additional effects. The precision of the method is illustrated by comparison of the computational results with finite-element simulations. These steps are explicitly shown in section 4.1 only, in further sections and chapters these steps will no longer be explicitly mentioned in this document.

This chapter begins with the presentation of the ideal slot model (Model 1.0), which is widely used in the literature (for example [77] and [68]) to calculate the circulating current, starting from its equations and characteristic curves. The precision of the inductance calculation is shown using a comparison between the calculated values using the analytical formula and a finite-element simulation. This study exhibits its limitations: correctly taking into account the strands dimensions and the iron saturation. Starting from the limitations of the Model 1.0, two additional analytical models (Model 2.0 and 3.0) will be elaborated to overcome some of the limitations of the ideal model: mainly the strand geometry limitations. Both models exhibit positive as well as negative aspects, but none of these analytical models permits to take accurately into account the saturation of the non-linear iron in the slot region. These two models are original contributions of this work. 0 As it will be shown in figure 4.11, to get a reliable and precise value for the slot inductance, it is fundamental to take the saturation of the iron into account as the inductance is strongly fluctuating within the magnetic permeance variation of the magnetic materials used in electrical machines. This leads to the novel differential inductance model (Model 4.0) which is presented, discussed and experimentally validated in section 4.6 and used in the circulating current calculation. As two doctoral theses ([84] and [12]) have already been published using the differential inductance model, the theoretical part is reduced and the reader should refer to the corresponding references

to get, if needed, a deep understanding of the theory of the differential inductances. This study is more focussed on a daily use of the differential inductances and tries to answer some practical questions arising from the use of this model. This "practical" study of the differential inductances is also an original contribution of this work as well as the comparison of the calculated circulating currents with measured circulating currents and a comparison with a transient finite-element simulation.

The observations of the ideal slot model (Model 2.0) are the basis of a more global original reflection about inductance calculation: the meaning of the formulae, what they take into account and their suitability for this problem, which is done in section 4.2.1. Section 4.5 applies the known concepts of "near-field" and "far-field", originating from the antenna world, to the field calculation in electrical machines. Using these concepts, one can divide the magnetic field calculation into two distinct zones: in this document, the "far-field"-zone where the magnetic field behaves proportional to $1/r$ in the 2-dimensional approximation and a "near-field"-zone where the magnetic field is highly dependant on the geometry of the current-carrying conductor. This division into two zones shows that precise analytical equations taking into account exactly the shape of the conductor are needed to obtain the inductances with enough precision, as the distances between the strands of a roebel bar are very small, which means that the strands are all within the "near-field"-zones. When calculating the induced voltage produced by all other roebel bars, the "far-field" approximation can be used if the distance between the source roebel bar and the calculation point is large enough. [68] uses a distance criteria to differentiate between near-field and far-field to reduce the calculation time, but it did not characterise and describe the distance criteria. The characterisation and theoretical description and its impact on the magnetic field calculation in the overhang of electrical machines is another original contribution of this work.

4.1 Calculation of the inductances in the slot, current situation (Model 1.0)

Figure 4.1 shows a schematic representation of the ideal slot as shown in [77]. $\underline{B} \cdot \underline{n} = 0$ stand for a tangential boundary condition while, $\underline{B} \cdot \underline{t} = 0$ stands for a normal boundary condition which is used to model the infinite iron permeability of the slot. The magnetic field B_x (refer for example to [77] among others) is given by

$$B_\text{x}(y) = \begin{cases} 0 & \text{for } y \in [0, y_0]; \\ \mu_0 \cdot I \frac{y - y_0}{b_\text{N} \cdot h_\text{Cu}} & \text{for } y \in [y_0, y_0 + h_\text{Cu}]; \\ B_\text{xmax} = \mu_0 \cdot \frac{I}{b_\text{N}} & \text{for } y \in [y_0 + h_\text{Cu}, h_\text{N}]. \end{cases} \tag{4.1}$$

where y_0 is h_0 of figure 4.1. As one can see, the magnetic field is considered one dimensional and that the strand width b_Cu is not taken into account in this model.

Figure 4.2 shows the influence of a change of slot width (b_N) on the magnetic field with

Figure 4.1 – Schematic representation of the ideal slot and its boundary conditions.
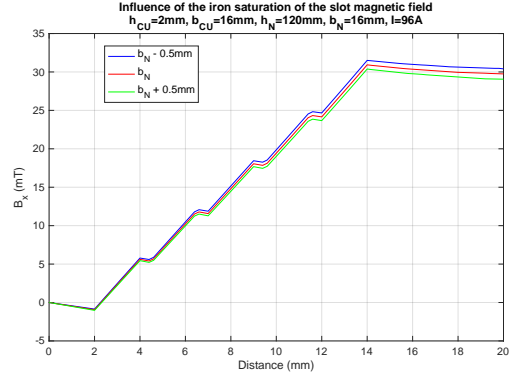
Figure 4.2 – Influence of the slot width (b_N) on the magnetic field B_x, where the distance refers to the y-axis.

constant conductor width (b_{Cu}). All the slot dimensions can be found in the title of this figure. This approach, coming from the plasma physics, will be used consequently in the whole chapter. One can see that each conductor induces a magnetic field ramp as stated by the analytical model and that the maximal amplitude B_{xmax} is a function of the slot width b_N, validating equation 4.1. Between each ramp, the magnetic field has a flat part. This flat part is due to the space between each strand. The length of this flat part is 0.21mm, as per input parameter of the finite-element simulation. The finite-element simulation confirms the analytical equations.

Starting from equation 4.1, one can calculate the self-inductance denoted L_{ii} and the mutual inductance denoted L_{ij} between this conductor (i-th conductor) and another conductor (j-th conductor) placed below the i-th conductor as already shown in [77]. The equations developed in [77] for the self and the mutual inductance will be recalled hereafter. Refer to [77] for the case of a conductor placed above the other.

The flux produced by this conductor (denoted 0) is given by

$$\phi_0 = \int_0^{h_N} l B_x(y) \, dy = B_{xmax} l \left((h_N - (y_0 + h_{Cu})) + \frac{1}{2} h_{Cu} \right). \tag{4.2}$$

The mutual inductance between this conductor and another placed above the first one in the slot, written L_{ij} is given by

$$L_{ij} = \frac{\phi_0}{I} = \mu_0 l \left(\frac{1}{2} \frac{h_{Cu}}{b_N} + \frac{h_N - (y_0 + h_{Cu})}{b_N} \right) \tag{4.3}$$

where the factor 1/2 comes from $\int_0^1 x \, dx$. The calculation of the self inductance is more or less the same, up to one crucial difference: how to take into account the "self flux", or the effect of

the magnetic field on the strand itself. The "self flux", denoted ϕ_{ii} is given by

$$
\begin{aligned}
\phi_{ii} &= \int_{y_0+h_{\text{Cu}}}^{h_{\text{N}}} l B_{\text{x}}(y)\,\mathrm{d}y + \int_{y_0}^{y_0+h_{\text{Cu}}} l B_{\text{xmax}} \frac{y-(y_0+h_{\text{Cu}})}{h_{\text{Cu}}}\,\mathrm{d}y \\
&= B_{\text{xmax}} l (h_{\text{N}}-(y_0+h_{\text{Cu}})) + \int_0^{h_{\text{Cu}}} l \mu_0 I \frac{z^2}{b_{\text{N}} h_{\text{Cu}}^2}\,\mathrm{d}z \\
&= B_{\text{xmax}} l (h_{\text{N}}-(y_0+h_{\text{Cu}})) + l \mu_0 I \frac{1}{3}\frac{h_{\text{Cu}}}{b_{\text{N}}}
\end{aligned}
\tag{4.4}
$$

where $z = y + y_0 + h_{\text{Cu}}$. The self inductance is then given by

$$
L_{ii} = \frac{\phi_{ii}}{I} = \mu_0 l \left(\frac{1}{3}\frac{h_{\text{Cu}}}{b_{\text{N}}} + \frac{h_{\text{N}}-(y_0+h_{\text{Cu}})}{b_{\text{N}}} \right)
\tag{4.5}
$$

where the factor $1/3$ comes from $\int_0^1 x^2\,\mathrm{d}x$. This $1/3$ factor takes into account the "self flux".

To validate these analytical formulae, a comparison between the analytically calculated inductances and the simulated inductances using finite-element simulation is carried out as no publications related this particular topic have been found. One can therefore also consider this validation of the formulae as an original contribution of this work. The considered ideal slot model is adapted to contain 10 strands. Its schematic representation with only two strands is depicted in figure 4.3. The goal of the comparison between the analytical equations and the finite-element simulation is to determine the error and precision of the analytical equation compared to an exact[1] finite-element simulation using exactly the same geometry and boundary conditions (refer to figure 4.1) and not a validation of the hypothesis of the boundary conditions, which will be done at a later stage.

Figures 4.4 and 4.5 show the validation of the equations of Model 1.0. As one can see, the relative error on the mutual inductance is around 5 per 1/10'000, and therefore the model can be considered as validated in the case of infinite permeable iron (with $b_{\text{Cu}} = b_{\text{N}}$).

Figures 4.6 and 4.7 show the comparison between the analytical equation and finite-element simulation. As one can see, the air and the conductor have been separated as the error is around one order of magnitude higher than for the mutual inductance. The "air"-part is located between the last conductor and the slot top, located at $y = h_N$, while the "strand"-part is located at the y-coordinates of the strands. This segregation has been done to find possible root causes for the much higher errors. The error in the air seems to be higher than the one in the conductor. In addition, the energy calculation is more sensitive to errors as one integrates the magnetic field squared. It can be concluded that the magnetic field calculation contains some errors that need to be corrected, as the error on the self inductance leads to errors of the order of magnitude of 1% in the circulating current (refer to table 4.1). The energy is plotted for the main inductance instead of the inductance, as it is more convenient to extract this

---

[1] Considering the geometry and the boundary conditions of figure 4.1, the finite-element simulation can be considered as exact by construction under the assumption that the mesh is very fine.
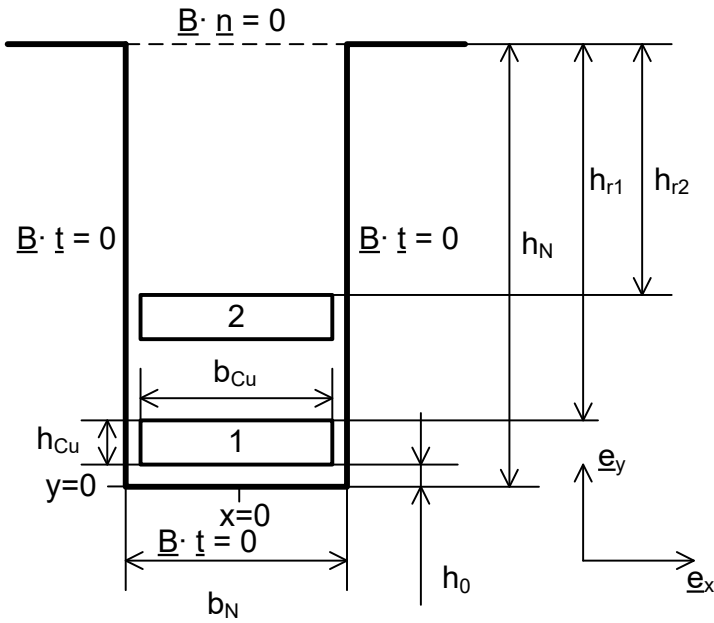
Figure 4.3 – Schematic representation of an ideal slot with 2 strands.
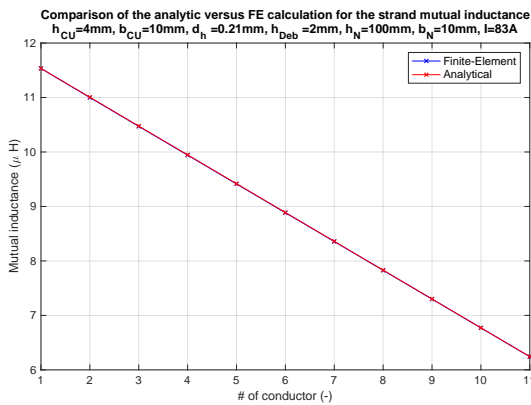
Figure 4.4 – Validation of the calculation of the mutual inductance - comparison between the analytical equation and finite-element simulations (absolute values) where $h_{Deb} = h_0$, refer to figure 4.3 for the definition of the quantities.
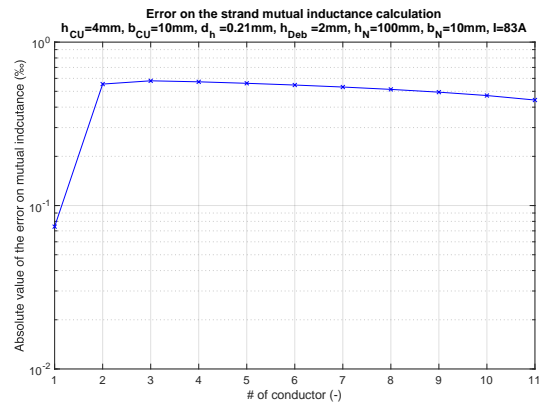
Figure 4.5 – Validation of the calculation of the mutual inductance - comparison between the analytical equation and finite-element simulations (error) where $h_{Deb} = h_0$, refer to figure 4.3 for the definition of the quantities.
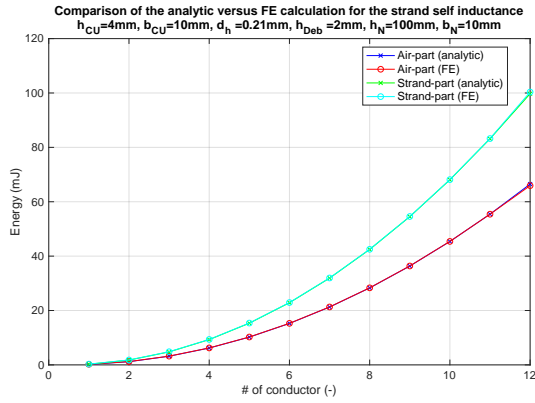
Figure 4.6 – Validation of the calculation of the self inductance - comparison between the analytical equation and finite-element simulatinos (absolute values) - the energy is plotted instead of the inductance, refer to figure 4.3 for the definition of the parameters. h_0 of figure 4.3 is h_{Deb} and d_h is the vertical distance between two strands.
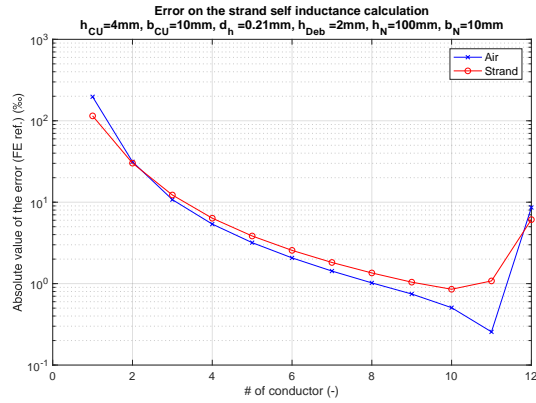
Figure 4.7 – Validation of the calculation of the self inductance - comparison between the analytical equation and finite-element simulations (error) - the energy is plotted instead of the inductance, refer to figure 4.3 for the definition of the parameters. h_0 of figure 4.3 is h_{Deb} and d_h is the vertical distance between two strands.

quantity from the finite-element simulation software and it has no influence on the result as the energy is proportional to the main inductance.

Other finite-element simulations have shown that the error increases as the ratio $b_{Cu}/b_N \rightarrow 0$ and that the error is different if the conductor is centred regarding the slot or not (as in the case of a real electrical machine where the fraction b_{Cu}/b_N is below 0.5 and non centred conductors).

4.1.1 Influence of the error on the strand mutual inductance on the strand circulating currents

As it can be seen in the previous section, the error on the self inductance is one order of magnitude higher than the error on the mutual inductance. This difference in the error and the error itself have certainly an impact on the calculated circulating currents. The goal of this original section is to quantify the influence of an error in the inductance calculation on the circulating currents by comparing an analytical calculation with a finite-element simulation. Figure 4.3 shows a schematic representation of the considered ideal slot. One strand is short-circuited and the other is fed by a sinusoidally time-varying voltage source. Table 4.1 shows the obtained results

Table 4.1 – Comparison of the circulating currents calculated with analytical calculation and finite-element simulation (FE).

Parameter	Analytical	Analytical [a]	Time-stepping FE-simulation
L_{11} (μH)	6.1994 (0.43%)	6.2261	6.2261
L_{12} (μH)	6.2832	6.2832	6.2832
L_{22} (μH)	11.980 (0.12%)	11.994	11.994
I_1 (A)	256.22 (0.63%)	254.86	254.86
I_2 (A)	132.28 (0.89%)	131.42	131.42

[a]Analytical calculation with mutual inductances from FE-calculation.

One can see that the relatively small error on the self inductance (0.43%) has a big influence on the error on the circulating currents (0.89%). To get the targeted precision, it is important to have an accurate inductance calculation, with an error around of no more than 0.1%.

4.1.2 Comparison between the self inductance and mutual inductance

During the analytical development of the inductance equations for the ideal slot, one can easily see by comparing equations 4.5 and 4.3 that the self inductance is smaller than the mutual inductance. Many authors uses this model to compute circulating current, but no publication mentioned this point. This difference is due to the term 1/2 in the mutual inductance in comparison with the term 1/3 in the self inductance. This term can be described as the "internal flux" of the conductor. For many people, this fact may sound bizarre, but there is no mathematical discrepancy having a self inductance smaller than a mutual inductance. The only condition that always needs to be fulfilled is that the magnetic energy must be null or positive at any time. It can be demonstrated that this condition is satisfied in the case of the ideal slot. Let L_{11}, L_{22} be the self inductance of the strand 1 and 2, L_{12} be their mutual inductance, i_1, i_2 the current in the strands and E_m the magnetic energy. The magnetic energy becomes

$$E_m = \frac{1}{2} L_{11} i_1^2 + \frac{1}{2} L_{22} i_2^2 + L_{12} i_1 i_2. \tag{4.6}$$

Defining X as $\frac{i_2}{i_1}$ leads to

$$E_m = \frac{1}{2} i_1^2 (L_{11} + L_{22} X^2 + 2 L_{12} X). \tag{4.7}$$

As the magnetic energy must always be greater than zero with non-zero currents, the following condition must always be fulfilled

$$L_{11} + L_{22} X^2 + 2 L_{12} X > 0 \Rightarrow L_{11} L_{22} > L_{12}^2 \tag{4.8}$$

where the last condition is nothing else than stating that the determinant of the quadratic equation in X to be negative, which imposes the magnetic energy to be null or positive at any

time. Using the equation presented above and the following definition for the inductances L_{11}, L_{22} and L_{12}

$$L_{11} = \frac{1}{3} \frac{h_{\text{Cu}}}{b_{\text{N}}} + \frac{h_{r1}}{b_{\text{N}}} \tag{4.9}$$

$$L_{22} = \frac{1}{3} \frac{h_{\text{Cu}}}{b_{\text{N}}} + \frac{h_{r2}}{b_{\text{N}}} \tag{4.10}$$

$$L_{12} = \frac{1}{2} \frac{h_{\text{Cu}}}{b_{\text{N}}} + \frac{h_{r2}}{b_{\text{N}}} \tag{4.11}$$

where the term $\mu_0 l$ was omitted as it cancels down and the geometric quantities come from figure 4.3, leads to

$$L_{11} L_{22} = \frac{1}{9} \frac{h_{\text{Cu}}^2}{b_{\text{N}}^2} + \frac{1}{3} \frac{h_{\text{Cu}}}{b_{\text{N}}^2} (h_{r1} + h_{r2}) + \frac{h_{r1} h_{r2}}{b_{\text{N}}^2} \tag{4.12}$$

$$L_{12}^2 = \frac{1}{4} \frac{h_{\text{Cu}}^2}{b_{\text{N}}^2} + \frac{h_{\text{Cu}}}{b_{\text{N}}^2} h_{r2} + \frac{h_{r2}^2}{b_{\text{N}}^2}. \tag{4.13}$$

Rewriting h_{r1} as $h_{r2} + \Delta X$ with $\Delta X > h_{\text{Cu}}$ leads to

$$L_{11} L_{22} = \frac{1}{9} \frac{h_{\text{Cu}}^2}{b_{\text{N}}^2} + \frac{2}{3} \frac{h_{\text{Cu}}}{b_{\text{N}}^2} h_{r2} + \frac{1}{3} \frac{h_{\text{Cu}}}{b_{\text{N}}^2} \Delta X + \frac{h_{r2}^2}{b_{\text{N}}^2} + \frac{h_{r2} \Delta X}{b_{\text{N}}^2} \tag{4.14}$$

$$L_{12}^2 = \frac{1}{4} \frac{h_{\text{Cu}}^2}{b_{\text{N}}^2} + \frac{h_{\text{Cu}}}{b_{\text{N}}^2} h_{r2} + \frac{h_{r2}^2}{b_{\text{N}}^2} \tag{4.15}$$

one can see easily that the condition $L_{11} L_{22} > L_{12}^2$ is fulfilled because term 2 and 3 of L_{12}^2 are bigger than term 4 and 5 of $L_{11} L_{22}$ as $\Delta X > h_{\text{Cu}}$ while term 1 of L_{12}^2 is also bigger than term 3 of $L_{11} L_{22}$ for the same reason. Therefore there is no mathematical discrepancy to have a self inductance smaller than the mutual inductance.

4.1.3 Influence of the iron saturation level on the slot magnetic field

In real electrical machines, the iron has a non-infinite permeability. Therefore it is interesting to study the influence of the non-infinite iron permeability in the teeth surrounding the slot on the magnetic field inside the slot. As no publications dealing with this question have been found, it was decided to perform an original study. To do so, the finite-element model is slightly changed to the model depicted in figure 4.8 with $h_{air} = 0$mm. The iron is modelled using a given constant permeability, which is changed from one simulation to the other to highlight the impact of the saturation of the surrounding iron. This hypothesis of constant iron permeability is not a problem, because the goal is to get an order of magnitude of variation and not numerical values. The air is not taken into account and is replaced by a tangential flux boundary condition as no flux passes through the air-gap.
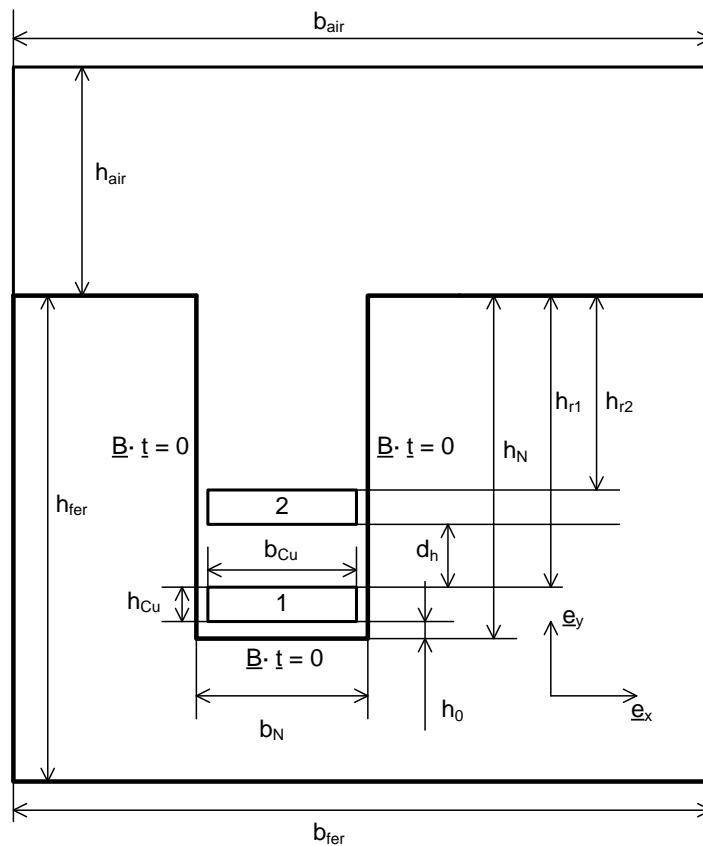
Figure 4.8 – Schematic representation of the ideal slot with teeth iron.

Figures 4.9 and 4.10 show the influence of the saturation of the iron teeth on the magnetic field. As one can see, the saturation has a significant influence on the results. The more the tooth is saturated, the higher influence on the magnetic field and therefore on the inductances. For a non-ideal slot, the magnetic field is negative previously the strand starts. This is due to the fact that a non-infinite permeability allows some flux to pass through the slot ground to close its path. The magnetic field is not anymore constant for $y > y_0 + h_{Cu}$, as the path length in the iron gets longer with increasing y. These two effects have an impact on the self and mutual inductances of the strands in the slot, which is presented in section 4.1.4. As it can be seen very well in figure 4.10, the decrease of the magnetic field is very fast along the slot and its rate of decrease increases with the lowering of the iron permeability. The more the permeability decreases the less the path-shortening effect of the iron can be seen. All the simulations have been conducted with a constant iron permeability, even if in practice, the tooth flux will be governed by the main flux, and that the iron has a non-linear permeability characteristic leading to non-constant permeability of the iron. As soon as the permeability is not infinite anymore, the results are also a function of the iron volume used for the finite-element simulation, meaning that these results are valid with this given iron volume only.
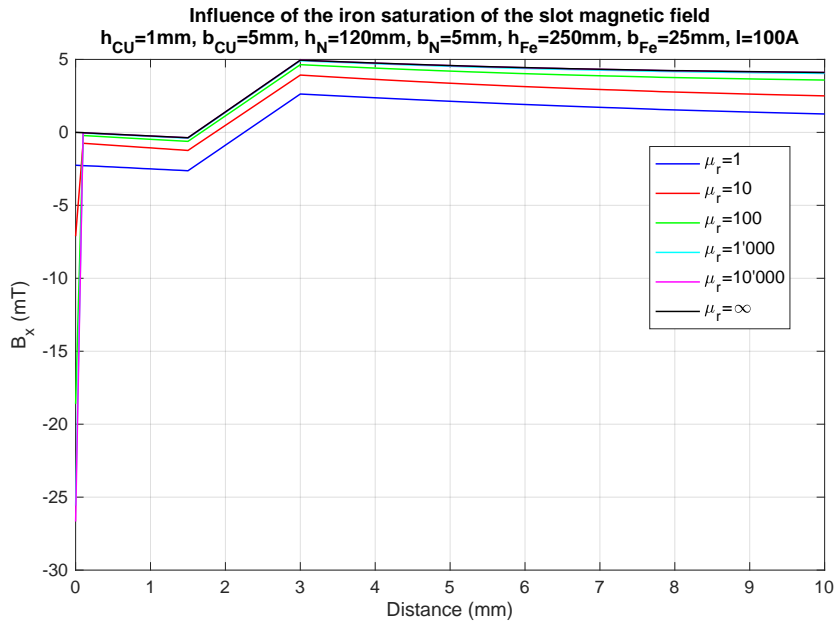
Figure 4.9 – Influence of the iron magnetic properties on the slot magnetic field (view on the first 10mm of the slot, along the y-axis). Refer to figure 4.8 for the definition of the simulation parameters with $h_{Fe} = h_{fer}$ and $b_{fer} = 2b_{Fe} + b_N$. The point at zero distance is located on the beginning of the slot in the iron, which explains its huge negative value. The strand is located between distance equals 1.5mm and 3mm.
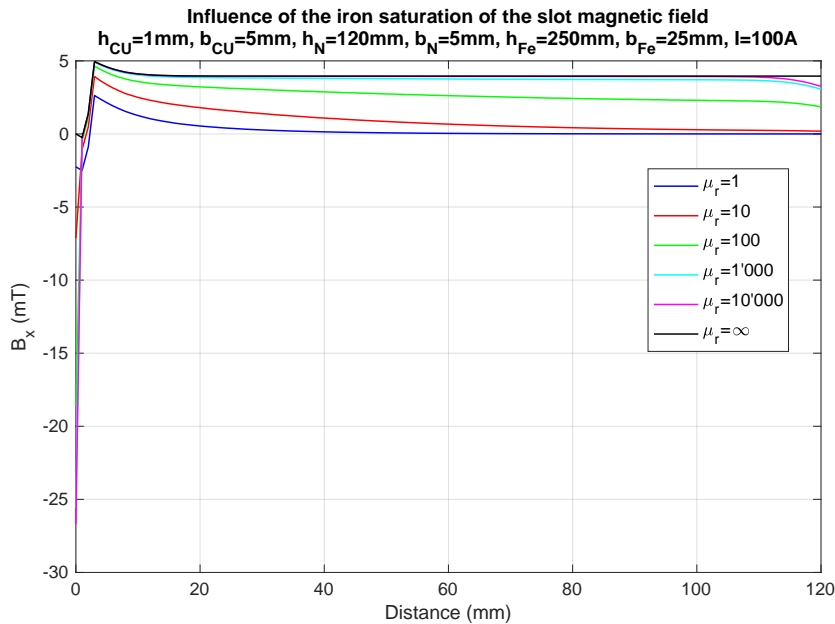
Figure 4.10 – Influence of the iron magnetic properties on the slot magnetic field (view on the total length of the slot, along the y-axis). Refer to figure 4.8 for the definition of the simulation parameters with $h_{Fe} = h_{fer}$ and $b_{fer} = 2b_{Fe} + b_N$.

4.1.4 Influence of the iron saturation level on the self and mutual inductances

The starting point for this study about the influence of the saturation level on the self and mutual inductances is the work of C. Lehmann. [92] studies the influence of the saturation of the teeth on the eddy current losses in massive and divided-in-strands conductors. These are placed in a slot composed of iron with constant permeability and with a non-linear permeability characteristic. The author could demonstrate that the saturation influences the eddy current distribution by tending to reduce the eddy current coefficient with increasing magnetic field. An external field, which is in electrical machines mainly due to the slot radial field coming from the rotor can significantly increase the eddy current losses. The more the permeability of the iron is reduced, the more the eddy current losses increase in the top strands.

Starting from the demonstrated observations in [92] and the fact there are no publications on this specific question, it is interesting to see if a similar behaviour can be observed in the strand inductance calculation by performing additional original studies on this question. Figure 4.8 presents the slot model used for the finite-element simulation, this slot model is inspired from the slot model used in [92].

The idea behind this study is to analyse the impact of a changing permeability on the slot inductance and not the impact of an external field to the slot permeability respectively strand inductance. In other words, this model has no pretensions to describe the magnetic state occurring in a real electrical machine where the permeability change in the slot obeys to a much more complex interaction than this simplified model wants to take into account. To take the magnetic state of an electrical machine better into account, the model of figure 4.8 must be enhanced with two coils able to produce a magnetisation field in the y-axis and x-axis to model the radial and tangential field in the electrical machine. This would enhance the model and decrease the gap between the model and the real magnetic state happening in the electrical machine, but this enhancement is not a good idea in the sense that if there is an impact of the slot permeability on the strand inductances then, it will be much more convenient to seek for a model taking as much as possible the complete electrical machine into account rather than just enhancing a model that reached its limits.

Figure 4.11 shows the influence of the permeability of the tooth iron on the self and mutual inductances based of the model shown in figure 4.8. The permeability has an influence of about one order of magnitude on the inductances. The mutual inductance becomes higher than the self inductance if the permeability is higher than 2'000. The variation of the inductance follows a transition between its lower value (with a permeability of 1) and its higher value (with an infinite permeability) with a curve similar to the saturation curve. The most difficult point is to take into account the transition zone between these two extremal values. In electrical machines, the magnetic field in the teeth in normal operation leads to an operation in the first elbow (starting from an infinite permeability) of the transition zone with relative permeabilities varying between 20 and 11'150 for M250-50A electrical steel. Taking the
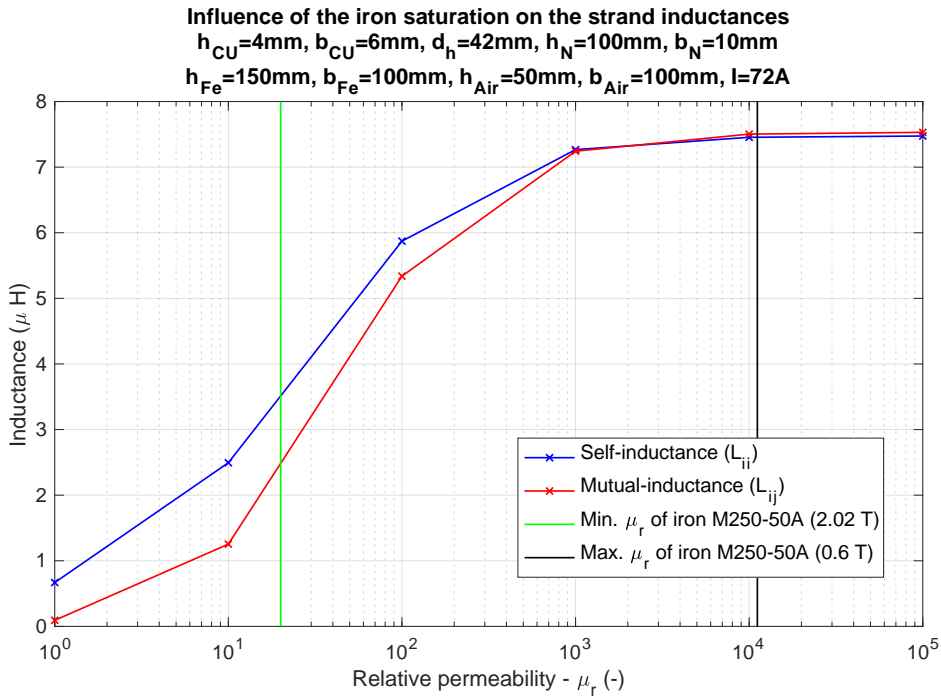
Figure 4.11 – Influence of the permability of the teeth iron on the self and mutual inductances, refer to figure 4.8 for the definition of the parameters with $h_{Fe} = h_{fer}$ and $b_{Fe} = b_{fer}$.

saturation into account when calculating the strand inductance is crucial if one is interested in precise results especially for incomplete transposition in the active part.

Comparing with the results of [92], it can be pointed out that the influence of the saturation on the inductances is similar to the one found by [92] for the eddy current losses. The impact of an external field was not taken into account for this study, but will be included in the study made with the differential inductance model (Model 4.0). At a first glance, the position of the strands seems not to have any influence on the inductance variation induced by a decrease of the permeability.

4.1.5 Conclusion of the analysis of the ideal slot (Model 1.0)

The analytical equations of the ideal slots do not take into account that the copper width b_{Cu} is not equal to the slot width b_N, which is not satisfactory in the context of this study. Comparisons using finite-element simulation show a very good agreement between the analytical formulae and the simulation results in the case $b_{Cu} = b_N$. To obtain an error below 1% for the circulating current calculation, one must calculate the inductances with a very high precision of around 0.1%. The saturation of the iron surrounding the slot has a significant impact on the magnetic field and therefore strand inductance, which needs to be taken into account to achieve the precision goal for the inductance calculation. The ideal slot model has many drawbacks making it uninteresting for this work. This model must be enhanced to

take both the complete strand geometry and the saturation into account. Three enhanced models will be presented in the following sections in a step-by-step approach. Each additional model takes another additional item into account. This approach permits to decompose and insulate the impact of each additional step on the inductance calculation.

The first enhanced model, also called Model 2.0 is described in section 4.3, while the next section is dedicated to some reflections on the calculation of self and mutual inductances.

4.2 Novel reflections on the calculation of the self and mutual inductances

As a first attempt to take the complete and exact strand geometry into account, let's start a novel reflection on the calculation of the self and mutual inductances and try to develop analytical formulae to calculate the inductances taking the exact and complete strand geometry into account. The definition of the self inductance is "flux created by conductor j and seen by conductor j" while the mutual inductance is defined by "flux created by conductor j and seen by conductor i". There is also a difference between the "flux created" defined by

$$\phi = \iint_{\Sigma} \underline{B} \cdot \mathrm{d}\underline{\sigma} \tag{4.16}$$

and the "coupled flux" (Ψ) used for the inductance and energy calculation. The relation between these two fluxes is $\Psi = N \cdot \phi$. This relation is true if and only if the dimensions of the conductors are negligible within the dimensions of the problem, which is not verified in this case. A possible correction is to define a $N(x)$-function as in equation 4.4. For one-dimensional problems, this correction is suitable, but this is not the case for 3-dimensional problems as in the winding overhang. For the mutual inductance the $N(x)$-correction is taken into account in equation 4.3, as the coupled flux is constant over a dx-element so that the resulting integral becomes

$$\psi_{ij} = \int_0^1 \phi_{ij} \, \mathrm{d}x = \phi_{ij} \int_0^1 \mathrm{d}x = \phi_{ij}. \tag{4.17}$$

The self inductance can also be obtained through the following relation

$$E_m = \frac{1}{2\mu_0} \iiint_V \underline{B}^2 \, \mathrm{d}x \, \mathrm{d}y \, \mathrm{d}z = \frac{1}{2} L_{ii} I_i^2. \tag{4.18}$$

where E_m is the magnetic energy and V is the volume considered. The main practical drawback from this formulation lies in the necessity to calculate $\underline{B}^2$ over big volumes, which is very time consuming. One must seek for other formulations to take the size of the conductors into account while limiting the amount of calculation to be done to obtain an accurate value of the inductance.

4.2.1 How to take the size of the conductors into account?

As shown in [99] the size of conductors has a non-negligible impact on the magnetic field and inductance calculation. The formulae used and developed until now permit to catch the self and mutual inductance with a simple correction (one-dimensional) to take into account the conductor size. They struggle to efficiently take into account the size of the conductors for a general three-dimensional problem and when the distance is in the range of the conductor sizes. For the necessary precision it is fundamental to overcome these drawbacks. Let's recall Neumann's formula for the mutual inductance calculation between two loops (relation 10.42 in [62])

$$L_{ij} \cong \frac{\mu}{4\pi} \oint_{C_j} \oint_{C_i} \frac{\mathrm{d}\underline{l}_i \cdot \mathrm{d}\underline{l}_j}{|\underline{r} - \underline{r}'|} \tag{4.19}$$

where C_i, $\underline{l}_i$ refers to the contour of the strand i and μ is equal to 1 (permeability of the medium). Figure 4.12 shows a schematic representation of the conductor i with the infinitesimal distance $\mathrm{d}\underline{l}_i$ and the conductor j with its infinitesimal distance $\mathrm{d}\underline{l}_j$.
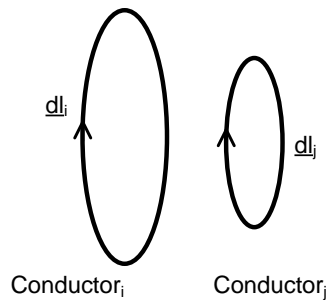
Figure 4.12 – Schematic view of the path of the conductor i and j.

It is interesting to mention that the mutual inductance decreases with $1/r$ and is proportional to the scalar product between $\mathrm{d}\underline{l}_i$ and $\mathrm{d}\underline{l}_j$. This means that this scalar product can also be negative transposing the fact that the loops are oriented one against the other. The relation is only approximative because the displacement current has been neglected[2] during the development of this equation. This equation considers that the B-field is constant over a perpendicular section of $\underline{l}_i$. In other words, the strands are considered as infinitely small, or as a filament with a zero cross-section. In the case of this work, this approximation is not anymore valid, and the equation needs to be extended, taking into account the fact that the cross-sections of the strands is in the same order of magnitude as the dimensions[3] of the problem to be considered.

---

[2]This approximation is also called "low-frequency" approximation. But one should take care with the words "low-frequency", because it can also happen that for a frequency of 50Hz one has to take into account the displacement current. A better definition for this approximation is "the dimensions of the problem are small enough that the B-field, E-field can be considered as propagating instantaneously".

[3]Imagine that the strands are located at the top of the bar.

Starting from the equation of the flux leads to

$$\phi = \iint_{\Sigma} \underline{B} \cdot \mathrm{d}\underline{\sigma} = \iint_{\Sigma} \underline{\nabla} \times \underline{A} \cdot \mathrm{d}\underline{\sigma} = \int_{\partial\Sigma} \underline{A} \cdot \mathrm{d}\underline{l} \tag{4.20}$$

where $\partial\Sigma$ is the border of the surface Σ and $\underline{B} = \underline{\nabla} \times \underline{A}$. In 2-dimensions, this equation simplifies to

$$\phi_{ij} = h(A_i - A_j) \tag{4.21}$$

where h is the length of the 2-dimensional plane considered and A_i and A_j are the 2 points considered for the flux calculation. To take the dimensions of the strands into account, a simple idea could be to average over the surface of the strands. The flux becomes then

$$\phi_{ij} = h \frac{1}{S_i S_j} \iint_{S_i} \mathrm{d}S_i \iint_{S_j} \mathrm{d}S_j \, (A_i - A_j) \tag{4.22}$$

The inductance is given by

$$L_{ij} = \frac{\phi_{ij}}{i_i} \tag{4.23}$$

considering that the flux is created by the current i_i. Using this approach, it is possible to take into account the strand dimensions into account. In 3-dimensions, the case gets more complicated, but it can be simplified using Frenet– Serret formulae. A Frenet-Coordinate system defined by a triplet $(\underline{t}, \underline{n}, \underline{b})$ forming a direct trihedron where $\underline{t}$ is along the tangent to the curvilinear abscissa and $(\underline{n}, \underline{b})$ define the perpendicular plane to $\underline{t}$ will be used. In this work, the conductors are oriented along $\underline{t}$, and their section can be defined in the plane $(\underline{n}, \underline{b})$. At a given point along the conductor $(\underline{t}_i)$ the average of the vector potential can be written as

$$\underline{A}_i = \frac{1}{S_{\underline{t}_i}} \iint_{S_{\underline{t}_i}} \underline{A}(\underline{t}, \underline{n}, \underline{b}) \, \mathrm{d}\underline{n} \, \mathrm{d}\underline{b} \tag{4.24}$$

where $\underline{A}_i$ is defined as the average over the cross-section of the conductor at the point $\underline{t}_i$ and $S_{\underline{t}_i} = \int \mathrm{d}\underline{n} \int \mathrm{d}\underline{b}|_{\underline{t}=\underline{t}_i}$ and $\underline{A}$ is the vector potential obtained from a direct integration (refer to the equations developed in the chapter 5 for example) or from a three-dimensional integration of punctual contributions, but both will give the same result for $\underline{A}$. This integration over the perpendicular surface to $\underline{t}_i$ can also be seen as a 2-dimensional $N(x)$-correction. Obtaining the flux becomes quiet straightforward after this step. One obtains

$$\phi = \int_{\partial\Sigma} \underline{A}_i \cdot \mathrm{d}\underline{l} = \int_{\partial\Sigma} (\frac{1}{S_{\underline{t}_i}} \iint_{S_{t_i}} \underline{A}(\underline{t}, \underline{n}, \underline{b}) \, \mathrm{d}\underline{n} \, \mathrm{d}\underline{b}) \cdot \mathrm{d}\underline{l}. \tag{4.25}$$

When using this formula, one should take care on the definition of the path $\partial\Sigma$, depending on its choice. The flux obtained with this formula represents a "global" flux with which one

can calculate circulating currents for example or it can also represent a "local" flux with which only eddy currents can be obtained. A special care must therefore be given to the choice of this path. The inductance becomes

$$L_{ij} = \frac{\phi}{i_i} \tag{4.26}$$

and as one can see, with this formula one can take into account the size of the conductors without any restriction regarding the distance between the considered conductors.

This very theoretical formalism is a necessary step, as the formulae presented above can be used for the calculation of the inductance in the slot, near some iron, in the air. Other formalism, for example the one used in [77] to calculate the overhang inductance follows more or less the same way as showed here, but with the main difference that this formalism is based on the assumption that the B-Field behaves as $B \sim 1/r$ which implies to consider a filament or far-field conditions (in other words, far away from the conductor). And again, the main goal of this new formalism is to try to take into account the size of the strands, to be applicable anywhere in the space and in any environment (air, iron, etc.).

4.2.2   Partial inductance

In equation 4.19, the integration is performed on the path C_i and C_j. These paths can be divided in sub-paths according to the segment addition postulate and the inductance can be calculated over these sub-paths leading to so-called partial inductances. These partial inductances can be summed to obtain the inductance of equation 4.19. This notion is introduced, discussed and detailed in many publications [112], [111], [124] and [2]. As the winding overhang is composed of multiple fundamental elements, which represent each section of the bended bar (refer for example to figure 5.14), dividing the inductance into partial inductances enables to catch the coupling between the elements or the bars with a higher resolution and increase the knowledge of the phenomena that take place in the winding overhang. Some practical examples of the usage of the partial inductance are shown in section 5.9.3.

4.3   Taking into account the strand width b_{Cu} - Model 2.0

To improve the calculation of the self-inductance, Model 1.0 is extended to take the conductor width (b_{Cu}) into account by the mean of the original development of novel analytical equations. The geometry of the problem is depicted in figure 4.3. The ideal slot has the following boundary conditions

$$\underline{B}(x = \pm b_{\text{N}}/2, y) = (B_{\text{x}}, 0) \tag{4.27}$$
$$\underline{B}(x, y = 0) = (0, B_{\text{y}}) \tag{4.28}$$
$$\underline{B}(x, y = h_{\text{N}}) = (B_{\text{x}}, 0). \tag{4.29}$$

The governing equations to be solved in the air are

$$\underline{\nabla} \times \underline{B} = 0 \tag{4.30}$$

$$\underline{\nabla} \cdot \underline{B} = 0 \tag{4.31}$$

while in the copper, they become

$$\underline{\nabla} \times \underline{B} = \mu_0 \underline{j} \tag{4.32}$$

$$\underline{\nabla} \cdot \underline{B} = 0 \tag{4.33}$$

considering an uniform current density $\underline{j}$. The linearity of the medium enables to solve the equation for $\underline{B}$ or $\underline{H}$ without any loss of generality. In terms of single terms, the equations become

$$\partial_x B_y - \partial_y B_x = 0 \quad \text{in the air} \tag{4.34}$$

$$\partial_x B_y - \partial_y B_x = \mu_0 j_z \quad \text{in the copper} \tag{4.35}$$

$$\partial_x B_x + \partial_y B_y = 0. \tag{4.36}$$

Keep in mind that "a priori" there is no constraint on the terms $\partial_x B_x$ and $\partial_y B_y$ so that they can vary "freely". They just need to satisfy the divergence equation. Analysing the curl-equations leads to the following consideration: the curl is produced in the copper, while it is conserved in the air, as the air is curl-free. As it has been seen, when $b_{\mathrm{Cu}} < b_{\mathrm{N}}$ there is some discrepancies between the results of the Model 1.0 and the finite-element simulations, especially for the self inductance. In order to find an explanation of this, some considerations are performed which will lead to Model 2.0. Let's consider at a first stage an application of Ampère's circuit law in the slot. At the position x inside the copper the curl-equation becomes

$$B_x \cdot b_{\mathrm{N}} = \mu_0 \cdot I \cdot \frac{y}{h_{\mathrm{Cu}}} \tag{4.37}$$

where $I = j_z \cdot h_{\mathrm{Cu}} \cdot b_{\mathrm{Cu}}$. This leads to

$$B_x \cdot b_{\mathrm{N}} = \mu_0 \cdot j_z \cdot b_{\mathrm{Cu}} \cdot y. \tag{4.38}$$

Calculating $\partial_y B_x$ leads to

$$\partial_y B_x = \mu_0 \cdot j_z \frac{b_{\mathrm{Cu}}}{b_{\mathrm{N}}} \tag{4.39}$$

one can therefore easily see that when the fraction $b_{\mathrm{Cu}}/b_{\mathrm{N}}$ is not equal to 1 a term is missing in the curl-equation. This missing term will induce discrepancies in the inductance calculation. To fulfil the curl-equation an additional term must be considered to fulfil the curl-equation.

The term $\partial_x B_y$ will be defined in a such way that the curl-equation is fulfilled.

$$\partial_x B_y - \partial_y B_x = \mu_0 \cdot j_z \tag{4.40}$$

$$\partial_x B_y - \mu_0 \cdot j_z \frac{b_{Cu}}{b_N} = \mu_0 \cdot j_z \tag{4.41}$$

$$\partial_x B_y = \mu_0 \cdot j_z \frac{b_N + b_{Cu}}{b_N}. \tag{4.42}$$

The additional term $\partial_x B_y$ must be considered in the copper only. Outside the copper the curl-free equation must still be fulfilled. As one can see, this term only gives us a certain value for the derivative of the function but no constraint for the function itself. At a first glance, let's state that $\partial_y B_x =$ constant over the height of the copper, this enables to have a linear function for B_y. This function must be 0 in $y = \pm b_N/2$ in order to fulfil the boundary conditions. The function describing B_y will be odd and piece-wise linear as the curl-equation authorises discontinuities in the derivatives. The function needs to be odd as the derivative is not null at $x = 0$ and the function is zero at both walls. The simplest function is therefore a "triangle" function. The function will be composed of 3-pieces corresponding to the 3 media (air-copper-air) to be considered. The rest of the development is realised considering a centered copper strand. Nevertheless, this development can be enhanced for displaced copper strands, like in a roebel-bar.

The maximal, respectively minimal value of this function is achieved for $y = \pm b_{Cu}/2$ with the following amplitude

$$B_{ymax/min} = \pm \mu_0 \cdot j_z \frac{b_N - b_{Cu}}{b_N} \frac{b_{Cu}}{2}. \tag{4.43}$$

Knowing the maximal respectively minimal value of B_y one can easily deduce the equation for the function

$$B_y = \begin{cases} \frac{2 \cdot B_{ymin}}{b_N - b_{Cu}}(x + \frac{bN}{2}) & \text{for } x \in [-\frac{b_N}{2}, -\frac{b_{Cu}}{2}]; \\ \frac{B_{ymax} - B_{ymin}}{b_{Cu}} & \text{for } x \in [-\frac{b_{Cu}}{2}, \frac{b_{Cu}}{2}]; \\ \frac{2 \cdot B_{ymax}}{b_N - b_{Cu}}(x - \frac{bN}{2}) & \text{for } x \in [\frac{b_{Cu}}{2}, \frac{b_N}{2}]. \end{cases} \tag{4.44}$$

The well known equation for B_x remains the same for the part inside the copper. Between the copper and the wall of the slot, the equation 4.44 for B_x is given by $\underline{\nabla} \times \underline{B} = 0$ and is deduced from the equation for B_y.

Figures 4.13 to 4.20 show the results obtained from a finite-element simulation. The new formulation allows to catch the y-component of the magnetic field with a very good accuracy, as one can see in figure 4.14, where the curves react to a variation of the strand width b_{Cu} as stated in equation 4.44. This is very promising, but the magnetic field governed by the divergence equation is missing in this new formulation. The effect of these terms can be seen in figures 4.13 and 4.16 with the interesting difference that B_x is reacting to any change in the
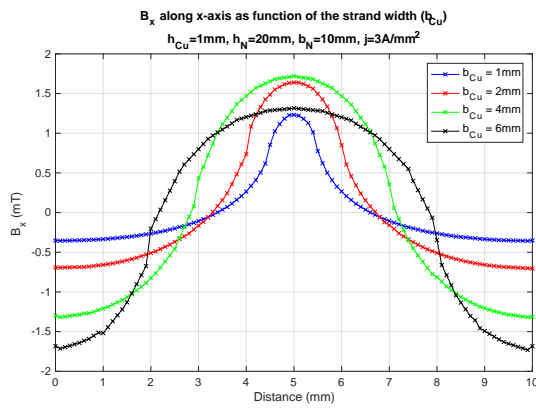
Figure 4.13 – X-component of the magnetic field as function of the copper strand width (b_{Cu}), distance along x-axis centred on the conductor. Refer to figure 4.1 for the definition of the simulation parameters.
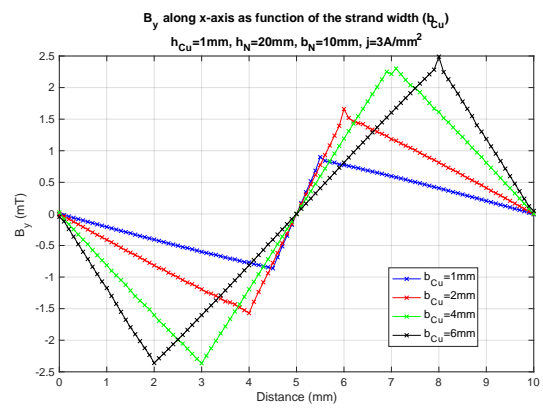
Figure 4.14 – Y-component of the magnetic field as function of the copper strand width (b_{Cu}), distance along x-axis centred on the conductor. Refer to figure 4.1 for the definition of the simulation parameters.
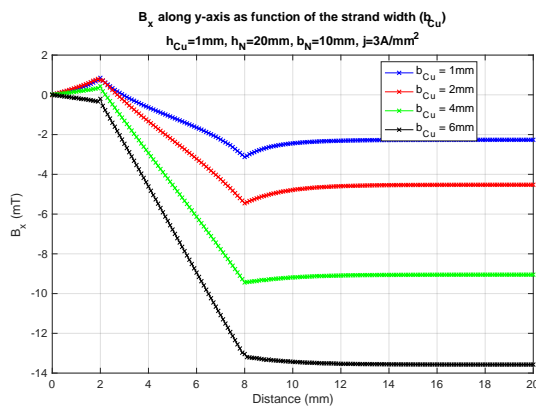
Figure 4.15 – X-component of the magnetic field as function of the copper strand width (b_{Cu}), distance along y-axis centred on the conductor. Refer to figure 4.1 for the definition of the simulation parameters.
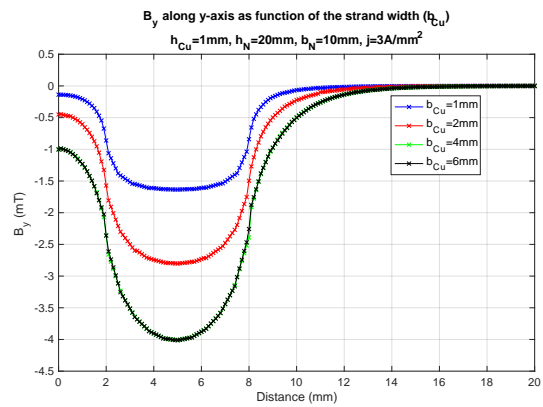
Figure 4.16 – Y-component of the magnetic field as function of the copper strand width (b_{Cu}), distance along y-axis centred on the edge of the conductor. Refer to figure 4.1 for the definition of the simulation parameters.
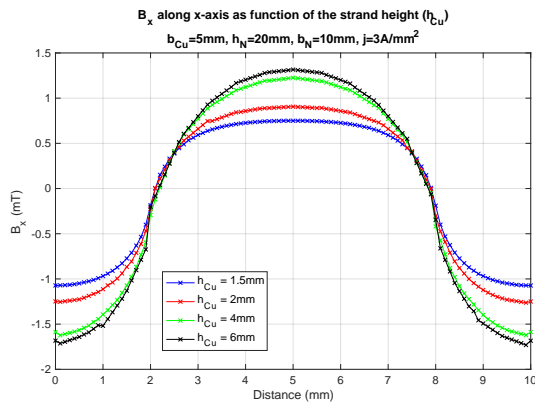
Figure 4.17 – X-component of the magnetic field as function of the copper strand height (h_{Cu}), distance along x-axis centred on the conductor. Refer to figure 4.1 for the definition of the simulation parameters.
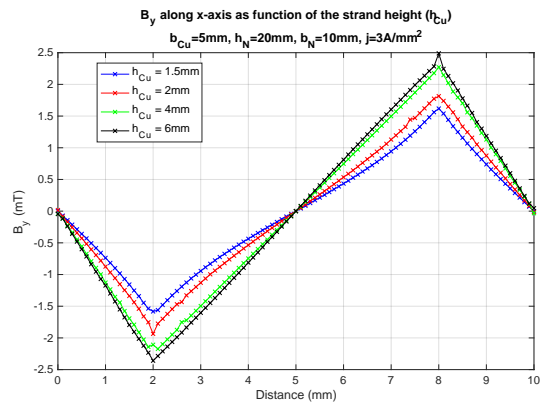
Figure 4.18 – Y-component of the magnetic field as function of the copper strand height (h_{Cu}), distance along x-axis centred on the conductor. Refer to figure 4.1 for the definition of the simulation parameters.
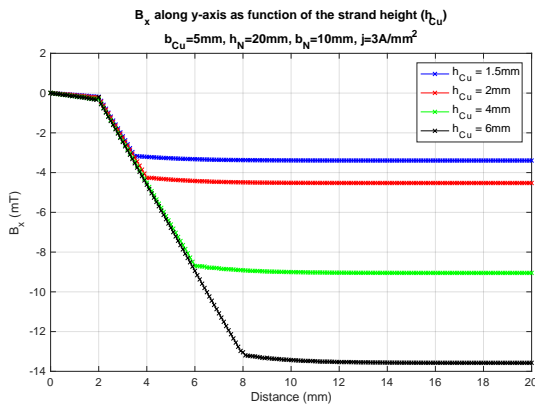
Figure 4.19 – X-component of the magnetic field as function of the copper strand height (h_{Cu}), distance along y-axis centred on the conductor. Refer to figure 4.1 for the definition of the simulation parameters.
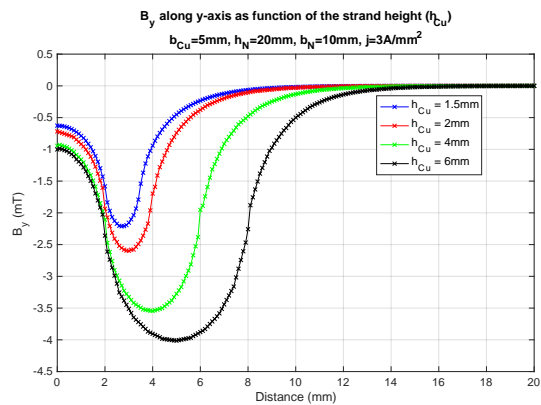
Figure 4.20 – Y-component of the magnetic field as function of the copper strand height (h_{Cu}), distance along y-axis centred on the conductor. Refer to figure 4.1 for the definition of the simulation parameters.

strand width, while B_y has a saturation behaviour as the curves for b_{Cu}=4mm and b_{Cu}=6mm are identical. In figure 4.13 the magnetic field does not reach zero at the boundary as the boundary condition only imposes a normal magnetic field but not its amplitude. The second drawback of this formulation leads in the fact that B_y is also influenced by h_{Cu} as it can be seen in figure 4.18 which is not taken into account. B_x along the y-axis behaves as stated in equation 4.1 for both cases (refer to figures 4.15 and 4.19). The smaller the ratio b_{Cu}/b_N gets, the more B_x behaves like the magnetic-field produced by a conductor in air, or in other words the effect of the infinite iron permeability is weakened with an increasing distance of the strand to the wall.

The x-component of the magnetic field reacts to a strand height (h_{Cu}) variation (refer to figure 4.17), which was not expected but the y-component of the magnetic field has an expected reaction to the strand height variation (figure 4.20).
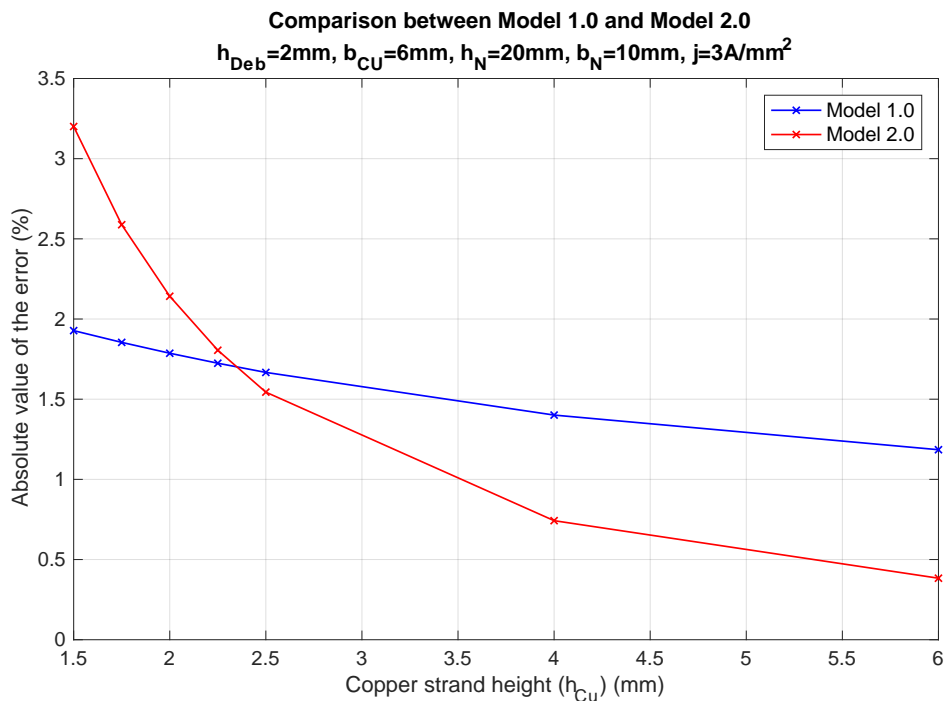
Figure 4.21 – Comparison between Model 1.0 and Model 2.0, error on the energy with a finite-element simulation as reference.

Figure 4.21 shows the error on the energy for both models comparing the inductance calculated using a 2-dimensional finite-element simulation of an ideal slot with the results of the analytical inductance calculation using Model 1.0 and Model 2.0. The base for the percentage are the results of the finite-element simulation. One can see that if $h_{Cu} \gg 1$mm, the error tends towards 0 for Model 2.0, while its seems that the error for Model 1.0 will tend to a constant value bigger than 0. This is due to the fact that Model 2.0 takes into account that the fraction b_{Cu}/b_N is smaller than one, but does not take into account the fact that $h_{Cu} \ll 1$mm. This is why the error is higher for Model 2.0 when $h_{Cu} \rightarrow 0$. The errors for both models are dependent

on the fraction b_{Cu}/b_N meaning that the lower this fraction is, the higher the error will be. When the copper strand is not anymore centred in the slot, as in electrical machines, the error will be increased for both models and reach the order of magnitude of 10% of the value which is not acceptable. Model 2.0 exhibits a significant lower error than Model 1.0 for big copper strand hights, independent from the ratio b_{Cu}/b_N. In electrical machines, especially in the stator the strand height is around 2mm to minimise the eddy current losses, making the current version of Model 2.0 no better than Model 1.0.

To reduce the error, it is obvious that the magnetic field governed by the following equation

$$\underline{\nabla} \cdot \underline{B} = 0 \tag{4.45}$$

must be integrated in the model. In addition, as one can see in figures 4.14 and 4.18, the linear approximation could not be sufficient, so one could think about adding some additional terms to the analytical equation to obtain a more accurate function.

Using only first and second order polynomials to approximate the magnetic field, it will be very difficult to obtain high accuracy numerical results. For example, the curves of figures 4.13 and 4.16 can be described with acceptable accuracy using only a second order polynomial. Higher order polynomials could be an option, but they can not precisely describe like-flat part of curves, like in figure 4.17. Maybe a solution could be found using Fourrier-series extending the curves by parity and/or imparity. The Fourrier-series can be helpful for the description of "flat" curves. Even with this trick, this option is not practicable as one would need a mathematical description of the curves governed by the divergence-equation, which could not be found. At this stage, the mirror-method or image-method could bring the expected breakthrough.

4.4   Taking into account the strand dimension and exact location in the slot using multiple mirrors - Model 3.0

To take the strand dimensions and the location of the strand in the slots into account, an enhancement of the Model 2.0 must be considered. As the ideal slot model uses iron of infinite permeability and a zero permeability boundary condition, one can use the "mirror-method" (refer to [72] and [24]) to calculate the magnetic field in the slot as shown in figure 4.22.

A priori, there is no limitation of the number of mirrors that can be considered, so that one could also consider polygonal boundaries. For the ideal slot, one needs to consider 4 mirrors, corresponding to the 4 boundary conditions. In the case of the ideal slot, there are 2 pairs of mirrors in front of each other, which will lead in 2 series of infinite terms, one along the X-axis, one along the Y-axis. The one along the X-axis is a summation over terms of the same signs, will the series along the Y-axis contains a summation over terms of both signs, as the boundary condition at $y = h_N$ is a boundary condition of zero permeability. In [15], the authors use multiple mirrors to calculate the electrical field. They refer to a so-called

"double series solutions" or "Roth's method". The application of "Roth's method" to the strand inductance calculation in an ideal slot is an original contribution of this work. This method is relatively simple to use, as it consists of a double infinite sum of single terms, and delivers the magnetic field in the whole calculation domain. The single term equation is the equation of the magnetic field generated by a long rectangular conductor of infinite length.

The study conducted in this section is an application of "Roth's method" to the problem of calculating the inductances in an ideal slot with the aim to see in practice how many terms of the double series must be calculated to obtain an acceptable accuracy for the inductance calculation.
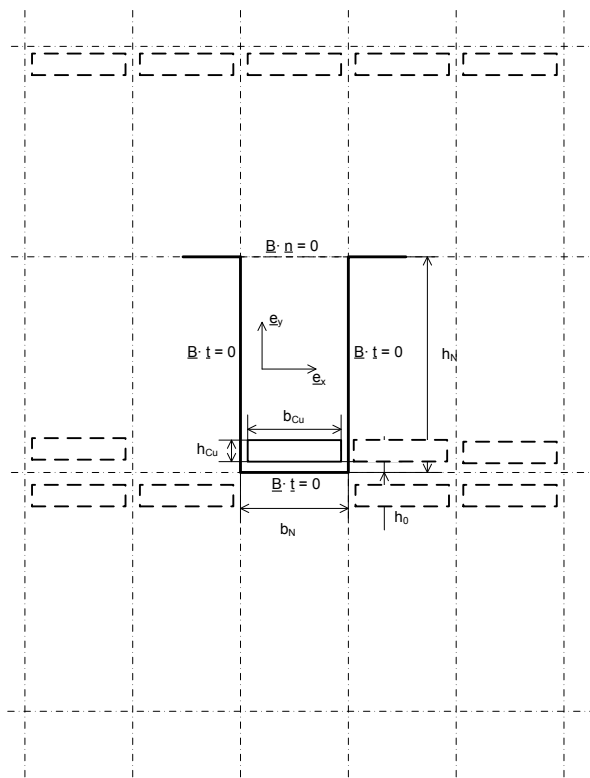
Figure 4.22 – Schematic representation of an ideal slot and multiple mirrors. Not all mirrored strands are drawn to ensure readability of the schema.

The magnetic field tends to its exact solution with the increase of the double terms considered (figures 4.24 and 4.26). To obtain "good" results, one needs to calculate more than 150 double series terms.
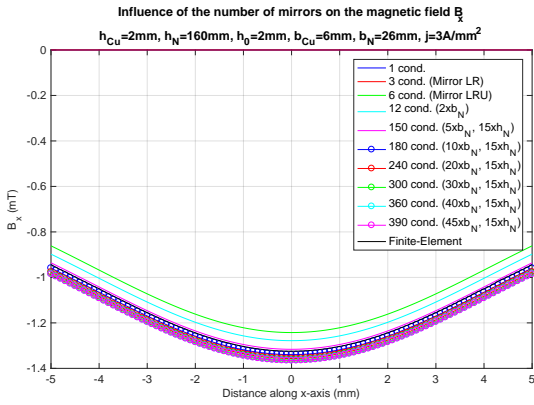
Figure 4.23 – Magnetic field along Y-axis centred on the conductor, multiple mirrors method
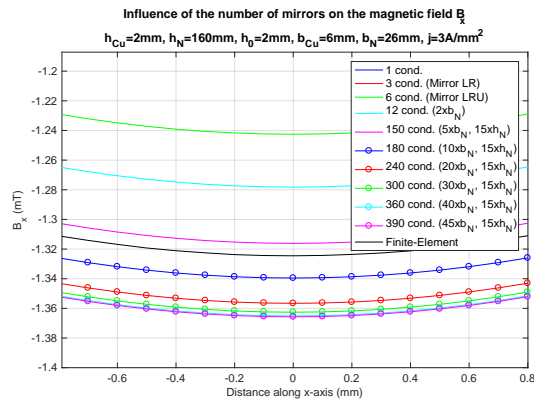
Figure 4.24 – Magnetic field along Y-axis centred on the conductor, multiple mirrors method (zoom)
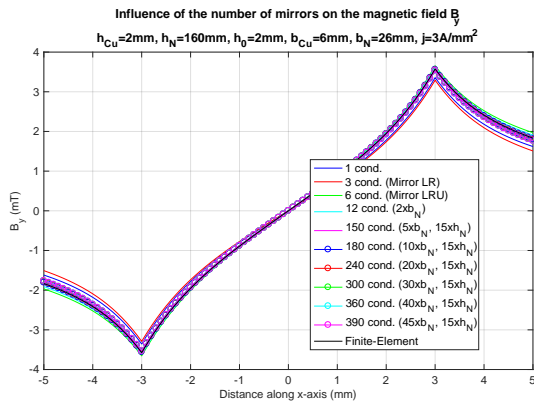
Figure 4.25 – Magnetic field along X-axis centred on the conductor, multiple mirrors method
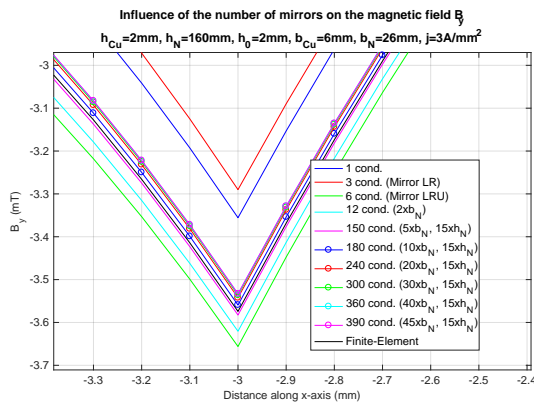
Figure 4.26 – Magnetic field along X-axis centred on the conductor, multiple mirrors method (zoom)
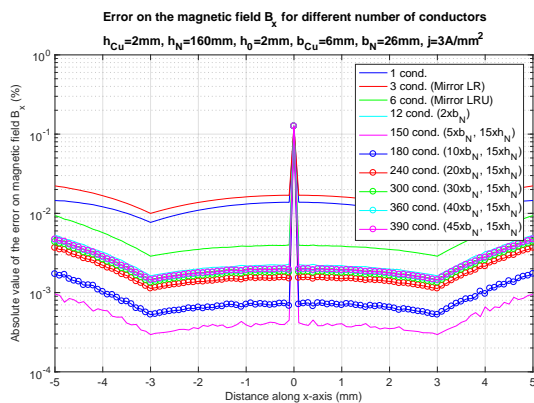
Figure 4.27 – Error on the magnetic field along X-axis, multiple mirrors method
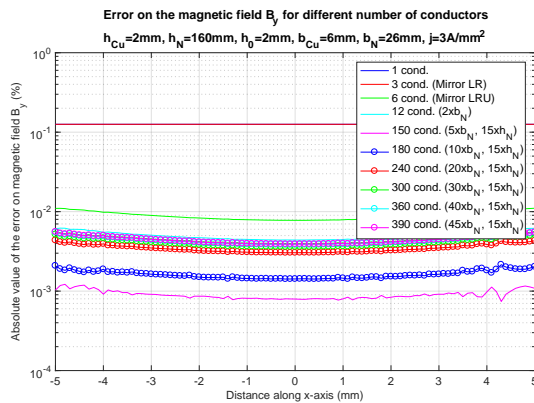
Figure 4.28 – Error on the magnetic field along Y-axis, multiple mirrors method
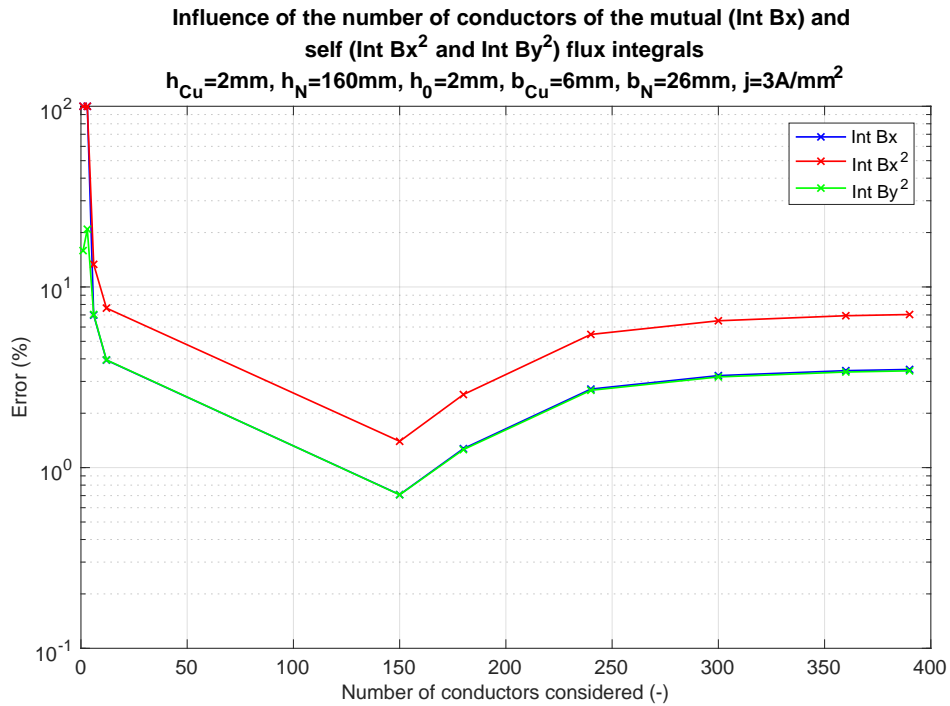
Figure 4.29 – Error on the integral of the magnetic field and magnetic field squared in function of the number of conductors, finite-element as reference. The integration path is along the y-axis in the middle of the slot.

As one can see in figures 4.27 and 4.28, even if the difference between the exact solution and the approximated solution using a finite number of conductors is very small, there is a significant error when calculating the flux (labelled "Int Bx" in figure 4.29) and the self flux (labelled "Int Bx^2" and "Int By^2" in figure 4.29) as the error is integrated (figure 4.29). Part of this amplification is certainly due to round-off errors of the numerical integration (Simpson's method). It is difficult to reduce them, using the magnetic field formulation, as one needs to integrate the magnetic field over a surface which leads to numerous numerical evaluations of the magnetic field. Surely changing the numerical integration method could improve the situation, but the problem due to the $1/r$-decay of the magnetic field remains and can't be solved. The error for the integration over Bx^2 is significantly higher than for the integration over By^2. To obtain an error below 1%, it is mandatory to calculate 250 or more terms in the double series. In addition, the error is not significantly lower than for Model 1.0 comparing figures 4.7 and 4.29.

To get a sufficient precision of the magnetic field calculation, one has to take into account multiple "magnetic mirrors". This method is not very interesting on a practical point of view, because it requires a lot of conductors in order to achieve a sufficient precision on the circulating current calculation, without being able to take into account the saturation in the inductance calculation. It does not make sense to calculate the magnetic field using Taylor's

series development (one could think to treat the mirrors as terms of a Taylor's series), as even with this trick one needs to sum over many terms to obtain a suitable precision.

Section 4.6 presents the last enhanced slot inductance model, also called Model 4.0 or slot differential inductance model. The following section is dedicated to another reflection point that came up when applying the mirror method, namely the concept of "near-field" and "far-field".

4.5 Near-field versus far-field

When applying the multiple mirror methods, one needs to sum contributions which expand towards infinity. The base contribution is always the same and is given by the analytical equation of the magnetic field for a rectangular conductor. How does the magnetic field behave when the distance between the source and the observing point becomes large? Can the analytical equations be simplified without loosing too much precision? [68] used a distance criteria to switch between the calculation approximations, but it lacked a proper theoretical background. The goal of this section is to develop a theoretical background to justify the use of the distance criteria to switch between calculation methods.

While working with in the topic of field calculation, it is important to have a common understanding about the notions of "near-field" and "far-field"[4]. In this document, the far-field is the region where the field decays according to $\sim 1/r$ in the case where only one conductor is considered. It becomes $\sim 1/r^2$ when the considered conductors are 3-dimensional. The near-field is defined as the region in the vicinity of the field source (in our case a conductor with a rectangular profile), where this approximative relation is not anymore valid and the shape of the conductor determines the magnetic field. This discussion is also important to face the problem of the inductance calculation in the winding overhang as one has to decide when the so-called XY-formulation (taking into account very precisely the shape of the conductor) or the so-called Rθ-formulation (based on an equivalent cylindrical conductor) should be used. It is crucial to have an understanding of the influence on the magnetic field of the two formulations. In the presented figures, the "equivalent" radius r_0 is defined by:

$$r_0 = \frac{1}{4}(h_{\mathrm{Cu}} + b_{\mathrm{Cu}}).$$
(4.46)

The concept of "equivalent" radius r_0 was introduced by [68] to describe the inductance of the strands in the winding overhang. The definition of r_0 differs from the one used in [68]. Numerically speaking, the values computed following the definition in [68] are slightly higher than the ones calculated using relation 4.46. In order to highlight the far-field, the graphs are

---

[4]The terms "near-field" and far-field are used primarily in the field of electromagnetic field, especially to characterise the field near an antenna (see also [62]). The definition of near-field and far-field is adjusted to this work, as these terms are very useful for the understanding of the phenomena even if they are only applied to magnetic field.

given in relative dimension scale, so that one can easily see when the transition from the "near field" to the far-field occurs. For the Rθ-formulation, the magnetic field is given by

$$B_\theta = \begin{cases} \mu_0 \frac{I}{2\pi} \frac{r}{r_0^2} & \text{for } r \leq r_0; \\ \mu_0 \frac{I}{2\pi r} & \text{for } r > r_0. \end{cases} \tag{4.47}$$

The study is a comparison of the magnetic field obtained with both formulations. The error between both formulations is plotted as the 10-base logarithm of the absolute value of the relative error with the XY-formulations taken as reference. The logarithm is used as the magnetic field decays as r^{-1}. The comparison starts with a square conductor of 3x3mm.

The shape of this conductor is not very different to the shape of the round conductor leading to the minimal difference between both formulations. The magnetic fields in both axes (x and y) are presented for different angles starting from 0 degrees up to 90 degrees. The idea is to see if the angle has a significant influence on the results. For the square conductor, one can see that the far field zone begins at a distance of about $3r_0$. The difference between both formulations is not huge and limited to the near field zone, which is the expected result. The angle influences the result in a significant way, but this is only a secondary effect. This comparison is shown on figures 4.30 and 4.31. With the square conductor, one can see that the inductance will be significantly influenced by the choice of the formulation used, mainly the main inductance as the magnetic field is squared. The equivalent conductor of figure 4.30 is smaller than the square conductor as one could expect, but the peak of the magnetic field of both formulations matches quasi-perfectly (figure 4.31), showing that the definition of the equivalent radius is suitable magnetically speaking.

The second comparison is made for a 1.8x7.5mm strand conductor. Its dimensions are in-line with those of the "typical" strands used in Roebel-bars for hydrogenerators. One can see that the begin of the far-field zone is dependent on the angle and is further than for the square conductor (about $5r_0$ instead of $3r_0$ for the square conductor). The difference between both formulations is bigger for the strand conductor than for the square conductor, the peaks of both formulations don't match anymore. The difference is bigger because r_0 doesn't match anymore with the dimensions of the conductor, this will automatically lead to bigger differences in the magnetic field and in the inductance. This comparison is shown in figures 4.32 to 4.33. The surrogate conductors will overlap using both relations to calculate r_0, which is a non-physical result. The maximal amplitude of the magnetic field is similar using the XY-formulation and the $R\Theta$-formulation.
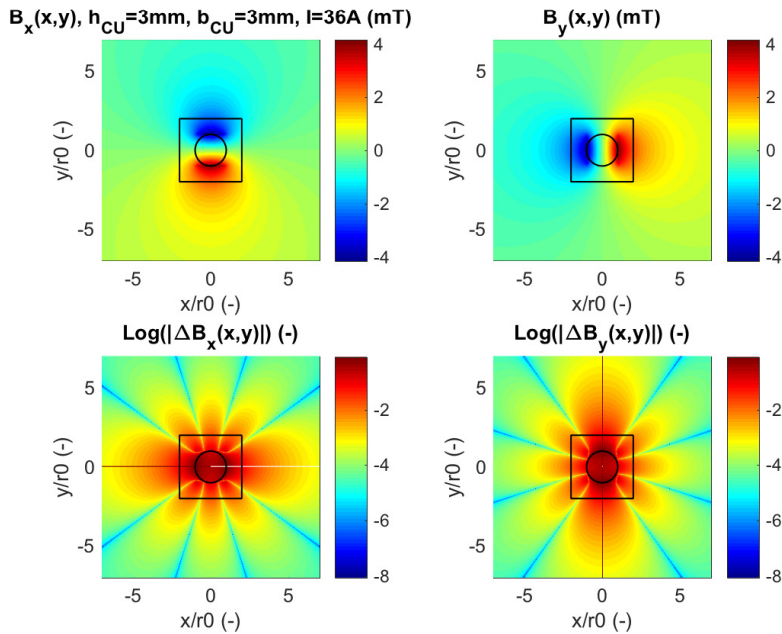
Figure 4.30 – Comparison of the XY-Formulation with the Rθ-Formulation on a 3x3mm square conductor (I=36A), r_0 is calculated using equation 4.46.

In conclusion, independently of the formulation chosen, at far-field the magnetic field behaves as $\sim 1/r$. The far-field zone begins at a distance of about $5r_0$, a distance which increases the more the conductor shape deviates from a square. For a precise inductance calculation it is very important to use a magnetic field formulation that very precisely takes the shape of the conductor especially for the neighbouring strands of a roebel-bar into account. In the far-field zone the choice of the formulation doesn't impact the calculation results significantly as the $1/r$-term is dominating the decay of the magnetic field. Using other definitions for r_0, as for example $r_0 = \sqrt{h_{\mathrm{Cu}}b_{\mathrm{Cu}}/\pi}$, which is based on an equivalence of the surface of the conductor, leads to other values for the transition from the "near-field"-zone to the "far-field"-zone, but doesn't change the basic principle namely that a transition exists from the near-field zone to the "far-field"-zone.

To come back to the questions stated at the beginning of this section, one can respond to them in the following way: The magnetic field behaves like $1/r$ when the distance gets large in the two-dimensional case and $1/r^2$ in the three-dimensional case. This can be demonstrated calculating the limit of the analytical equation for r expanding towards infinity. The analytical equations can be simplified in the far-field zone using only a $1/r$-term respectively $1/r^2$-term in the far-field zone.
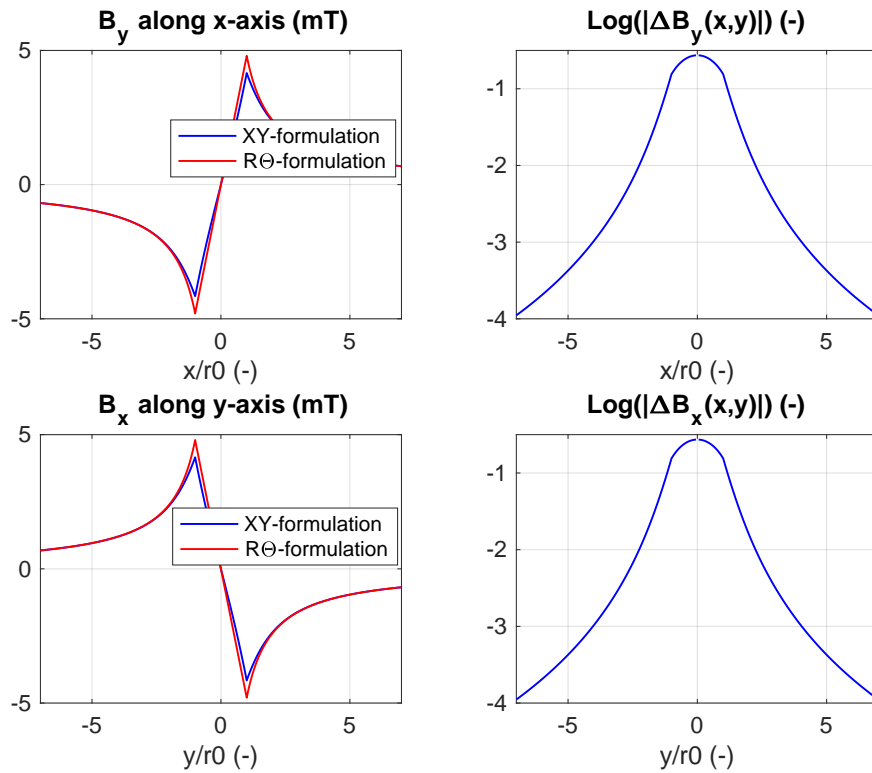
Figure 4.31 – Comparison of the XY-Formulation with the Rθ-Formulation on a 3x3mm square conductor (I=36A), r_0 is calculated using equation 4.46.
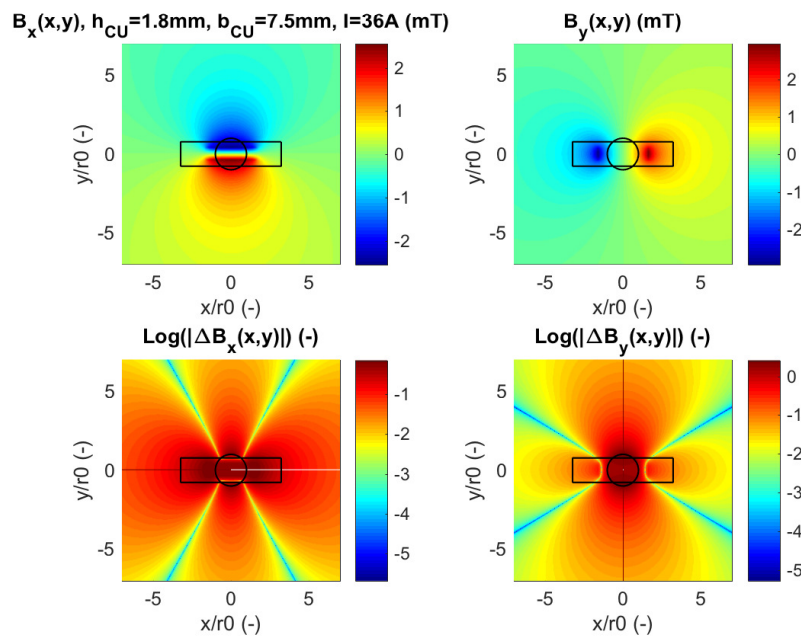
Figure 4.32 – Comparison of the XY-Formulation with the Rθ-Formulation on a 1.8x7.5mm strand conductor (I=36A), r_0 is calculated using equation 4.46.
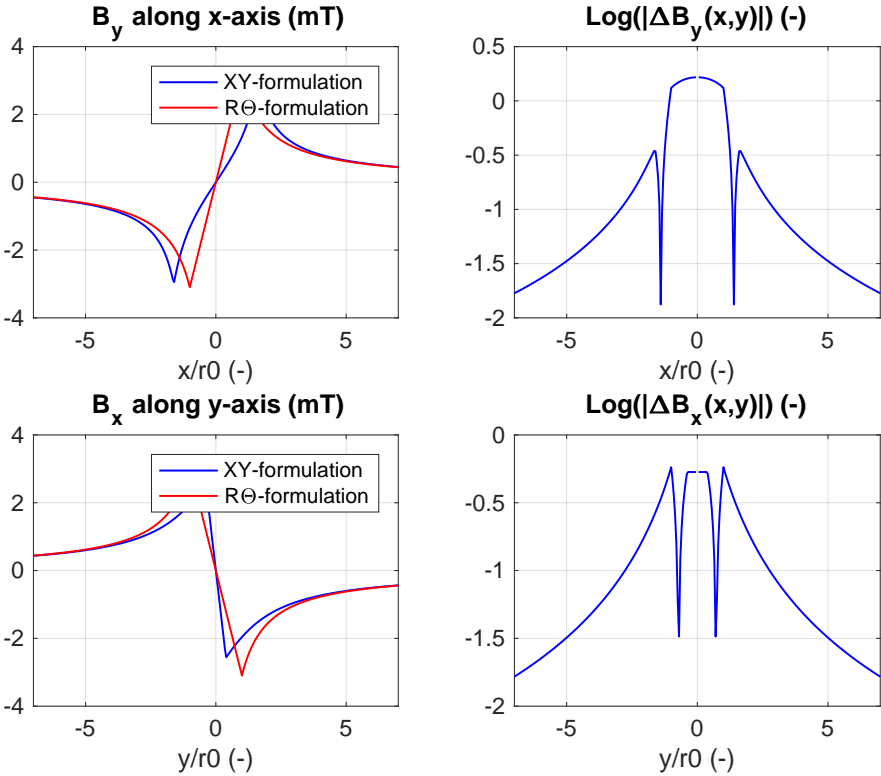
Figure 4.33 – Comparison of the XY-Formulation with the Rθ-Formulation on a 1.8x7.5mm strand conductor (I=36A), r_0 is calculated using equation 4.46.

4.6 Taking into account the non infinite permeable iron: differential inductance model - Model 4.0

[106], [100], [27], [4] and [81] show different possible methods to obtain a saturated value of the slot inductance. [106] uses a magnetic resistance network to obtain saturated fluxes. [100] uses a concept which is very similar to the differential inductance model and has an error of around 5%, which is above the precision target of this work. [27] uses a finite-element simulation to determine the machine parameters. [4] uses magnetic harmonics functions to take into account the iron saturation, but the precision of the presented method is unfortunately also above the precision target of this work. Despite their very promising results, it has been decided to use the method described in [84] and [12], because the differential inductance model permits to achieve the precision goal.

The differential inductance method can be applied to any operating point of the machine, whereas the differential inductances obtained with this method can only be used for a same or a very similar magnetic state of the electric machine [12]. The flux seen by the strand i is a non-linear function of all other currents and can be expressed as

$$\phi_i(t, i_1, ..., i_i, i_n) \tag{4.48}$$

where i_1 to i_n represent all the currents in the considered model. Adding a current Δi to i_i leads to the new flux $\phi_{i+\Delta i}$ given by

$$\phi_{i+\Delta i}(t, i_1, ..., i_i + \Delta i, i_n) \tag{4.49}$$

Remembering that an inductance is defined by a quotient of a flux over a current leads to the definition of the differential inductance

$$L_{diffi} = \frac{\Delta \phi}{\Delta i} = \frac{\phi_{i+\Delta i}(t, i_1, ..., i_i + \Delta i, i_n) - \phi_i(t, i_1, ..., i_i, i_n)}{\Delta i}. \tag{4.50}$$

If there is no saturation, the differential inductance definition is mingled with the normal or classical inductance. If there is saturation, the differential inductance may have a different value than the normal or classical inductance definition. Another way to introduce the differential inductance is to start the voltage equation 2.5 and express the flux as a sum of currents times inductances. This gives

$$\frac{d}{dt}\psi_i(t) = \frac{d}{dt}\sum_{i=0}^{n} L_{ij} i_j = \sum_{i=0}^{n} \frac{\partial}{\partial t} L_{ij} i_j = \sum_{i=0}^{n} i_j \frac{\partial L_{ij}}{\partial i_j} \frac{\partial i_j}{\partial t} \tag{4.51}$$

where $\frac{\partial L_{ij}}{\partial i_j}$ is called differential inductance. Both definitions are equivalent, even if one should keep in mind that the differential inductance may be a function of the current i_i for high variations of the current i_i. As long as the currents don't have a big excursion, the linear approximation of the derivative given by equation 4.50 is sufficient to describe the differential inductance with enough precision. The time-variation of the currents in electrical machines

requires the differential inductance to be recalculated for every time-step. Depending on the saturation level of the electrical machine, the differential inductance can be constant, but this can not be generalised and be considered to always be true.

Before applying the differential inductance to this problem the following questions must be answered. These questions have not been treated in the published literature and must be considered as an original contribution of this work to the theory of differential inductances:

- In which interval is the linear approximation of the flux derivative valid;

- What is the optimal current level for Δi;

- Is it necessary to calculate the differential inductance for every time-step or is a time-constant approximation sufficient;

The following subsection provides answers to these questions. The differential inductance method is applied on a 2-dimensional approximation of the electrical machine in the active part. The 2-dimensional model is based on the hypothesis and methodology defined in [114] applied on a DFIG. Figures 4.34 and 4.35 show the 2-dimensional model in the GUI of Flux2D. Details about the practical use of the differential inductance method can be found in [84] and [12]. The injected currents in the magneto-static computation are derived from the magneto-evolutive simulation for the nominal operation point of the machine as well as the sustained short-circuit operating point. The magneto-evolutive model has been validated with measurements on a full scale DFIG and showed an error of less than 3-5% on the measured currents, which validated this model[5]. The electromagnetic torque is used as a comparison variable to see if the models, namely magneto-static and magneto-evolutive, are similar. The torque difference is less than 1% showing a very good agreement between both models, so that the approach of taking the currents from a magneto-evolutive computation and use them to determine the differential inductance will not induce errors into the simulation. In addition, as one may see especially in figure 4.35, six slots have a detailed geometry. Only one slot is used for the circulating current calculation, the two neighbouring slots are used to analyse a potential coupling between the strands of neighbouring bars. In addition, the other slots are also monitored. With this additional information, one can see if there are additional couplings that one should take into account in the calculation model. This is a major change in the calculation model, compared to the ideal slots model (refer to section 4.1), where the calculation domain is strictly bound to one slot. Taking saturation into account can extend the domain of the study up to all slots. Figures 4.36 and 4.37 show the finite-element model used for the calculation of the differential inductances in the experimental setup. Figure

---

[5]Even if, the error is bigger than the 1%-rule, the model can be considered as validated as in a full scale machine, there many other effects that should be taken into account. For exemple: the end-winding inductances, the core sheet punching and stacking, the measurement precision of the rotor currents, the mechanical and construction tolerances, the thermal expansion of the machine, oscillation of the operating point, change of the grid parameters and so one.

4.38 presents the strand numeration used in this section, while figure 4.39 shows the strand numeration for the slot used in the experiments.
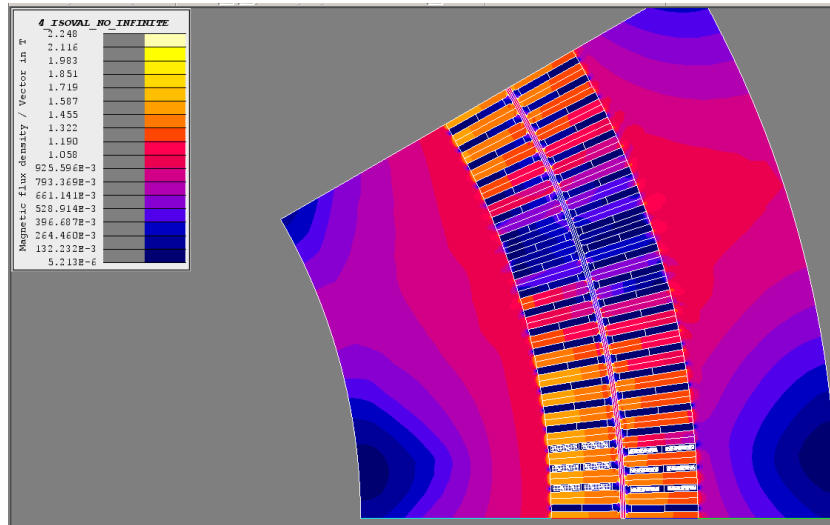
Figure 4.34 – View of the 2-dimensional model of the DFIG in the GUI of Flux2D (B-field).
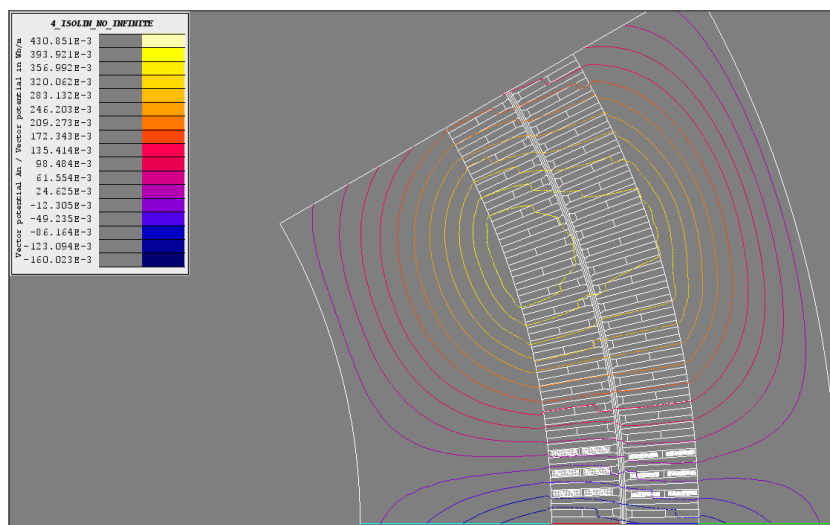
Figure 4.35 – View of the 2-dimensional model of the DFIG in the GUI of Flux2D (Flux).
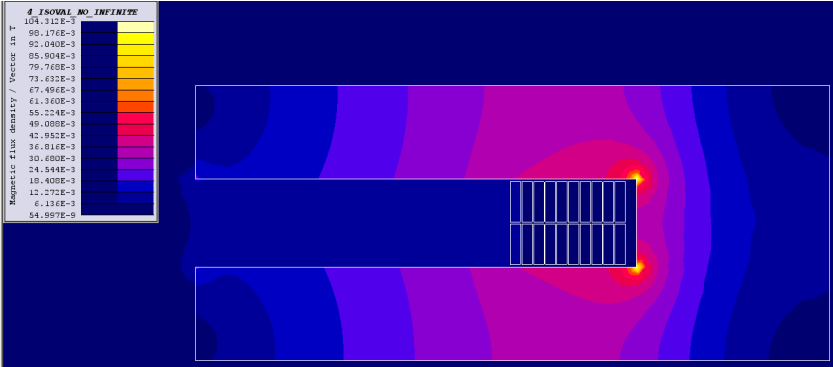
Figure 4.36 – View of the 2-dimensional model of the experimental setup in the GUI of Flux2D (B-field).
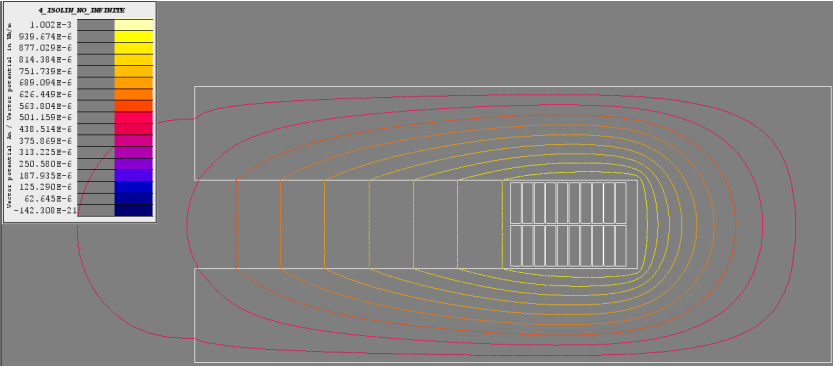
Figure 4.37 – View of the 2-dimensional model of the experimental setup in the GUI of Flux2D (Flux).
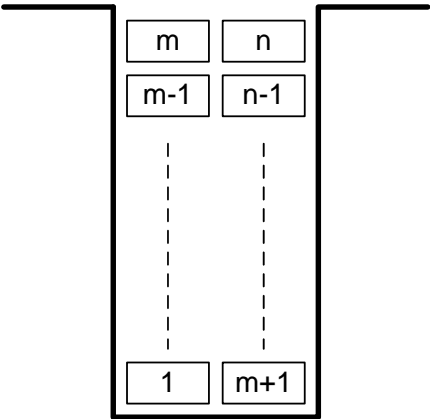
Figure 4.38 – Strand numbering in the slots (finite-element simulation of DFIG's slots).
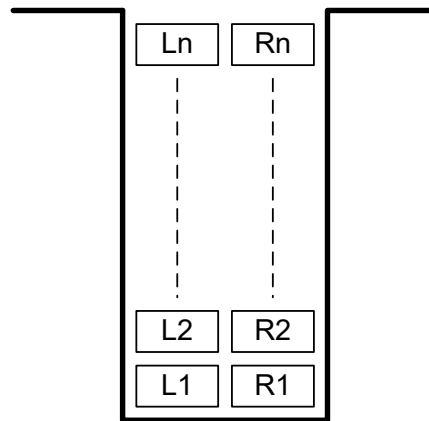
Figure 4.39 – Strand numbering in the slots (finite-element simulation of experiment's slots and DFIG's slots in the case of figures 4.54, 4.55, 4.56, 4.57 and 4.79).

4.6.1 Influence of the iron saturation curves on the inductances

This subsection responds to the question "In which interval is the linear approximation of the flux derivative valid?". A first set of magneto-static simulations shows the impact of the saturation of the phase flux of one stator phase. Figure 4.40 shows the obtained results using the model defined in figure 4.34.

The saturation behaviour of the flux is very similar to the results obtained by [12], indicating that the used model is correct. The flux-current function can be approximated using a local spline approximation or a high order polynomial. All other mathematical functions lead to higher approximation errors. It is possible to use a high-order polynomial interpolation of the flux, but one should keep in mind the definition of the flux given in equation 4.48. If the current i_i has a large excursion, then certainly other currents in the model will also experience this huge excursions, meaning that the flux will also be a function of other currents and that even with a high-order approximation there will be a huge error on the total flux ϕ_i. To counter-act this error, it could be possible to use a second order Taylor-approximation of the flux function around the operating point considered.

Figure 4.41 shows the impact of the strand current on the strand flux. For a strand current within the ranges of figure 3.2, the flux is a linear function of the strand current. The linear approximation of the differential inductance according to equation 4.50 can be used for this problem regardless of the saturation level and time-step. All the simulations performed until now validate this hypothesis (nominal operation point and sustained short-circuit).

The phase flux shows a typical saturation behaviour, while the strand flux is linear over a span from 0 to 2.5 times the DC-strand current. The linear differential approximation
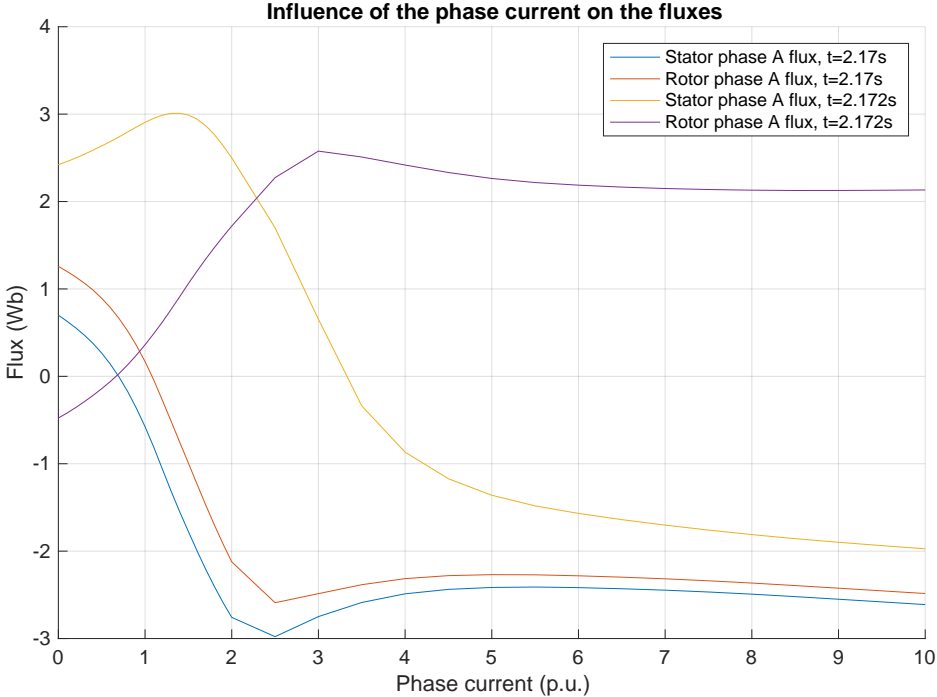
Figure 4.40 – Influence of the phase current on the phase flux. DFIG at rated conditions.
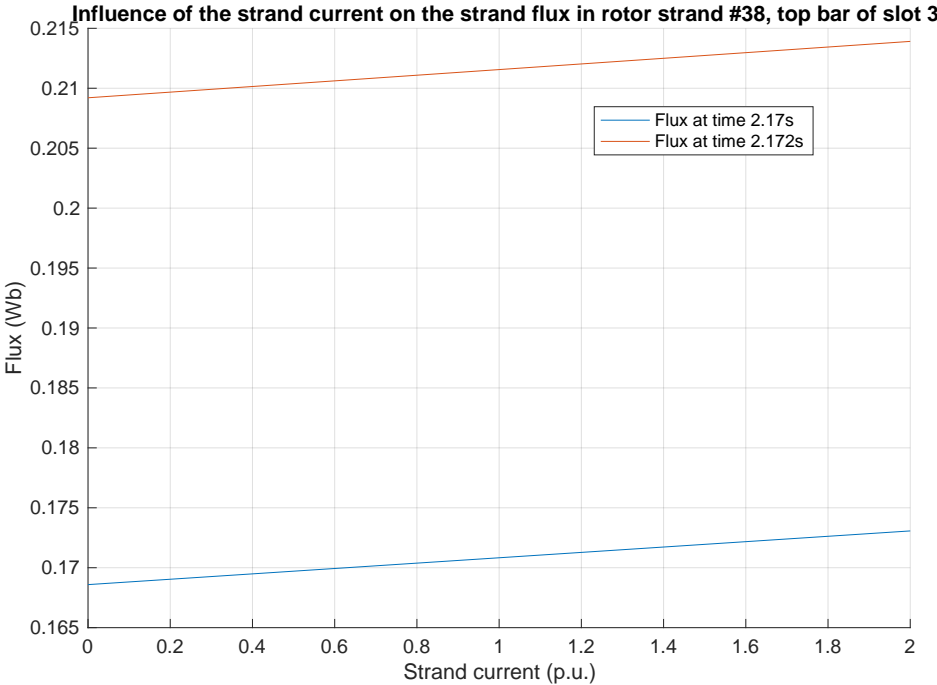
Figure 4.41 – Influence of the strand current on the strand flux. DFIG at rated conditions.

is therefore sufficient to approximate the strand flux with enough precision. Seeing the differential inductance as a Taylor-approximation of the flux function around a given operating point enables to use the results of Taylor's theorem[6], especially the results for the reminder, to numerically evaluate the approximation error on the fluxes.

4.6.2 Influence of the current level Δi on the differential inductances

This section deals with the question "What is the optimal current level for Δi?". This influence is studied using the model (figure 4.37) used for the experimental validation of the differential inductance model. Two sets of simulations are carried out, one with Δi=0.1I_n and the other with Δi=1.0I_n where I_n is the DC-strand current. The slot model has no external field, so that the only source of magnetic excitation are strand currents. For both cases, the calculated differential inductances are plotted and the circulating currents are calculated and compared to the simulated ones with a time-stepping finite-element simulation. The inductance is a function of the current level Δi transposing the fact that the chosen operating point has no initial saturation level. Every additional current will increase the saturation level, making the differential inductance method very sensitive when the initial saturation level is zero. In electrical machines, this case can happen when the machine operates in steady-state short-circuit. In this case, one should use a second order differential inductance calculation, using a second order term of Taylor's series for a multivariable function could reduce this difference.

Figure 4.42 shows the influence of the current level Δi on the differential inductances with a DC-strand current of 5A. There is no inductance given for t=0.005s, as the currents and fluxes are null for this particular time-step. The inductance difference is 0.028μH or about 1.8% for the self inductance of strand 1, 5 and 10. The impact of this difference is negligible on the circulating currents, as this difference is virtually constant for all strands. Its impact will be larger for the complete model, as this difference acts like an offset on the inductance. This offset can impact the global calculation by artificially lowering or increasing the circulating currents. It is very interesting to point out that the inductances grow unexpectedly with an increasing Δi, while one would expect the inductance to decrease with an increasing Δi, as an increasing Δi means an increase of the saturation level and therefore a decrease of the inductances. Some numerical errors are may be affecting the results for Δi=0.5A.

For a DC-strand current of 40A, the inductances are lower than for a current of 5A. An increase of the current level from 0.1 to 1 I_n produces an expected reduction of the inductance. For a current level of 1I_n, the inductance difference is 0.551 μH or 32.4%, while this difference accounts for 0.288 to 0.333 μH in the other case.

The current level Δi has a non-negligible impact on the differential inductance. In the case of the experimental model, as the saturation level is very low, its impact is highlighted. The finite-element simulation reacts heavily to changes in Δi. In the case of the experimental validation, as the considered slot can be represented with a small error as a 2-dimensional

---

[6]https://en.wikipedia.org/wiki/Taylor%27s_theorem
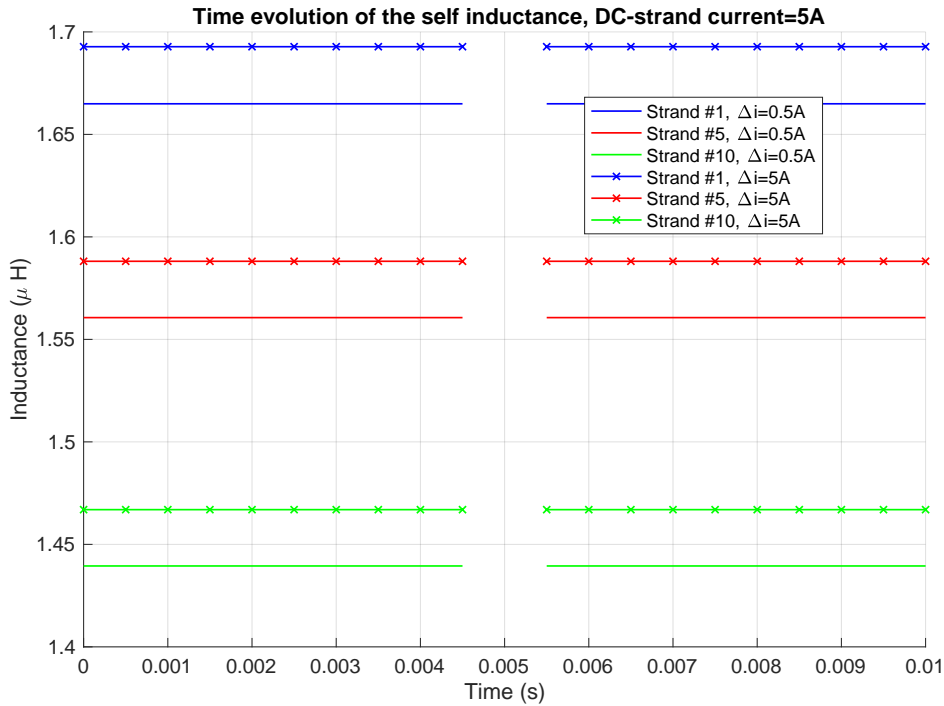
Figure 4.42 – Influence of the current level Δi on the differential inductances with a DC-strand current of 5A. There is no inductance given for t=0.005s, as the currents and fluxes are null for this particular time-step: the current is a cosine-function with a frequency of 50Hz.
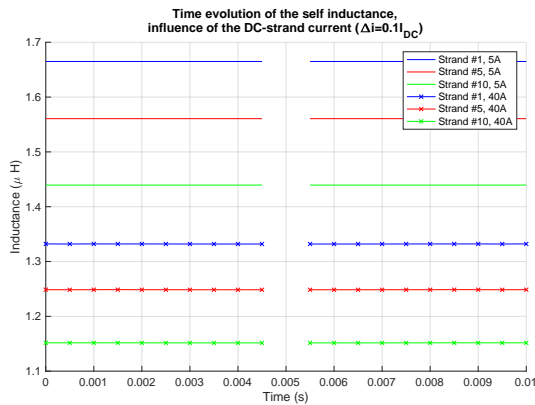
Figure 4.43 – Time evolution of the self inductance, influence of the DC-strand current with Δi=0.1I_n. There is no inductance given for t=0.005s, as the currents and fluxes are null for this particular time-step: the current is a cosine-function with a frequency of 50Hz.
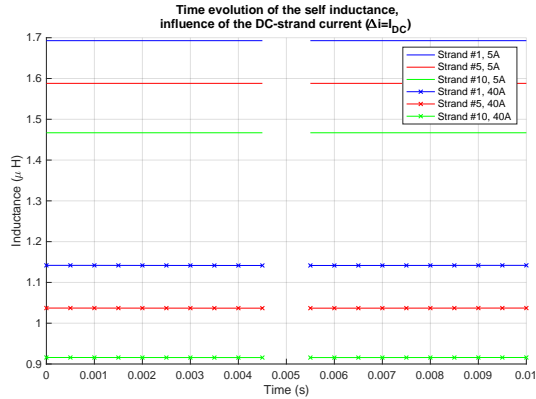
Figure 4.44 – Time evolution of the self inductance, influence of the DC-strand current with Δi=1I_n. There is no inductance given for t=0.005s, as the currents and fluxes are null for this particular time-step: the current is a cosine-function with a frequency of 50Hz.

model, the influence of Δi on the calculated circulating current is negligible as no overhang inductances are considered, keeping in mind that the numerical value of the difference is $0.028\mu H$ which is a very small quantity. If Δi is too small, this can lead to numerical errors as the flux difference will be too small, and the used software has a repetitive error around 1e-12, but a small value transposes the derivative character of the differential inductance with the highest fidelity. A higher value of Δi, around I_n, which is in line with the highest amplitude of a circulating current calculated in figure 3.2 leads to the expected value of the current level. Probably one should use this value for the determination of the differential inductance, whereas this recommendation is based on three simulated cases only. To have a broader base and to draw a more reliable recommendation, one should simulate 10-20 different cases mixing different machines and different operating cases, but this is out of the scope of this study.

4.6.3 Influence of the time-step on the differential inductances

This section answers the last question: Is it necessary to calculate the differential inductance for every time-step or is a time-constant approximation sufficient? This influence is studied using the model defined for the experimental validation of the differential inductance model (refer to figure 4.36). Two sets of simulations are done, one with a DC-strand current of 5A and another with a DC-strand current of 40A. Time plots highlight the influence of the time-step on the differential inductances. As for the previous section, the slot is in short-circuit-condition without any external field. The saturation level is low, so that the sensitivity to the current level is high.

With a current level of 40A, the inductance becomes a function of time as stated in [12] and as one can see in figure 4.45. The time variation of the inductance is the first sign of a saturation-like behaviour of the inductance. The higher the time-dependent component of the inductance, the higher the saturation of the inductance. To achieve the highest possible calculation precision, one should use a time-dependent differential inductance matrix. In this particular case, the mean value of the inductance is 1.0371 μH and the time-dependent inductance value is 0.0002367e-4 μH or 0.023% of the mean value. The time-dependent inductance is negligible. The validation of the model is based on a constant inductance.

As one can see, it is impossible to state a priori, if the time-step has an influence on the differential inductances. Its influence is strongly related to the saturation level of the model or operating point the machine. When this phenomenon occurs, one can use a sine-function-interpolation and calculate the differential inductances over a quarter-period to limit the number of simulations to a minimum.

Due to this influence, it is recommended to make a simulation over a quarter-period and numerically evaluate the impact of the time variation of the inductance.
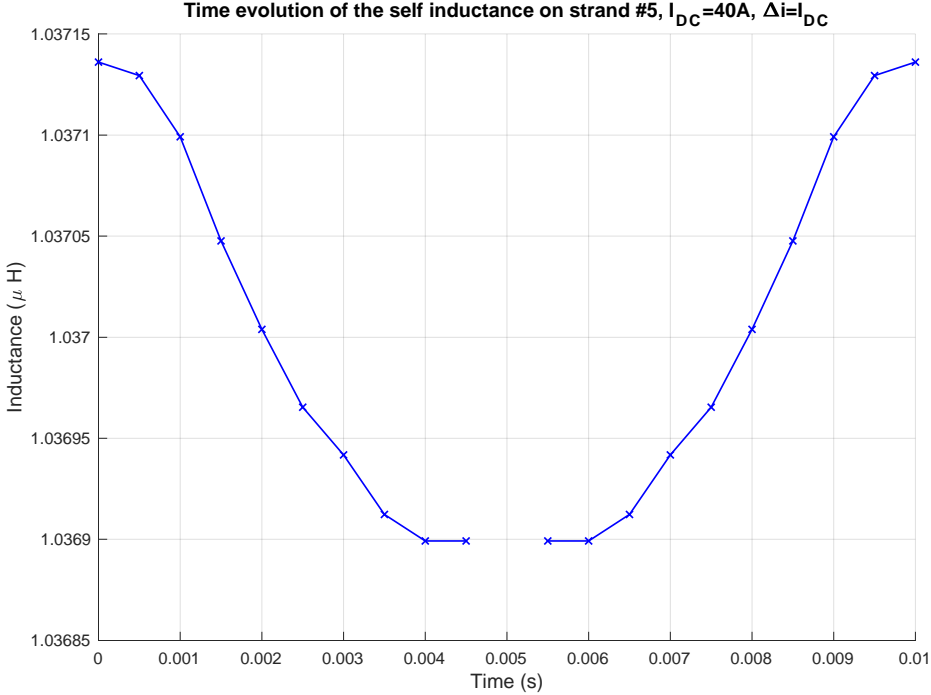
Figure 4.45 – Self-inductance time variation for the strand #5, DC-strand current of 40A and $\Delta i = 1 I_n$. There is no inductance given for t=0.005s, as the currents and fluxes are null for this particular time-step: the current is a cosine-function with a frequency of 50Hz.

4.6.4   Influence of the operating point on the differential inductance

To analyse the influence of the operating point on the differential inductance two simulations have been carried out: the first for a DFIG operating at nominal operation point, another for a machine operating with a short-circuited stator. The model used for this study is given by figure 4.34 which has been validated against measurements. Figures 4.46 and 4.47 show the differential inductance matrix depicted for two different time steps for a DFIG operating at nominal operation point. The pictures present two radical opposed situations: the left picture shows the differential inductance matrix when the neighbouring teeth are very saturated. The inductances covers a range from 18 to 21.5 μH. The picture on the right shows the non-saturated teeth with its typical inductance arrangement. The inductances span over a range from 22 to 35 μH which is much more than in the saturated case.
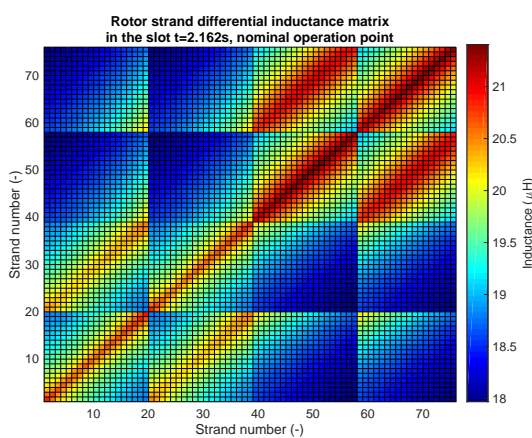
Figure 4.46 – Rotor differential inductance matrix for slot #2, each bar has 38 strands, nominal operation point.
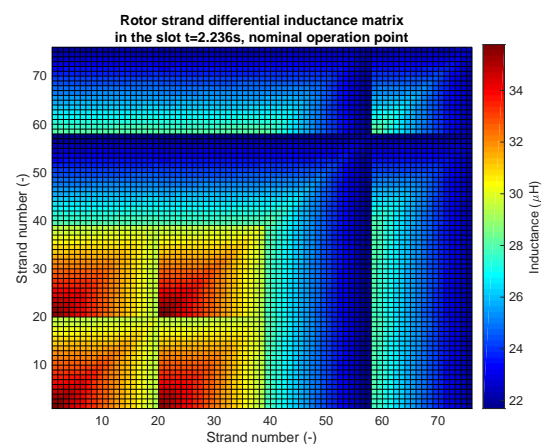
Figure 4.47 – Rotor differential inductance matrix for slot #2, each bar has 38 strands, nominal operation point.

In the case of the stator short-circuit operation, the differential inductance matrix is shown in figure 4.48. This figure shows a similar inductance value variation as the one presented in figure 4.47, except that the inductance range is 49 to 35 μH. It is very interesting to point out that the inductance is the highest in the stator short-circuit operation point, followed by the nominal operation point in the unsaturated time step and finally the saturated time step of the nominal operation point. Figure 4.49 presents the time evolution of the strand self inductance (top, middle and bottom of the bar) for a stator and rotor bar for a DFIG operating at a nominal operation point. One can see that the inductance varies as a function of time. The stator strand inductance seems to follow a cosine function, while the rotor strand inductance has more a step-like time variation. The origin of this inductance time-variation is the variation of the main flux and the saturation of the teeth. On the contrary, for the stator short-circuit case, the inductance does not depend on the time. In this operation point, the stator and the rotor fluxes are in phase opposition and cancel themselves out. This leads to a very small slot saturation, so that the inductance remains constant over the time. Even in this case, the differential inductance matrix is significantly different from the slot differential inductance
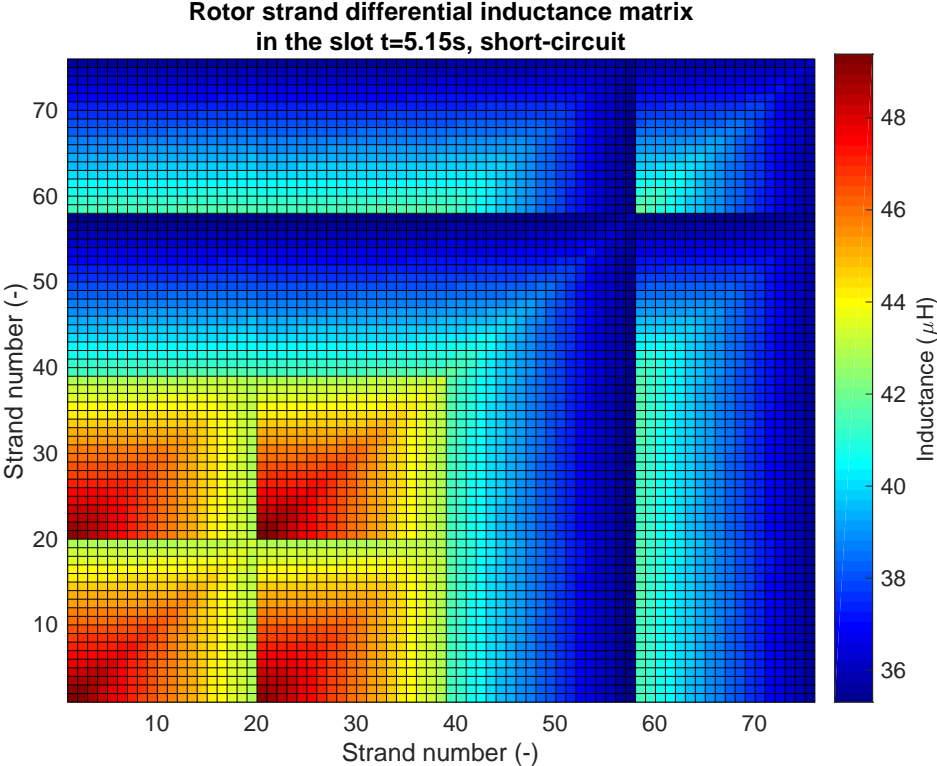
Figure 4.48 – Rotor differential inductance matrix for slot #2, each bar has 38 strands, stator short-circuit operation.

matrix of Model 3.0 (refer to figures 4.71 and 4.72). The coupling between the top and bottom bar is not negligible and will be integrated in the calculation using differential inductances.
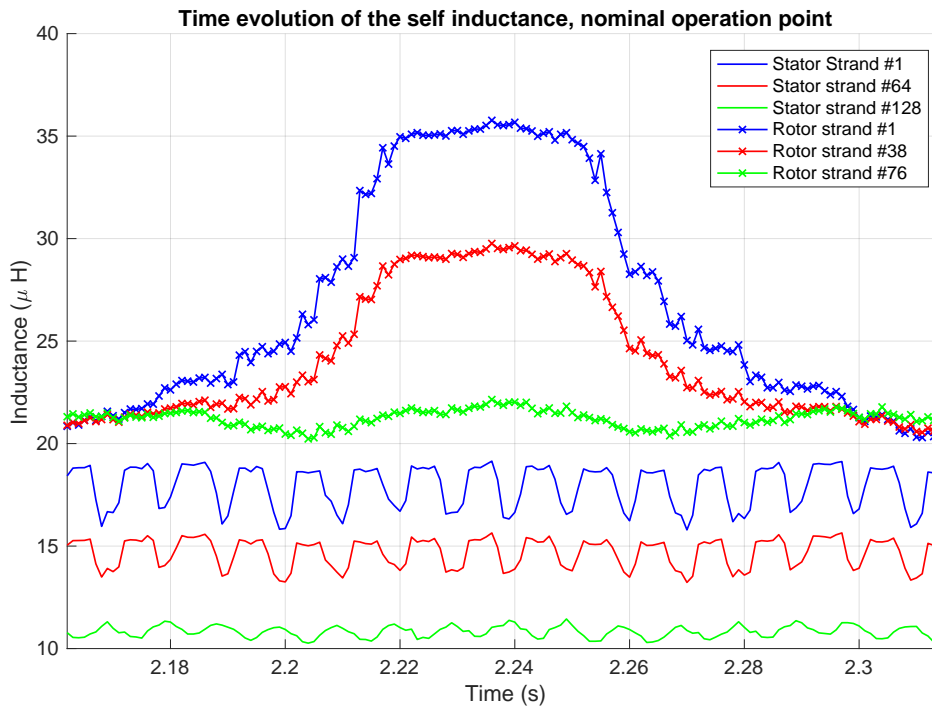
Figure 4.49 – Time evolution of the strand self inductance (one stator slot has 128 strands and one rotor slot has 76 strands), nominal operation point, slot # 2.

Figures 4.51 and 4.52 present the time-evolution of the stator and rotor currents for the nominal operating point. Theses figures help to understand if there is a correlation between the inductance change and the current of the phase A (slot # 2 belongs to phase A). At a first glance, the stator inductance variation is not coupled to the stator current. The correlation coefficients are 46.65%, 43.84% and 64.09% for the strands of figure 4.49. The low values from the correlation coefficients confirm that point. The variation seems to be due to the slotting effect of the rotor teeth, which can be confirmed comparing the time with the mechanical speed and the number of rotor teeth. The rotor current seems to have much more significant influence on the inductance variation. The correlation coefficients are 81.56%, 78.86% and 0.41%. Theses values are significantly higher than for the stator but still below the 95% limit, which should be applied when working with correlation coefficients. It seems that the rotor current has an impact on the inductance variation, which could be validated. The stator slotting seems not to have any impact on the rotor inductance variation.

The difference in the inductance variation can be also be highlighted, when one plots the evolution of the strand inductance as a function of the strand position in one Roebel bar. When the neighbouring teeth are highly saturated (refer to figure 4.54), the inductance variation follows a curved line and the inductance value is the same for both columns only after eight strands, while in the unsaturated case (figure 4.55) the inductances are the same after five
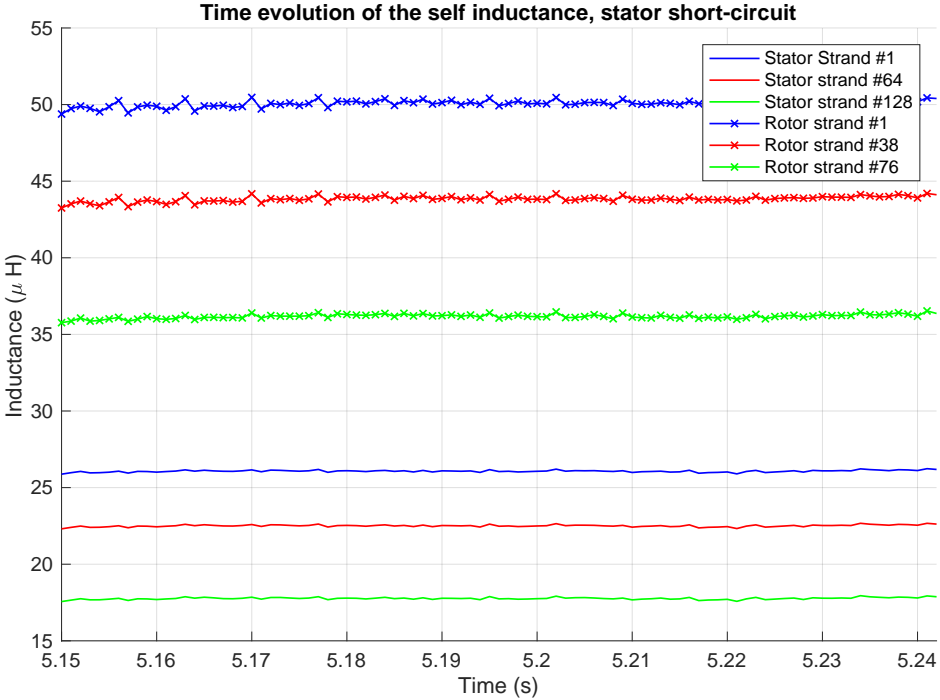
Figure 4.50 – Time evolution of the strand self inductance (one stator slot has 128 strands and one rotor slot has 76 strands), stator short-circuit operation point, slot # 2.
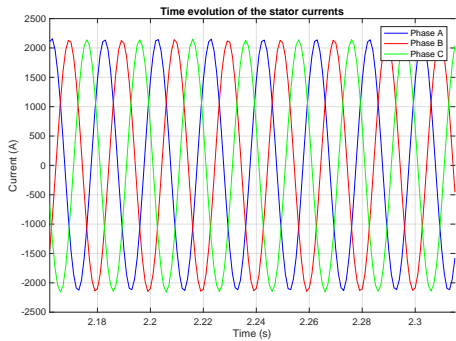
Figure 4.51 – Time evolution of the stator currents for the nominal operating point.
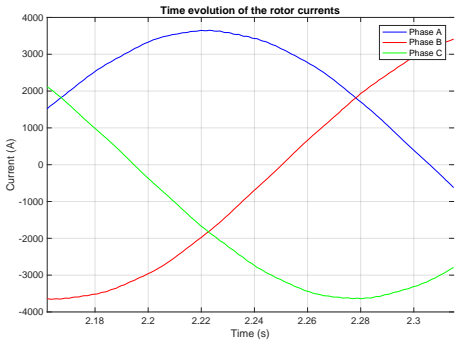
Figure 4.52 – Time evolution of the rotor currents for the nominal operating point.

strands and the inductance variation follows a straight line. The difference between both lines is more or less the same and is about $0.5\,\mu H$.

Figure 4.53 – Rotor flux of phase A as a function of the rotor current of phase A for different operating points (represented by CC=short-circuit and OP=nominal operation point). The results are shown for particular times only, which corresponds to maximal respectively minimal value of the inductance.

Figure 4.53 presents the influence of a rotor current variation on the rotor flux of phase A. As one can see, the flux depends strongly on the time and operation point. The differential inductance is an image of the slope of the flux around 1.0p.u. of rotor current. It is obvious that the calculated differential inductance is in relation to the flux variation occurring at the particular time in the electrical machine for the considered operation point, which explains the strong inductance variation that can be seen in figures 4.49 and 4.50 as well as the value of the inductances. It is very interesting to point out that stator short-circuit operation and nominal operation at its most saturated time has a linear slope, but not with the same slope which is transposed in different differential inductances values.

In the case of the stator short-circuit operation (figure 4.56), the behaviour is similar to the one of figure 4.54. Putting all the inductance evolutions in one figure leads to figure 4.57, where the inductances are presented in a scale normalised to the first inductance of the left column. In the saturated case, the inductance variation is smallest, while in the short-circuit case it is the highest, but always less than in the ideal case. The inductance variation is an important factor to be taken into account especially when studying under-roebeling and extended roebeling. Nevertheless, the inductance variation stays inline with the results of figure 4.11, where the
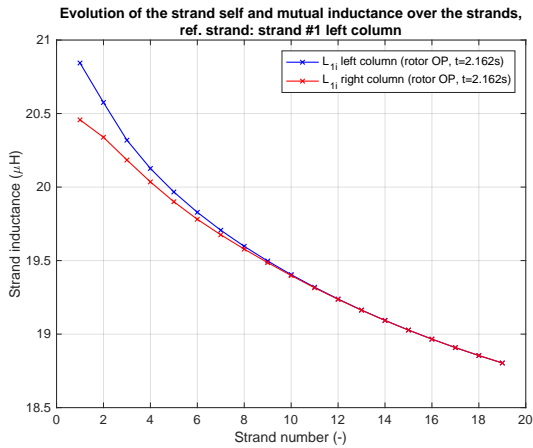
Figure 4.54 – Evolution of the rotor strand differential inductance in slot #2, top bar with 38 strands in function of the strand position, nominal operation point, t=2.162s.
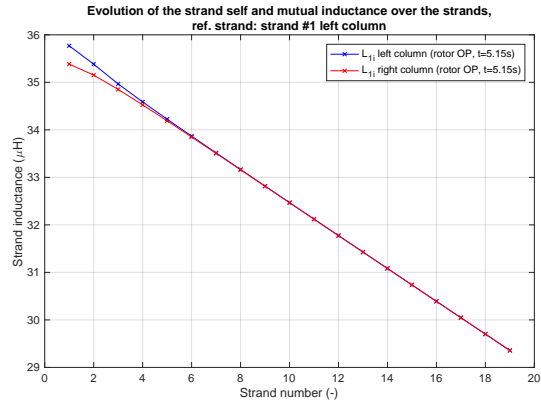
Figure 4.55 – Evolution of the rotor strand differential inductance in slot #2, top bar with 38 strands in function of the strand position, nominal operation point, t=2.236s.

inductance variation lies around factor 3.
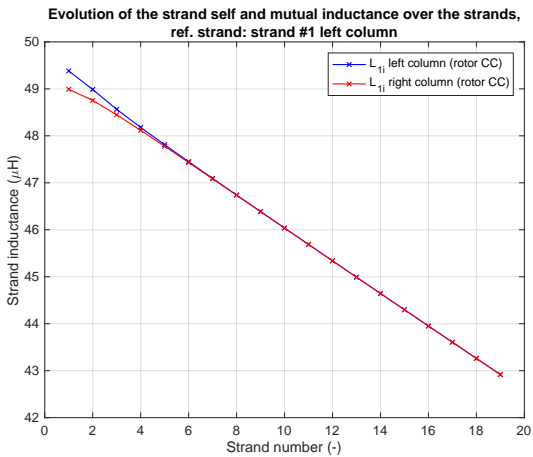
Figure 4.56 – Evolution of the rotor strand differential inductance in slot #2 top bar with 38 strands in function of the strand position, stator short-circuit operation point, t=5.15s.
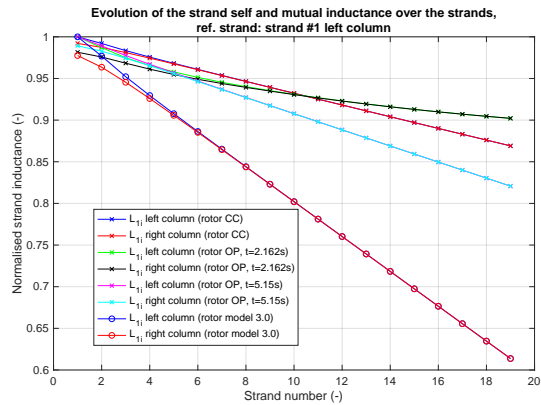
Figure 4.57 – Evolution of the rotor strand differential inductance in slot #2 top bar with 38 strands in function of the strand position (nominal operation point and stator short-circuit point).

To summarise, the strand inductance is a function of the machine operating point and shall be computed for any operation point. The differential inductance matrix can be time-dependent, especially when the machine is operated in a under- or over-excited nominal operation point. The stator short-circuit operation point as well as the unsaturated time steps of the nominal operation point have similar differential inductance matrices than the ideal inductance matrix. Nevertheless, the inductance variations are not in a comparable range

between these three unsaturated operation points. The difference between the first strand inductance in both columns is more or less the same value as these strands are located in the near-field-zone where only the strand dimension plays a role.

4.6.5 Differential strand inductance in the ventilation ducts

[77] presented a calculation method to obtain the strand inductance in the ventilation ducts. Its approach is based on a non-validated field assumption, from which the strand inductances are derived. The main drawback is that the strand self inductance is not the same for all strands, which is counter-intuitive for a strand located in air. To eliminate this drawback, a novel method based on the differential inductance method is proposed.

The strand inductance in the ventilation ducts is also computed using the differential inductance method. To validate this approach a finite-element simulation of the magnetic field in these ducts have been carried out. The goal of this simulation is to analyse the behaviour of the magnetic field in these ducts and to look for the applicability of the concept of differential inductance in the ventilation ducts and to see if the finite-element model can be "decomposed" into an iron and an air part.
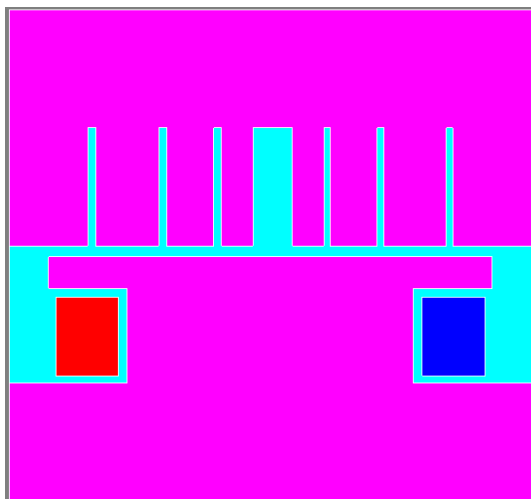
Figure 4.58 – View of the ventilation ducts finite-element model.
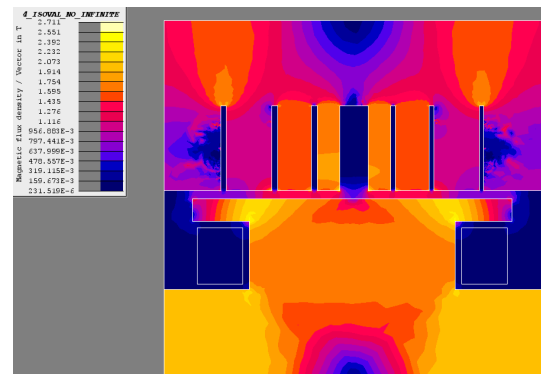
Figure 4.59 – Magnetic flux in the ventilation ducts model.

Figures 4.58 and 4.59 present the model and the magnetic flux in this model. The magnetic flux amplitude has been chosen to be aligned with the magnetic flux densities occurring in the DFIG in operation. The model represents a cut of a salient-pole machine in a rz-plane. The r-axis is vertically arranged while the z-axis is horizontally arranged. The ventilation ducts are not running through the whole machine, as for a real machine, because it was chosen to close the flux in iron and not in air. To simplify the model, symmetry conditions have been used at both horizontal limits. Nevertheless, this model is a good approximation of the magnetic field in the ventilation slits, as the magnetic field is mainly radial in teeth and tangential in the yoke

but with a significant smaller amplitude so that the magnetic field in the ventilation ducts must be much smaller in the yoke region than in the slot region, so that it has been decided to concentrate on the teeth region also because the strands are located in the teeth and not in the yoke. The simulated ventilation ducts are 10mm and 8 mm wide. The results are very similar for all ventilation ducts with a same width so that only one curve per width will be presented. The remaining magnetic field in the ventilation ducts lies between 30mT and 1mT depending mainly on their position respective to the center of the pole.
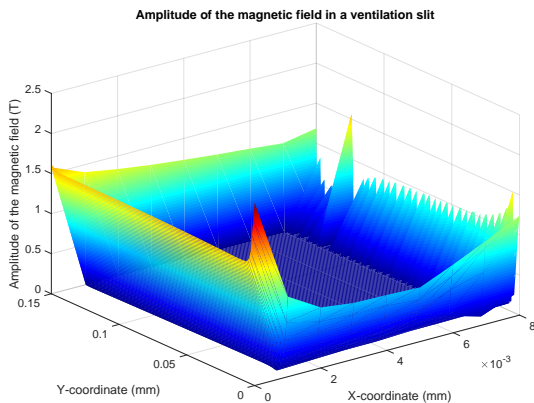
Figure 4.60 – Amplitude of the magnetic field inside a 8mm ventilation duct.
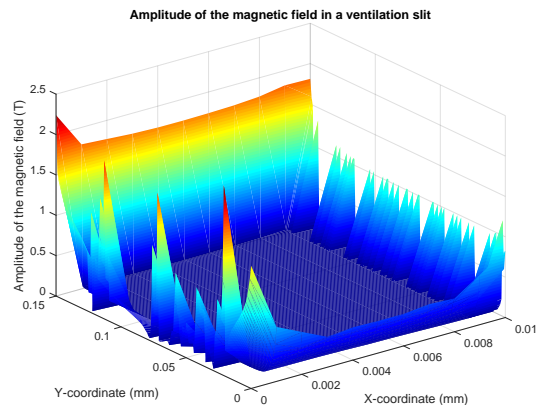
Figure 4.61 – Amplitude of the magnetic field inside a 10mm ventilation duct.

Analysing figures 4.60 and 4.61 shows that the magnetic field is around 2.0T in the teeth and yoke (as the yoke height is small) and drops quasi-instantly in the ventilation duct even in the case of a 8mm-width ventilation duct. The mesh is not very coarse in the ducts so that one could have the impression that it takes 1mm to drop the magnetic field, but in reality it is much less. The amplitude of the remaining magnetic field is constant in the ventilation duct. As the remaining magnetic field remains constant, the concept differential inductance can be applied and will produce relevant results. The fast drop in the magnetic field amplitude confirms the fact that the ventilation duct inductances can be calculated independently of the slot differential inductances using two separate 2D-models and concatenate the computed results later on.

The finite-element model depicted in figure 4.34 is used and the iron zones are replaced by air. The differential inductance matrix computed is given in figure 4.62, which exhibits similar behaviour as for figure 4.49.

Figure 4.62 confirms this similar behaviour as the curves have an identical form as figure 4.46. The mutual inductance between bars in the ventilation ducts is negligible as shown in figures 4.63 and 4.64, as their amplitude is an order of magnitude smaller than the differential inductance in presence of iron. One could consider to take this effect into account as a third order contribution, whereas it could very well be considered using an induced voltage approach instead of an inductance approach. Figure 4.62 also shows that the coupling between the top bar and the bottom bar is negligible, it could also be integrated in the calculation using
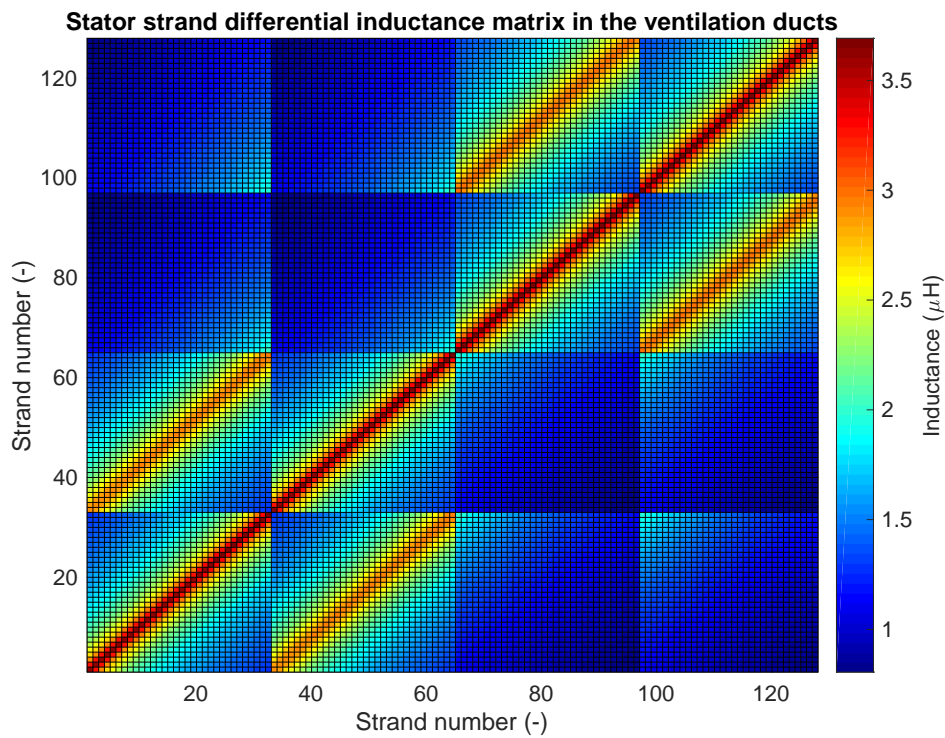
Figure 4.62 – Stator strand differential inductance matrix in the ventilation ducts (slot # 2, one bar has 64 strands).

an induced voltage approach.
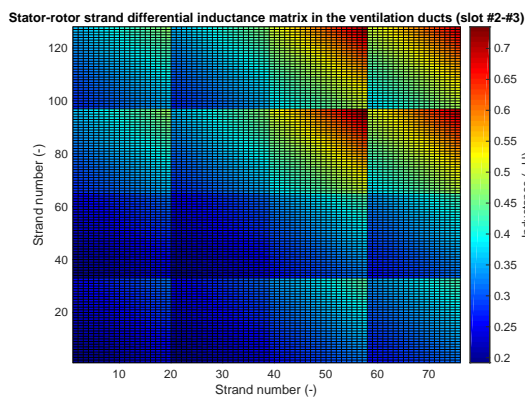
Figure 4.63 – Stator-rotor strand differential inductance matrix (#2-#3).
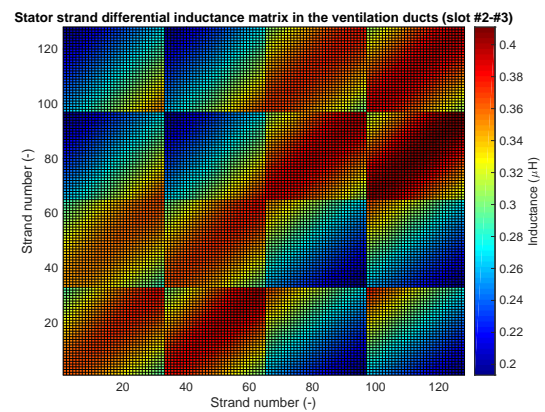
Figure 4.64 – Stator strand differential inductance matrix (#2-#3).

4.6.6 The differential strand inductance between neighbouring bars

As the iron is not anymore infinite permeable, a coupling between neighbouring bars could occur. To study this possible interaction the differential inductance matrix between neigh-

bouring stator bars has been computed for the two considered operation points.
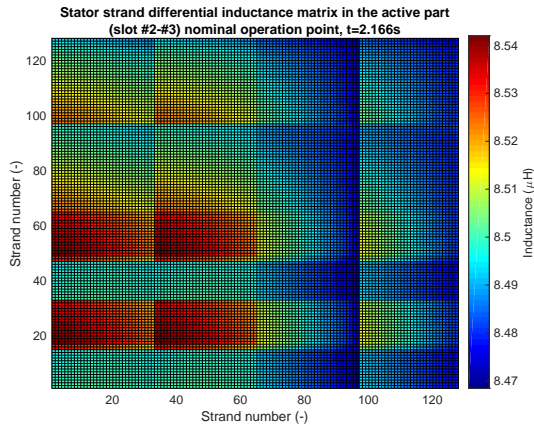
Figure 4.65 – Stator differential inductance matrix in the active part (slot #2-#3) nominal operation point, t=2.166s.
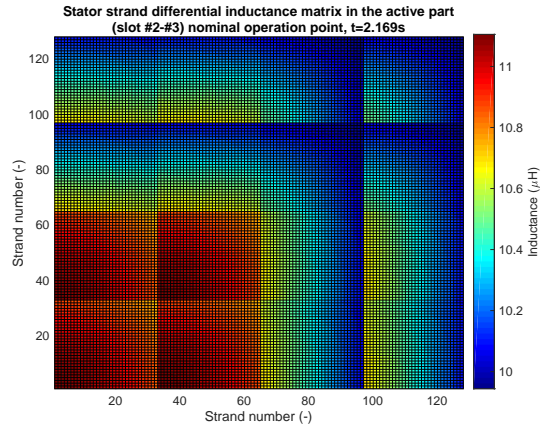
Figure 4.66 – Stator differential inductance matrix in the active part (slot #2-#3) nominal operation point, t=2.169s.

Figures 4.65 and 4.66 presents the differential inductance matrix between the slot #3 and slot #2 for two distinct time-steps for the nominal operation point. The inductance is not null transposing a certain coupling between the stators bars. As the inductance is not constant one should consider to take this interaction into account using inductances instead of induced voltage. Depending on the saturation level of the iron, the inductance variation is 0.07 μH or above 1.5 μH.
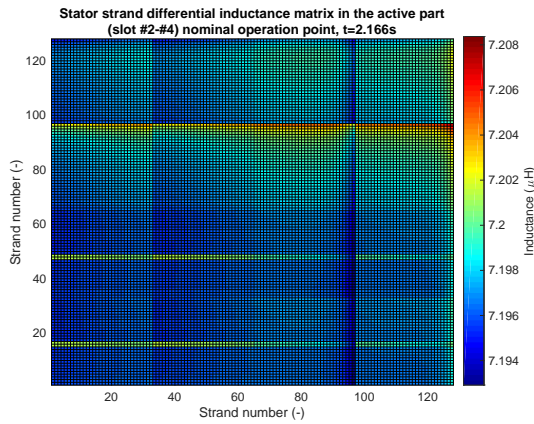
Figure 4.67 – Stator differential inductance matrix in the active part (slot #2-#4) nominal operation point, t=2.166s.
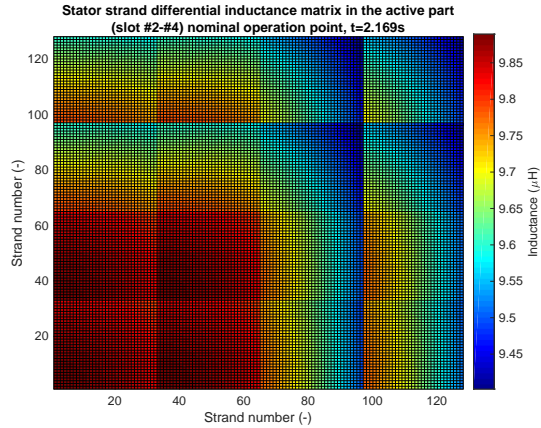
Figure 4.68 – Stator differential inductance matrix in the active part (slot #2-#4) nominal operation point, t=2.169s.

Figures 4.67 and 4.68 present the differential inductance matrix between the slot #4 and slot #2 for two distinct time-steps for the nominal operation point. The inductance has a similar behaviour as in figures 4.65 and 4.66 with the main difference that the amplitude of the inductance is smaller as well as the amplitude of the variation.
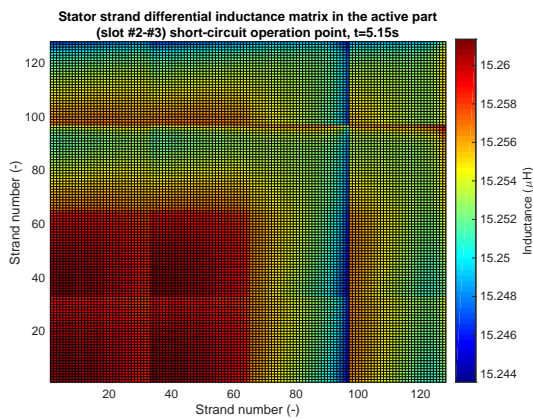
Figure 4.69 – Stator differential inductance matrix in the active part (slot #2-#3) nominal operation point, t=5.15s.
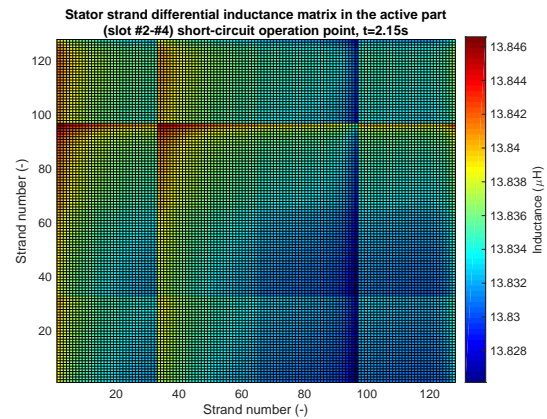
Figure 4.70 – Stator differential inductance matrix in the active part (slot #2-#4) nominal operation point, t=5.15s.

Figures 4.69 and 4.70 present the differential inductance matrix between the slot #3 and slot #2 as well as between slot #4 and slot #2 for one time-step for the short-circuit operation point. The amplitude variation between the slots is in the same range as for the nominal operation point, while the inductance is quasi constant, so that one could consider this interaction using induced voltage and not inductances.

To sum up, when the iron is not infinite permeable, then one should not only consider the differential inductance matrix in a slot but also between the slots. Depending on the operation point, the inductance can be constant or not. The decision of considering the neighbouring bars as well as the rotor bars using an inductance approach or an induced voltage approach must therefore be taken on a case-by-case base. In this work, the neighbouring bars will be not be considered as it extents over the frame of this study, but will be studied later on.

4.6.7 Comparison between the different strands in slot inductance models

Figures 4.71 and 4.72 present the differential inductance matrix for the Model 3.0. The form of the matrix is very similar to the matrix obtained in the short-circuit conditions and for the non-saturated time-step for the nominal operation point. Which is logic as the differential inductance Matrix obtained using Model 3.0 is neglecting also the saturation. The amplitude of the inductances is quite different. For the rotor differential inductance matrix, the inductances vary from 49 to 35.5 μH, while the inductances span from 24 to 3.5 μH for Model 3.0. For the stator a similar reduction of the span can be found. This reduction of the span will have an impact on the circulating currents, especially in the case of an incomplete transposition in the active part, which will be calculated in the following section for an untransposed active roebel bar in a slot.
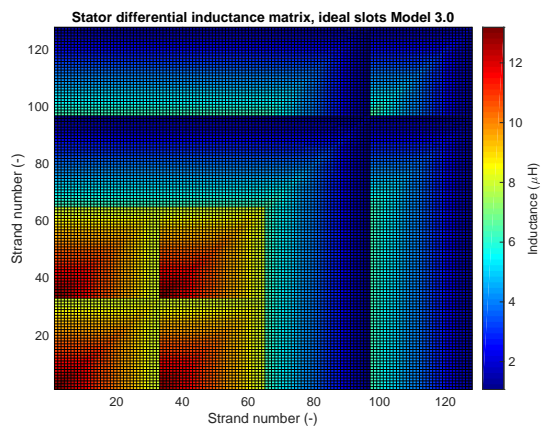
Figure 4.71 – Stator differential inductance matrix, ideal slot Model 3.0.
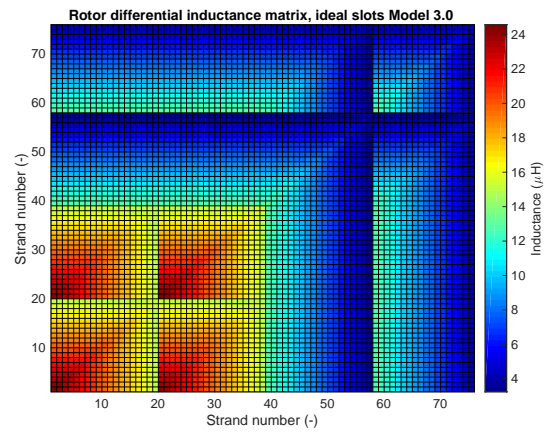
Figure 4.72 – Rotor differential inductance matrix, ideal slot Model 3.0.
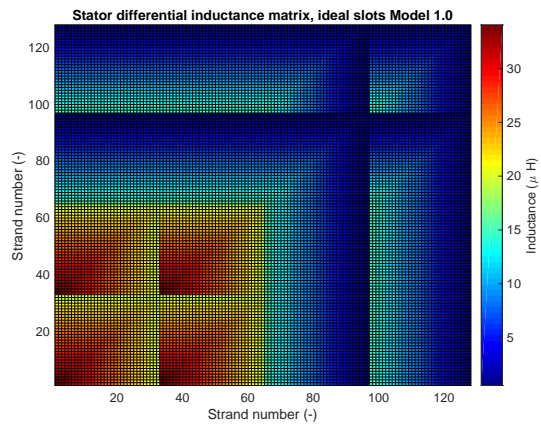
Figure 4.73 – Stator differential inductance matrix, ideal slot Model 1.0.
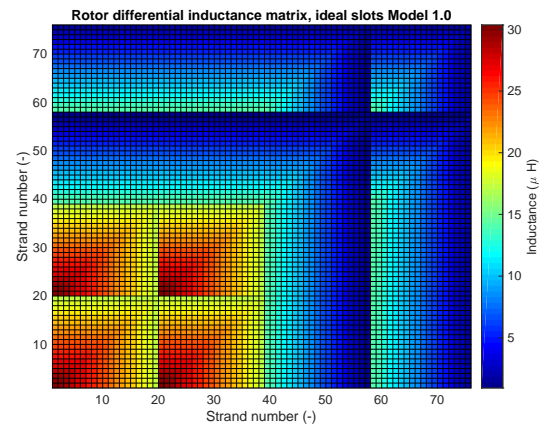
Figure 4.74 – Rotor differential inductance matrix, ideal slot Model 1.0.

Figures 4.73 and 4.74 present the differential inductance matrix for the Model 1.0. The amplitude of the inductances are in the same range as for Model 3.0, with some major differences. The first lies in the smaller inductance variation inside one bar. The second lies in the coupling between the top and bottom bar. According to the theory of model 1.0, the coupling is governed by the strand position, so that the coupling is governed by the mutual inductance of the bottom bar while it is the contrary in the case of Model 3.0.

4.6.8 Experimental validation of the differential inductance model - strands in slot

Figure 4.75 presents the dimensions and a schematic view of the experimental validation of the differential inductance model. The slot is 153.5mm deep and is composed of stacked and pressed electrical steel sheets, which have been laser cutted.
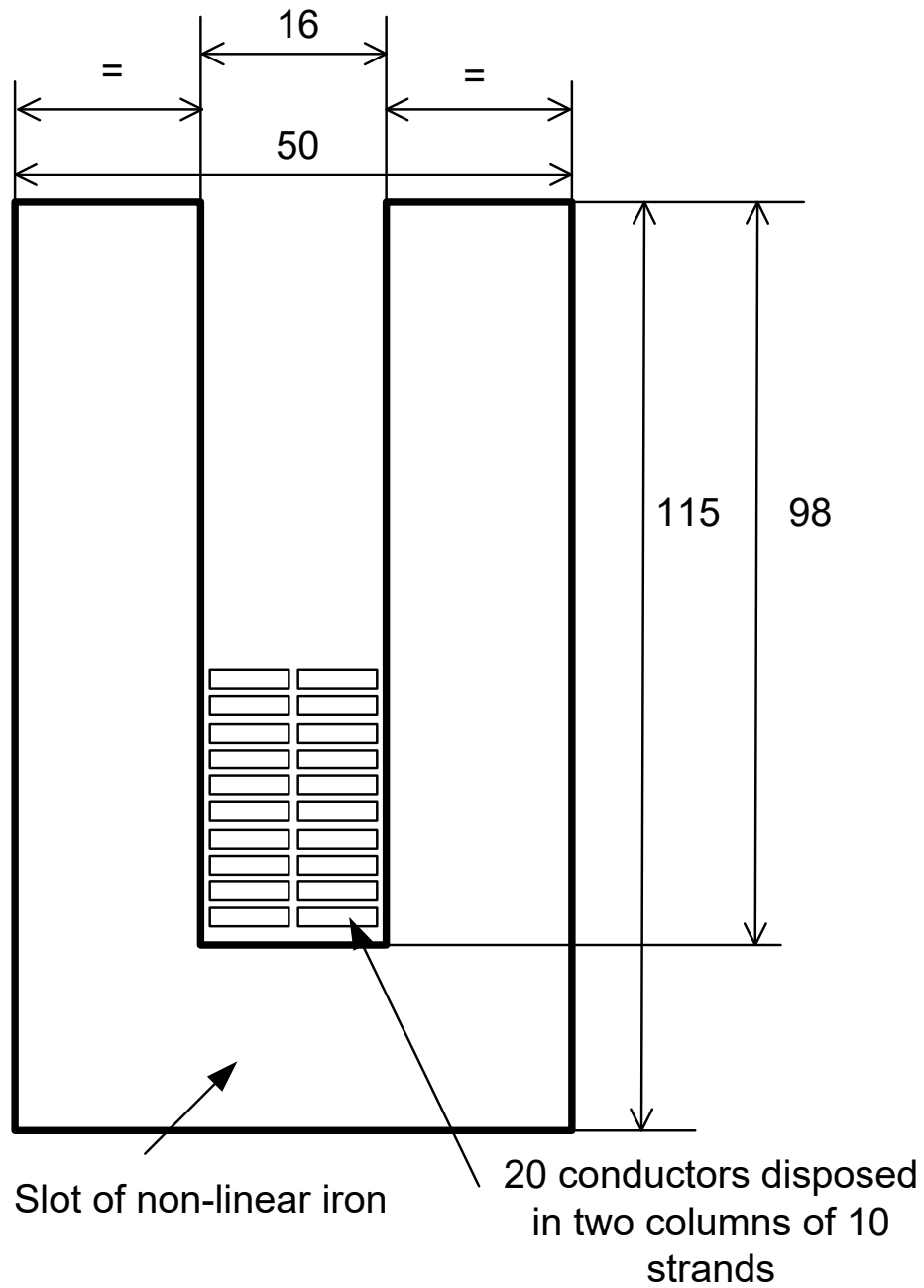
Figure 4.75 – Slot experiment - Schematic view and dimensions. The dimensions are given in mm. The strands are 7.4mm wide and 1.8mm in height with an edge radius of 0.5mm.
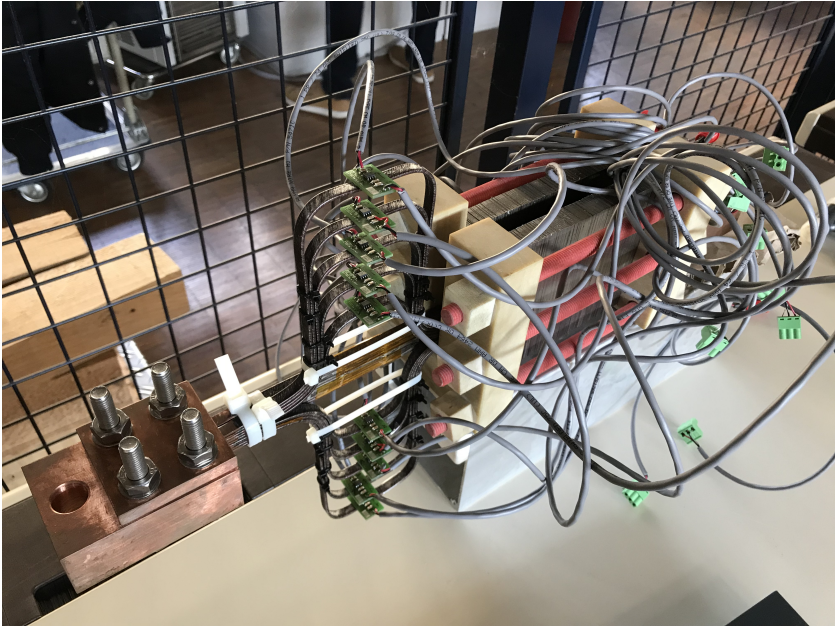
Figure 4.76 – Slot experiment - Picture of the experimental setup.
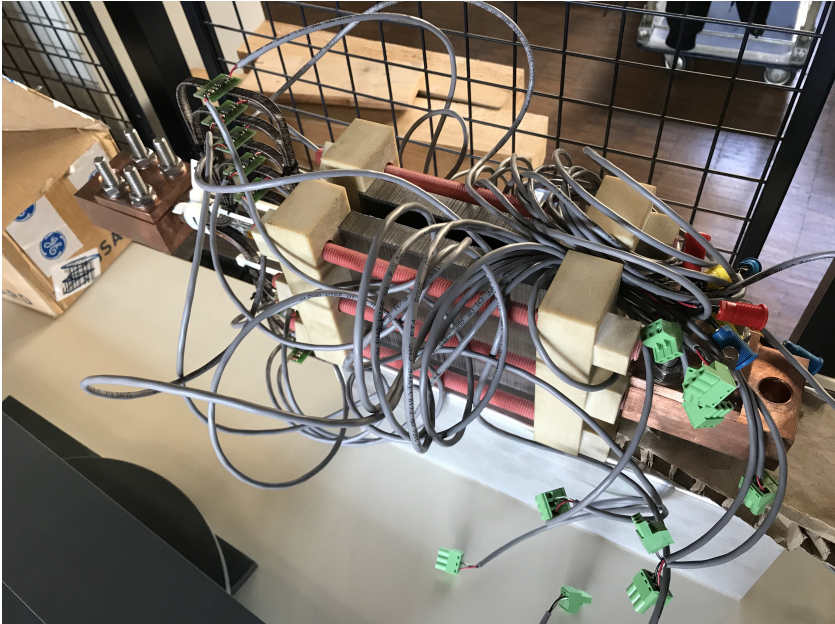
Figure 4.77 – Slot experiment - Picture of the experimental setup (2nd).

4.6. Taking into account the non infinite permeable iron: differential inductance model - Model 4.0

Pictures 4.76 and 4.77 show the experiment. The composite clamping system is yellow-white and tightened using red bolts and squared nuts. At both ends of the strands, there are two copper connection devices to ensure the proper experiment current feeding of around 300A. On the left side of picture 4.76, the conductors are widened to decrease the magnetic coupling at the hall sensors. One can also see the glued hall sensors and the strand fastening system, which function is to tighten the strands together to ensure a very precision calibration of the measurements.

Basically, the calibration process as well as the problems explained in section 5.12 are the same for this experiment. But there are some significant differences. Only one column has widened conductors which will have an important impact on the measured currents. It has been decided to widen only one column, because even with the thermal camera confirmation there is no absolute certainty that the current will be the same in the widened legs. A measurement with only one hall sensor would lead to a kind of average value of both currents, which is not wanted. In addition, there was not enough conductors to widen both columns and as the delivery time for these conductors is very long, it has been decided to widen only one. The best option would have been to widen both columns and use 20 hall sensors instead of only 10, but the measurement equipment of the laboratory can only handle only 16 hall sensors at the same time. A reduction of the number of strands is theoretically possible but will reduce drastically the amplitude of the effect to be measured, so that the reduction of the number of strands can't be considered.
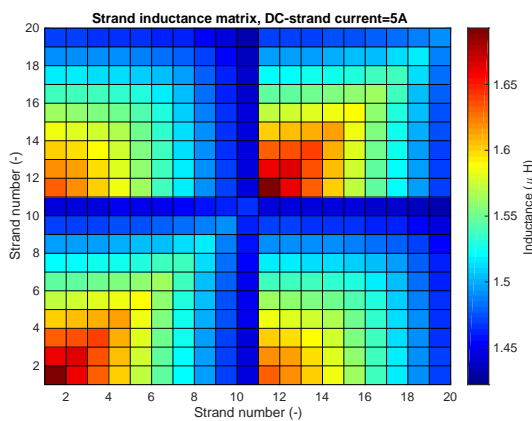
Figure 4.78 – Slot experiment - Differential inductance matrix.
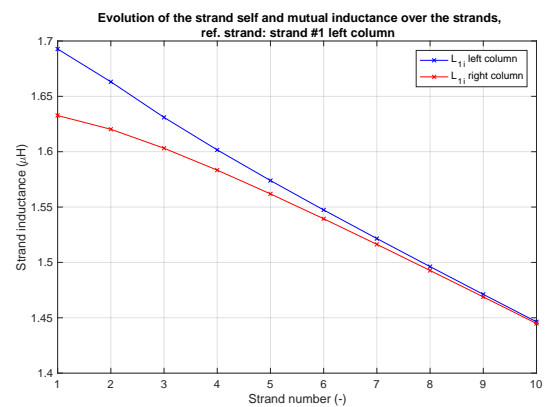
Figure 4.79 – Slot experiment - Evolution of the self- and mutual inductance as a function of the strand position.

Figures 4.78 and 4.79 present the differential inductance matrix of the experimental slot as well as the evolution of the inductance as a function of the strand position. As there is no main flux, which magnetises the slot, the slot behaves like in the short-circuit case presented in figure 4.56. The differential inductance matrix is as expected time independent.

The simulation model contains the slot modelled using the differential inductance matrix, the inductance of the strands outside the slot, the resistance calculated using the real copper

length and the skin effect resistance in the slot. The skin effect coefficient lies between 0.0159% and 4.4907% with a mean value of 1.6553%. The skin effect has a big impact on the resistance of the highest located strands. Even with all these additional effects taken into account, the calculated curves and the simulated ones don't match very well. Due to the problem of the calibration, it has been decided to present the curves not the leg current but the hall sensor voltage. Figures 4.80 and 4.81 presents the hall sensor voltage versus total current. For the sensors 1 to five, the match is not really bad, while the match is really bad for the sensors 6 to 10. The time series of figures 4.82 and 4.83 confirm that point of view.
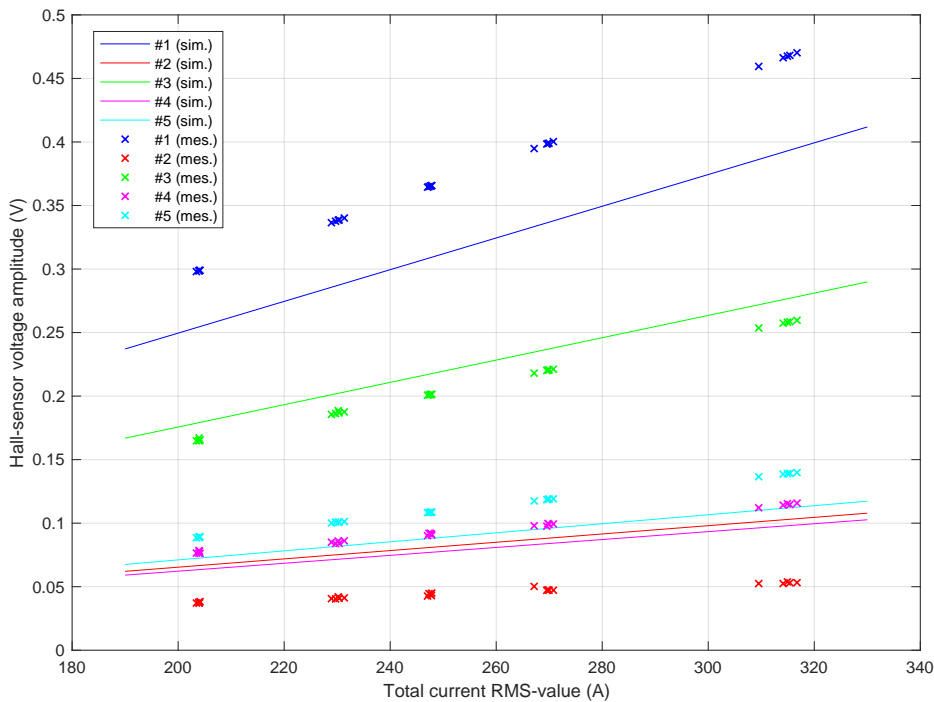
Figure 4.80 – Slot experiment - Branch voltage 1 to 5 vs Total current.

The slot differential inductance model can't be validated using that data. Another experiment should be designed to validate this model. The root causes of this discrepancy could not be found. The most probable root causes are the missing elbow in the air conductor model, errors in the hall sensors (it was not possible to make a cross-check due to the presence of the slot in the experimental setup), problems in the calibration (the calibration has been repeated another time without any changes in the results) and temperature respectively resistivity of the copper (the temperature of the experiment is difficult to obtain as some current in flowing the conductors and the resistivity of the copper is not known). Despite the practical issues caused by the widening of the strand column, it has been decided to make a comparison of Model 1.0, Model 3.0 and Model 4.0 versus the experimental data to see if another model could fit better to the experimental data.
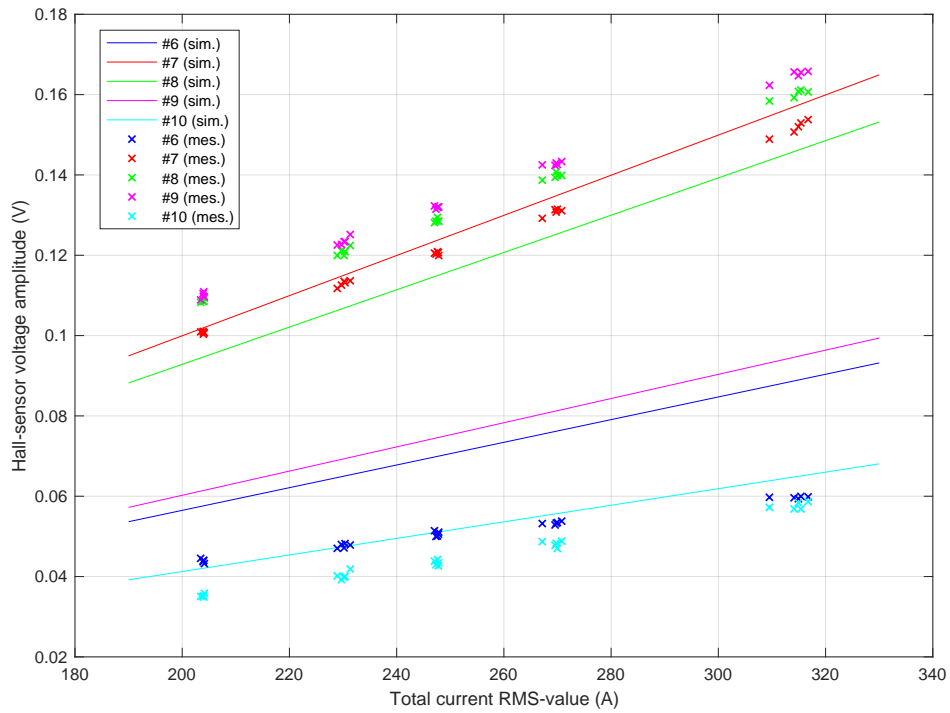
Figure 4.81 – Slot experiment - Branch voltage 6 to 10 vs Total current.
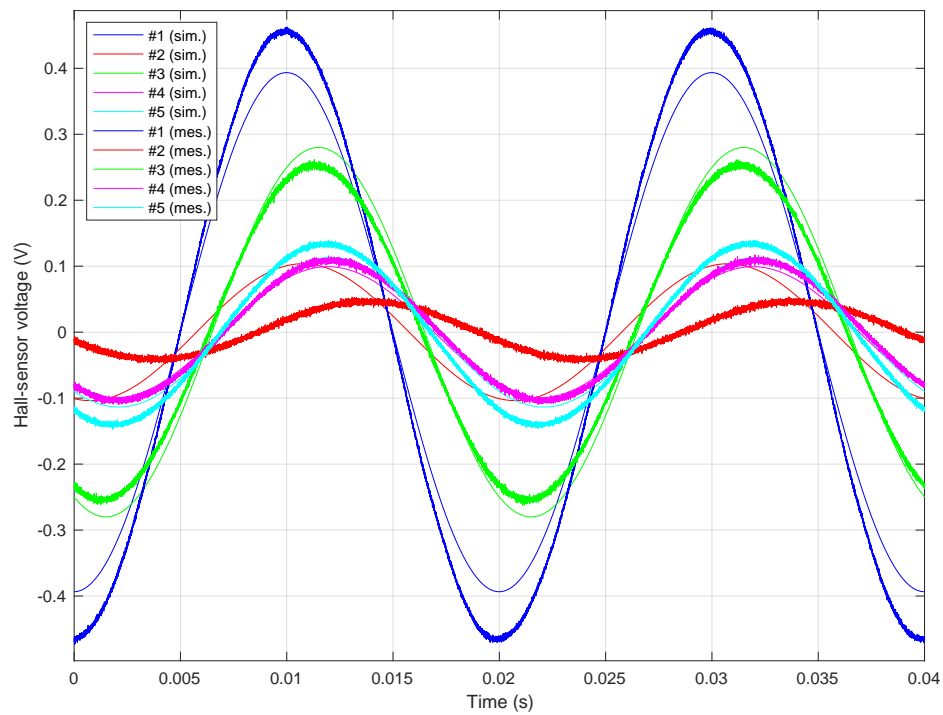
Figure 4.82 – Slot experiment - Time series of branch voltage 1 to 5.
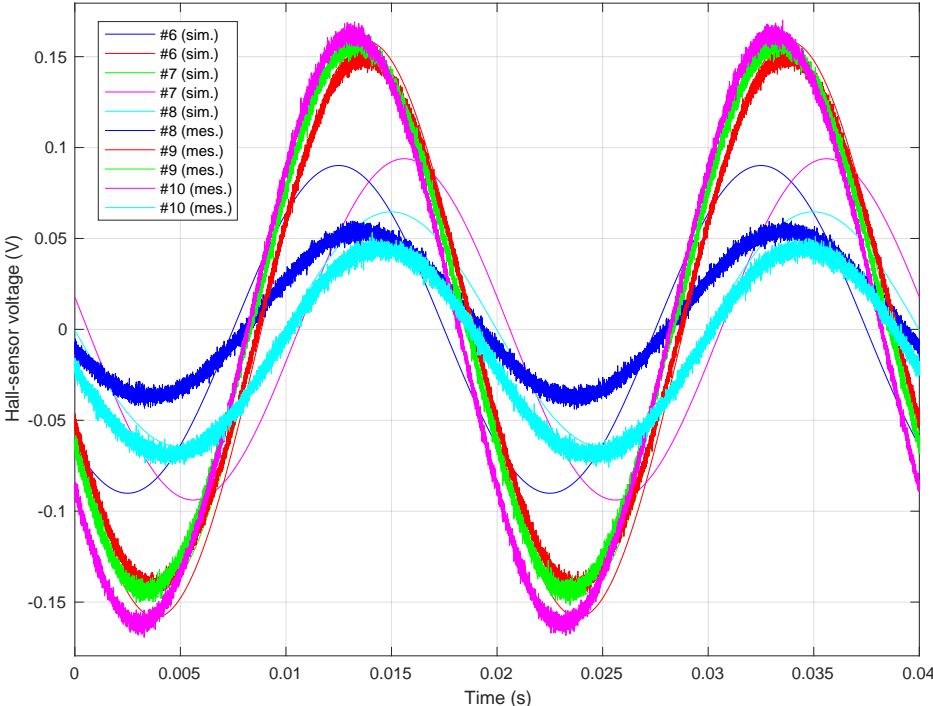
Figure 4.83 – Slot experiment - Time series of branch voltage 6 to 10.

4.7 Comparison between the slot inductance models

Finally, the slot models 1.0, 3.0 and 4.0 are compared to a time-stepping finite-element simulation using the model of the experimental slot. The comparison is not done against measurements as the matching between the measurement and the calculation is not good enough.

Table 4.2 – Comparison of the circulating currents calculated with different slot inductance models including a time-stepping finite-element simulation (FE).

Parameter	Model 1.0	Model 3.0	Model 4.0	Time-stepping FE
I_{1g} (A)[a]	3.088	3.5556	3.392	3.377
I_{1d} (A)	3.088	3.5556	3.392	3.376
I_{2g} (A)	3.173	3.5664	3.414	3.422
I_{2d} (A)	3.173	3.5664	3.414	3.421
I_{3g} (A)	3.347	3.6469	3.511	3.541
I_{3d} (A)	3.347	3.6469	3.511	3.541
I_{4g} (A)	3.707	3.9038	3.791	3.837
I_{4d} (A)	3.707	3.9038	3.791	3.837
I_{5g} (A)	4.362	4.4552	4.373	4.425
I_{5d} (A)	4.362	4.4552	4.373	4.425
I_{6g} (A)	5.306	5.3814	5.340	5.380
I_{6d} (A)	5.306	5.3814	5.340	5.380
I_{7g} (A)	6.638	6.7149	6.728	6.739
I_{7d} (A)	6.638	6.7149	6.728	6.739
I_{8g} (A)	8.381	8.4710	8.559	8.524
I_{8d} (A)	8.381	8.4710	8.559	8.524
I_{9g} (A)	10.585	10.6788	10.867	10.772
I_{9d} (A)	10.585	10.6788	10.867	10.772
I_{10g} (A)	13.334	13.3966	13.717	13.551
I_{10d} (A)	13.334	13.3966	13.717	13.552

[a]Ampere peak value.

The finite-element time-stepping simulation uses a first order time integration, while Model 4.0 and 3.0 uses a 4th order Runge-Kutta numerical integration scheme. Model 4.0 is very close to the finite-element time-stepping simulation. Model 1.0 has the biggest difference to Model 4.0. Model 3.0 has a bigger error than Model 4.0 but smaller than Model 1.0. All Models give results which are in the same "range", confirm the fact that small effects can make a big impact on the circulating current calculation, which is nothing else than a short-circuit calculation.

5 Magnetic field in the winding over-hang

The developed equations in this chapter can be used not only for the winding overhang of electrical machines but more generally to any 3-dimensional geometry as for example: MRI-scanners, supra-conductive coils, transformers, etc. Only the geometry of the coils, respectively magnetised bodies must be known and the current density. To do so, a HPC-compatible original C++ application have been developed. This application can be understood as a 3D magnetic field and vector potential calculation tool, where any shape of current carrying conductor can be modelled. The iron can also easily be modelled, as well as the boundaries (mirror method with or without air-gap conductor) and the rotation of part of the model along one axis. The currents are given with a separate file, while the requested calculations are given within an extra input file. When doing non-linear iterations, the magnetisation vector is stored, to ensure further post-processing possibilities. The results are written in vtk-file format to facilitate their visualisation. The file storage is done in a way that the calculation of the magnetic state is separated from the post-processing (calculation of the magnetic force, inductances, induced voltages and so one) as it happens quiet often that the need for post-processing changes during the analysis of the datas.

Even if in most of the applications, the magnetic field is the most important result, there is a big focus in this work to be able to calculate the vector potential, as this quantity enables to catch the induced flux and the inductances. Most importantly it enables to perform transient simulations and possibly to couple the magnetic field calculation in the overhang with a 2D finite-element calculation in the active part through the state-variable of the problem, as equation 5.1 shows

$$-\frac{1}{\mu}\nabla^2 \underline{A} + \sigma \frac{\partial \underline{A}}{\partial t} = \underline{j} + \frac{u_s}{R}. \tag{5.1}$$

In equation 5.1 μ stands for the local[1] permeability, $\underline{A}$ is the local vector potential, σ is the local conductivity, $\underline{j}$ is an applied constant current density, u_s an external voltage (for example

---

[1]The adjective local refers to the sub-space of $\mathbb{R}^3$ where equation 5.1 is applied.

the coupling induced voltage between the 3D-calculation and the 2D-calculation) and R the DC-resistance of the medium. The coupling of both calculation schemes (3D-integral field calculation and 2D-finite elements) needs some additional work, which exceeds the frame of this study, but one should keep in mind that both schemes has the same base, namely a known current density from which the magnetic field and vector potential are derived. This fact will be useful when the coupling of both schemes needs to be implemented in a computational program. Therefore, one can say that the vector potential is the key element of this problem and its calculation is of crucial importance.

This chapter presents the analytic equations used to calculate the magnetic field and the vector potential coming from the sources (modelled with a constant current density $\underline{j}$) and from the magnetised parts (modelled with a constant magnetisation $\underline{M}$). Some of the presented equations are novel equations derived in this work and some are taken as it from publications. The origin of the equation is always detailed before presenting its equation and there are summary tables. It starts with the integral equation for the source components in section 5.1 and goes on with the presentation of the analytical equation for the magnetised parts in section 5.2. Section 5.3 is dedicated to presentation of the publication-based iterative algorithm to take the non linear iron permeability characteristic into account. The reduction of the equation system to take the tangential symmetry of an electrical machine is then presented and is an original contribution of this work. The hypotheses of the 3-dimensional model as well as a novel way to characterise the active part boundary are presented and motivated in section 5.5, while a new iterative algorithm to compute the inductance and fluxes is detailed in section 5.7. When working with integrals one must be aware of the singularities that can appear. These singularities can be easily handled with original developments, as shown in section 5.8. Section 5.9 shows the validation of the analytical equation using comparing it with 3D-finite-elements and results from the literature. Finally, section 5.11 gives an outlook of some numerical results obtained with the 3-dimensional model of the overhang applied to the DFIG.

5.1 Analytical equations for the current conducting pieces in free space

The analytical equations used in this work are based on the following papers [133], [135], [134] and [136]. The equations are mainly used "as is", but some adjustments needed to be done, mainly due to typographic errors in the papers. All calculations are performed assuming a constant given current density $\underline{j}$ in the conductor considered. [8] presents analytical formulas in the case of an axial current density. Table 5.1 divides each equation into original contributions (C) and equations taken "as is" from publications (P). The original contributions will therefore not be mentioned explicitly in the text afterwards. The original contributions can extend from a simpler analytical equation for a given equation up to a complete new development of an analytical equation. This difference will also not be highlighted explicitly in the text.

As one can read in [36] the presented equations full-fill the Laplace equation for the current

Table 5.1 – Division of the equations into original contributions (C) and equations taken "as it" from publications (P) for the current carrying conductor.

Equation	Filament approximation	Rectangular approximation
A_r	C	C
A_ϕ	P, C^a	C
H_r	P, C^a	C
H_ϕ	C	C
H_z	P, C^a	C
A_z	P	P
H_x	P	P
H_y	P	P

^{a}For the calculation in the case $r = 0$.

density $\underline{j}$.

5.1.1 Filament approximation

Figure 5.1 shows a schematic view of the filament where the most important variables are defined. The equations can be used "as is" from [133], and will not be reproduced here. For two equations, namely for A_r and H_ϕ a simplification to the integral was found, without using elliptical integrals. The simple equations very helpful, as they don't require the additional calculation of sn, cn, dn, so that the numerical evaluation of the formulas is faster. Let's first recall the notation used by Urankar in his papers. The following variables, originating from [133], need to be recalled

$$\phi_i = \rho'_i - \rho \tag{5.2}$$

$$\gamma = z' - z \tag{5.3}$$

$$D^2(\phi) = \gamma^2 + r'^2 + r^2 - 2 \cdot r \cdot r' \cdot \cos(\phi) \tag{5.4}$$

with $i = 1, 2$. The radial component of the vector potential is therefore given by

$$A_r = -\int_{\rho_1}^{\rho_2} d\phi \quad r' \cdot \sin(\phi) \cdot D(\phi) = -\int_{\rho_1}^{\rho_2} d\phi \frac{r' \cdot \sin(\phi)}{|\underline{r} - \underline{r}'|}. \tag{5.5}$$

Using the variable substitution $u = -2 \cdot r \cdot r' \cdot \cos(\phi)$ leads to the following equations without elliptical integrals

$$A_r = \frac{1}{r} \sqrt{\gamma^2 + r^2 + r'^2 - 2 \cdot r \cdot r' \cdot \cos(\phi)} \Big|_{\phi=\phi'_2}^{\phi=\phi'_1}. \tag{5.6}$$
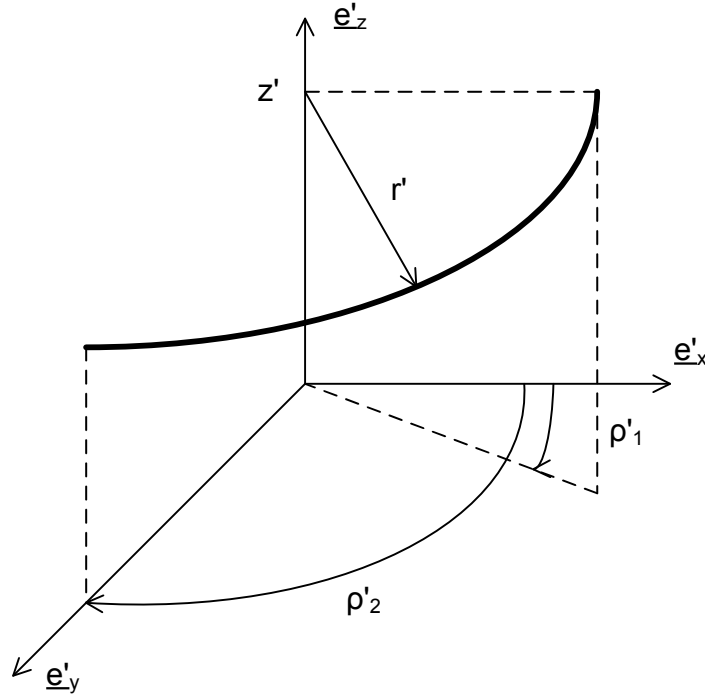
Figure 5.1 – Schematic representation of the filament.

Using the same substitution, H_ϕ becomes

$$H_\phi = \frac{\gamma}{r} \frac{1}{\sqrt{\gamma^2 + r^2 + r'^2 - 2 \cdot r \cdot r' \cdot \cos(\phi)}} \Bigg|_{\phi=\phi'_2}^{\phi=\phi'_1}. \tag{5.7}$$

The equation become singular when $r = 0$ or when $\underline{r} - \underline{r}' = 0$, but this is wanted, showing that the filament approximation is not physical. When $r = 0$, the equation is very simple, so that its integration is straightforward. Only the final results are therefore showed in the following equations

$$A_r = \frac{r'}{\sqrt{\gamma^2 + r'^2}} \cos(\phi) \Bigg|_{\phi=\phi'_1}^{\phi=\phi'_2} \tag{5.8}$$

$$A_\phi = \frac{r'}{\sqrt{\gamma^2 + r'^2}} \sin(\phi) \Bigg|_{\phi=\phi'_1}^{\phi=\phi'_2} \tag{5.9}$$

$$H_r = \frac{-r'\gamma}{(\gamma^2 + r'^2)^{3/2}} \sin(\phi) \Bigg|_{\phi=\phi'_1}^{\phi=\phi'_2} \tag{5.10}$$

$$H_\phi = \frac{r'\gamma}{(\gamma^2 + r'^2)^{3/2}} \cos(\phi) \Bigg|_{\phi=\phi'_1}^{\phi=\phi'_2} \tag{5.11}$$

$$H_z = \frac{r'\gamma}{(\gamma^2 + r'^2)^{3/2}} (r' \cdot \phi - r \sin(\phi)) \Bigg|_{\phi=\phi'_1}^{\phi=\phi'_2}. \tag{5.12}$$

In the case of a straight filament, the equation for A_z needs some adjustment for points laying on the filament axis, but not in the filament (in other words, for points with a z-coordinate not inside the filament), which have not been calculated in [133]. The equation to be integrated is then given by

$$A_z = \int_{z_1'}^{z_2'} dz' \frac{1}{\sqrt{(z-z')^2}} = \frac{(z'-z)}{\sqrt{(z'-z)^2}} \log z - z' \bigg|_{z=z_1'}^{z=z_2'}. \tag{5.13}$$

5.1.2 Rectangular cross-section
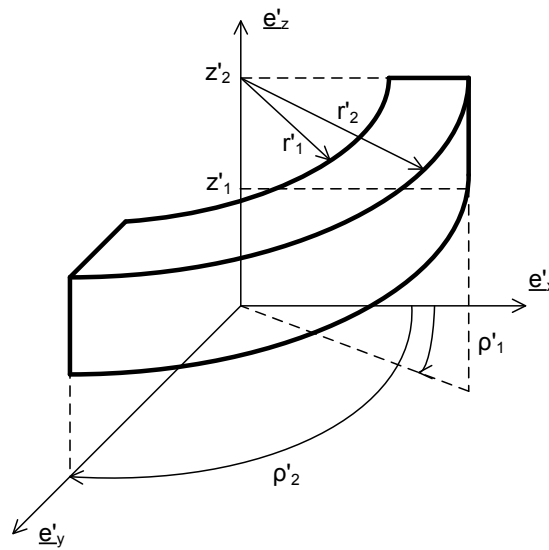
Figure 5.2 – Schematic representation of the rectangular cross-section.

Figure 5.2 presents the main variable used in the rectangular cross-section approximation. The equations presented in [134] have some typographic errors so that, it was necessary to correct them. Danilov did some earlier researches on this topic ([143] and [35]), with the solenoid covering an angle of 2π and [134] published the equation in the case of an angle different from 2π. Let's first recall some variables used in [134]

$$B^2(\phi) = r^2 + r'^2 - 2 \cdot r \cdot r' \cdot \cos(\phi) \tag{5.14}$$

$$D^2(\phi) = \gamma^2 + B^2(\phi) \tag{5.15}$$

$$G^2(\phi) = \gamma^2 + r^2 \sin(\phi) \tag{5.16}$$

$$\beta_1(\phi) = (r' - r\cos(\phi))/G(\phi) \tag{5.17}$$

$$\beta_2(\phi) = \gamma/B(\phi) \tag{5.18}$$

$$\beta_3(\phi) = \gamma(r' - r\cos(\phi))/[r\sin(\phi)D(\phi)]. \tag{5.19}$$

To transform the integral to integrals of Jacobi elliptic functions the same angle transformation

as in [134] is used

$$\phi = \pi - 2\alpha. \tag{5.20}$$

The following constants can be defined

$$k^2 = \frac{4rr'}{\gamma^2 + (r+r')^2} \tag{5.21}$$

$$a^2 = \gamma^2 + (r+r')^2 \tag{5.22}$$

$$n^2 = \frac{4rr'}{(r+r')^2}. \tag{5.23}$$

Using these constants and the angle transformation leads to the following equations

$$B^2(\alpha) = r^2 + r'^2 - 2 \cdot r \cdot r' \cdot \cos(\phi) = (r+r')^2(1 - n^2\sin(\alpha)^2) \tag{5.24}$$

$$D^2(\alpha) = \gamma^2 + B^2(\phi) = a^2(1 - k^2\sin(\alpha)^2). \tag{5.25}$$

while for $G(\phi)$, the equation will be the following

$$G^{-2}(\alpha) = \frac{1}{2\sqrt{\gamma^2 + r^2}} \left(\frac{1}{(\sqrt{\gamma^2 + r^2} - r)(1 - n_1^2\sin(\alpha)^2)} + \frac{1}{(\sqrt{\gamma^2 + r^2} + r)(1 - n_2^2\sin(\alpha)^2)} \right) \tag{5.26}$$

with

$$n_1^2 = \frac{2r}{r - \sqrt{\gamma^2 + r^2}} \tag{5.27}$$

$$n_2^2 = \frac{2r}{r + \sqrt{\gamma^2 + r^2}}. \tag{5.28}$$

The novel equation for the radial component of the vector potential can be easily obtained using direct integration, first over ϕ and then over r' and z'. The change of the sequence of the integration permit to get rid of the elliptic integrals presented in [134], which reduces drastically the computational time. Starting from the general equation for the radial component of the vector potential one obtains finally

$$\begin{aligned} A_r &= \frac{j}{4\pi} \int_\phi \int_{r'z'} \frac{-\sin(\phi)}{D(\phi)} d\phi dr' dz' \\ &= \frac{j}{\pi} \Big(\frac{a}{4r} \big(\gamma D(\phi) + B^2(\phi) \operatorname{arcsinh}(\beta_2(\phi)) \big) + \frac{1}{12r} \big(a\gamma D(\phi) - a(a^2 - 3b^2) \operatorname{arcsinh}(\beta_2(\phi)) \\ &\quad - 4b^3 \arctan(\beta_3(\phi)) + (2\gamma^3 + 6b^2\gamma) \operatorname{arcsinh}(\frac{a}{\sqrt{(b^2 + \gamma^2)}}) \big) \Big) \end{aligned} \tag{5.29}$$

where $a = r' - r\cos(\phi)$ and $b = r\sin(\phi)$.

The following equation for A_ϕ presented in [134] must be integrated

$$A_\phi = \frac{1}{2} \int_{\rho_1}^{\rho_2} d\phi \quad \left(\gamma D(\phi) + 2\gamma r \cos(\phi) \operatorname{arcsinh} \beta_1(\phi) \right.$$
$$\left. + \left(r'^2 - r^2 \cos(2\phi) \right) \operatorname{arcsinh} \beta_2(\phi) - r^2 \sin(2\phi) \arctan \beta_3(\phi) \right) \cos(\phi). \tag{5.30}$$

The original development of the novel equation can be found in A.5.1

For the H-field, the following equations presented in [134] have to be integrated

$$H_r = \int_{\rho_1}^{\rho_2} d\phi \quad [\cos(\phi) D(\phi) + r \cos(\phi)^2 \operatorname{arcsinh} \beta_1(\phi)] \tag{5.31}$$

$$H_\phi = \int_{\rho_1}^{\rho_2} d\phi \int_{r'_1}^{r'_2} dr' \int_{z'_1}^{z'_2} dz' \quad \frac{-\gamma r' \sin(\phi)}{D(\phi)^3} \tag{5.32}$$

$$H_z = \int_{\rho_1}^{\rho_2} d\phi \quad [\gamma \operatorname{arcsinh} \beta_1(\phi) - r \cos(\phi) \operatorname{arcsinh} \beta_2(\phi) - r \sin(\phi) \arctan \beta_3(\phi)]. \tag{5.33}$$

The original development of the novel equations of H_r, H_ϕ and H_z can be found in A.5.2

5.2 Analytical equations for the magnetic bodies

In a magnetic material ($\underline{M} \neq 0$) the following relations must be fulfilled:

$$\underline{\nabla} \cdot \underline{B} = 0 = \underline{\nabla} \cdot (\mu_0 * \underline{H} + \underline{M}) = \mu_0 \underline{\nabla} \cdot \underline{H} + \underline{\nabla} \cdot \underline{M}. \tag{5.34}$$

$$\underline{\nabla} \cdot \underline{H} = -\frac{1}{\mu_0} \underline{\nabla} \cdot \underline{M}. \tag{5.35}$$

The magnetisation vector ($\underline{M}$) acts like a charge source showing the symmetry between the magnetic and electric field. Where as in this case the magnetic field is solenoid. There exist therefore two main models to calculate the magnetic field produced by a magnetisation: the coulombian model and the amperian model. Both give theoretically the same magnetic field. In [118], the authors give an detailed explanation about both models: their advantages and drawbacks, which are recalled and summarised hereafter.

5.2.1 Coulombian model

In the coulombian model, the magnetisation vector, also called "polarisation vector" or "magnetic polarisation" by some authors is driven by fictive magnetic charges placed at the outer surfaces of the magnetised body or inside the volume depending on the orientation of the magnetisation vector and / or magnetisation approach chosen. The fictitious magnetic

charge density is defined by

$$\sigma_m = -\underline{\nabla}' \cdot \underline{M} = \sigma_{mv} \tag{5.36}$$

which coincides with the volume charge density (σ_{mv}). The surface charge density (σ_{ms}) is given by

$$\sigma_{ms} = \underline{M} \cdot \underline{n} \tag{5.37}$$

where $\underline{n}$ is the unit vector normal to the surface of the magnetised body. In this electrostatic-like model the magnetic field is deduced from the gradient of the potential function (ϕ) as the magnetic field is curl-free as per equation 5.35. The potential function is then given by

$$\phi = -\frac{1}{4\pi\mu_0} \iiint_V \frac{\underline{\nabla}' \cdot \underline{M}(\underline{r}')}{|\underline{r} - \underline{r}'|} dV' + \frac{1}{4\pi\mu_0} \iint_{\partial V'} \frac{\underline{M} \cdot d\underline{\sigma}'}{|\underline{r} - \underline{r}'|}. \tag{5.38}$$

The magnetic field becomes

$$\underline{H} = -\underline{\nabla}\phi \tag{5.39}$$

$$\underline{H} = \frac{1}{4\pi\mu_0} \underline{\nabla} \iiint_V \frac{\underline{\nabla}' \cdot \underline{M}(\underline{r}')}{|\underline{r} - \underline{r}'|} dV' - \frac{1}{4\pi\mu_0} \underline{\nabla} \iint_{\partial V'} \frac{\underline{M} \cdot d\underline{\sigma}'}{|\underline{r} - \underline{r}'|}. \tag{5.40}$$

The main drawback of this formulation lies in the necessity to have analytical equation for the calculation of the gradient. It may be appropriate to calculate the gradient of the potential function before ending the integration to obtain this function.

5.2.2 Amperian model

The magnetisation vector is expressed using fictive currents. There exist surface currents densities ($\underline{k}_s$) defined as

$$\underline{k}_s = \underline{M} \tag{5.41}$$

and volume current densities ($\underline{k}_v$) given by

$$\underline{k}_v = \underline{\nabla}' \wedge \underline{M} \tag{5.42}$$

Knowing the surface and volume current densities the vector potential (refer to equation 5.45) and afterwards the magnetic field can be obtained using the fact that $\underline{H} = \underline{\nabla} \wedge \underline{A}$. There exist also another formulation putting the "curl"-operator into the integrals. In this formulation, the magnetic field is given by

$$\underline{H} = \frac{1}{4\pi\mu_0} \iiint_V \frac{(\underline{\nabla}' \wedge \underline{M}(\underline{r}')) \wedge (\underline{r} - \underline{r}')}{|\underline{r} - \underline{r}'|^3} dV' + \frac{1}{4\pi\mu_0} \iint_{\partial V'} \frac{(\underline{M}(\underline{r}') \wedge \underline{n}) \wedge (\underline{r} - \underline{r}')}{|\underline{r} - \underline{r}'|^3} \tag{5.43}$$

where $\underline{n}$ is the normal unit vector pointing out of the surface $\partial V'$.

5.2.3 Vector potential

The vector potential is given by

$$\underline{A} = \frac{1}{4\pi} \iiint_V \frac{\underline{M}(\underline{r}') \wedge (\underline{r} - \underline{r}')}{|\underline{r} - \underline{r}'|^3} dV' \tag{5.44}$$

This formula is not very practicable, but can be simplified using a "curl" version of the integration by parts

$$\underline{A} = \frac{1}{4\pi} \iiint_V \frac{\nabla' \wedge \underline{M}(\underline{r}')}{|\underline{r} - \underline{r}'|} dV' + \frac{1}{4\pi} \iint_{\partial V'} \frac{\underline{M} \wedge d\underline{\sigma}'}{|\underline{r} - \underline{r}'|}. \tag{5.45}$$

This "curl"-version of the integration by parts is nothing else than the vector potential equation in the amperian model. Even if there is an integral more to be computed, the final result will be more simple.

5.2.4 Summary

The amperian as well as the coulombian model should theoretically produce exactly the same results. Depending on the magnetisation approach chosen and / or orientation of the magnetisation vector one model can give simpler integrals to be evaluated. It is possible that one model can be integrated analytically while the other can't be integrated. It is a choice that must be done on a case-by-case basis to obtain the most simple analytical formulas.

In cartesian coordinates, there are no significant differences between the different equations to obtain the H-field and A-field. In cylindrical coordinates or in other curvilinear coordinate system, the choice of the wise formulation will lead to analytical equations or not. As one can see in the following sections, the analytical equations leads normally to elliptical integrals in cylindrical coordinates.

More than 50 publications were found dealing with the magnetic field calculation produced by a given magnetisation vector for cartesian coordinates and cylindrical coordinates. This work places itself in a summary mode compiling the equations for cartesian and cylindrical coordination and comparing them with finite element calculation as no summary publication was found during the literature survey. The equations copied from the literature are duly referenced. There exist certainly more than one reference for each equation but it was decided to cite only one reference per equation. Sometimes the equations have been re-derived and transformed, mainly to reduce the computational effort, to obtain a more simple equation. Finally, the equations for the vector potential are derived in nearby all cases for the cartesian and cylindrical coordinates. For this calculation the literature is more sparse, attributable to a lack of application of the vector potential produced by the magnetisation, so that more

original contributions have been produced.

[113] uses a coulombian approach to develop semi-analytical formulas for the magnetic field produced by a radial polarisation. [115], [61], [122], [117], [119], [121], [116] give analytical equations for the magnetic created by cylindrical polarisation using a coulombian model as well as amperian model. [123] discusses some possible simplifications of the analytical formulas used for the magnetic field calculation - namely a 2-dimensional approximation. [11] calculates the magnetic field using Heuman's Lambda function instead of elliptical integrals in addition the authors also propose a singularity treatment. [120] presents a short synthesis including various analytical formulas to calculate the magnetic field. [79] obtains the magnetic field using separation of variable in polar coordinates applied on magnetic gears. [126] and [125] introduce a magnetic field calculation employing toroidal harmonics while [142] uses a symmetrical second rank tensor to obtain the same quantity. [75] proposes some improvements in the magnetic field calculation in the case of arbitrary geometry coil with rectangular cross section. In [137] and [138], the author presents compact analytical formulas for a basic conic sub-domain. In [140], the author proposes another interesting calculation formula for the magnetic field, which is given by

$$
\begin{aligned}
\underline{H} &= -\frac{1}{4\pi\mu_0}\nabla\iiint_V \frac{\underline{M}(\underline{r}')\cdot(\underline{r}-\underline{r}')}{|\underline{r}-\underline{r}'|}dV' \\
&= -\frac{1}{4\pi\mu_0}\nabla\iint_{\partial V'} \frac{d\underline{\sigma}'}{|\underline{r}-\underline{r}'|}\cdot(\underline{M}(\underline{r}')+(\underline{r}-\underline{r}')M_1)
\end{aligned}
\tag{5.46}
$$

where M_1 is half of the divergence using the linear approach. To pass from the volume to the surface integral, the divergence theorem is used. The gradient operator in front of the integrals acts on the variables x, y and z, while the integration is over the variables x', y' and z'. One can permute the two operators without changing the final result. This result is useful when considering magnetisation approach of high order in cartesian coordinates.

Table 5.2 shows a division of the equation into original contributions and taken "as it" form publication. This helps to distinguish the original contributions form the equation taken from the literature in the following summary of equations.

Table 5.2 – Division of the equations (Eq.) into original contributions (C) and equations taken "as is" from publications (P) for the magnetised body in cartesian coordinates (cart. coord.) and cylindrical coordinates (cyl. coord.). NA stands for Not Applicable.

Eq.	Cart. coord.	Cyl. coord. (M_r)	Cyl. coord. (M_θ)	Cyl. coord. (M_z)
A_r	NA	C	C	C
A_ϕ	NA	C	C	C
A_z	NA	C	C	C
H_r	NA	P,C	P	C
H_ϕ	NA	C	P	P
H_z	NA	P	P	C
A_x	P,C[a]	NA	NA	NA
A_y	P,C[a]	NA	NA	NA
A_z	P,C[a]	NA	NA	NA
H_x	P,C[a]	NA	NA	NA
H_y	P,C[a]	NA	NA	NA
H_z	P,C[a]	NA	NA	NA

[a]The development of the equations starting with the approach of equation 5.47 are original contributions, while the equation for a constant magnetisation can be taken from the literature.

5.2.5 Magnetisation approach - cartesian coordinates
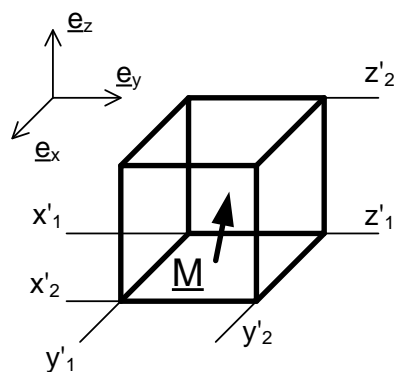
Figure 5.3 – Schematic representation of the magnetised body in cartesian coordinates.

Figure 5.3 presents a schematic representation of the magnetised body in cartesian coordinated as well as the definition and denomination of the variables. As the magnetisation vector field (also called M-field) is not computable explicitly, an approach must be made to express it. The magnetisable domain is be therefore divided in small volumes (cubic, quadratic, etc...) as in the finite element approximation. The most simple one is the linear approach also denoted approach of first order or Urankar-approach ([140]) and is given by

$$\underline{M} = \underline{M}_0 + \underline{M}_1 x' + \underline{M}_2 y' + \underline{M}_3 z'. \tag{5.47}$$

The main advantage of this approach is its constant divergence given by

$$\underline{\nabla}' \cdot \underline{M} = M_{1x'} + M_{2y'} + M_{3z'} = 2M_1. \tag{5.48}$$

The complete first order - finite element equivalent approach would be

$$\underline{M} = \underline{M}_0 + \underline{M}_1 x' + \underline{M}_2 y' + \underline{M}_3 z' + \underline{M}_4 x' y' + \underline{M}_5 x' z' + \underline{M}_6 y' z' + \underline{M}_7 x' y' z'. \tag{5.49}$$

This approach is not very practicable as it contains a third order term $(x' y' z')$. For the case of the constant magnetisation, the equation for the magnetic field are given by [119]. For the development of the novel equations, it have been decided to use the approach defined by equation 5.47 applied in equation 5.46 considering a surface element on the x-axis, where $\underline{d\sigma}'$ gets then $\underline{d\sigma}' = dy' dz' \underline{e}_{x'}$ and where x' has a given value x'_i becomes then the following integral (the 4π-term is omitted as the goal is too seek for family of integrals)

$$I = \underline{\nabla} \iint_{\partial V'} \frac{dy' dz'}{|\underline{r} - \underline{r}'|} [M_{0x'} + M_{1x'} x' + M_{2x'} y' + M_{3x'} z' + (x - x') M_1]$$

$$= \alpha \underline{\nabla} \iint_{\partial V'} \frac{dy' dz'}{|\underline{r} - \underline{r}'|} + \beta \underline{\nabla} \iint_{\partial V'} \frac{y'}{|\underline{r} - \underline{r}'|} dy' dz' + \gamma \underline{\nabla} \iint_{\partial V'} \frac{z'}{|\underline{r} - \underline{r}'|} dy' dz' \tag{5.50}$$

with

$$\alpha = M_{0x'} + M_{1x'} x' + (x - x') M_1 \tag{5.51}$$

$$\beta = M_{2x'} \tag{5.52}$$

$$\gamma = M_{3x'}. \tag{5.53}$$

[140] presents also a magnetic field calculation based on the magnetisation approximation of equation 5.47 but its equation contains some typographic errors that have been corrected in

this work, which makes them original contributions. The first integral gets

$$
\begin{aligned}
I_{s_1} =& \underline{\nabla} \iint_{\partial V'} \frac{dy'\,dz'}{|\underline{r} - \underline{r}'|}\Big|_{x'=x_1', x_2'} \\
=& -\underline{\nabla} \int_{z_1'}^{z_2'} dz'\, \mathrm{arcsinh}\Big(\frac{y-y'}{\sqrt{(x-x')^2 + (z-z')^2}}\Big)\Big|_{x'=x_1', x_2'}\Big|_{y'=y_1'}^{y'=y_2'} \\
=& \underline{\nabla} \int_{z_1'}^{z_2'} dz'\, \mathrm{arcsinh}\Big(\frac{y-y'}{\sqrt{(x-x')^2 + (z-z')^2}}\Big)\Big|_{x'=x_1', x_2'}\Big|_{y'=y_2'}^{y'=y_1'} \\
=& \underline{\nabla}\Big[(y-y')\,\mathrm{arcsinh}(\frac{z-z'}{\sqrt{(x-x')^2 + (y-y')^2}}) \\
& - (x-x')\arctan(\frac{(y-y')(z-z')}{(x-x')\sqrt{(x-x')^2 + (y-y')^2 + (z-z')^2}}) \\
& + (z-z')\,\mathrm{arcsinh}(\frac{y-y'}{\sqrt{(x-x')^2 + (z-z')^2}})\Big|_{x'=x_1', x_2'}\Big|_{y'=y_2'}^{y'=y_1'}\Big|_{z'=z_2'}^{z'=z_1'}\Big]
\end{aligned}
\tag{5.54}
$$

where it was supposed that the integration bounds are x_1' and x_2' for x' and so one for the two other variables. The arcsinh-function is used instead of the log-function, but both functions give the same result.

The second integral turns into (please note that for symmetry reasons the second and the third integrals are the same)

$$
\begin{aligned}
I_{s_2} =& \underline{\nabla} \iint_{\partial V'} \frac{y'}{|\underline{r} - \underline{r}'|}dy'\,dz' \\
=& \underline{\nabla} \int_{z_1'}^{z_2'} dz' - y\,\mathrm{arcsinh}\Big(\frac{y-y'}{\sqrt{(x-x')^2 + (z-z')^2}}\Big) \\
& + \sqrt{(x-x')^2 + (y-y')^2 + (z-z')^2}\Big|_{y'=y_1'}^{y'=y_2'}
\end{aligned}
\tag{5.55}
$$

As the first two integrals are known, only the last two integrals must be calculated (where the subscript 1,2 is replaced by i and the minus sign is implicit)

$$
\begin{aligned}
I_{s_{2a}} =& \underline{\nabla} \int_{z_1'}^{z_2'} dz'\sqrt{(x-x')^2 + (y-y_i')^2 + (z-z')^2} \\
=& -\underline{\nabla}\frac{1}{2}((z-z')\sqrt{(x-x')^2 + (y-y_i')^2 + (z-z')^2} \\
& + ((x-x')^2 + (y-y_i')^2)\,\mathrm{arcsinh}(\frac{z-z'}{\sqrt{(x-x')^2 + (y-y_i')^2}}))\Big|_{z'=z_1'}^{z'=z_2'}.
\end{aligned}
\tag{5.56}
$$

Taking the gradient is straightforward.

The novel equation for the vector potential is calculated in this work using equation 5.45 resulting in simpler integrals with the linear approach, as the rotational of the magnetisation

gets constant over the considered volume. The curl of the magnetisation gets

$$
\underline{\nabla}' \wedge \underline{M}(\underline{r}') = \begin{pmatrix} \partial'_x \\ \partial'_y \\ \partial'_z \end{pmatrix} \wedge \begin{pmatrix} M_{x'} \\ M_{y'} \\ M_{z'} \end{pmatrix} = \begin{pmatrix} \partial'_y M_{z'} - \partial'_z M_{y'} \\ \partial'_z M_{x'} - \partial'_x M_{z'} \\ \partial'_x M_{y'} - \partial'_y M_{x'} \end{pmatrix} = cste
\tag{5.57}
$$

and the volume integral becomes

$$
I_{v_1} = \iiint_V \frac{dx' dy' dz'}{|\underline{r} - \underline{r}'|}.
\tag{5.58}
$$

The result of this integral can be found in [134] and has been validated numerically. For the surface integral, the result will be presented only for one surface, the five others can be obtained by permutation of variables. Let's again consider a surface element $\underline{d\sigma}' = dy' dz' \underline{e}_{x'}$ oriented along the x-axis with x' having a given value. One obtains then

$$
\underline{M}(\underline{r}') \wedge \underline{d\sigma}' = \begin{pmatrix} M_{x'} \\ M_{y'} \\ M_{z'} \end{pmatrix} \wedge \begin{pmatrix} 1 \\ 0 \\ 0 \end{pmatrix} = \begin{pmatrix} 0 \\ M_{z'} \\ -M_{y'} \end{pmatrix}
\tag{5.59}
$$

with

$$
M_{y'} = M_{0y} + M_{1y} x' + M_{2y} y' + M_{3y} z'
\tag{5.60}
$$

$$
M_{z'} = M_{0z} + M_{1z} x' + M_{2z} y' + M_{3z} z'.
\tag{5.61}
$$

The surface integral comes to

$$
\begin{aligned}
A_y &= \frac{\mu_0}{4\pi} \iint_{\partial V'} \frac{M_{z'}}{|\underline{r} - \underline{r}'|} dy' dz' \\
&= \alpha \iint_{\partial V'} \frac{1}{|\underline{r} - \underline{r}'|} dy' dz' + \beta \iint_{\partial V'} \frac{y'}{|\underline{r} - \underline{r}'|} dy' dz' + \gamma \iint_{\partial V'} \frac{z'}{|\underline{r} - \underline{r}'|} dy' dz'
\end{aligned}
\tag{5.62}
$$

with

$$
\alpha = M_{0z} + M_{1z} x'
\tag{5.63}
$$

$$
\beta = M_{2z}
\tag{5.64}
$$

$$
\gamma = M_{3z}.
\tag{5.65}
$$

The first integral is I_{s1} while the second and third are I_{s2}. For the contribution to A_z one can obtain a similar equation with permuted variables.

5.2.6 Magnetisation approach - cylindrical coordinates

Figure 5.4 shows a schematic representation of the magnetised body in cylindrical coordinates as well as the definition and denomination of the used variables. First of all, let's recall the
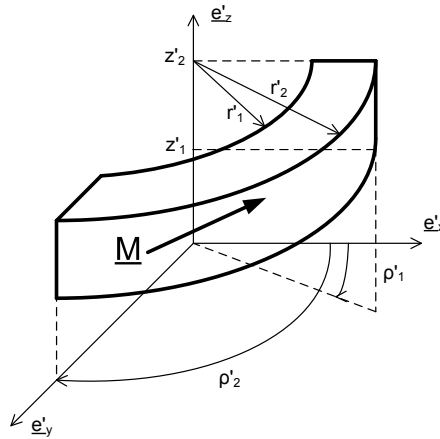
Figure 5.4 – Schematic representation of the magnetised body in cylindrical coordinates.

equation of the rotational and divergence of a vector in cylindrical coordinates. This will help to make a wise choice of the magnetisation approach and computational model used. The divergence of a vector is given by the following equation

$$\underline{\nabla} \cdot \underline{M} = \frac{1}{r}\partial_r(rM_r) + \partial_\phi M_\phi + \partial_z M_z \tag{5.66}$$

while the rotational is defined by

$$\underline{\nabla} \wedge \underline{M} = (\frac{1}{r}\partial_\phi M_z - \partial_z M_\phi)\underline{e}_r + (\partial_z M_r - \partial_r M_z)\underline{e}_\phi + \frac{1}{r}(\partial_r(rM_\phi) - \partial_\phi M_r)\underline{e}_z. \tag{5.67}$$

The crucial choices will be for M_r and M_ϕ as they have a non-zero term in the divergence or rotational, leading to a volume integral which is very difficult to calculate analytically in cylindrical coordinates.

Radial magnetisation

Let's assume a magnetisation vector given by

$$\underline{M} = M_r\underline{e}_r. \tag{5.68}$$

Its divergence and rotational gets

$$\underline{\nabla}' \cdot \underline{M} = \frac{1}{r'}\partial'_r(r'M_r) = \frac{M_r}{r'} \tag{5.69}$$

$$\underline{\nabla}' \wedge \underline{M} = \partial_z M_r\underline{e}_\phi - \frac{1}{r'}\partial_\phi M_r\underline{e}_z = 0. \tag{5.70}$$

The approach of the potential function Φ is not the most practicable here, as the integration doesn't lead to an analytical function. The magnetic field is calculated using the amperian

model and is given by

$$
\underline{H} = \frac{J}{4\pi\mu_0} \int_{\rho_1}^{\rho_2} d\phi \int_{z_1'}^{z_2'} dz' \frac{r'}{D(\phi)^3} \begin{pmatrix} r - r'\cos(\phi) \\ -r'\sin(\phi) \\ \gamma \end{pmatrix} \Bigg|_{r'=r_1'}^{r'=r_2'}
$$
$$
- \frac{J}{4\pi\mu_0} \int_{r_1'}^{r_2'} dr' \int_{\rho_1}^{\rho_2} d\phi \int_{z_1'}^{z_2'} dz' \frac{1}{D(\phi)^3} \begin{pmatrix} r - r'\cos(\phi) \\ -r'\sin(\phi) \\ \gamma \end{pmatrix} \tag{5.71}
$$

where the second integral is the volume integral due to the non-zero divergence of $\underline{M}$.

H_r-component

Let's first recall the surface term (H_{rs}) as defined in [118].

$$
\begin{aligned}
H_{rs} &= \frac{Jr'}{4\pi\mu_0} \int_{\rho_1}^{\rho_2} d\phi \int_{z_1'}^{z_2'} dz' \frac{r - r'\cos(\phi)}{D(\phi)^3} \Bigg|_{r'=r_1'}^{r'=r_2'} \\
&= \frac{Jr'}{4\pi\mu_0} \int_{\rho_1}^{\rho_2} d\phi \frac{r - r'\cos(\phi)}{D(\phi)B^2(\phi)} \Bigg|_{r'=r_1'}^{r'=r_2'} \Bigg|_{z'=z_1'}^{z'=z_2'} \\
&= \frac{2Jr'}{4\pi\mu_0 a(r+r')^2} \int_{\alpha_1}^{\alpha_2} d\alpha \frac{\alpha_0 + \alpha_2 \sin(\alpha)^2}{(1 - n^2\sin(\alpha)^2)\sqrt{1 - k^2\sin(\alpha)^2}} \Bigg|_{r'=r_1'}^{r'=r_2'} \Bigg|_{z'=z_1'}^{z'=z_2'}.
\end{aligned} \tag{5.72}
$$

The result of the elliptic integral can be found in [22]. The volume term (H_{rv}) is given by

$$
\begin{aligned}
H_{rv} &= \frac{J}{4\pi\mu_0} \int_{r_1'}^{r_2'} dr' \int_{\rho_1}^{\rho_2} d\phi \int_{z_1'}^{z_2'} dz' \frac{r - r'\cos(\phi)}{D(\phi)^3} \\
&= \frac{J}{4\pi\mu_0} \int_{\rho_1}^{\rho_2} d\phi \int_{z_1'}^{z_2'} dz' \frac{rr'\sin(\phi)^2 + \gamma^2\cos(\phi)}{D(\phi)G^2(\phi)} \Bigg|_{r'=r_1'}^{r'=r_2'} \\
&= \frac{J}{4\pi\mu_0} \int_{\rho_1}^{\rho_2} d\phi - \sin(\phi)^2 \operatorname{arctanh}(\frac{\gamma(r' - r\cos(\phi))}{r\sin(\phi)D(\phi)}) \\
&\quad + \cos(\phi)\operatorname{arcsinh}(\beta_2(\phi)) \Bigg|_{r'=r_1'}^{r'=r_2'} \Bigg|_{z'=z_1'}^{z'=z_2'}.
\end{aligned} \tag{5.73}
$$

The term containing $\operatorname{arctanh}(\cdot)$ must be evaluated numerically as no integration by parts can be done due to the $\sin(\phi)^2$ term. The second term is well known and was calculated in equation A.28. These formulas have significant discrepancies when comparing its results with a 3D-finite-element calculation. The equations presented in [118] have also some discrepancies while the equation of [113] show a perfect agreement with the numerical computation results. This fact is very surprising as equation 5.71 delivers correct numerical results for the tangential and axial component of the magnetic field. The computation of the radial magnetic field component is therefore based on [113] where the equations were rewritten and extended to avoid as much as possible numerical integration. The coulombian model is used in this

publication. The radial magnetic field is given by

$$H_r = \frac{J}{4\pi\mu_0} \int_{\rho_1}^{\rho_2} d\phi - \frac{r'\gamma(r - r'\cos(\phi)}{B^2(\phi)G(\phi)} + \sin(\phi)\arctan(\beta_3(\phi)) - \cos(\phi)\log(G(\phi) + \gamma)$$

(5.74)

which is equation 21 of [113]. The equations presented in [113] can be further reduced to more compact equations, which are a novel contribution of the work and will be shown in the following paragraphs. The first and third integrals can be transformed into elliptical integrals while the second integral must be evaluated numerically. The first integrand becomes

$$
\begin{aligned}
I_1 &= \int_{\rho_1}^{\rho_2} d\phi - \frac{r'\gamma(r - r'\cos(\phi))}{B^2(\phi)G(\phi)} \\
&= 2r'\gamma \int_{\alpha_1}^{\alpha_2} d\alpha \frac{(r - r'(1 - 2\sin(\alpha)^2)}{(r + r')^2(1 - n^2\sin(\alpha)^2)a\sqrt{1 - k^2\sin(\alpha)^2}} \\
&= \frac{2r'\gamma}{a(r + r')^2} \int_{\alpha_1}^{\alpha_2} d\alpha \frac{(r - r'(1 - 2\sin(\alpha)^2)}{(1 - n^2\sin(\alpha)^2)\sqrt{1 - k^2\sin(\alpha)^2}}
\end{aligned}
$$

(5.75)

whose result is given in [22]. The third integral gets

$$
\begin{aligned}
I_3 &= \int_{\rho_1}^{\rho_2} d\phi - \cos(\phi)\log(G(\phi) + \gamma) \\
&= \sin(\phi)\log(G(\phi) + \gamma)|_{\rho=\rho_1}^{\rho=\rho_2} + \int_{\rho_1}^{\rho_2} d\phi \frac{rr'\gamma\sin(\phi)}{B^2(\phi)G(\phi)}.
\end{aligned}
$$

(5.76)

The last integral can be transformed into an elliptical integral using the same approach as for I_1. When $r = 0$ the equations become

$$
\begin{aligned}
H_{rs} &= -\frac{J}{4\pi\mu_0} \int_{\rho_1}^{\rho_2} d\phi \int_{z_1'}^{z_2'} dz' \frac{r'\cos(\phi)}{(\gamma^2 + r'^2)^{3/2}}\Big|_{r'=r_1'}^{r'=r_2'} \\
&= -\frac{Jr'}{4\pi\mu_0} \sin(\phi)\Big|_{\phi=\phi_1'}^{\phi=\phi_2'} \frac{\gamma}{\sqrt{\gamma^2 + r'^2}}\Big|_{z'=z_1'}^{z'=z_2'}
\end{aligned}
$$

(5.77)

while for the volume integral one gets

$$
\begin{aligned}
H_{rv} &= -\frac{J}{4\pi\mu_0} \int_{r_1'}^{r_2'} dr' \int_{\rho_1}^{\rho_2} d\phi \int_{z_1'}^{z_2'} dz' \frac{r'\cos(\phi)}{(\gamma^2 + r'^2)^{3/2}} \\
&= \frac{J}{4\pi\mu_0} \sin(\phi)\Big|_{\phi=\phi_1'}^{\phi=\phi_2'} \int_{z_1'}^{z_2'} dz' \frac{1}{\sqrt{\gamma^2 + r'^2}}\Big|_{r'=r_1'}^{r'=r_2'} \\
&= \frac{J}{4\pi\mu_0} \sin(\phi)\operatorname{arcsinh}(\frac{\gamma}{r'})\Big|_{r'=r_1'}^{r'=r_2'}\Big|_{\phi=\phi_1'}^{\phi=\phi_2'}\Big|_{z'=z_1'}^{z'=z_2'}
\end{aligned}
$$

(5.78)

note that the absolute value operators $|\cdot|$ have been omitted as per definition of the cylindrical coordinate system r_1' and r_2' are always positive and greater than zero.

131

H_ϕ-component

The equation for this component is an original contribution of this work. Let's first compute the surface term ($H_{\phi s}$).

$$
\begin{aligned}
H_{\phi s} &= \frac{J r'^2}{4\pi\mu_0} \int_{\rho_1}^{\rho_2} d\phi \int_{z_1'}^{z_2'} dz' \frac{-\sin(\phi)}{D(\phi)^3} \Big|_{r'=r_1'}^{r'=r_2'} \\
&= \frac{J r'^2}{4\pi\mu_0 r} \int_{z_1'}^{z_2'} dz' \frac{1}{D(\phi)} \Big|_{r'=r_1'}^{r'=r_2'} \Big|_{\phi=\phi_1'}^{\phi=\phi_2'} \\
&= \frac{J r'^2}{4\pi\mu_0 r} \operatorname{arcsinh} \frac{\gamma}{\sqrt{\gamma^2 + r^2 + r'^2 - 2 r r' \cos(\phi)}} \Big|_{r'=r_1'}^{r'=r_2'} \Big|_{\phi=\phi_1'}^{\phi=\phi_2'} \Big|_{z'=z_1'}^{z'=z_2'} \\
&= \frac{J r'^2}{4\pi\mu_0 r} \operatorname{arcsinh}(\beta_2(\phi)) \Big|_{r'=r_1'}^{r'=r_2'} \Big|_{\phi=\phi_1'}^{\phi=\phi_2'} \Big|_{z'=z_1'}^{z'=z_2'}.
\end{aligned} \tag{5.79}
$$

The volume term ($H_{\phi v}$) is given by

$$
\begin{aligned}
H_{\phi v} &= \frac{J}{4\pi\mu_0} \int_{r_1'}^{r_2'} dr' \int_{\rho_1}^{\rho_2} d\phi \int_{z_1'}^{z_2'} dz' \frac{r' \sin(\phi)}{D(\phi)^3} \\
&= -\frac{J}{4\pi\mu_0 r} \int_{r_1'}^{r_2'} dr' \int_{z_1'}^{z_2'} dz' \frac{1}{D(\phi)} \Big|_{\phi=\phi_1'}^{\phi=\phi_2'} \\
&= -\frac{J}{4\pi\mu_0 r} \int_{z_1'}^{z_2'} dz' \operatorname{arcsinh}(\beta_2(\phi)) \Big|_{r'=r_1'}^{r'=r_2'} \Big|_{\phi=\phi_1'}^{\phi=\phi_2'} \\
&= -\frac{J}{4\pi\mu_0 r} (r' - r\cos(\phi) \operatorname{arcsinh}(\beta_1(\phi)) - r\sin(\phi) \arctan(\beta_3(\phi)) \\
&\quad + \gamma \operatorname{arcsinh}(\beta_2(\phi)) \Big|_{r'=r_1'}^{r'=r_2'} \Big|_{\phi=\phi_1'}^{\phi=\phi_2'} \Big|_{z'=z_1'}^{z'=z_2'}.
\end{aligned} \tag{5.80}
$$

When $r = 0$, the equations become

$$
\begin{aligned}
H_{\phi s} &= \frac{J r'^2}{4\pi\mu_0} \int_{\rho_1}^{\rho_2} d\phi \int_{z_1'}^{z_2'} dz' \frac{-\sin(\phi)}{(\gamma^2 + r'^2)^{3/2}} \Big|_{r'=r_1'}^{r'=r_2'} \\
&= \frac{J r'^2}{4\pi\mu_0} \cos(\phi) \Big|_{\phi=\phi_1'}^{\phi=\phi_2'} \frac{\gamma}{\sqrt{\gamma^2 + r'^2}} \Big|_{z'=z_1'}^{z'=z_2'}
\end{aligned} \tag{5.81}
$$

while for the volume integral one gets

$$
\begin{aligned}
H_{\phi v} &= \frac{J}{4\pi\mu_0} \int_{r_1'}^{r_2'} dr' \int_{\rho_1}^{\rho_2} d\phi \int_{z_1'}^{z_2'} dz' \frac{r' \sin(\phi)}{(\gamma^2 + r'^2)^{3/2}} \\
&= \frac{J r'}{4\pi\mu_0} \cos(\phi) \Big|_{\phi=\phi_1'}^{\phi=\phi_2'} \int_{z_1'}^{z_2'} dz' \frac{1}{\sqrt{\gamma^2 + r'^2}} \Big|_{r'=r_1'}^{r'=r_2'} \\
&= \frac{J r'}{4\pi\mu_0} \cos(\phi) \operatorname{arcsinh}(\frac{\gamma}{r'}) \Big|_{r'=r_1'}^{r'=r_2'} \Big|_{\phi=\phi_1'}^{\phi=\phi_2'} \Big|_{z'=z_1'}^{z'=z_2'}
\end{aligned} \tag{5.82}
$$

note that the absolute value operators $|\cdot|$ have been omitted as per definition of the cylindrical coordinate system r_1' and r_2' are positive and greater than zero.

H_z-component

The equation presented in this section are taken from a publication. The surface term (H_{zs}) is given by

$$
\begin{aligned}
H_{zs} &= \frac{Jr'}{4\pi\mu_0} \int_{\rho_1}^{\rho_2} d\phi \int_{z_1'}^{z_2'} dz' \frac{\gamma}{D(\phi)^3} \\
&= \frac{Jr'}{4\pi\mu_0} \frac{1}{D(\phi)} \Big|_{z'=z_1'}^{z'=z_2'} \\
&= \frac{2Jr'}{4\pi\mu_0 a} (F(\alpha_2, k) - F(\alpha_1, k)) \Big|_{z'=z_1'}^{z'=z_2'}.
\end{aligned}
\tag{5.83}
$$

The volume term (H_{zv}) is given by

$$
\begin{aligned}
H_{zv} &= \frac{J}{4\pi\mu_0} \int_{r_1'}^{r_2'} dr' \int_{\rho_1}^{\rho_2} d\phi \int_{z_1'}^{z_2'} dz' \frac{\gamma}{D(\phi)^3} \\
&= \frac{J}{4\pi\mu_0} \int_{r_1'}^{r_2'} dr' \int_{\rho_1}^{\rho_2} d\phi \frac{1}{D(\phi)} \Big|_{z'=z_1'}^{z'=z_2'} \\
&= \frac{J}{4\pi\mu_0} \int_{\rho_1}^{\rho_2} d\phi \, \text{arcsinh}(\beta_1(\phi)).
\end{aligned}
\tag{5.84}
$$

This integral must be evaluated numerically as no analytical treatment is possible. When $r = 0$, the equations become

$$
\begin{aligned}
H_{zs} &= \frac{Jr'}{4\pi\mu_0} \int_{\rho_1}^{\rho_2} d\phi \int_{z_1'}^{z_2'} dz' \frac{\gamma}{(\gamma^2 + r'^2)^{3/2}} \\
&= -\frac{Jr'}{4\pi\mu_0} \phi \Big|_{\phi=\phi_1'}^{\phi=\phi_2'} \frac{1}{\sqrt{\gamma^2 + r'^2}} \Big|_{z'=z_1'}^{z'=z_2'}
\end{aligned}
\tag{5.85}
$$

while for the volume integral one obtains

$$
\begin{aligned}
H_{zv} &= \frac{J}{4\pi\mu_0} \int_{r_1'}^{r_2'} dr' \int_{\rho_1}^{\rho_2} d\phi \int_{z_1'}^{z_2'} dz' \frac{\gamma}{(\gamma^2 + r'^2)^{3/2}} \\
&= -\frac{J}{4\pi\mu_0} \phi \Big|_{\phi=\phi_1'}^{\phi=\phi_2'} \int_{r_1'}^{r_2'} dr' \frac{1}{\sqrt{\gamma^2 + r'^2}} \Big|_{z'=z_1'}^{z'=z_2'} \\
&= -\frac{J}{4\pi\mu_0} \phi \, \text{arcsinh}(\frac{r'}{|\gamma|}) \Big|_{r'=r_1'}^{r'=r_2'} \Big|_{\phi=\phi_1'}^{\phi=\phi_2'} \Big|_{z'=z_1'}^{z'=z_2'}.
\end{aligned}
\tag{5.86}
$$

For the vector potential the following integrals have to be calculated

$$
\underline{A} = \frac{\mu_0 J}{4\pi} \int_{\rho_1}^{\rho_2} d\phi \int_{r_1'}^{r_2'} dr' \frac{r'}{D(\phi)} \begin{pmatrix} \sin(\phi) \\ \cos(\phi) \\ 0 \end{pmatrix} \Bigg|_{z'=z_1'}^{z'=z_2'}
$$
$$
+ \frac{\mu_0 J}{4\pi} \int_{r_1'}^{r_2'} dr' \int_{z_1'}^{z_2'} dz' \frac{1}{D(\phi)} \begin{pmatrix} 0 \\ 0 \\ 1 \end{pmatrix} \Bigg|_{\phi=\phi_1'}^{\phi=\phi_2'}
\tag{5.87}
$$

A_r-component

The formulas for the vector potential are identical to the ones published in [61] with the difference that [61] did not calculate explicitly each component of the vector potential. This calculation is another original contribution of this work. Integrating first along ϕ and then along r' leads to the following equation

$$
\begin{aligned}
A_r &= \frac{\mu_0 J}{4\pi} \int_{\rho_1}^{\rho_2} d\phi \int_{r_1'}^{r_2'} dr' \frac{r'\sin(\phi)}{D(\phi)} \Bigg|_{z'=z_1'}^{z'=z_2'} \\
&= \frac{\mu_0 J}{4\pi r} D(\phi) \Bigg|_{\phi=\phi_1'}^{\phi=\phi_2'} \Bigg|_{z'=z_1'}^{z'=z_2'} \\
&= \frac{\mu_0 J}{8\pi r} [(\gamma^2 + r^2 \sin(\phi)^2) \operatorname{arcsinh}(\beta_1(\phi)) + (r' - r\cos(\phi))D(\phi)] \Bigg|_{r'=r_1'}^{r'=r_2'} \Bigg|_{\phi=\phi_1'}^{\phi=\phi_2'} \Bigg|_{z'=z_1'}^{z'=z_2'}.
\end{aligned}
\tag{5.88}
$$

When $r = 0$ the equation simplifies to

$$
\begin{aligned}
A_r &= \frac{\mu_0 J}{4\pi} \int_{\rho_1}^{\rho_2} d\phi \int_{r_1'}^{r_2'} dr' \frac{r'\sin(\phi)}{\sqrt{\gamma^2 + r'^2}} \Bigg|_{z'=z_1'}^{z'=z_2'} \\
&= \frac{\mu_0 J}{4\pi r} (-\cos(\phi)) \Bigg|_{\phi=\phi_1'}^{\phi=\phi_2'} \sqrt{\gamma^2 + r'^2} \Bigg|_{r'=r_1'}^{r'=r_2'} \Bigg|_{z'=z_1'}^{z'=z_2'}.
\end{aligned}
\tag{5.89}
$$

A_ϕ-component

For the novel equation of A_ϕ one gets

$$
\begin{aligned}
A_\phi &= \frac{\mu_0 J}{4\pi} \int_{\rho_1}^{\rho_2} d\phi \int_{r_1'}^{r_2'} dr' \frac{r'\cos(\phi)}{D(\phi)} \Bigg|_{z'=z_1'}^{z'=z_2'} \\
&= \frac{\mu_0 J}{4\pi} \int_{\rho_1}^{\rho_2} d\phi \cos(\phi)D(\phi) + r\cos(\phi)^2 \operatorname{arcsinh}(\beta_1(\phi)) \Bigg|_{r'=r_1'}^{r'=r_2'} \Bigg|_{z'=z_1'}^{z'=z_2'}.
\end{aligned}
\tag{5.90}
$$

The solution to these integrals are given by I_1 (equation A.5) and I_2 (equation A.6). When $r = 0$, the equation reduce to

$$
\begin{aligned}
A_\phi &= \frac{\mu_0 J}{4\pi} \int_{\rho_1}^{\rho_2} d\phi \int_{r_1'}^{r_2'} dr' \left. \frac{r' \cos(\phi)}{\sqrt{\gamma^2 + r'^2}} \right|_{z'=z_1'}^{z'=z_2'} \\
&= \frac{\mu_0 J}{4\pi} (-\sin(\phi)) \Big|_{\phi=\phi_1'}^{\phi=\phi_2'} \left. \sqrt{\gamma^2 + r'^2} \right|_{r'=r_1'}^{r'=r_2'} \Big|_{z'=z_1'}^{z'=z_2'}.
\end{aligned}
\tag{5.91}
$$

A_z-component

For the novel equation of A_z one has

$$
\begin{aligned}
A_z =& \frac{\mu_0 J}{4\pi} \int_{r_1'}^{r_2'} dr' \int_{z_1'}^{z_2'} dz' \left. \frac{1}{D(\phi)} \right|_{\phi=\phi_1'}^{\phi=\phi_2'} \\
=& \frac{\mu_0 J}{4\pi} \int_{z_1'}^{z_2'} dz' \, \mathrm{arcsinh}(\beta_2(\phi)) \Big|_{r'=r_1'}^{r'=r_2'} \Big|_{\phi=\phi_1'}^{\phi=\phi_2'} \\
=& \frac{\mu_0 J}{4\pi} \Big(-\gamma + r\sin(\phi)\arctan(\frac{\gamma}{r\sin(\phi)}) - r\sin(\phi)\arctan(\beta_3(\phi)) + \gamma\,\mathrm{arcsinh}(\beta_1(\phi)) \\
&+ (r' - r\cos(\phi))\,\mathrm{arcsinh}(\beta_2(\phi)) \Big) \Big|_{r'=r_1'}^{r'=r_2'} \Big|_{\phi=\phi_1'}^{\phi=\phi_2'} \Big|_{z'=z_1'}^{z'=z_2'}.
\end{aligned}
\tag{5.92}
$$

When $r = 0$ the equation become

$$
\begin{aligned}
A_z &= \frac{\mu_0 J}{4\pi} \int_{r_1'}^{r_2'} dr' \int_{z_1'}^{z_2'} dz' \left. \frac{1}{\sqrt{\gamma^2 + r'^2}} \right|_{\phi=\phi_1'}^{\phi=\phi_2'} = \frac{\mu_0 J}{4\pi} \phi \Big|_{\phi=\phi_1'}^{\phi=\phi_2'} \int_{z_1'}^{z_2'} dz' \, \mathrm{arcsinh}(\frac{r'}{|\gamma|}) \Big|_{r'=r_1'}^{r'=r_2'} \\
&= \frac{\mu_0 J}{4\pi} \phi (r'\,\mathrm{arcsinh}(\frac{\gamma}{r'}) + \gamma\,\mathrm{arcsinh}(\frac{r'}{|\gamma|})) \Big|_{r'=r_1'}^{r'=r_2'} \Big|_{\phi=\phi_1'}^{\phi=\phi_2'} \Big|_{z'=z_1'}^{z'=z_2'}
\end{aligned}
\tag{5.93}
$$

Tangential magnetisation

Let's assume a magnetisation vector given by

$$
\underline{M} = M_\phi \underline{e}_\phi.
\tag{5.94}
$$

Its divergence and rotational get

$$
\underline{\nabla}' \cdot \underline{M} = \partial_\phi M_\phi = 0
\tag{5.95}
$$

$$
\underline{\nabla}' \wedge \underline{M} = \partial_z M_\phi \underline{e}_r + \frac{1}{r'} \partial_{r'} (r' M_\phi) \underline{e}_z = \frac{1}{r'} M_\phi \underline{e}_z.
\tag{5.96}
$$

To calculate the magnetic field, the most simple approach is to use the potential function Φ. The equation for the H-field can be taken from [117]. The calculation of the vector potential for the tangential magnetisation is an original contribution of this work. For the calculation of the vector potential, the non-zero term in the rotational will lead to the following complicated

volume integral

$$
\underline{A} = \frac{\mu_0 J}{4\pi} \int_{\rho_1}^{\rho_2} d\phi \int_{z_1'}^{z_2'} dz' \frac{r'}{D(\phi)} \begin{pmatrix} 0 \\ 0 \\ 1 \end{pmatrix} \Big|_{r'=r_1'}^{r'=r_2'} + \frac{\mu_0 J}{4\pi} \int_{\rho_1}^{\rho_2} d\phi \int_{r_1'}^{r_2'} dr' \frac{r'}{D(\phi)} \begin{pmatrix} 1 \\ 0 \\ 0 \end{pmatrix} \Big|_{z'=z_1'}^{z'=z_2'}
$$

$$
+ \frac{\mu_0 J}{4\pi} \int_{\rho_1}^{\rho_2} d\phi \int_{r_1'}^{r_2'} dr' \int_{z_1'}^{z_2'} dz' \frac{1}{D(\phi)} \begin{pmatrix} 0 \\ 0 \\ 1 \end{pmatrix}. \tag{5.97}
$$

The three integrals are named $\underline{A}_1$, $\underline{A}_2$, $\underline{A}_3$ respectively. The calculation of $\underline{A}_1$, $\underline{A}_2$, $\underline{A}_3$ can be found in A.5.3.

Axial magnetization

Let's assume a magnetization vector given by

$$
\underline{M} = M_z \underline{e}_z. \tag{5.98}
$$

Its divergence and rotational gets

$$
\underline{\nabla}' \cdot \underline{M} = \partial_z M_z = 0 \tag{5.99}
$$

$$
\underline{\nabla}' \wedge \underline{M} = \frac{1}{r'} \partial_\phi M_z \underline{e}_r - \partial_{r'} M_z \underline{e}_\phi = 0. \tag{5.100}
$$

The approach of the potential function Φ is not very interesting as the integration should be performed along r' and ϕ leading to elliptic functions. To get the magnetic field, one should derivate the elliptic function, which is not very easy. The simplest way is here to integrate directly to obtain the magnetic field which is given by

$$
\underline{H} = \frac{J}{4\pi\mu_0} \int_{\rho_1}^{\rho_2} d\phi \int_{r_1'}^{r_2'} dr' \frac{r'}{D(\phi)^3} \begin{pmatrix} r - r'\cos(\phi) \\ -r'\sin(\phi) \\ \gamma \end{pmatrix} \Big|_{z'=z_1'}^{z'=z_2'}. \tag{5.101}
$$

[115] integrates also this equation but their equation for the radial and axial component differs from this work. The equation of this work has been reduced to a more compact form than in [115] which is an original contribution of this work. The tangential component has the same equation but it has been included in this work to have a complete set of equations.

H_r-component

$$H_r = \frac{J}{4\pi\mu_0} \int_{\rho_1}^{\rho_2} d\phi \int_{r_1'}^{r_2'} dr' r' \frac{r - r'\cos(\phi)}{D(\phi)^3} \Big|_{z'=z_1'}^{z'=z_2'}$$

$$= \frac{J}{4\pi\mu_0} \int_{\rho_1}^{\rho_2} d\phi \frac{r(r^2 + \gamma^2 - rr'\cos(\phi)) + \cos(\phi)(r'(\gamma^2 - r^2\cos(2\phi)) + r(r^2 + \gamma^2)\cos(\phi))}{G^2(\phi)D(\phi)}$$

$$- \cos(\phi)\operatorname{arcsinh}(\beta_2(\phi)) \Big|_{r'=r_1'}^{r'=r_2'} \Big|_{z'=z_1'}^{z'=z_2'}. \tag{5.102}$$

The last term of the integral is well known and its equation can be found at equation A.28. The first term will be converted to an elliptic integral. One obtains

$$I = \int_{\rho_1}^{\rho_2} d\phi \frac{r(r^2 + \gamma^2 - rr'\cos(\phi)) + \cos(\phi)(r'(\gamma^2 - r^2\cos(2\phi)) + r(r^2 + \gamma^2)\cos(\phi))}{G^2(\phi)D(\phi)}$$

$$= -2\int_{\alpha_1}^{\alpha_2} d\alpha \frac{\alpha_0 + \alpha_2\sin(\alpha)^2 + \alpha_4\sin(\alpha)^4 + \alpha_6\sin(\alpha)^6}{G^2(\alpha)D(\alpha)}. \tag{5.103}$$

In the case $r = 0$ one gets

$$H_r = -\frac{J}{4\pi\mu_0} \int_{\rho_1}^{\rho_2} d\phi \int_{r_1'}^{r_2'} dr' \frac{r'^2\cos(\phi)}{D(\phi)^3} \Big|_{z'=z_1'}^{z'=z_2'}$$

$$= -\frac{J}{4\pi\mu_0} \sin(\phi)(\operatorname{arcsinh}(\frac{r'}{\gamma}) - \frac{r'}{\sqrt{\gamma^2 + r'^2}}) \Big|_{r'=r_1'}^{r'=r_2'} \Big|_{\phi=\phi_1'}^{\phi=\phi_2'} \Big|_{z'=z_1'}^{z'=z_2'}. \tag{5.104}$$

H_ϕ-component

$$H_\phi = \frac{J}{4\pi\mu_0} \int_{\rho_1}^{\rho_2} d\phi \int_{r_1'}^{r_2'} dr' \frac{-r'^2\sin(\phi)}{D(\phi)^3} \Big|_{z'=z_1'}^{z'=z_2'}$$

$$= \frac{J}{4\pi\mu_0} \int_{r_1'}^{r_2'} dr' \frac{r'}{r D(\phi)} \Big|_{\phi=\phi_1'}^{\phi=\phi_2'} \Big|_{z'=z_1'}^{z'=z_2'}$$

$$= \frac{J}{4\pi\mu_0 r} (D(\phi) + r\cos(\phi)\operatorname{arcsinh}(\beta_2(\phi))) \Big|_{r'=r_1'}^{r'=r_2'} \Big|_{\phi=\phi_1'}^{\phi=\phi_2'} \Big|_{z'=z_1'}^{z'=z_2'}. \tag{5.105}$$

In the case $r = 0$ one obtains

$$H_\phi = \frac{J}{4\pi\mu_0} \int_{\rho_1}^{\rho_2} d\phi \int_{r_1'}^{r_2'} dr' \frac{-r'^2\sin(\phi)}{(\gamma^2 + r'^2)^{3/2}} \Big|_{z'=z_1'}^{z'=z_2'}$$

$$= \frac{J}{4\pi\mu_0} \cos(\phi)(\operatorname{arcsinh}(\frac{r'}{|\gamma|}) - \frac{r'}{\sqrt{\gamma^2 + r'^2}}) \Big|_{r'=r_1'}^{r'=r_2'} \Big|_{\phi=\phi_1'}^{\phi=\phi_2'} \Big|_{z'=z_1'}^{z'=z_2'}. \tag{5.106}$$

H_z**-component**

$$
\begin{aligned}
H_z &= \frac{J}{4\pi\mu_0} \int_{\rho_1}^{\rho_2} d\phi \int_{r_1'}^{r_2'} dr' \frac{\gamma r'}{D(\phi)^3} \bigg|_{z'=z_1'}^{z'=z_2'} \\
&= -\frac{J\gamma}{4\pi\mu_0} \int_{\rho_1}^{\rho_2} d\phi \frac{r^2 - r'r\cos(\phi) + \gamma^2}{G^2(\phi)D(\phi)} \bigg|_{r'=r_1'}^{r'=r_2'} \bigg|_{z'=z_1'}^{z'=z_2'} \\
&= \frac{2J\gamma}{4\pi\mu_0} \int_{\alpha_1}^{\alpha_2} d\alpha \frac{\alpha_0 + \alpha_2\sin(\alpha)^2}{G^2(\alpha)D(\alpha)} \bigg|_{r'=r_1'}^{r'=r_2'} \bigg|_{z'=z_1'}^{z'=z_2'} .
\end{aligned}
\tag{5.107}
$$

In the case $r = 0$ one gets

$$
\begin{aligned}
H_z &= \frac{J}{4\pi\mu_0} \int_{\rho_1}^{\rho_2} d\phi \int_{r_1'}^{r_2'} dr' \frac{\gamma r'}{(\gamma^2 + r'^2)^{3/2}} \bigg|_{z'=z_1'}^{z'=z_2'} \\
&= -\frac{J\gamma}{4\pi\mu_0} \phi \frac{1}{\sqrt{\gamma^2 + r'^2}} \bigg|_{r'=r_1'}^{r'=r_2'} \bigg|_{\phi=\phi_1'}^{\phi=\phi_2'} \bigg|_{z'=z_1'}^{z'=z_2'} .
\end{aligned}
\tag{5.108}
$$

The vector potential calculation is an original contribution of this work. The vector potential is given by the following integrals

$$
\begin{aligned}
\underline{A} &= \frac{\mu_0 J}{4\pi} \int_{r_1'}^{r_2'} dr' \int_{z_1'}^{z_2'} dz' \frac{1}{D(\phi)} \begin{pmatrix} -1 \\ 0 \\ 0 \end{pmatrix} \bigg|_{\phi=\phi_1'}^{\phi=\phi_2'} \\
&+ \frac{\mu_0 J}{4\pi} \int_{\rho_1}^{\rho_2} d\phi \int_{z_1'}^{z_2'} dz' \frac{r'}{D(\phi)} \begin{pmatrix} \sin(\phi) \\ \cos(\phi) \\ 0 \end{pmatrix} \bigg|_{r'=r_1'}^{r'=r_2'} .
\end{aligned}
\tag{5.109}
$$

The first integral has already been calculated (refer to equation 5.92). For the second integral, the radial component can be easily integrated performing first an integration over $d\phi$ and then dz'. The integral for the tangential component is given by equation A.10 (integral I_{3b1}) . In the case $r = 0$, refer to the corresponding calculation in the section where the reference has been defined.

5.3   Saturable iron

The calculation of the magnetic field produced by the nonlinear saturable iron is based on the works of [107], [108] and [45], where as this algorithm has been published in many other papers. The theory, based on the previously listed publications, underlining this algorithm is recalled hereafter. The H-field is composed of two orthogonal components, namely $\underline{H} = \underline{H}_{div} + \underline{H}_{curl}$ (in other words, two 3-component vectors), decomposed using Helmholtz-Hodge decomposition. The curl-component is originated by the current densities and is obtained using the relations developed and presented in section 5.1, while the div-component is created by the magnetisation and the corresponding equations are given in section 5.2.

The curl-component is calculated first as the location and the amplitude of the current sources are known. In this problem, $\underline{H}_{div}$ is supposed known wherever it is needed. The div-component is a linear function of the magnetisation, which is the unknown. The magnetic domain is divided in subdomains where the magnetisation vector is supposed to be uniform over that subdomain. One can therefore write

$$\underline{H}_{div}(x) = G(x, x')\underline{M} \tag{5.110}$$

where $G(x, x')$ is the integral magnetisation operator, which maps the magnetisation vector $\underline{M}$ over the complete subspace of R^3. The magnetisation vector $\underline{M}$ is constant according to the magnetisation approach (refer to equation 5.47 for example). The magnetic field $\underline{B}$ is given by the following relation in magnetised bodies

$$\underline{B} = \mu_0\underline{H} + \underline{M} = \mu\underline{H} \tag{5.111}$$

Using the orthogonal decomposition for the H-field leads to

$$\underline{H}_{div} = (\frac{1}{\mu - \mu_0} - G)\underline{M}. \tag{5.112}$$

This nonlinear matrix equation needs to be solved using an iterative process. The number of equations is 3N, where N is the number of iron subdomains considered. The G-matrix is a full matrix, which is not obviously symmetric positive definite. To ensure a symmetric positive matrix, one can use the procedure described in [108], which is based on a finite element approximation subspace.

Using a finite element approximation subspace increases the calculation costs to obtain the G-matrix, but the computational effort to invert the matrix is drastically reduced. On the other hand the G-Matrix is calculated only once per problem, while the G-Matrix is inverted many times in the nonlinear solving process. So that, the finite element approximation subspace is a very good compromise for the calculation of the elements of the G-Matrix. The elements of the G-Matrix are given by the following formula

$$G_{i,j,k,l} = \int_{\tau_i} \frac{\partial}{\partial x_j} \int_{\tau_k} \frac{\partial}{\partial x'_l} \frac{1}{|\underline{x} - \underline{x}'|} d\underline{x}' d\underline{x} \tag{5.113}$$

which is taken from [107] or [108]. To obtain a symmetric matrix, equation 5.113 can only be used when the differential operators $\partial/\partial x_j$ and $\partial/\partial x'_l$ commute, which is not the case when considering a cylindrical coordinate system. These considerations are made in conjunction with the hypothesis that the integrals are calculated using quadrature approximation of the volume integrals, leading to analytical equations to be derivated. [107] proposes another formula (using symmetric quadrature) to calculate the elements of the Gram-matrix taking the

non-commutivity of the derivation operator into account, leading to the following equation

$$G_{i,j,k,l} = V(\tau_i)\frac{\partial}{\partial x_j}\int_{\tau_k}\frac{\partial}{\partial x'_l}\frac{1}{|\underline{x}-\underline{x}'|}d\underline{x}' + V(\tau_k)\frac{\partial}{\partial x_l}\int_{\tau_i}\frac{\partial}{\partial x'_j}\frac{1}{|\underline{x}-\underline{x}'|}d\underline{x}' \qquad (5.114)$$

which was defined in [107]. The difference between the two previous equations lies in the fact that in the second equation of the Gram-matrix element uses the permutation of the differential operator, so that the result is by construction symmetric even if the differential operators do not commute.

The nonlinear algorithm is described in [107] and [108]. To have a better conditioning of the problem, [108] proposed to solve the following equation

$$\left(\frac{1}{\mu} - \frac{\mu-1}{\mu}G\right)M = \frac{\mu-1}{\mu}\underline{H}_{div} \qquad (5.115)$$

instead of relation (5.112). To increase the convergence of this algorithm, [107] proposes to solve the matrix system using a conjugate gradient matrix solver, which is run only on 2-3 iterations from which the new value of the relative permeability μ is calculated using the known material properties of the magnetised body. Using this technique, [107] states that the convergence of the nonlinear solver is exponential asymptotic.

This algorithm should theoretically give excellent results. Unfortunately, it has some drawbacks which deterrer dramatically its convergence capabilities for high permeabilities or even worse can produce some so-called "iron loops" [6]. The convergence remains unchanged in case of low permeability, but this is not the case of the problems solved in this work, where the permeability of the iron will remain high. These drawbacks not only affected integral formulation of the computation of 3D magnetic field of non linearly magnetised bodies but also finite elements formulations [7], [127] and [128]. In a series of three papers ([46], [47] and [48]), Friedman analysed in the early 80's this nonlinear equation and in a common paper with Pasciak, they presented the spectral properties of the integral operator (also called G-Matrix) [50]. A first attempt to overcome the drawback of the formulation was proposed by Friedman in 1984 in [49]. This attempt uses a solenoidal vector space to calculate the magnetisation. Using this spectral properties of the integral operator, one can describe the drawback of the formulation of equation 5.112 and proposed afterwards a novel integral formulation [110] and [109]. In parallel to these new developments in finding a new formulation of the integral equation, several papers proposed a novel formulation for the finite element approximation, based on the approach of the reduced and total scalar magnetic potential [20], [7], [127] and [128].

In a first step, one needs to understand why equation (5.112) has huge error for high permeabilities. Let's imagine that the H-field coming from the current sources has small

numerical errors, which are increased by a factor $(\mu - \mu_0)$. From the spectral properties of the integral operator ([110]), one can demonstrate that the error on $\underline{H}_{div}$ will be much less increased for the components of $\underline{H}_{div}$ lying in a subspace of gradient function. From this fundamental finding, Pasciak could develop his novel integral formulation in a subspace of gradient functions [110].

This novel formulation uses subspaces of gradient functions. The total magnetic field $\underline{H}$ as well as the magnetic field coming from the current sources $\underline{H}_{div}$ are projected into subspaces of gradient functions. The equation to be solved becomes therefore

$$(I - G\chi)\underline{H} = \underline{H}_{div} \tag{5.116}$$

for both $\underline{H}$ and $\underline{H}_{div}$ in a subspace of gradient functions. This equation will be solved in this work to obtain the magnetisation in the case of nonlinear iron. For the practical implementation of this equation, the iron domain is divided in tetrahedrons. To express gradient function, a scalar potential is sufficient so that one can use first order nodal finite element basis function to describe the subspace of gradient functions. On each element, one constant vector can be described. The magnetic field $\underline{H}_{div}$ is therefore evaluated at the barycentre of each tetrahedron, using the calculated source magnetic field the source potential Φ_{div} can be obtained. Equation 5.116 can be solved neither in form of a magnetic field or in form of a potential, given that $\underline{H} = -\nabla\Phi$. Solving this equation in a potential form leads to number of nodes equations.

The right-hand side of equation 5.116 is evaluated using the same procedure as used in [25]. The potential Φ_{div} is obtained using a weak formulation of the following condition

$$\min_{\Phi_{div}}((\nabla\Phi_{div} + \underline{H}_{div})^2) \tag{5.117}$$

in the subspace of gradient function solved using a Galerkin approximation of this subspace. The left-hand side of equation 5.116 can be calculated in a collocation approach as in [25]. In this approach, the integral operator becomes

$$\frac{1}{4\pi}\int_{\Omega_i}\frac{\nabla\alpha_j(\underline{r'})(r_i - \underline{r'})}{|\underline{r_i} - \underline{r'}|^3}d\Omega' \tag{5.118}$$

where $d\Omega'$ is the infinitesimal volume element of the tetrahedron i with volume Ω_i, $\underline{r'}$ is the position vector in the volume Ω_i and $\underline{r_i}$ is the position of the node i and $\nabla\alpha_j(\underline{r'})$ is the gradient of the basis function of the node j with j running over all nodes [25]. The calculation of the integral defined in relation 5.118 can be done numerically using gaussian quadrature formulas for example.

The algorithm used to take into account the nonlinear iron is the same as the one presented in [107]. The matrix-equation is solved using a GMRES-solver with an ILU-preconditionner. It was found that this approach has similar convergence behaviour as the one presented in [25], with the advantage that there is no need to calculate at each step the Jacobian-matrix. The evaluation of the integral in equation (5.118) has an important impact on the numerical results of the algorithm. On can use exact analytical formulas as developed in [25] or in [33] or use numerical quadrature. The advantage of the analytical equations lies in their correctness, but their drawback lies in their significative computational cost.

The publication-based programmed non-linear algorithm has been validated comparing the computed relative permeability of a saturable iron cube using a 3-dimensional finite element calculation and the procedure described in the previous paragraphs. The geometry is composed by an iron cube with a side length of 0.1m as shown in figure 5.3 placed in the centre of the coil depicted in figure A.1. By changing the current in the coil, one changes the permeability in the iron cube. The validation consists in a comparison of the calculated permeability, using both methods, with a current variation from 10A to 10MA. Figure 5.5 shows the results, where one can denote that both methods show a very similar saturation behaviour. Comparing the calculated cases of figures 5.5, 5.6 and 5.7 for different numerical quadrature order and mesh size, it is possible to notice that the order of integration has a marginal influence on the calculated curves using the procedure of this work, while a reduction of the mesh size leads to a significant diminution of the difference between the finite element calculation and the procedure of this work.

One important drawback of the integral method to calculate the magnetic field in non-linear magnetised bodies lies in the calculation and handling of a full matrix. To limit the amount of memory used in the calculation some techniques have been developed. The first option is to use matrix compression techniques. These techniques are described in [25] and its referenced papers. This method has not been implemented in this work, but this method is a very valuable option.

In this work, another option constituting an original contribution is used. If the distance between the node i and the node j is above a given threshold, then the interaction is supposed to be null. Using this technique, one can use "sparse"-matrix which is very interesting from a computing point of view. Practically speaking, a practicable distance lies in the range of 10-20 times the tetrahedron ridge length. This technique is very useful when combined to the use of symmetry to reduce the number of nodes and equations to solve. All simulations done until now, show no loss of precision due to this novel option. It must be pointed out that this novel option can't be used in combinaison with the matrix compression algorithms.

Electrical machines have the remarkable property to have a symmetry along the tangential direction. The number of repetitive sections is equal to the number of poles. A priori all
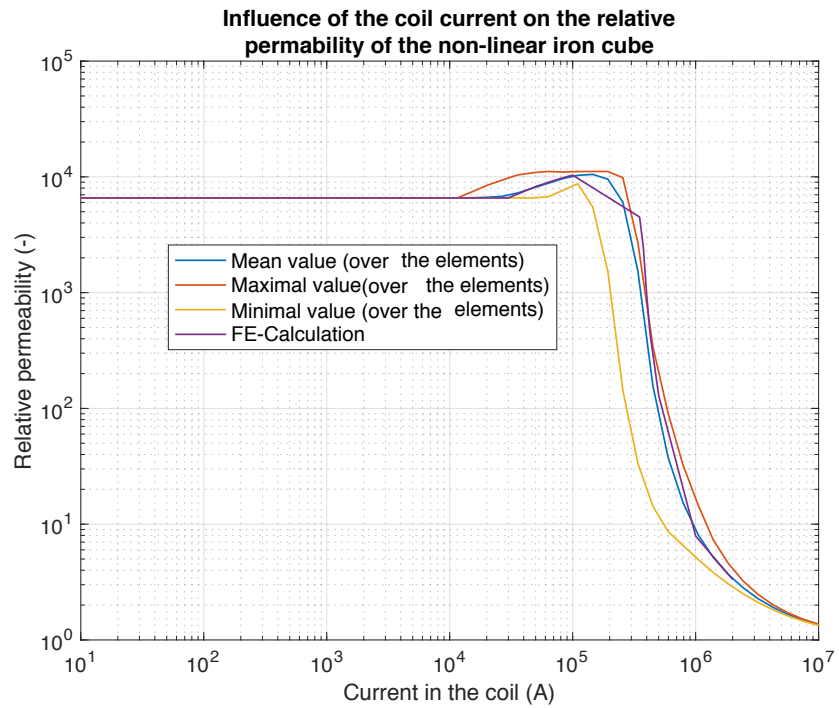
Figure 5.5 – Comparison between the calculated iron permeability using 3-d finite element and the analytical procedure using a first order quadrature approximation and a coarser mesh (Δ=0.1m).
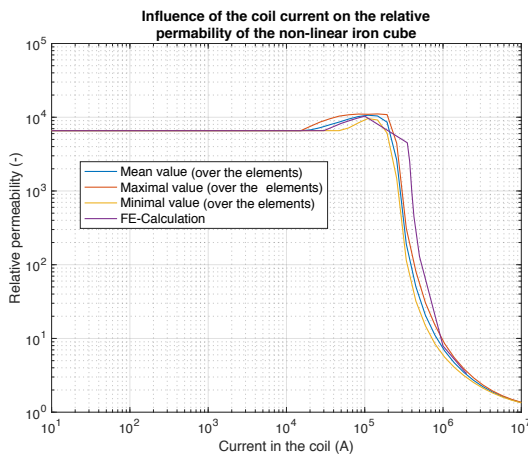
Figure 5.6 – Comparison between the calculated iron permeability using 3-d finite element and the analytical procedure using a first order quadrature approximation (Δ=0.05m).
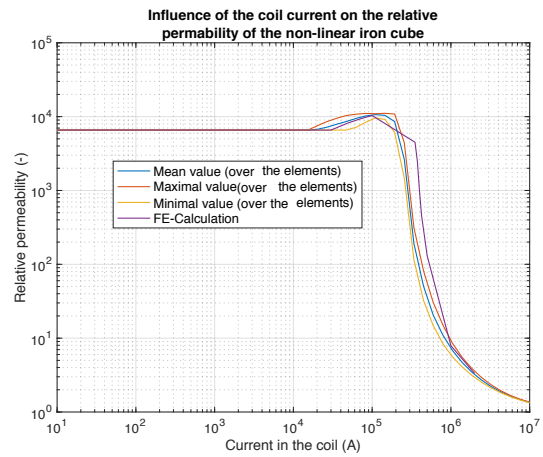
Figure 5.7 – Comparison between the calculated iron permeability using 3-d finite element and the analytical procedure using a fifth order quadrature approximation (Δ=0.1m).

the poles should be meshed leading to an excessive huge number of equations. To reduce the amount of equations, the idea is to start from the symmetry condition used in [45] and extended its definition to a tangential symmetry. Let's first recall the symmetry conditions developed in [45]. [45] solved equation (5.112) to calculate the magnetisation vector. In the case of an infinite iron mirror boundary at the end of the active part of the machine, then the magnetic field given by the current carrying conductors satisfies the following relation

$$H_{div_x} = -H_{div'_x} \tag{5.119}$$

$$H_{div_y} = -H_{div'_y} \tag{5.120}$$

$$H_{div_z} = H_{div'_z}. \tag{5.121}$$

Noting that the elements of the integral magnetisation operator have some symmetry properties, namely that $G_{ij} = G_{i'j'}$ and $G_{ij'} = G_{i'j}$ then the magnetisation vector becomes

$$M_x = -M_{x'} \tag{5.122}$$

$$M_y = -M_{y'} \tag{5.123}$$

$$M_z = M_{z'}. \tag{5.124}$$

so that the number of equations can be reduced by factor two. In the case of the tangential symmetry, then magnetisation can be described using the following relation

$$M_x = -M_{x'} \tag{5.125}$$

$$M_y = -M_{y'} \tag{5.126}$$

$$M_z = -M_{z'} \tag{5.127}$$

where x stands for the odd poles and x' stands for the even poles. Based on this knowledge, it is possible to develop a novel contribution to the reduction of the number of equations considering the tangential symmetry in an electrical machine. Using the same technique as for the mirror boundary one can divide the number of equations by the number of poles, while the reduction in memory is about 1 over number of poles squared. The use of the symmetry can be combined with the nulling of the interactions.

Figure 5.8 shows a schematic representation of the folding over four poles. The relations become

$$\begin{pmatrix} G_{11} & G_{12} & G_{13} & G_{14} \\ G_{21} & G_{22} & G_{23} & G_{24} \\ G_{31} & G_{32} & G_{33} & G_{34} \\ G_{41} & G_{42} & G_{43} & G_{44} \end{pmatrix} \begin{pmatrix} M_i \\ -M_i \\ M_i \\ -M_i \end{pmatrix} \tag{5.128}$$

with $i = x, y, z$. One can directly see that the relations can be simplified in

$$(G_{j1} - G_{j2} + G_{j3} - G_{j4})M \tag{5.129}$$
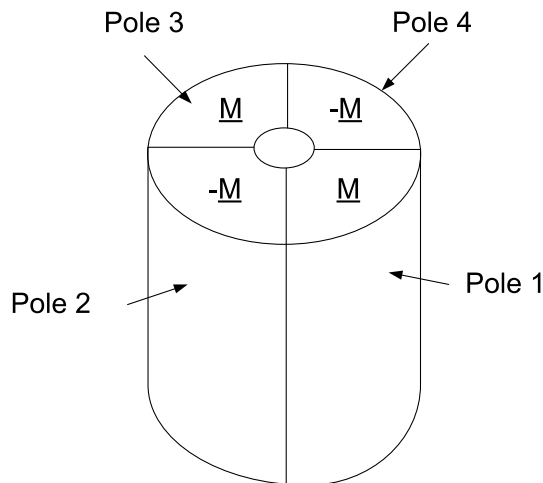
Figure 5.8 – Schematic representation of the folding of four poles.

where j can be chosen arbitrarily between one and four. In the cases calculated in this work, more than one iron domain must be considered. The folding becomes then
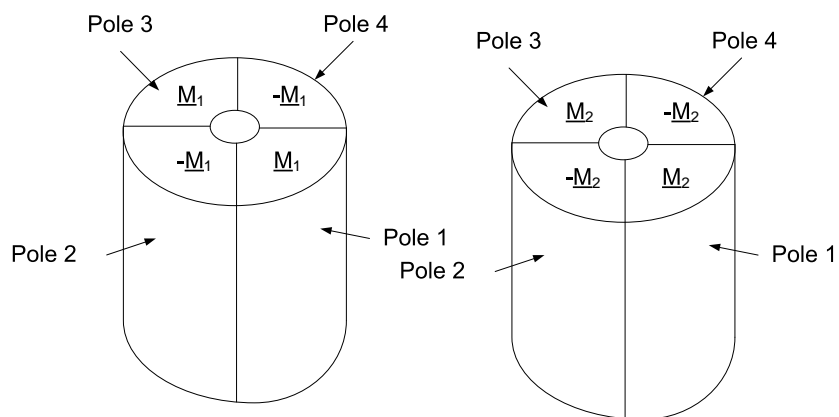
Figure 5.9 – Schematic representation of the folding of four poles (two domains).

Figure 5.9 shows a schematic representation of the folding over four poles for two magnetic domains. The relations become

$$\begin{pmatrix} G_{11} & G_{12} \\ G_{21} & G_{22} \end{pmatrix} \begin{pmatrix} M_{1i} \\ M_{2i} \end{pmatrix} \tag{5.130}$$

with $i = x, y, z$, G_{kl} the folded matrix of equation 5.129.

Figures 5.10 and 5.11 show the G-matrix calculated over one pole (figure 5.10) and its folded counter-part (figure 5.11) calculated over 12 poles. The folding acts like an amplitude increase on the amplitude of the non-diagonal elements. The G-Matrix is a full matrix, but is practically composed of diagonal stripes with a significant amplitude and an ocean of quasi-null value in
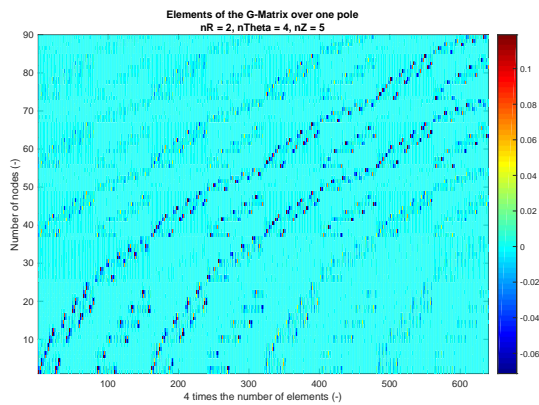
Figure 5.10 – G-matrix calculated over a magnetised annular region spanning over one pole (the considered machine has totally 12 poles) with a radial discretisation (nR) of two elements, a tangential discretisation (nTheta) of 4 elements and an axial discretisation (nZ) of 5 elements.
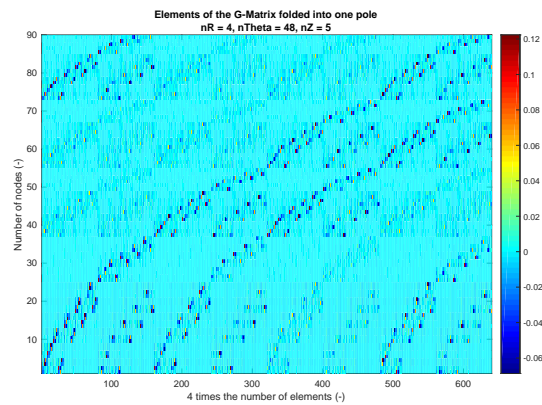
Figure 5.11 – G-matrix calculated over a magnetised annular region spanning over one pole (the considered machine has totally 12 poles) with a radial discretisation (nR) of two elements, a tangential discretisation (nTheta) of 4 elements and an axial discretisation (nZ) of 5 elements with folding of 11 poles.

between. This particular topology can be used to compress the matrix [25].

There exists also another approach using volume integrals to obtain the magnetisation vector. This approach uses Whitney elements also called edge elements [87], [86], [88], [85], [18] and [17]. This class of elements has the particularity to be curl-free, which is a very interesting characteristic as the magnetic field produced by the magnetised bodies is curl-free. Using this kind of elements one can therefore have a discretisation of the magnetic field which takes into account the field characteristics. As these elements are curl-free one can use a tree-generation algorithm to reduce the number of equations as the sum of all edges elements forming a closed loop must be by construction zero. Using this technique one can reduce the number of equations by 60-80%, which is very interesting from a computational time point of view. The rest of the drawbacks of the integral methods, namely the full matrix and the numerical evaluation of the integral operator remains. It was not possible to find an application of the tree-generation algorithm for symmetrical entities so that, it was decided not to use this class of elements in this work, as the use of the symmetry leads to an unbeatable reduction of the number of equations to be solved.

5.4 Numerical calculation of the elliptical integrals

The numerical evaluation of the elliptical integrals and jacobian function is the key element to obtain a precise numerical field computation for the arc elements. These integrals respectively functions are widely used in physics, so that it is not difficult to find already programmed and validated functions. Precision and computation speed are the key drivers of the research

in this topic. Historically, [21] and [74] but also [23] have early presented solutions that are still in use. Urankar presented also some methods to compute accurately the elliptic integral of first, second and third kind accurately and in an extended range [141] and [139]. More recently, Toshio Fukushima reflected on this topic and presented a series of papers that allow to calculate all the elliptic integrals (complete and incomplete) and elliptic functions with the same precision as Carslon or Bulrisch but which are between 5 to 100 times faster than their algorithm. In this work, the novel algorithm and methods presented by Fukushima are widely used. [58] shows the calculation of the complete integrals of the first and second kind using the auxiliary functions $B(m)$ and $D(m)$. There is another paper from Fukushima where the same process have been applied directly to $K(m)$ and $E(m)$. [56] is dedicated to the incomplete elliptical integral of the first kind and [57] presents the incomplete elliptic integral of the second kind. The practical implementation used in this work uses again the auxiliaries function $B(m, \phi)$ and $D(m, \phi)$ as for any computation the incomplete integral of the first and second kind are always used together in the analytical equations. In [59], Fukushima shows the calculation process to calculate the incomplete and complete (described in [60]) elliptical integral of the third kind. Finally, the elliptical functions can determined using the algorithm shown in [54] and [55].

5.5 Hypothesis of the 3D-model

5.5.1 Stator and Rotor bars

Figures 5.12 and 5.13 present the model of the complete stator and rotor bar used in the 3-dimensional magnetic field calculation. The bars are divided in straight and arc elements. Figures 5.14 and 5.15 show the details of the model of the stator and rotor bars. The stator bars can be exactly modelled using straight and arc elements as the stator bars are bend using a bending machine, which is an original contribution of this work. For the rotor bars, the model is only quasi-exact as the involute describes a cylinder and not a conus like for the stator bar. The cylindrical unwinding can't be described exactly using arc elements. Is was not possible to find analytical equations for this case, so that the rotor bar will only be modelled quasi-exactly. This small error is not expected to have a huge impact on the results.

When the distance from the point where the magnetic field is calculated is beyond a given threshold, defined as $5r_0$, then the filament approximation is used instead of the rectangular approximation. This enables to reduce the computational time without a significant reduction of the calculation precision. The threshold can be disabled in the case of very precise simulations.

Having defined the modelling of the stator and rotor bar is the first step of the modelling of the windings. The next step lies in the use of the strand bar approximation, where the magnetic field and vector potential are obtained using a green bar divided in all strands, or to use the green bar approximation, where the green bar is seen as one conductor with its
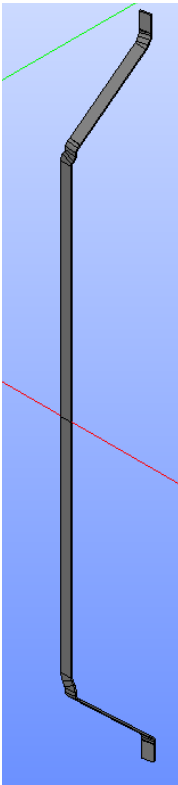
Figure 5.12 – View of the model of the complete stator bar.
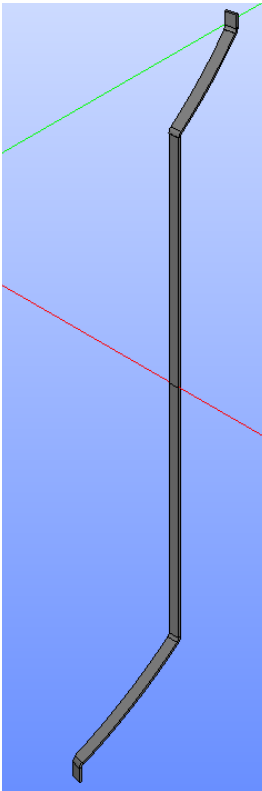
Figure 5.13 – View of the model of the complete rotor bar.
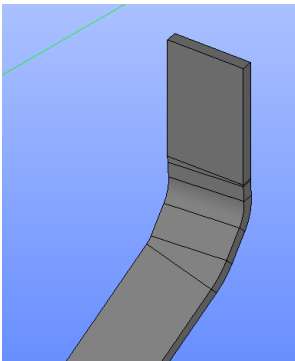
Figure 5.14 – View of a detail of the model of the complete stator bar.
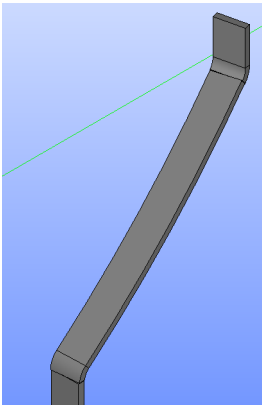
Figure 5.15 – View of a detail of the model of the complete rotor bar.

cross-section with a constant current density. The last step is to define if one should take the circulating currents of neighbouring bars into account or use a constant current density for the neighbouring bars.

5.5.2 Influences of the winding approximation on the magnetic field and vector potential

This subsection is dedicated to an original study of the impact of the winding approximation (strand bar or green bar) on the magnetic field and vector potential. In addition, the impact of the circulating currents to the DC-current is also highlighted.

In all figures presenting the impact of the strand bar approximation (with or without circulating currents) and the green bar approximation the source bar is depicted with its calculated circulating current, so that one keeps in mind the real physics while it is very easy to keep in mind the constant current approximation (strand or green bar). As the pictures have the circulating currents drawn, it makes it more easy to appreciate the impact of the used approximation on the results. The DC-strand current is 51.4A for all simulations performed in this section, while the DC-green bar current is 3288.6A. One green bar has 64 strands.

Strand bar approximation or green bar approximation
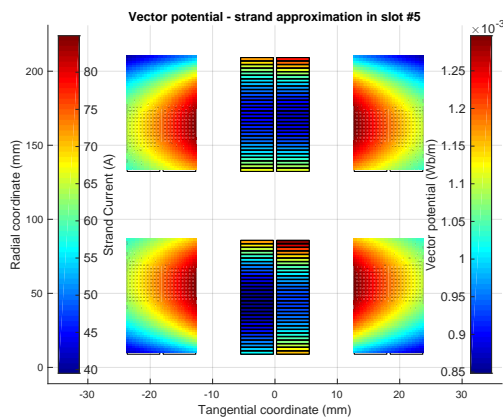
Figure 5.16 – Vector potential in the strand bar approximation (strands depicted with circulating currents, calculated with DC-strand current). The DC-strand current is 51.4A.
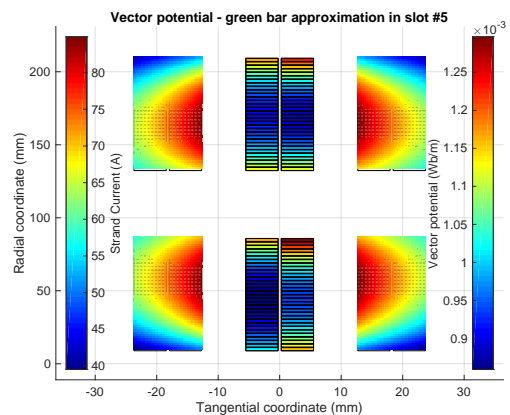
Figure 5.17 – Vector potential in the green bar approximation (strands depicted with circulating currents). The DC-bar current is 3288.6A.

To highlight the influence of the bar model used an analytical calculation is done to obtain the vector potential on the neighbouring bars using both approximations. The axial length of the model is 100mm and the results are plotted in the middle of the axial length. The distance between the green bar corresponds to real values taken from an assembled DFIG. Figures 5.16 and 5.17 show the results. The vector potential is not influenced by the choice of the

approximation as figure 5.18 highlights. The maximal value of the vector potential difference is 1.2%, while the maximal value of the vector potential is 9e-4 Wb.
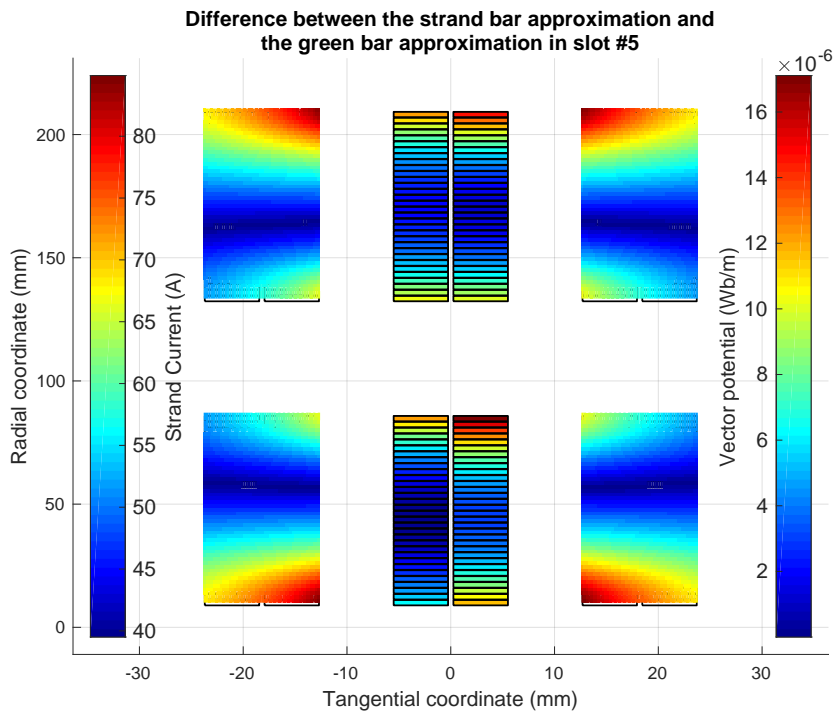
Figure 5.18 – Difference of the vector potential between the strand bar approximation and the green bar approximation (depicted with circulating currents, calculated with DC-strand current).

Figure 5.19 shows the amplitude of the magnetic field in the strand bar approximation. Its maximal value is around 16'200 A/m. The maximal value of the amplitude of the magnetic field is around 475 A/m or 3% of the maximal amplitude. This is higher than for the vector potential and one should think about taking the strand bar approximation into account for the forces calculation in the winding overhang. If an approximate result is wanted, then the green bar approximation is sufficient, while a strand bar approximation is much more suitable when a very precise result is required.

Strand bar approximation with or without circulating currents

The impact of taking into account the circulating currents in the strand approximation is studied in the same configuration as in section 5.5.2. The currents in the considered bar are one time the bar current divided by the number of strands and another time the circulating currents.

Figure 5.21 shows the obtained results, plotted in form of the difference between the vector potential calculated with and without circulating currents. The circulating currents have a significant impact on the vector potential of neighbouring bars as the difference accounts for
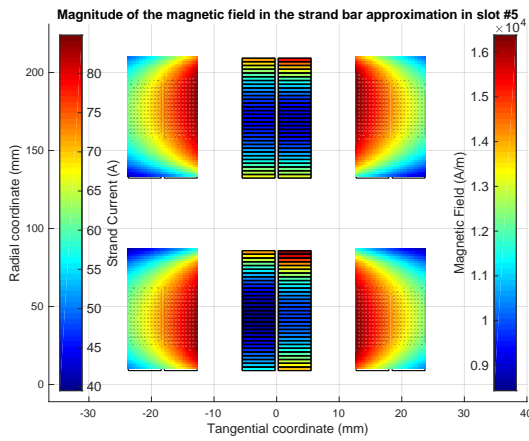
Figure 5.19 – Amplitude of the magnetic field in the strand bar approximation (depicted with circulating currents, but calculated with DC-strand current).
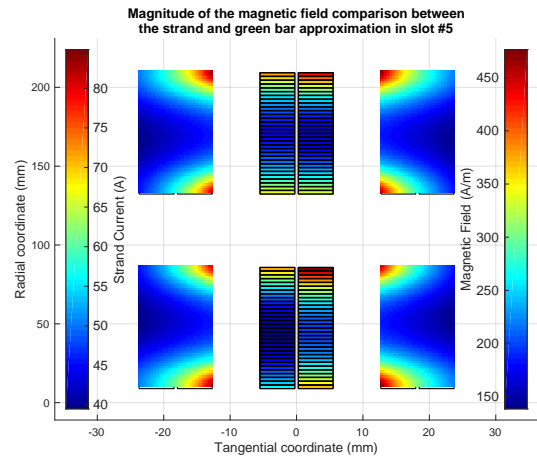
Figure 5.20 – Difference of the amplitude of the magnetic field between the strand bar approximation and the green bar approximation (depicted with circulating currents).
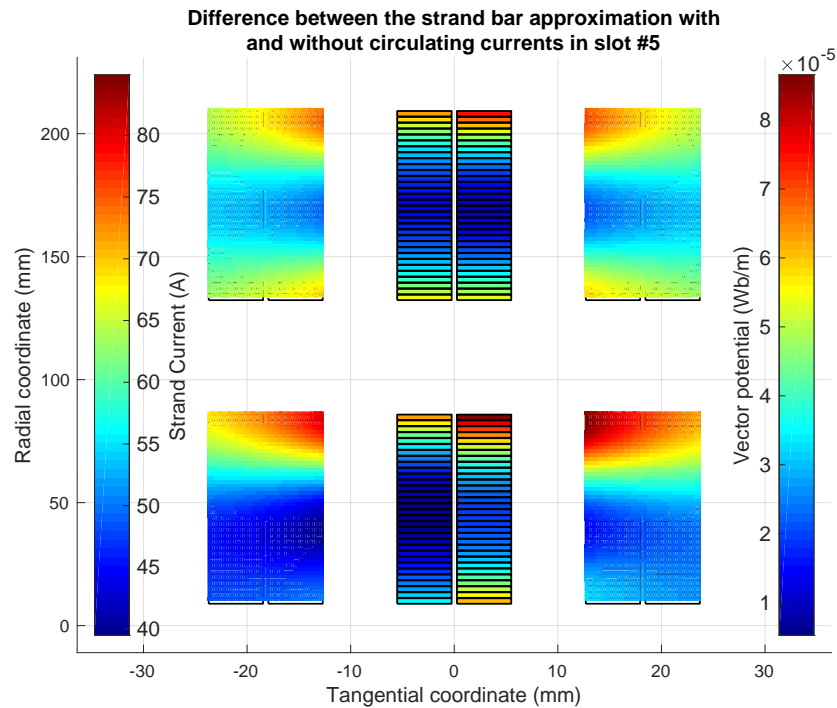
Figure 5.21 – Influence of the circulating currents on the vector potential in the strand bar approximation.

about half of the maximal amplitude of figure 5.16. In this work, this effect is not included in the circulating current calculation, but it will be object of further investigations.
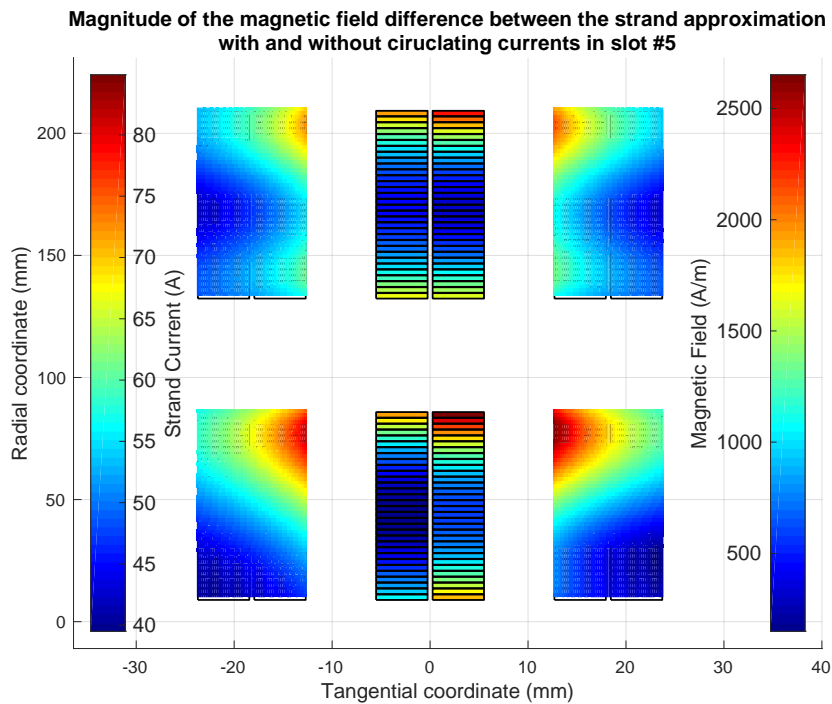
Figure 5.22 – Influence of the circulating currents on the magnetic field in the strand bar approximation.

As for the vector potential, in the case of the magnetic field the circulating currents have a significant influence on the magnetic field difference, which can account up to around 2'700 A/m or about 17% of the maximal amplitude of the magnetic field.

There is practically no significant difference between the strand approximation and the green bar approximation. Only the strand approximation with circulating currents has a significant impact on the results.

5.5.3 Iron

The iron can be modelled using two options. The first option is to model the iron using a mirror method (section 5.5.3), which can be used for the active part iron. This option has the drawback of implying a constant permeability of the iron over the complete mirror plane. The mirror method could also be used to model the rotor overhang iron, but the mathematical equation would be very complicated in this case. The second option is the use of saturable iron discretised in elements as described in section 5.2 using the equations presented in section 5.3 to calculate the magnetisation for a saturable iron. The second option has the advantage of a very precise modelling of the iron in the active part (last stack) and in the rotor overhang.

The drawback lies in the heavy calculation of the G-Matrix and the non-linear solving process as well as in the analytical calculation of the magnetised bodies to be carried out over all poles to obtain the total contribution of the iron to the magnetic field. In this study, the mirroring is used in some cases, but mainly the discretised saturable iron is used.

Rotor overhang

The rotor overhang is modelled as shown in figure 5.23 pastel red colored based on the same model defined in [45]. The rotor overhang is composed of five annular saturable iron regions spaced by ventilation ducts. The model spans over one pole and its discretisation is a compromise between calculation time and precision of the calculation.
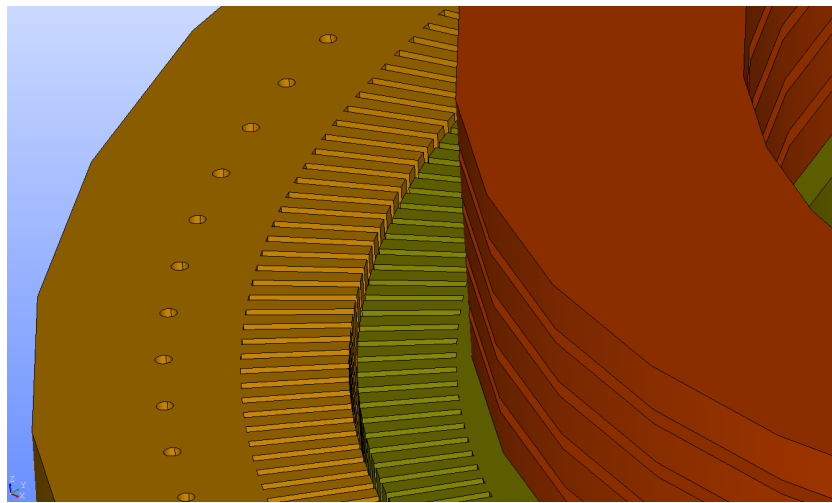
Figure 5.23 – Model of the rotor overhang and active parts.

Iron of the active part

The iron of the active part is modelled taking only the last iron stack into account, which is an original contribution of this work. Two dimensional finite-element calculation have shown that the magnetic flux is quasi null in the ventilation ducts also when the main flux is over 1T, so that the main flux is constrained in a plane perpendicular to the machine axis in the active part (including the last stack). In the last stack, there could be some axial flux entering or leaving the last stack due to its contact with the overhang. This effect is very small as the amplitude of the main flux is significantly higher than the axial flux and that the saturation is a function of the amplitude of the magnetic flux and not of its components. Therefore, there could be some axial component in the magnetisation of the last stack, but not in the other stacks. So only the last stack must be considered in the winding overhang calculation. The roebel bar ends at the same axial level as the last stack, to produce the main magnetic field. This is possible as a straight bar has a magnetic field exclusively in the perpendicular plane to its carried current. With this trick, one can produce the main field without any external

or additional field sources. Figure 5.23 depicts the complete iron model of the calculated machine. The ventilation ducts are not shown in this figure. The hole for the stator clamping bolts are not considered, but are drawn to have a familiar view of the electrical machine, while the slots and core are fully considered in the calculation model. The stator is shaded in yellow in the figure, while the rotor core is coloured in pastel green.

Mirroring the active parts

In the case where one would like to have a fast calculation with lower precision, neglecting the impact of the air-gap, slots and local saturation on the magnetic field in the winding overhang, then the "mirror"-method can be used to model the active part of the electrical machine. This method was originally proposed by [72] and [24]. This method is today widely used for the winding overhang field calculation when fast calculation are required. Its main advantage lies in the linearity of the calculated solution leading to a big optimisation potential of the calculation time. Some authors like [68] or [77] or [45] among others add an air-gap conductor, which is originally introduced by [24] to take the effect of the air-gap (magnetic potential difference) into account, in their model. They use this conductor to keep the relation $\underline{\nabla} \cdot \underline{j} = 0$ valid in all the space. This air-gap conductor enables to tackle the main-drawback of the solution proposed by [24] in the case of an infinite boundary, namely the fact that some conductors have a semi-infinite length. without air-gap conductor or semi-infinite conductor, then the real current and the mirror current "face each other" at the interface provoking a "current-step" of $2I$ at the mirror-plane, when considering an infinite permeability boundary plane. The artificial conductor which lies in the mirror plane carries this $2I$-current so that the sum of all currents is also zero at the symmetry plane. In this work, the fringing effect of the air-gap and the magnetic potential difference is not taken into account when working with the mirror method as these effects are fully taken into account using magnetisable elements.

The solution of the semi-infinite conductors has one drawback, which is also mentioned by its author in [24], namely the fact that in the case of an infinite boundary the magnetic field line are not perpendicular to the boundary[2] but one should respect another condition, namely $\oint \vec{H} \cdot \vec{dl} = I$, but only for partly embedded circuits. When the circuits are not embedded in the iron, then the image method can be directly applied. The problem is how to take the conductor getting out of the active part of the electrical machine into account. In this context, the solution is to use semi-infinite conductors that crosses the boundary plane.

Starting from the consideration that for a zero permeability the mirror conductor is in a such way that the conductor and its mirror conductor generates a close-loop, I asked myself "what would happen if in the case of an infinite permeability I would just change the sign of the current?". This would imply that at the boundary the currents are not continuous, but this would theoretically produce the correct magnetic field at the boundary. To valid this

---

[2] "Before examining further the possibility of applying the image method ... Thus the tangential component of the field is not zero and the flux lines do not enter the iron at right angles, however large the permeability. (Extract of section 3.1 of [24]"

novel hypothesis, a 3D-finite-element calculation has been carried out: one with a boundary condition with μ=0 and another with μ=inf. For both cases, the simulated magnetic field is compared to the calculated magnetic field using the mirror method without any additional conductor. The criteria used to decide if this hypothesis would be true is based on the comparison of the mean error between the two cases. If the mean value of the error remains the same, then the demonstration of the hypothesis is successful, and one could think about leaving the additional conductor as well as the semi-infinite conductors.

But there must be a reduction of the space as one has to exclude the current step from the calculation domain, so that the current divergence is satisfied in the calculation domain. This condition is derived from the current condition used in finite-element calculations. In the case of electrical machines the reduction of space is defined as the winding overhang without its mirrored components which is more than enough for all calculation purposes.

The 3-dimensional simulation is realised using a vector potential formulation, so that the precision of the results is diminished even with a coarser meshing, taking into account the limited memory of the computer that could be used for this calculation.
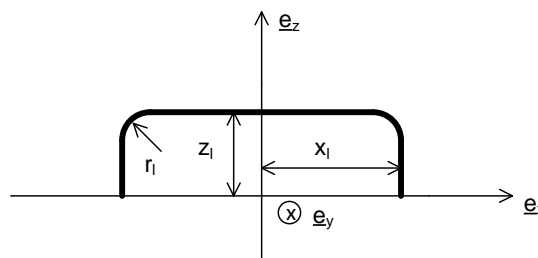
Figure 5.24 – Schematic representation of the coil used to demonstrate the mirror-weak condition. $x_l = 0.5m$, $z_l = 0.35m$, $r_l = 0.15m$. The coil has a square base of 0.01m.

The used coil for this demonstration is shown in figure 5.24. The dimensions of this coil can be found in the caption of the figure. The comparison is done by comparing the mean value of the difference between the analytical magnetic field value and its numerical counter-part over a grid of points. This grid spans from $x = -1$ to $x = 1$ with steps of 0.1m along the x-axis and from $y = -1$ to $y = 1$ with steps of 0.1m along the y-axis. Three axial positions ($z = 0$, $z = 0.05$, $z = 0.15$) are also used for this demonstration.

Table 5.3 shows the results obtained. The maximal respectively minimal value of the mean value of the difference is similar for the same z-coordinate. The extremal values are a function of the z-coordinate because the mesh gets sparser for increasing z-components. There is no significative difference on the mean value of the difference of magnetic field so that the hypothesis can be considered as correct. This hypothesis will be used in this work. To make that demonstration even more strong, one could redo the simulations with a coarser mesh to obtain an even lower error.

Nevertheless, it seems that as long as the calculation model is a cut of the complete model,

Table 5.3 – Comparison between the analytical calculation (mirror without artificial conductor) and 3D-finite-element calculation (mean value of the difference of magnetic field components (maximal value over all components) expressed in A/m) depicted in figure 5.24.

Z-coordinate of the grid	First quadrant	Second quadrant	Third quadrant	Fourth quadrant	FE Average
$z = 0, \mu = 0^a$	5.4857	5.0638	-4.6180	-5.4011	138.532
$z = 0, \mu = \inf^b$	-8.3319	-7.2226	10.0160	7.2829	147.424
$z = 0.05, \mu = 0^c$	11.0442	0.9581	-8.5747	-0.4893	137.712
$z = 0.05, \mu = \inf^c$	18.6678	24.2959	21.8135	22.7113	134.316
$z = 0.15, \mu = 0^c$	-35.1426	-48.3476	48.4739	37.6440	130.846
$z = 0.15, \mu = \inf^c$	15.0706	-11.2051	-29.8824	32.4947	164.503

[a]The mean value with the highest deviation between the x- and y-component is shown only.

[b]The mean value of the z-component is shown only.

[c]The mean value with the highest deviation between the x-, y- and z-component is shown only.

there will be some trade-offs to be made as it seems that all conditions can't be met at the same time. To remove these trade-offs, the only solution is to use a complete model of the electrical machine, taking at the same time the complete geometry of the electrical machine into account. This would be possible using the 3D-model used in the winding overhang that could be extended to the active part of the machine. Another option would be to couple the 3D overhang calculation with a 2D-finite element computation for the active part. Both options, will be studied at a later stage as they are out of scope of this study.

5.6 Complete model

The following figures present the complete model starting with the complete model for the stator, then the rotor and finally the complete electrical machine.

Figure 5.25 shows the complete 3-dimensional stator model. The stator core is drawn in yellow, while the stator bars are shaded in blue. Dark blue stands for the top bar and light blue for the bottom bar.

The complete 3-dimensional rotor model is depicted in figure 5.26. The rotor bars are colored in green, with the same color shaded as for the stator bars. The rotor core is pastel green coloured while the rotor overhang is coloured in pastel red.

Figure 5.27 shows the complete view of the DFIG modelled in this study.

5.7 Iterative calculation of the inductance and induced fluxes

One of the main goal of this work is to know and master the precision of the calculation. This goal must be also followed in the inductance respectively induced flux calculation. To
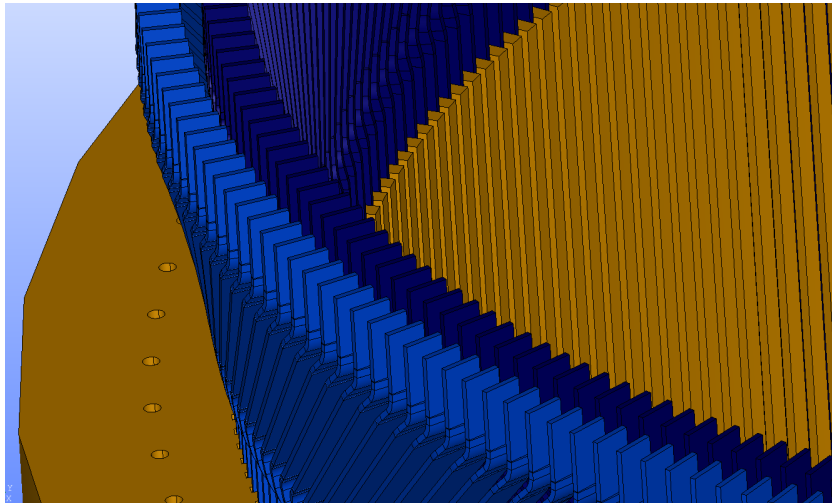
Figure 5.25 – Complete 3-dimensional model of the stator including the iron of the active part (full view and not only last stack).
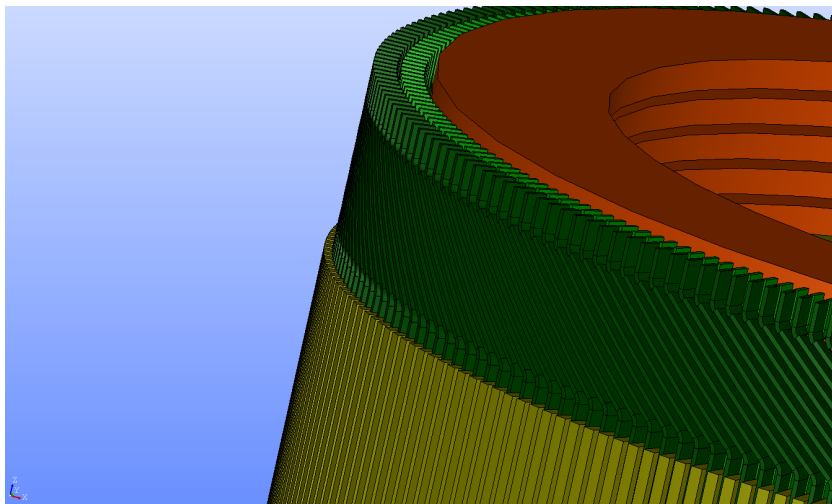
Figure 5.26 – Complete 3-dimensional model of the rotor including the iron of the active part (full view and not only last stack).
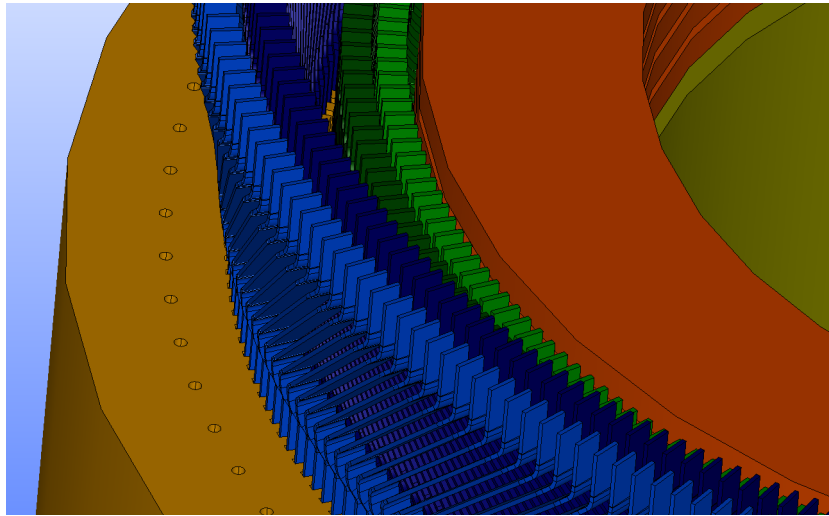
Figure 5.27 – Complete 3-dimensional model of the electrical machine (full view and not only last stack).

do so a novel iterative calculation algorithm was developed for the numerical integration of equation (4.25) to calculate the inductance or induced flux. Basically the order of the numerical quadrature and the number of integration intervals are increased until reaching the required relative error. Of course, this algorithm can be bypassed to make a direct calculation with given parameters, but in this case the error can not be monitored. Figure 5.28 shows the flow diagram of the algorithm. This algorithm can be seen as a brut-force variant of any three dimensional numerical integration algorithm. With the main difference that the integration is first performed over the surface perpendicular to $\underline{t}$ and then over the path $\mathrm{d}\underline{l}$.

5.8 Handling of the calculation singularities

The main drawback of the analytical calculation is the presence of singularities in the obtained equation. Their root cause is located in the presence of a $1/|\underline{r} - \underline{r}'|$-term in the integrand, depending on the integration limits, this term can become infinite as the distance $|\underline{r} - \underline{r}'|$ tends towards zero leading to an infinite value of the integral. Some of those singularities can have a strong physical background, but others are just a calculation artefact.

5.8.1 Filament approximation

In the case of the filament approximation, the singularity lies on the filament. The magnetic field is not defined on the filament. In some papers [68] or [77] for example, the authors use the following correction get rid of this singularity. The mathematical treatment is then to consider a filament with a radius $r_f > 0$ instead of radius which is equal to zero. The main disadvantage of this correction is the necessity to define a conductor radius. It can be defined arbitrarily, but then one could logically discuss about the numerical value considered or one
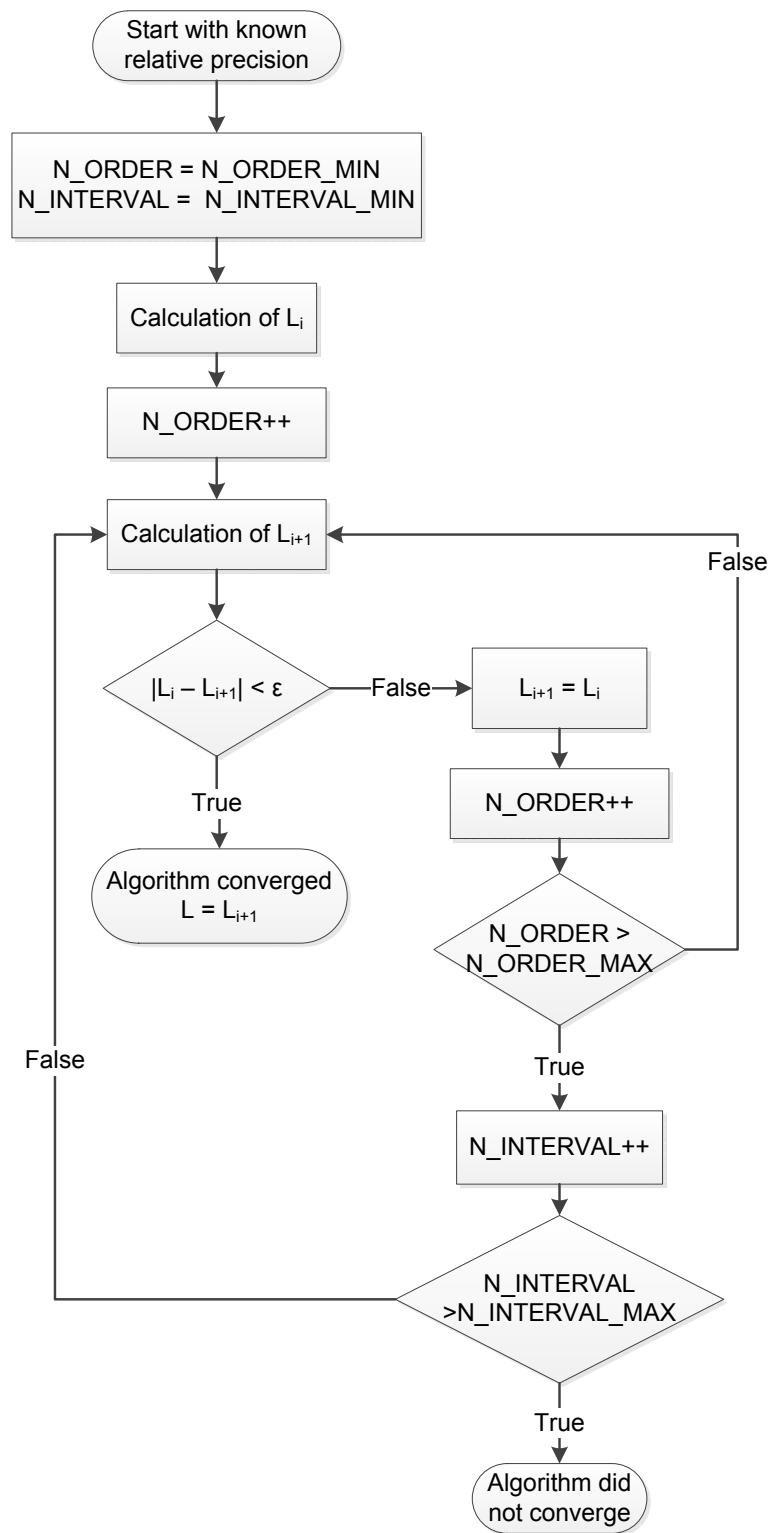
Figure 5.28 – Iterative algorithm to calculate the inductances and induced fluxes.

could also use the definition of the radius given by equation 4.46. Has it have been shown in section 4.5 the radius has a significant impact on the magnetic field in the near field zone, while its impact is reduced in the far field zone. A reduction of the radius leads to a reduction of the near field zone. It becomes evident that the ideal choice would be to have a zero radius conductor in order to limit the near field zone to its minima but will lead to a singularity on the filament. To overcome this, the magnetic field is set to zero on the filament, which tackles the infinite singularity without perturbing too much the filament effect (which can be mainly seen in big values near the filament). This choice does not induce any mathematical error in the field calculation as the magnetic field is zero in the center on a non zero radius conductor and keeping this strong filament effect keeps the user aware of the danger related to the use of this approximation. Practically, in the application of this work, the filament approximation is only used in the far field calculation, so that this singularity should never occur. Nevertheless, this topic must be treated to avoid numerical errors in the calculation software.

5.8.2 Rectangular approximation

The novel principle to analyse the singularities in the rectangular approximation is based on the following consideration. One can always divide the integration path in two or more integration paths. Taking the example of the surface singularity located at $x = x_2'$, this singularity occurs as the rectangle ends at $x = x_2'$. Let's consider now one rectangle spanning from x_1' to $2x_2'$, which can be divided in two rectangles spanning from x_1' to x_2' and from x_2' to $2x_2'$. As the magnetic field calculated at $x = x_2'$ must be the same for one rectangle and for two rectangles, by comparing the calculated equations, can be get rid of the singularities in the surfaces.
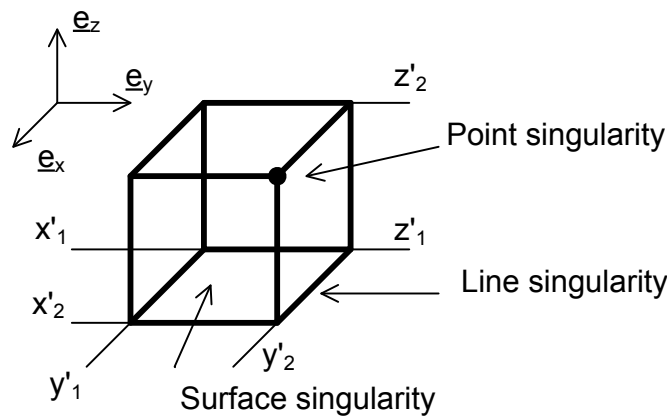
Figure 5.29 – Schematic representation of the singularities for a straight coil.

The same principle can be applied to the line singularity using one and four rectangles. For the point singularity, one and eight rectangles are needed, but the principle remains the same.

5.9 Validation of the 3-dimensional model

The validation of the 3-dimensional model is based on a comparison of the calculated results with 3-dimensional finite-element, as no published literature presented results that could be compared with a precision of 1e-9. The 3-dimensional finite-element simulations use the scalar approximation for the magnetic field, so that they have an impressive precision without a too coarse mesh. For the rectangular approximation a comparison with published literature ([44]) have been undertaken as the published results have sufficient precision.

The analytical calculation is considered as validated as the error is below 1e-6 T for all simulated cases.

5.9.1 Case of the round edges rectangular coil - 3D finite elements versus analytical calculation

The details of the comparison are shown in section A.5.4. The comparison shows very little discrepancies between the results coming from the analytical equations and the results form the numerical simulation. The analytical equations can therefore be considered as completely validated.

5.9.2 Comparison with [44]

[44] compared the analytical equations of [134] with a numerical quadrature. The results presented in this publication can be compared to the 3D finite element simulation and to the analytical equations developed in this work. [44] defines 23 points where the amplitude of the H-field is computed. These points are shown in figure 5.30 and in table 5.4.

In addition to the amplitude, the three components are also given in table 5.5 for the 3D finite element and the formulas of this work.

The H-field amplitude must be the same for all A_i, B_i, C_i, F_i, G_i, H_i, I_i by construction of the geometry. This is the case for both Urankar and This Work for all points except F_i and G_i, located at a line singularity. For all points, the difference between This Work and 3D FE is significantly lower than Urankar and 3D FE, transposing the excellent precision of the formulations developed in this work. It seems that the typographic errors have a significant impact on the precision of the numerical results. Unfortunately it was not possible to correct these errors. Once again, the very small difference between the 3D FE and This Work must be pointed out. The error is significantly higher for F_i and G_i, points located at a line singularity. For these points, the integral must be changed to take this singularity into account. For the results presented in tables 5.4 and 5.5, the change of the integrals has been done, to show the impact of this singularity on the error. The values coming from the finite volume (Fontana Fin. Vol.) and numerical evaluation of Urankar's equation (Fontatna N. Urankar) have the biggest difference to the 3D Finite Element simulation. The amplitude is different for every point in the
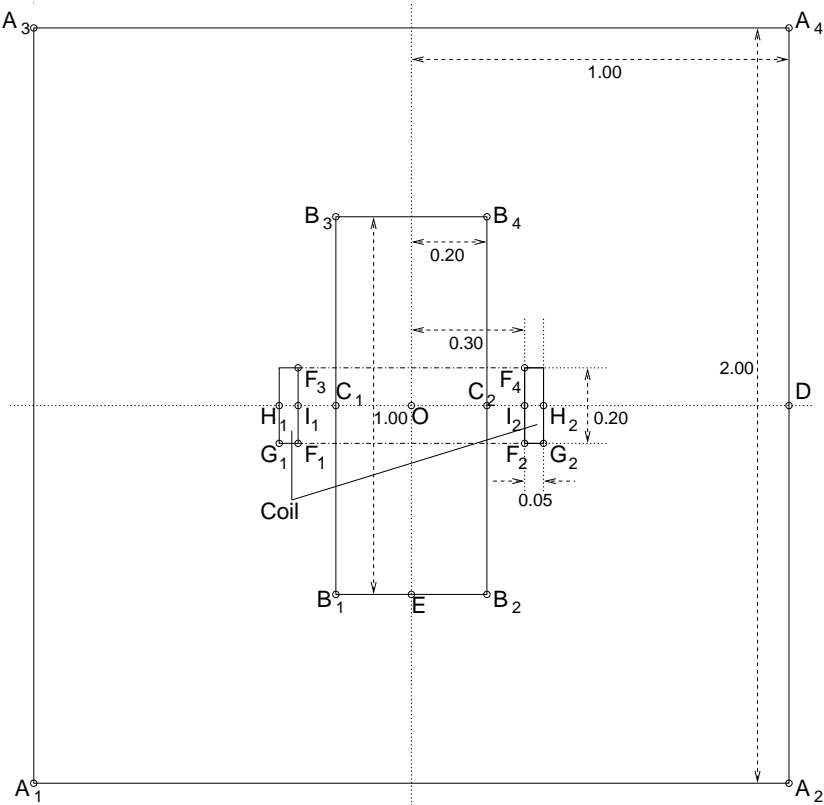
Figure 5.30 – Geometry and points considered for the comparison in [44], image copied from [44].

Table 5.4 – Comparison of [44], a 3D finite element computation and the formulas developed in this work (amplitude of H-field expressed in A/m).

Point	Fontana, Fin. Vol. 39078	Fontana, N. Urankar	Fontana, Urankar	3D FE, amp.	This work, amp.
A_1	0.0147455	0.0147471	0.0147479	0.014749272	0.014749273
A_2	0.0147434	0.0147577	0.0147479	0.014749272	0.014749273
A_3	0.0147433	0.0147577	0.0147479	0.014749272	0.014749273
A_4	0.0147453	0.0147471	0.0147479	0.014749272	0.014749273
B_1	0.227051	0.227081	0.227077	0.227065653	0.227065651
B_2	0.227041	0.227118	0.227077	0.227065653	0.227065651
B_3	0.227033	0.227118	0.227077	0.227065653	0.227065651
B_4	0.227038	0.227081	0.227077	0.227065653	0.227065651
C_1	1.94055	1.93924	1.9387	1.939178471	1.939178439
C_2	1.94027	1.94024	1.9387	1.939178471	1.939178439
D	0.0294561	0.0295239	0.0294932	0.02947806	0.029478052
E	0.257634	0.257673	0.257639	0.257641717	0.257641717
F_1	2.50891	2.56669	2.56669	2.556833886	2.565356046
F_2	2.51103	2.56381	2.56381	2.556833886	2.565356046
F_3	2.50699	2.56669	2.56669	2.556833886	2.565356046
F_4	2.50811	2.56381	2.56381	2.556833886	2.565356046
G_1	1.77891	1.82984	1.82984	1.817141741	1.828521794
G_2	1.77643	1.82685	1.82685	1.817141741	1.828521794
H_1	1.29946	1.36610	1.34769	1.364030783	1.364031179
H_2	1.29565	1.36135	1.34769	1.364030783	1.364031012
I_1	2.85931	2.93927	2.94681	2.9373836	2.93738354
I_2	2.85431	2.93520	2.94681	2.9373836	2.93738354
O	0.000000	0.000000	0.000000	1.472740124	1.472740124

finite volume calculation, while there are 2 series of distinct values in the numerical evaluation of Urankar's equation. The more volume elements considered, to more the numerical values tend to reach the values of the 3D finite element simulation. May be, the numerical integration of Urankar's equation is not done with a sufficient small integration step, so that a relevant error remains.

Table 5.5 – Comparison of a 3D finite element computation and the formulas developed in this work (components of H-field expressed in A/m).

Point	3D FE, x-comp.	This work, x-comp.	3D FE, y-comp.	This work, y-comp.	3D FE, z-comp.	This work, z-comp.
A_1	0.013802583	0.013802583	-1.69e-18	1.32e-18	0.005199013	0.005199015
A_2	-0.013802583	-0.013802583	0.0	3.53e-15	0.005199013	0.005199015
A_3	-0.013802583	-0.013802583	1.69e-18	-1.32e-18	0.005199013	0.005199015
A_4	0.013802583	0.013802583	0.0	3.54e-15	0.005199013	0.005199015
B_1	0.095321964	0.095321964	-1.17e-17	-8.79e-16	0.206088656	0.206088653
B_2	-0.095321964	-0.095321964	0	8.74e-16	0.206088656	0.206088653
B_3	-0.095321964	-0.095321964	1.17e-17	-8.90e-16	0.206088656	0.206088653
B_4	0.095321964	0.095321964	0	8.95e-16	0.206088656	0.206088653
C_1	0.0	4.42e-16	0.0	0.0	1.939178471	1.939178439
C_2	0.0	4.42e-16	0.0	0.0	1.939178471	1.939178439
D	0.0	-5.41e-32	0.0	-1.77e-15	-0.02947806	-0.029478052
E	0.0	-8.85e-16	0.0	-4.42e-16	0.257641717	0.257641717
F_1	1.822921448	1.834855538	-2.23e-16	-5.53e-17	1.792862771	1.792862738
F_2	-1.822921448	-1.834855538	0.0	4.21e-17	1.792862771	1.792862738
F_3	-1.822921448	-1.834855538	2.23e-16	5.53e-17	1.792862771	1.792862738
F_4	1.822921448	1.834855538	0.0	-4.21e-17	1.792862771	1.792862738
G_1	1.729663763	1.741615621	-2.12e-16	-6.06e-17	-0.557016495	-0.55701614
G_2	-1.729663763	-1.741615621	0.0	6.32e-17	-0.557016495	-0.557016145
H_1	0.0	2.21e-16	0.0	-8.83e-16	-1.364030783	-1.364031179
H_2	0.0	2.21e-16	0.0	-8.83e-16	-1.364030783	-1.364031012
I_1	0.0	4.42e-16	0.0	8.83e-16	2.9373836	2.93738354
I_2	0.0	-4.42e-16	0.0	-8.83e-16	2.9373836	2.93738354
O	0.0	8.83e-16	0.0	-8.83e-16	1.472740124	1.472740124

Table 5.5 shows a more detailled comparison between This Work and 3D FE. The goal of this table is to show which component of the H-field is impacted by the line singularity. The x-component or r-component in cylindrical coordinates is the only component impacted by this singularity. So that, the correction can be reduced to this component only. This correction is presented and detailed in section 5.8.2, while the "corrected" results are presented in table 5.6.

5.9.3 Analytical comparisons - filament approximation

In this section, the analytical equations of the A-field and H-field in the filament approximation are validated against analytical formulas developed to calculate the force and the mutual

Table 5.6 – Comparison of a 3D finite element computation and the formulas developed in this work (components of H-field expressed in A/m), corrected line singularities.

Point	3D FE, x-comp.	This work, x-comp.	3D FE, y-comp.	This work, y-comp.	3D FE, z-comp.	This work, z-comp.
F_1	1.834855565	1.834855538	-2.23e-16	-5.53e-17	1.792862771	1.792862738
F_2	-1.834855565	-1.834855538	0.0	4.21e-17	1.792862771	1.792862738
F_3	-1.834855565	-1.834855538	2.23e-16	5.53e-17	1.792862771	1.792862738
F_4	1.834855565	1.834855538	0.0	-4.21e-17	1.792862771	1.792862738
G_1	1.741615634	1.741615621	-2.12e-16	-6.06e-17	-0.557016495	-0.55701614
G_2	-1.741615634	-1.741615621	0.0	6.32e-17	-0.557016495	-0.557016145

inductance between two coils.

Maxwell's filament

For the analytical equations of the arc-segments, the validation consists in a comparison of the force between two coils (H-field) and the calculation of the mutual inductance between the two coils (A-field). Two circular concentric coils are the geometry under study. These coils are named "Maxwell's Filament", as Maxwell was the first person to calculate the analytical equation for the force and mutual inductance for this geometry. Figure 5.31 depicts the two coils.
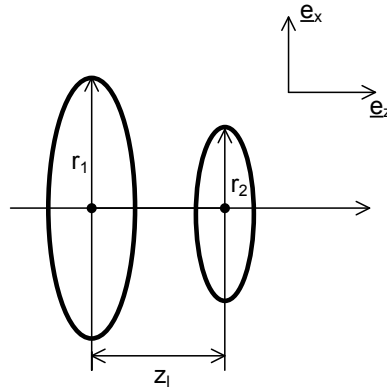
Figure 5.31 – Schematic representation of the Maxwell's filament.

The force between the two coils is given by

$$F = \frac{\mu_0 I_1 I_2}{4\sqrt{r_1 r_2}} \left(K - \frac{2 - k^2}{1 - k^2} E \right) \tag{5.131}$$

165

while their mutual inductance is

$$M_{12} = 2\frac{\mu_0 \sqrt{r_1 r_2}}{k}\left((1 - \frac{k^2}{2})K - E\right). \tag{5.132}$$

These equations can be found in many publications as for example [10]. The numerical application is done with the values given in table 5.7.

Table 5.7 – Parameter of the numerical application used in the Maxwell filament

Parameter	Value
I_1	1 (A)
I_2	1 (A)
r_1	0.159 (m)
r_2	0.1004 (m)
c	0.287 (m)

Table 5.8 presents the numerical values and in parenthesis the error obtained for the force and mutual inductance. The numerical values match perfectly with the numerical values of the analytical formulas enabling to validate the H-field and A-field without any restriction.

Table 5.8 – Parameter of the numerical application used in the Maxwell filament

Value according to formula	Value on ring 1	Value on ring 2
F = 9.899592416765108e-08 (N)	9.899592397141404e-08	9.899592415990960e-08
Error (N)	-1.962370462694097e-16	-7.741484091210280e-18
M_{12} = 1.290380456238827e-08 (H)	1.290380456238817e-08	1.290380456238842e-08
Error (H)	1.025703959565754e-22	1.455837878093329e-22

Let's divide each coil into four segments and calculate the partial inductance from each segment of the coil 2 with the segments of coil 1. The segments of coil 1 are numbered from zero to three, while the segments of coil 2 are numbered from four to seven. Table 5.9 shows the results obtained. The partial inductances can be negative, while their sum (L_{12}) is positive and coincides with the direct computed value with a difference of around 2e-14 (H).

Table 5.9 – Partial inductance calculation in the Maxwell filament

Partial inductance	Value
L_{04} (H)	0.0000000117065981883805670
L_{05} (H)	0.0000000141860770729464634
L_{06} (H)	-0.0000000092875949238944472
L_{07} (H)	-0.0000000035861519890040906
L_{14} (H)	0.0000000010456044131737193
L_{15} (H)	0.0000000074958069134304165
L_{16} (H)	0.0000000010211236756522245
L_{17} (H)	-0.0000000070323678744064226
L_{24} (H)	-0.0000000106003154917277127
L_{25} (H)	-0.0000000002781211388285067
L_{26} (H)	0.0000000135654672267528171
L_{27} (H)	0.0000000015632366311005598
L_{34} (H)	0.0000000012361345130846305
L_{35} (H)	-0.0000000059622742005056981
L_{36} (H)	-0.0000000018031553881225942
L_{37} (H)	0.0000000091736701442564911
L_{12} sum (H)	0.0000000129038045623888842
L_{12} direct (H)	0.00000001290380456238881719
Difference (H)	-1.923108665867620e-14

Rectangular coil

The validation of the analytical calculation of the vector potential is done by calculating the inductance of two ticks rectangular annular current carrying conductors spanning over an angle of 2π once using the results of the publication [9] and once using the formulas developed in this work. The tick coils have an internal radius of 0.5m and an external radius of 1.5m and spans over an axial length of 1m and are separated by 1mm. Table 5.10 shows the obtained results.

Table 5.10 – Comparison of the calculated inductance for a rectangular coil

Method	Value (H)
Publication [9]	0.5394560188988065e-6
Axisymmetric 2-dimensional FE	0.5394560188988065e-6
This work	0.5269494344586753838e-6
Numerical integration of equation 5.30	0.5269494344586753838e-6

Both methods don't show the exact same results, while it has not been found why these results differ.

5.9.4 Magnetised bodies in cartesian coordinates - comparison between 3D finite-elements and analytical formulas

The details of the comparison are shown in section A.5.5. The comparison shows very little discrepancies between the results coming from the analytical equations and the results from the numerical simulation. The analytical equations can therefore be considered as completely validated.

5.9.5 Magnetised bodies in cylindrical coordinates - comparison between 3D finite-elements and analytical formulas

The details of the comparison are shown in section A.5.6. The comparison shows very little discrepancies between the results coming from the analytical equations and the results from the numerical simulation. The analytical equations can therefore be considered as completely validated.

5.10 Moving mesh

As the calculation is not anymore depending on a mesh, except for the magnetised bodies, it is not anymore mandatory to rely on a mesh. The mesh can become the eyes, and one can do "special things" with it. Everybody knows the travelling of the camera in the movies. The moving mesh is nothing else than the application of a "travelling camera" to the 3-dimensional magnetic field calculation, which is also a novel contribution of this work.
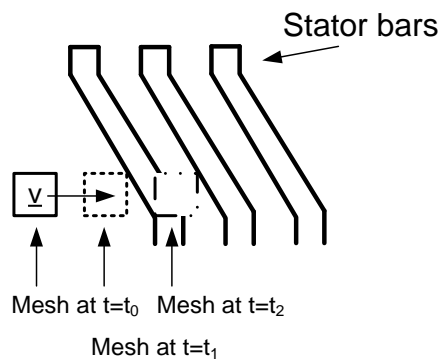
Figure 5.32 – Schematic representation of the moving mesh.

Figure 5.32 shows a schematic representation of the moving mesh. The mesh is moving with a speed $\underline{v}$, where the position at different time-steps t_0, t_1 and t_2 are depicted. The computation is carried out for the mesh and the magnetic field obtained is stored. Finally, the film is showed using the initial mesh at t_0, as the visualisation softwares use fixed meshes. Depending on the speed of the mesh, different types of phenomena can be studied. When the mesh is moving at the rotating field speed, then one can study the higher harmonics in the stator field or rotor harmonics. With this unique technique, the possibility of visualisation of the magnetic field is

completely changed and enhanced.

5.11   Original results of the 3D-model
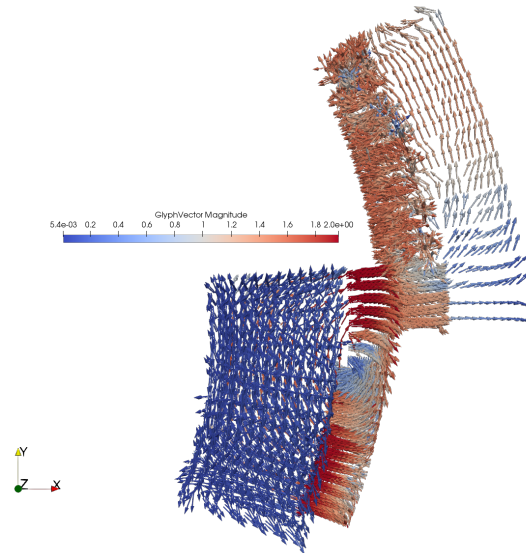
Figure 5.33 – 3D-Model magnetisation for a given time-step, view in the XY-plane.
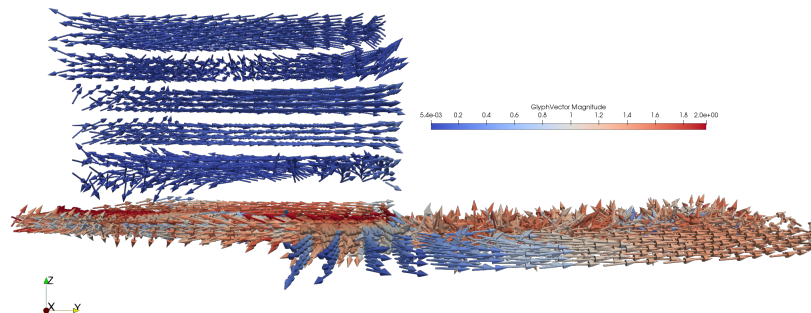
Figure 5.34 – 3D-Model magnetisation for a given time-step, view in the YZ-plane.

Figures 5.33 and 5.34 present some results of the 3D-Model. The amplitude of the vector is in tesla. The rotor overhang has a small magnetisation, compared to the active part. Its magnetisation is around 0.2 T, which will contribute to the induced voltage in the overhang of the windings. The magnetisation of the active part behaves very similarly to the one shown in figure 4.34. The rotor magnetisation is really good, while the stator magnetisation can be improved using a coarser mesh for the teeth, as one could see in the last teeths of the stator

core sheet.

5.12 Experimental validation of the 3D-model (current carrying conductors)

The experimental validation of the 3D-model is carried out over the current carrying conductors only. The laboratory equipment did not allow to perform any experimental validation for the magnetised bodies as well as the current carrying conductors with magnetised bodies. The experimental validation consists in a comparison between calculated and simulated circulating currents in two basic designs: straight circuit and rounded circuit which are depicted in figures 5.35 and 5.43. For both circuits, a comparison of the calculated currents with the inductance calculation presented in [68] is made to see if the novel approach is more or less precise than the actual used inductance calculation.

5.12.1 Straight circuit in air

Figure 5.35 shows the straight circuit designed and used. As this circuit is in air, the magnetic field as well as the inductances will be linear and small compared to the ohmic resistances leading to circulating currents governed by resistive effect more than inductive effect. It was not possible to find a suitable design to increase the inductance compared to the resistance of the circuit.

The current measurement is indirect and uses hall sensors to convert the magnetic field into a voltage, which is recorded using a precision time-recording device. To reduce measurement noise, all cables are twisted and shielded (refer to figure 5.36) and each hall sensor has its own DC-current source . 7 hall sensors are used, one per leg. As the circuit is linear and the distances are short, the magnetic field generated by the different legs can be measured by the hall sensor of another leg. To get rid of that perturbation, one need to perform a calibration measurement to obtain the transfer function (in fact a 7-by-7 matrix) between the current in each leg and the measured voltage in each hall sensor. To do so, only one of the 7 legs of the circuit is driven by a known current I. The 7 induced voltages are recorded and their amplitude is determined using curve fitting. This process is repeated 7 times per leg with a current spanning from 5A to 60A, covering the complete current measurement range. These steps enable to get a vector transposing the coupling between the leg i and the 7 hall sensors. Repeating the whole process for the 7 legs leads to a transfer matrix, which can be used to recalculate the current in each branch with a known voltage measurement. This calibration step is crucial and has a significant impact on the current measurement precision. It is fundamental to use the exact same circuit geometry between the calibration and the measurement. For example, if one replaces the amovible lower part of the circuit by a current clamp during the calibration step (refer to the right part of figure 5.37), then the computed currents will have an increased error of about 5% (tables 5.12 and 5.13 show the impact of
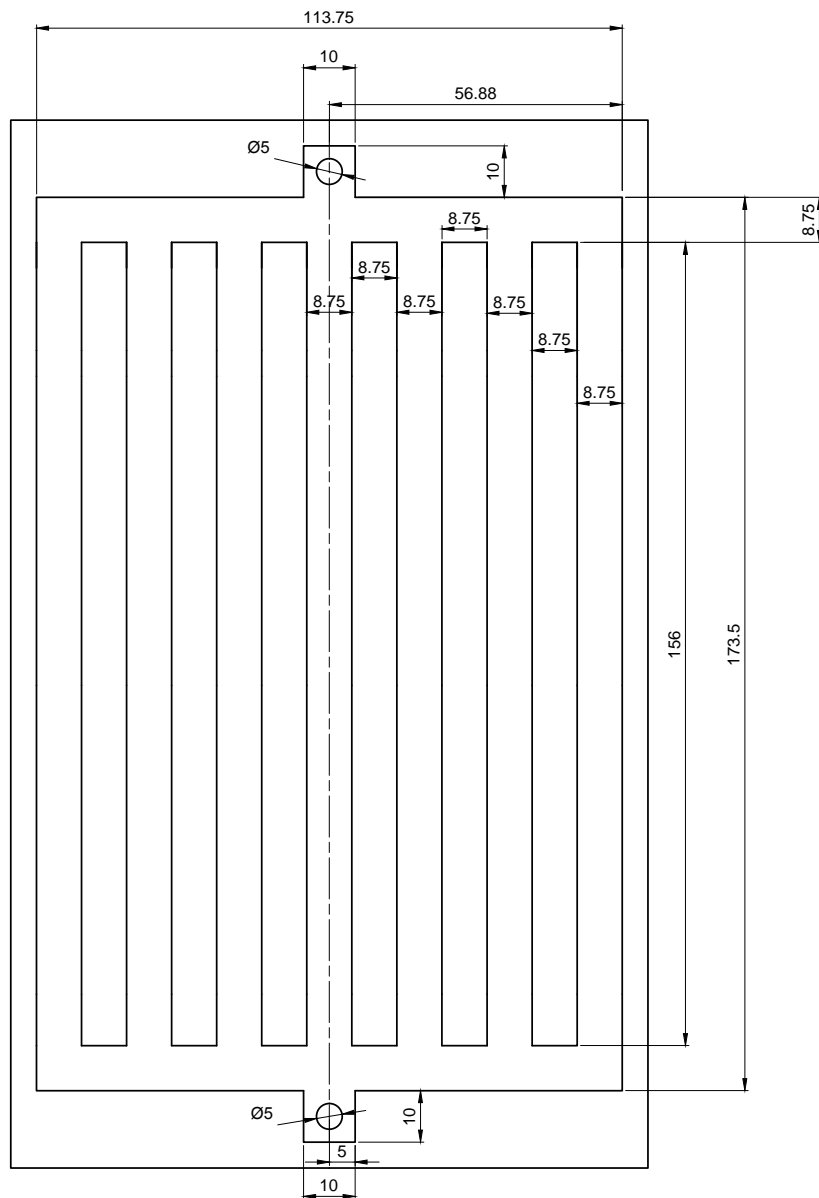
Figure 5.35 – Detail design of the straight circuit - dimensions in mm.

the calibration on the error in the case of moving the current feed). This huge error can be explained by the fact that the circuit is not perfectly in quadrature and that the hall sensors are also not perfectly in quadrature with its corresponding current leg (as it can be seen in figure 5.37), so that a coupling will remain and that the calibration must also take this "not wanted" coupling into consideration to obtain a high fidelity current computation.

Once the calibration is performed for the complete circuit, a cross-check measurement is performed. In this measurement, a current is injected in the symmetrical current legs to ensure that the current will be divided in two equal parts. A thermal camera is used to confirm that hypothesis. In all cases, no thermal divergence was observed, so that one can conclude that the current must be equal and that the error observed is a measurement error only. The results of this cross-check are presented in table 5.11.

Table 5.11 – Straight circuit: cross-check between the calculated current (from hall sensor) and the measured current (current sensor).

Parameter	M 1/7[a]	M 2/3	M 3/5	M 4
I_1[b] (A)	**33.844**	1.393	1.333	1.470
I_2 (A)	0.530	**31.794**	0.508	0.457
I_3 (A)	0.167	0.168	**30.144**	0.179
I_4 (A)	1.217	1.326	1.617	**57.623**
I_5 (A)	1.054	0.834	**30.152**	1.278
I_6 (A)	0.680	**31.357**	0.795	0.721
I_7 (A)	**30.6249**	0.228	0.084	0.042
I_{tot}[c] (A)	65.523	64.549	62.473	58.314
$I_{tot}/2$[d] (A)	32.762	32.274	31.237	58.314
ϵ_1[e] (%)	3.303	1.488	3.499	1.185
ϵ_2[f] (%)	6.525	2.841	3.472	-

[a]M stands for measurement and 1/7 means leg 1 with leg 7 and so one.

[b]The numbering of the legs starts from the left of figure 5.35.

[c]Sum of the current flowing in two legs.

[d]Sum of the current flowing in two legs dived by two, except for the last case as the current is flowing only in one leg.

[e]Error for the first leg with current.

[f]Error for the second leg with current.

The cross-check error is above the target of 1%, so that the model can't be validated using the wanted precision. The measurement precision is around 2.8% with an outliner for the hall sensor of leg number 7. The "threshold" current, in other words the minimal current that can be determined with this measurement method is around 1.5A. It was not possible to reduce this precision to 1%. The hall sensors have an intrinsic precision, which can be enhanced using calibration, but they also have a thermal draft as well as a thermal offset which can be removed using calibration. In addition, it is possible that the magnetic fields adds in such a way that they can't be subtracted anymore even using calibration. The measurement circuit design is not according to the specification recommended circuit design for the current level

in this experiment. In the specification, they recommend to use a current leg in the PCB with the sensor placed a few tens of millimetres above the current leg, while the straight circuit is made of raw copper and the sensor is mounted on a PCB leading to a distance of 1.5-2 millimetres between the copper and the sensor (refer also to the picture of the experiment - figure 5.37). All these effects reduce the measurement precision leading to a measurement precision of around 2%.

Figure 5.36 – Picture of the straight slot experiment.
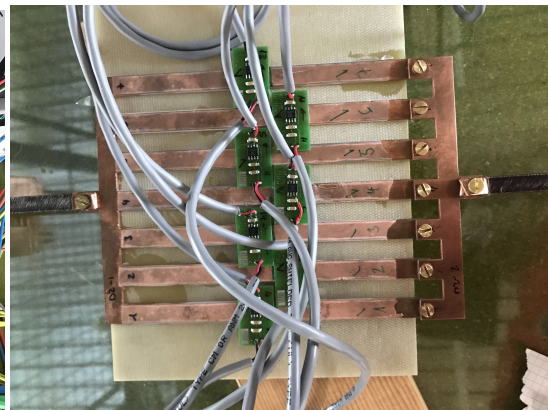
Figure 5.37 – Picture of the straight slot experiment (zoom on the hall sensors).

At a first glance, the computation model is composed by the green-highlighted elements in figure 5.38 and in the picture 5.39. Using this model and the equations developed in this chapter leads to the straight curves shown in figures 5.40 and 5.41.

As one can recognise easily the agreement between the measurements and the computation is not inside the 1% precision goal (the errors bars on the measured currents correspond to the measured errors presented in table 5.11). On another hand, the computational model is not complete as also highlighted in figure 5.38, which causes an unquantifiable but not negligible error. In other words, this measurement is nothing else than a short-circuit measurement where any piece of resistance and inductance will influence the result. It is therefore straight-forward to understand that even small "misses" in the model will have a significant impact on the calculated values. In addition to that fact, one has also to note that the T-crossings (refer to the "T" in figure 5.38) can't be modelled using lumped element circuit so that a very small precision can't be achieved with the used theory. To highlight the impact of the missed parts the corner resistance (marked with "R" in figure 5.38) as well as an additional resistance for the T-crossing was added to the computational model (dotted lines in figures 5.40 and 5.41). The precision increases as expected, but as the model is still not complete the requested precision is not achieved at any rate 6 of 7 currents are inside the measurement precision, which is a very good result.

The location of the current feeding was also changed using current clamps to highlight this "model miss effect". The results of these measurements are shown in table 5.12. The error depends on the location of the current clamping and spans from 0.1% to 39.445% with an
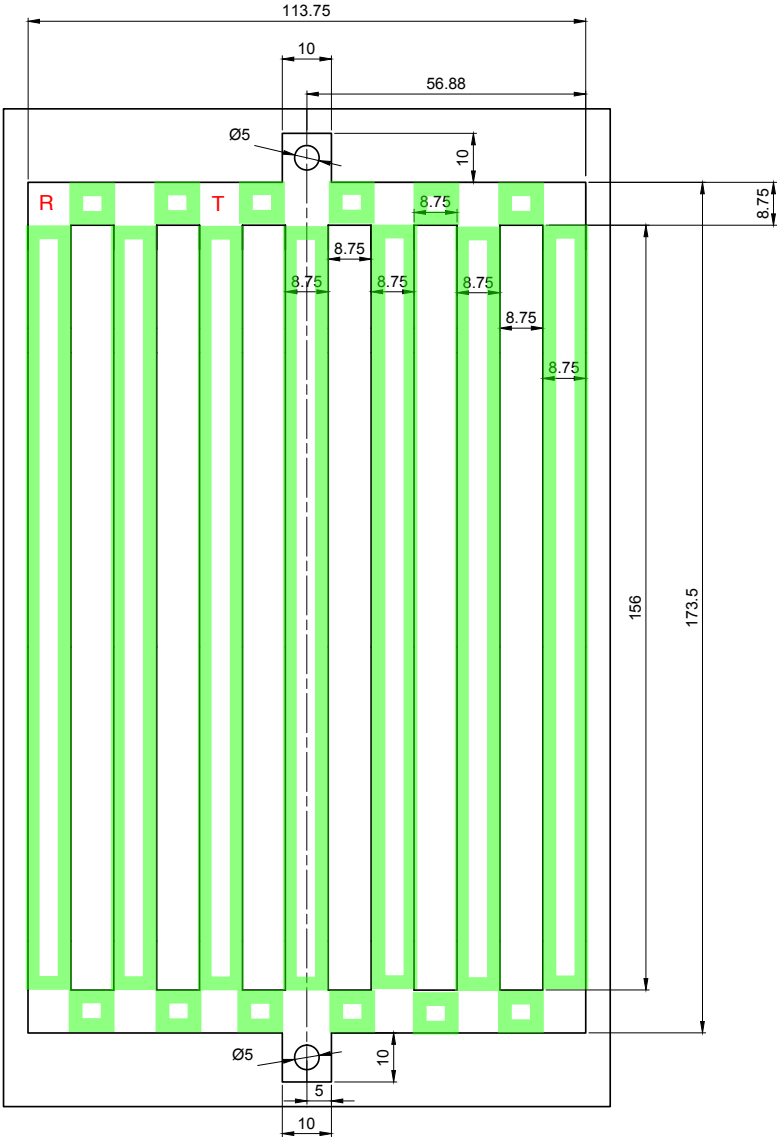
Figure 5.38 – Detail design of the straight circuit - dimensions in mm, parts highlighted in green are part of the computational model.
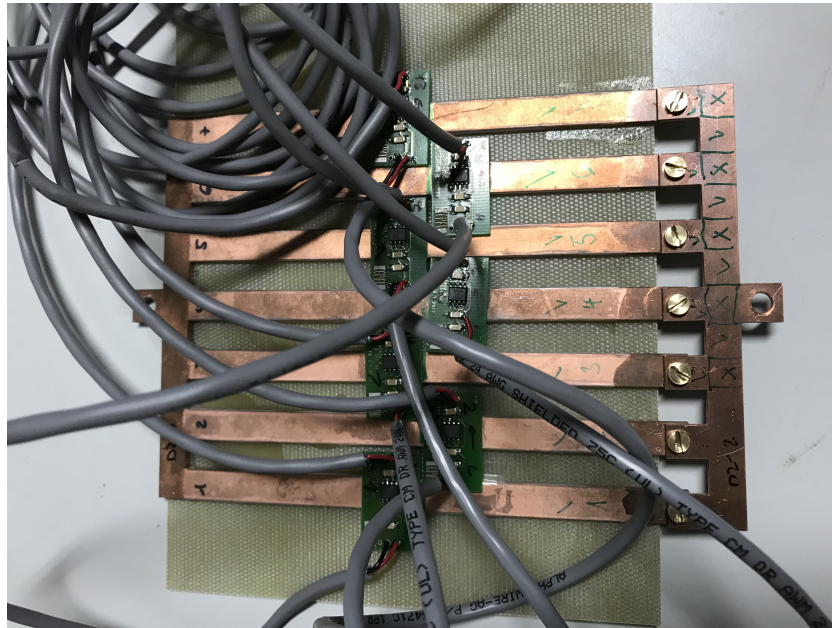
Figure 5.39 – Picture of the straight circuit - "v" stands for "in the model" and "x" stands for not in the model.
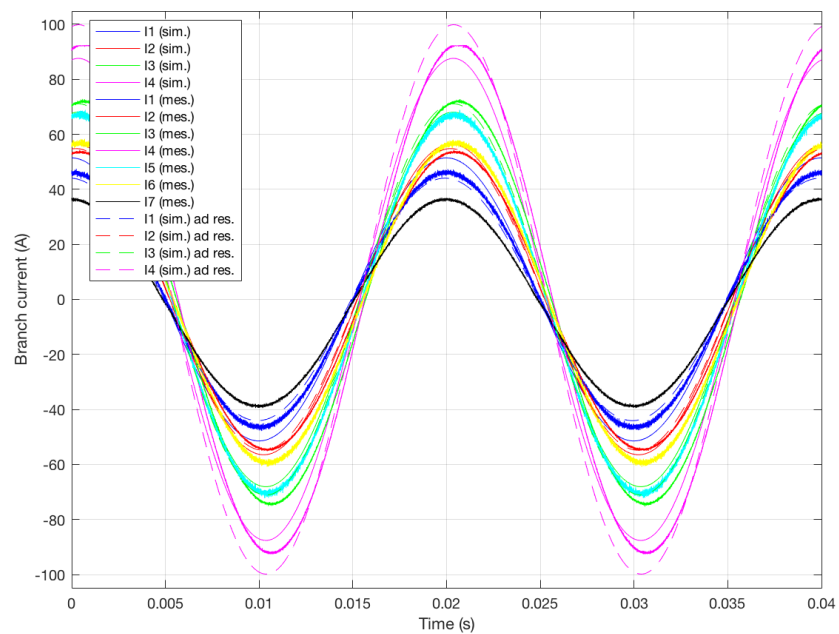
Figure 5.40 – Straight circuit - Time series of branch current, due to symmetry reasons only the different simulated currents are plotted (for example I1=I7 and so on).
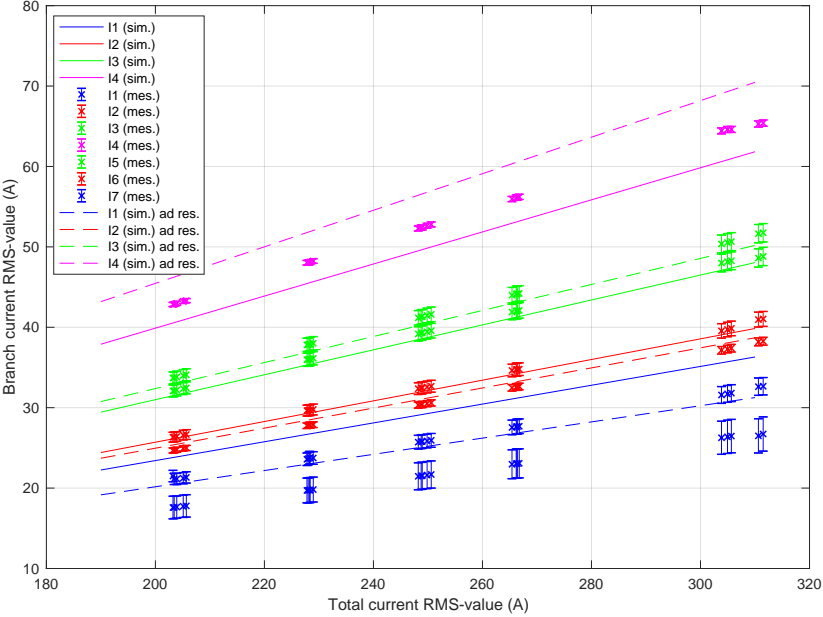
Figure 5.41 – Straight circuit - Branch current vs Total current, due to symmetry reasons only the different simulated currents are plotted (for example I1=I7 and so on).

average at 7.397% and a median at 4.954%.

Table 5.12 – Straight circuit: impact of the current feeding location on the error.

Para-meter	Case 2 (sim.)	Case 2 (mes.)	Case 2 (eps.)	Case 3 (sim.)	Case 3 (mes.)	Case 3 (eps.)	Case 4 (sim.)	Case 4 (mes.)	Case 4 (eps.)	Case 5 (sim.)	Case 5 (mes.)	Case 5 (eps.)	Case 6 (sim.)	Case 6 (mes.)	Case 6 (eps.)
I_1[a] (A)	13.357	14.157	**5.987**	9.106	10.356	**13.724**	6.276	7.358	**17.234**	4.562	5.282	**15.777**	3.643	4.424	**21.426**
I_2 (A)	16.81	16.042	**4.572**	11.405	11.515	**0.959**	7.809	7.741	**0.863**	5.608	5.283	**5.781**	4.43	4.115	**7.122**
I_3 (A)	11.296	11.407	**0.977**	14.864	14.133	**4.915**	10.128	10.474	**3.413**	7.211	7.162	**0.686**	5.652	5.631	**0.359**
I_4 (A)	7.759	8.227	**6.026**	10.183	10.687	**4.953**	14.221	13.827	**2.771**	10.075	10.695	**6.158**	7.856	8.534	**8.632**
I_5 (A)	5.581	5.304	**4.954**	7.289	7.114	**2.39**	10.129	10.283	**1.512**	14.709	13.998	**4.835**	11.436	11.418	**0.161**
I_6 (A)	4.375	4.369	**0.133**	5.668	5.59	**1.381**	7.815	8.326	**6.537**	11.286	12.423	**10.067**	17.018	16.946	**0.42**
I_7 (A)	3.605	2.183	**39.445**	4.613	3.258	**29.362**	6.287	5.603	**10.873**	9.014	8.405	**6.756**	13.518	12.471	**7.749**
I_{tot}[b] (A)	62.583	62.583		62.984	62.984		62.565	62.565		62.327	62.327		63.357	63.357	

[a]The numbering of the legs starts from the left of figure 5.35.

[b]Total current flowing in all legs.

Table 5.13 – Straight circuit: impact of the current feeding location on the error (calibration with current clamp instead of fixation device).

Para-meter	Case 2 (sim.)	Case 2 (mes.)	Case 2 (eps.)	Case 3 (sim.)	Case 3 (mes.)	Case 3 (eps.)	Case 4 (sim.)	Case 4 (mes.)	Case 4 (eps.)	Case 5 (sim.)	Case 5 (mes.)	Case 5 (eps.)	Case 6 (sim.)	Case 6 (mes.)	Case 6 (eps.)
$I_1{}^a$ (A)	13.147	14.157	**7.678**	9.755	10.356	**6.154**	7.327	7.358	**0.419**	5.779	5.282	**8.603**	4.927	4.424	**10.201**
I_2 (A)	14.554	16.042	**10.222**	10.758	11.515	**7.038**	8.042	7.741	**3.742**	6.289	5.283	**15.983**	5.326	4.115	**22.747**
I_3 (A)	10.65	11.407	**7.105**	13.022	14.133	**8.537**	9.696	10.474	**8.019**	7.529	7.162	**4.872**	6.342	5.631	**11.207**
I_4 (A)	7.988	8.227	**2.983**	9.746	10.687	**9.658**	12.48	13.827	**10.796**	9.643	10.695	**10.915**	8.09	8.534	**5.492**
I_5 (A)	6.262	5.304	**15.288**	7.61	7.114	**6.507**	9.699	10.283	**6.019**	12.886	13.998	**8.628**	10.782	11.418	**5.891**
I_6 (A)	5.26	4.369	**16.933**	6.357	5.59	**12.073**	8.051	8.326	**3.404**	10.646	12.423	**16.682**	14.732	16.946	**15.033**
I_7 (A)	4.873	2.183	**55.207**	5.845	3.258	**44.254**	7.343	5.603	**23.694**	9.658	8.405	**12.973**	13.303	12.471	**6.256**
$I_{tot}{}^b$ (A)	62.583	62.583		62.984	62.984		62.565	62.565		62.327	62.327		63.357	63.357	

[a]The numbering of the legs starts from the left of figure 5.35.

[b]Total current flowing in all legs.
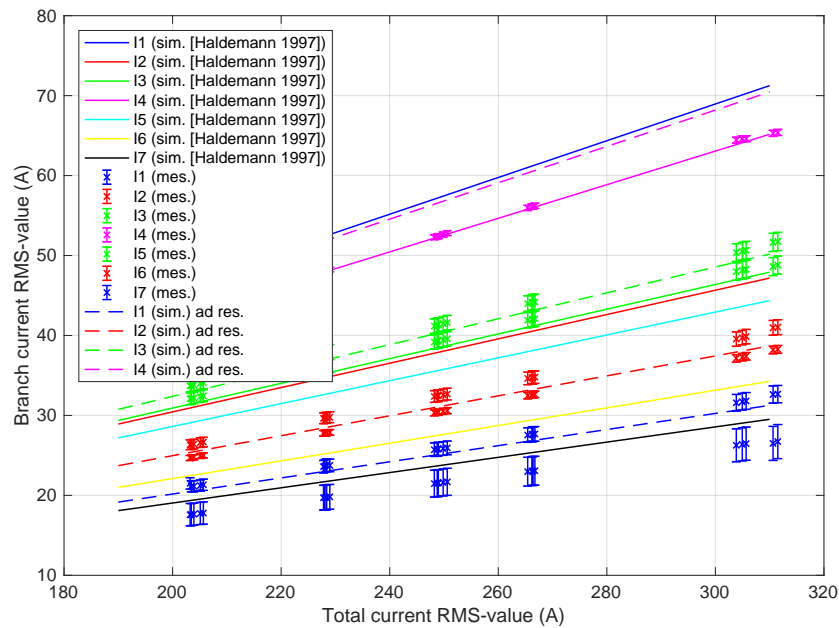
Figure 5.42 – Straight circuit - Branch current vs Total current comparison of [68] with this study.

Figure 5.42 presents a comparison of the calculated branch currents using the inductance calculation presented in [68] with this study. The currents computed with the model described in [68] present no symmetry. This is due to the fact that the distance with respect to the return conductor has no symmetry. 3 currents are in-line with the measurements, which is not bad. But in a global perpective, this gives less precise results than the model described in this work.

As a conclusion one can say that, the sensors even with calibration don't have the requested precision and it was not possible to find another sensor with a better precision, so that the postulated precision can't be achieved experimentally. To have a high fidelity agreement between the simulations and the measurements, the model must be complete or as complete as possible as the circulating currents are nothing else than short-circuit currents. Any piece of missing resistance and or inductance will impact the currents in a significant way. Increasing the completeness of the model could lead to a reduction of the error between measurements and simulations. The sensor of leg 7 seems to present some disfunction, but due to missing material it was not possible to exchange it, but as the current in leg 1 should be the same as the current in leg 7 this missing measurement don't represent a big issue. Using a lumped element equivalent circuit don't allow to model correctly the T-crossings so that an unquantifiable error will always remain. To reduce that effect, one should redesign the experiment to minimise geometrically the T-crossing effect, but this out of the timeframe of this study and would have led to other manufacturing, measurement and design issues. Adding additional resistances to the computational model produces the remarkable result that 6 of 7 calculated branch current lie inside the measurement precision, starting with only 4 with the "green" model

(refer to the green marked parts in figure 5.38). The skin effect and the proximity effect may also impact the measurement, this effect could not be quantified. In general, one has to say that this measurement is very sensitive to external effects.

To achieve the requested precision, one would need to find sensors with a much better precision and use an even more enhanced model, but the requested precision seems to be achievable.

5.12.2 Rounded circuit in air

The principle of the circuit as well as the calibration and measurement process is the same as explained in section 5.12.1, excepted that there was no measurement with displaced current feeding as this what constructively not possible to feed the circuit (even with current clamps) from somewhere else. Figure 5.43 presents the design of the circuit used for this experiment. The arc part is not very long due to manufacturing constraints (maximal size of the copper plate and water-cutting capabilities).

Table 5.14 – Rounded circuit: cross-check between the calculated current (from hall sensor) and the measured current (current sensor).

Parameter	M1 1/6[a]	M2 1/6	M1 2/5	M2 2/5	M1 3/4	M2 3/4
I_1[b] (A)	**32.493**	**32.65**	1.427	1.367	1.123	1.274
I_2 (A)	1.157	1.146	**28.764**	**28.783**	1.263	1.373
I_3 (A)	1.544	1.548	1.45	1.49	**30.813**	**30.784**
I_4 (A)	1.916	1.801	2.01	1.933	**30.565**	**30.607**
I_5 (A)	2.283	2.016	**30.789**	**30.54**	1.983	1.862
I_6 (A)	**29.549**	**29.832**	2.522	2.418	2.516	2.425
I_{tot}[c] (A)	63.546	63.775	61.189	61.194	62.396	62.425
$I_{tot}/2$[d] (A)	31.773	31.887	30.594	30.597	31.198	31.212
ϵ_1[e] (%)	2.265	2.391	5.984	5.929	1.234	1.372
ϵ_2[f] (%)	7.001	6.446	0.636	0.186	2.028	1.941

[a]Mi stands for measurement i and 1/6 means leg 1 with leg 6 and so one.

[b]The numbering of the legs starts from the left of figure 5.35.

[c]Sum of the current flowing in two legs.

[d]Sum of the current flowing in two legs dived by two, except for the last case as the current is flowing only in one leg.

[e]Error for the first leg with current.

[f]Error for the second leg with current.

Analysing the cross-check errors, one can say that there are two outliers with a significant error difference. The precision is 3.118% with all results and 1.507% without outliers. As in the case of the straight circuit, it is not correct to simply remove the outliers as this error only appears if there is a current in more than one current leg. When the hall sensor is again in the calibration case, then the error is below 1% for all sensors for the straight as well as the round conductor experiment. The root cause of this effect could not be determined.
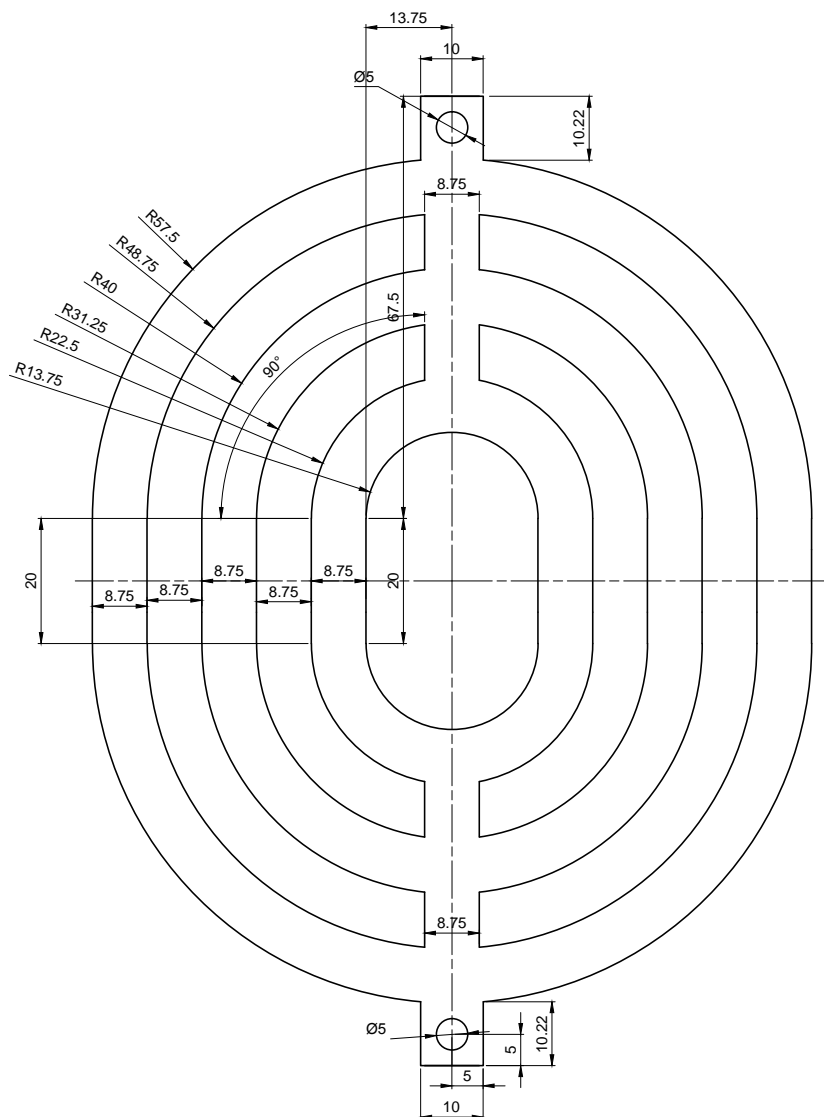
Figure 5.43 – Detail design of the rounded circuit - dimensions in mm.
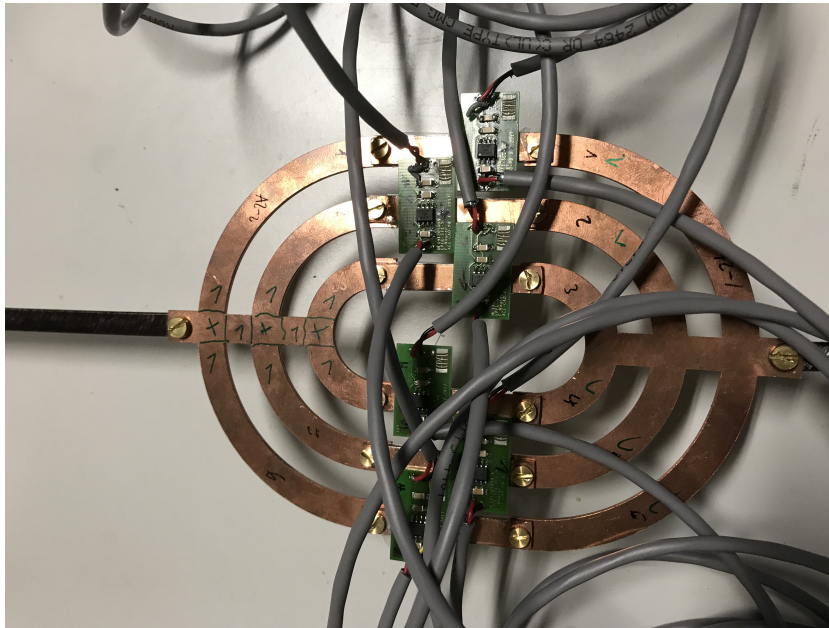
Figure 5.44 – Picture of the rounded circuit - "v" stands for "in the model" and "x" stands for not in the model.

As in the case of the straight conductor experiment, the rounded conductor experiment has also missing parts in its computational model, which are shown in picture 5.44. In addition, this circuit has not only T-crossings but also X-crossings which can both not be modelled using lumped elements. The impact is estimated to be the same as for the straight circuit, namely an unquantifiable error.

Figures 5.45 and 5.46 show the results. Without any additional resistance, only 2 currents are inside the measurement tolerance (neglecting I6 due to its very large error). With the additional resistances, 4 currents are inside and the last two are "very close" to the measurement transposing the positive impact of the adding of additional elements into the model. The error is smaller than in the straight circuit experiment due also above the 1% target.
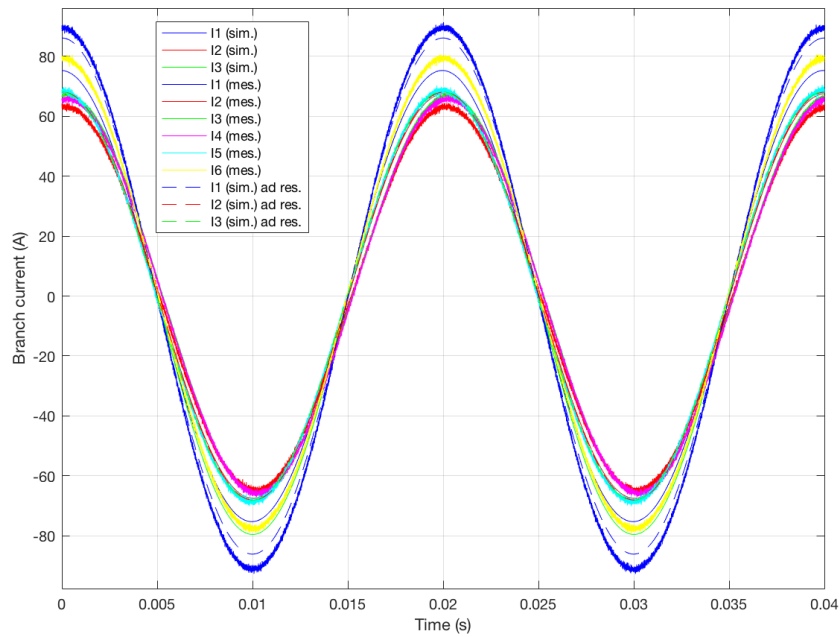
Figure 5.45 – Rounded circuit - Time series of branch current, due to symmetry reasons only the different simulated currents are plotted (for example I1=I6 and so on).
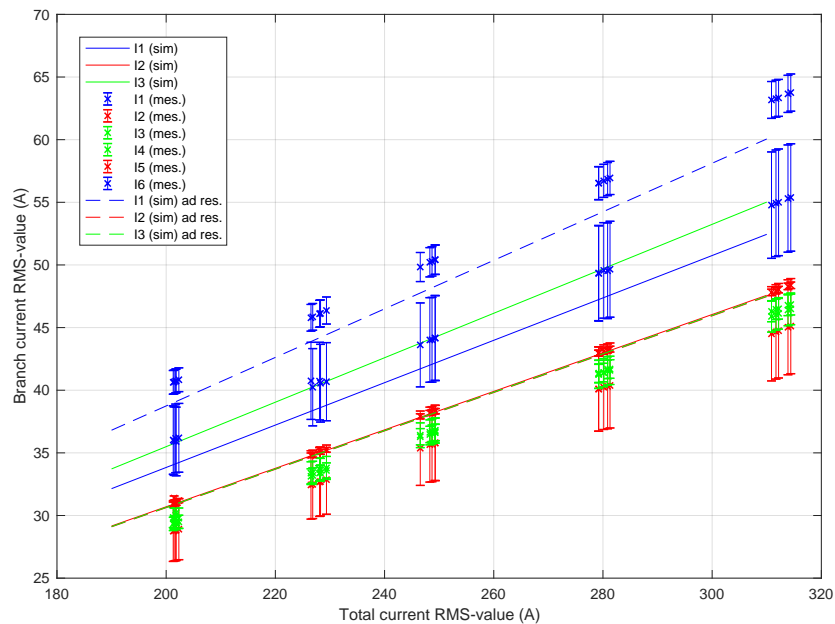
Figure 5.46 – Rounded circuit - Branch current vs Total current, due to symmetry reasons only the different simulated currents are plotted (for example I1=I6 and so on).

6 Transient calculation

The current and torques transients are a very important machine-related issue, as the maximal current and torques determine the mechanical design of a generator, which needs to withstand theses torques and current without any damages. From a more grid perspective, the phenomena occurring during a FRT[1] or LVRT[2] are much more relevant. In these cases, the grid owner normally requires that the machine can stay connected to the grid after such a transient phenomenon. The current and torque amplitudes of these phenomena are lower than for a short-circuit fault, so that they don't impact the mechanical design of the generator. The grid faults are normally simulated using numerical simulation softwares like SIMSEN, as the grid topology is different for every project.

[82] presents the complete equation set for an induction machine. The original contribution of this study lies in the transient equation for a double-fed induction machine, which can be derived using the work done in [82] and the exact analytical equation for the 2-phase short-circuit.

This chapter deals with transient analytical equations for the induction machine (IM) as well as for the double-fed induction motor-generator (DFIG), which are the base for the end-winding magnetic force and mechanical stress computation, as the winding overhang force is maximal during a severe transient like a short-circuit or false synchronisation. In addition, the analytical equations provide a frequency information, which is used to ensure that no mechanical eigenmodes can be triggered by a severe transient in the complete operating range of a DFIG. Starting with a literature review, the discussion is afterwards continued by the presentation of the novel developed analytical equations in section 6.2. These equations, validated in section 6.3, have been obtained to predict the short-circuit air-gap torque for a two-phase and three-phase short-circuit or faulty synchronisation. In a double-fed induction motor-generator a crow bar can be inserted in the rotor to limit the current passing through the VSI in case of major transients.

---

[1]Fault ride through, see: https://en.wikipedia.org/wiki/Low_voltage_ride_through
[2]Low voltage ride through, see: https://en.wikipedia.org/wiki/Low_voltage_ride_through

6.1 Introduction, constitutive assumptions

The numerical applications shown in this chapter are based on the following values of the parameters of the considered machine and equivalent diagram where the "'"-sign refers to a value referred to the stator.

6.1.1 Constitutive assumptions

The resistances are given assuming a constant and given temperature. To obtain analytical equations, the saturation is neglected, so that no inductance is a function of the current but the main inductance is recalculated for each operating point. This hypothesis is valid, as the main inductance has quasi no influence on the amplitude of the short-circuit torques and currents. These quantities are governed by the saturation of the stator and rotor leakage reactance, which can be integrated by reducing the leakage reactances by 10-20% depending on the initial saturation level of the machine. The machine is considered in steady-state conditions before the short-circuit with constant speed during the short-circuit. The VSI is modelled with a constant voltage source, so that its influence is neglected during the short-circuit. The VSI is assumed to continue to provide the same rotor voltage as before the transient. Which is not very realistic, as the semi-conductors can't handle easily this huge amount current flowing during the transients. In reality, there is a resistive crowbar going into operation, when the machine and or the VSI protection decides to fire the crowbar. This firing is done to limit the current in the VSI. But it will take from 5-10ms to fire the crowbar, implying that the first and most important current and torque peak will happen without the impact of the crowbar. In the case of the firing of the crowbar, the rotor voltage drops down to zero and is replaced by the resistive crowbar. To model this case, the rotor resistance can be adapted to reflect the crowbar resistance and the firing of the crowbar is modelled by a rotor voltage step towards zero. The action of the crowbar is out of the scope of this work, but all equations have been derived in a way that it will be very easy to perform that last step.

The equivalent diagram of the DFIG presented in [28] is recalled in figure 6.1.
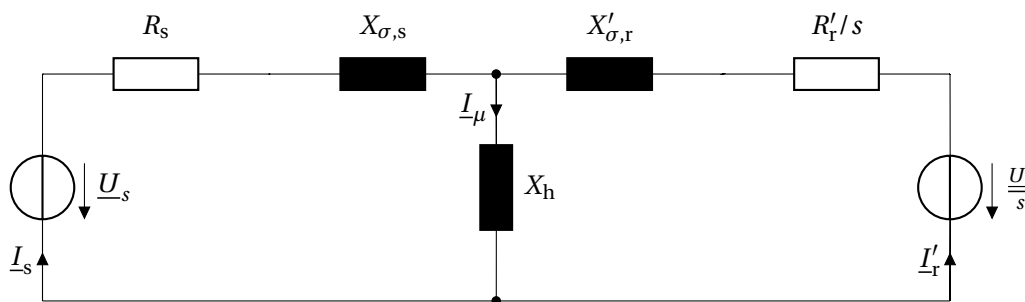
Figure 6.1 – Equivalent scheme of the DFIG

Table 6.1 – Numerical values of the parameter of the considered machine and equivalent diagram

Parameter	Numerical Value
S_n [MVA]	265.5
U_n [kV]	18.0
I_n [A]	8515.7
f_n [Hz]	50.0
n_n [rpm]	158.51
p [-]	18
ü [-]	0.6323
Z_n [Ω]	1.2204
R_s [mΩ]	4.5056
r_s [p.u.]	3.6920e-3
$X_{\sigma s}$ [Ω]	0.1525
$x_{\sigma s}$ [p.u.]	0.1249
X_{hs} [Ω]	1.9387
x_{hs} [p.u.]	1.5886
R'_r [mΩ]	1.93641
r'_p [p.u.]	1.5867e-3
$X'_{\sigma r}$ [Ω]	0.1957
$x'_{\sigma r}$ [p.u.]	0.1604

Table 6.1 presents the numerical values of the parameters of the considered machine. From the equivalent diagram of figure 6.1, one can easily deduce the voltage equations

$$\underline{U}_s = R_s \underline{I}_s + j(X_{\sigma,s} + X_h)\underline{I}_s + X_h \underline{I}'_r \tag{6.1}$$

$$\frac{\underline{U}'_r}{s} = R'_r/s \underline{I}'_r + j(X'_{\sigma,r} + X_h)\underline{I}'_r + X_h \underline{I}_s \tag{6.2}$$

$$\tag{6.3}$$

which have been published in [28]. They become in transient mode replacing the time derivative by their Laplace-form, written in pu

$$u_s = r_s i_s + (p + j\omega_s)\psi_s \tag{6.4}$$

$$u_r = r_r i_r + (p + j\Delta\omega)\psi_r \tag{6.5}$$

where the $'$-sign is omitted not to create confusion for the transient equation (x'_s and x'_r) of the inductances. The slip is taken into account into the definition of $\Delta\omega = s\omega_s$, as it is defined by

$$\Delta\omega = \omega_s - \omega_{mec} = \omega_s - \omega_s(1 - s) \tag{6.6}$$

$$= s\omega_s. \tag{6.7}$$

187

The fluxes are given by

$$\psi_s = x_s i_s + x_h i_r \tag{6.8}$$

$$\psi_r = x_h i_s + x_r i_r. \tag{6.9}$$

The voltage equations are written in the stator reference frame. The following relations are used to refer rotor quantities to the stator

$$U_r' = U_r \cdot \ddot{u} \tag{6.10}$$

$$I_r' = \frac{I_r}{\ddot{u}} \tag{6.11}$$

$$X_{\sigma r}' = X_{\sigma r} \cdot \ddot{u}^2 \quad \text{idem for every impedance referred to the stator} \tag{6.12}$$

where ü is the transformation ratio. All equations below are written in pu unless explicitly expressed. The equations are written in the rotating reference frame aligned with the stator voltage phasor. To get the phase quantities, it is sufficient to apply the inverse Park's transformation with the corresponding angle. This step is omitted in the presented equations.

6.2 Transient equations used in the DFIG machine

6.2.1 Initial conditions

The principle of the derivation of the transient equation have been taken from [28] and is different from the one presented in [82] as I have also derived the complete set of equations but I did not publish it before [82]. To calculate the transients, some initial conditions (written with the subscript 'o') are needed. The stator voltage u_s, the speed n and the mechanical power p_{mec} are known. From these three parameters one can deduce the initial values of the stator current (i_{s0}), rotor (i_{r0}) current and rotor voltage (u_{r0}). For the stator and rotor fluxes (used to calculate the torque) their initial conditions are given by

$$u_s = r_s \cdot i_{s0} + j\omega_s \psi_{s0} \tag{6.13}$$

$$\psi_{s0} = \frac{u_s - r_s \cdot i_{s0}}{j\omega_s} \tag{6.14}$$

and

$$u_{r0} = r_r \cdot i_{r0} + j\Delta\omega \psi_{r0} \tag{6.15}$$

$$\psi_{r0} = \frac{u_{r0} - r_r \cdot i_{r0}}{j\Delta\omega}. \tag{6.16}$$

where equations 6.15 and 6.16 are written in the stator reference frame as stated in section 6.1.1.

6.2.2 Transient equation for the stator current

Starting from the transient equation of the stator and rotor voltages where the time-derivative d/dt have been replaced by the Laplace-operator p leads to

$$u_s = r_s i_s + (p + j\omega_s)\psi_s \tag{6.17}$$

$$u_r = r_r i_r + (p + j\Delta\omega)\psi_r \tag{6.18}$$

where the stator flux ψ_s is defined by

$$\psi_s = x_s i_s + x_h i_r \tag{6.19}$$

with

$$x_s = x_{\sigma,s} + x_h \tag{6.20}$$

and the rotor flux ψ_r is given by

$$\psi_r = x_r i_r + x_h i_s. \tag{6.21}$$

Injecting the equation for the rotor flux in equation 6.18 leads to

$$u_r = [r_r + (p + j\Delta\omega)x_r] i_r + (p + j\omega_s)x_h i_s$$
$$i_r = \frac{u_r - (p + j\Delta\omega)x_h i_s}{r_r[1 + (p + j\Delta\omega)T_r]}. \tag{6.22}$$

Putting the equation of i_r into equation 6.17 gives

$$
\begin{aligned}
u_s &= [r_s + (p + j\omega_s)x_s)] i_s + (p + j\omega_s)x_h \Big[\frac{u_r - (p + j\Delta\omega)x_h i_s}{r_r[1 + (p + j\Delta\omega)T_r]}\Big] \\
&= r_s i_s + (p + j\omega_s)\Big[x_s - \frac{x_h^2(p + j\Delta\omega)}{r_r[1 + (p + j\Delta\omega)T_r]}\Big] i_s + (p + j\omega_s)\frac{x_h}{r_r}\frac{u_r}{1 + (p + j\Delta\omega)T_r} \\
&= \frac{r_s r_r(1 + (p + j\Delta\omega)T_r) + (p + j\omega_s)x_s - (p + j\omega_s)(p + j\Delta\omega)x_h^2}{r_r(1 + (p + j\Delta\omega)T_r)} i_s \\
&\quad + \frac{x_h}{x_r}\frac{(p + j\omega_s)}{1/T_r + (p + j\Delta\omega)} u_r \\
&= \frac{p^2 + p[\frac{T_s + T_r}{T_s' + T_r'} + j(\omega_s + \Delta\omega)] + \frac{1}{T_s \cdot T_r'}[1 + j\Delta\omega T_r + j\omega_s T_s(1 + j\Delta\omega T_r')]}{x_r(1/T_r + (p + j\Delta\omega))} i_s \\
&\quad + \frac{x_h}{x_r}\frac{(p + j\omega_s)}{1/T_r + (p + j\Delta\omega)} u_r \tag{6.23} \\
&\cong \frac{(p + 1/T_s' + j\omega_s)(p + 1/T_r' + j\Delta\omega)}{x_r(1/T_r + (p + j\Delta\omega))} i_s + \frac{x_h}{x_r}\frac{(p + j\omega_s)}{1/T_r + (p + j\Delta\omega)} u_r. \tag{6.24}
\end{aligned}
$$

The numerator of equation 6.23 is a second order polynom, its simplification using the "high power machines approximation" is detailed in section 6.2.6. Equation 6.23 is the exact equa-

tion of the stator current transfert function, while equation 6.24 is the simplified one using the "high power machines approximation". Solving the equation to get the stator current leads to

$$
i_s = \frac{T_r}{r_s T_s T_r'} \frac{p + 1/T_r + j\Delta\omega}{(p + 1/T_s' + j\omega_s)(p + 1/T_r' + j\Delta\omega)} u_s
$$

$$
+ \frac{x_h}{x_r} \frac{p + j\omega_s}{(p + 1/T_s' + j\omega_s)(p + 1/T_r' + j\Delta\omega)} u_r
$$

$$
= \frac{x_r}{x_s x_r'} \frac{p + 1/T_r + j\Delta\omega}{(p + 1/T_s' + j\omega_s)(p + 1/T_r' + j\Delta\omega)} u_s \tag{6.25}
$$

$$
+ \frac{x_h}{x_r} \frac{p + j\omega_s}{(p + 1/T_s' + j\omega_s)(p + 1/T_r' + j\Delta\omega)} u_r \tag{6.26}
$$

$$
= G_{i_s u_s}(p) u_s + G_{i_s u_r}(p) u_r. \tag{6.27}
$$

Applying an inverse Laplace-transform leads to the transient equation of the stator current. As it will be shown later on, it is very difficult to find approximative equation for i_{s0}, i_{s1} and i_{s2} (cf. section 6.2.7 for the definition of these currents) as $\Delta\omega$ has a large amplitude variation and that the equations are not linear in $\Delta\omega$. The current calculation is done using the exact solution to obtain the zeros of the numerator of equation 6.23 as well as the coefficients i_{s0}, i_{s1} and i_{s2}. The simplification of the transfer function has only an "educational" purpose to show the frequencies that are produced by the machine.

6.2.3 Simplified equation for the current in short-circuit

As for the synchronous machine, it would be very useful to have simplified equations for the short-circuit current. As the rotor voltage remains constant the stator current equation becomes

$$
i_s = \frac{x_r}{x_s x_r'} \frac{p + 1/T_r + j\Delta\omega}{(p + 1/T_s' + j\omega_s)(p + 1/T_r' + j\Delta\omega)} u_s. \tag{6.28}
$$

In the case of a three-phase short-circuit the stator voltage gets

$$
u_s = \frac{u_{s0}}{p}. \tag{6.29}
$$

Rewriting equation 6.28 leads to

$$
i_s = \frac{p - z_0}{(p - p_1)(p - p_2)} \frac{u_{s0}}{p} = \frac{\alpha}{p} + \frac{\beta}{p - p_1} + \frac{\gamma}{p - p_2} \tag{6.30}
$$

where α, β and γ have now another meaning. They represent here i_{s0}, i_{s1} and i_{s2}. Using multiplication and identification leads

$$\alpha = -\frac{z_0}{p_1 p_2} \tag{6.31}$$

$$\beta = \frac{1}{p_2 - p_1} \frac{z_0 - p_1}{p_1} \tag{6.32}$$

$$\gamma = \frac{1}{p_1 - p_2} \frac{z_0 - p_2}{p_2}. \tag{6.33}$$

As one can see $\Delta\omega$ appears in a non-linear way in theses equations, so that it is not any more possible to find easy approximation for these equations. One could find approximation for $\Delta\omega \to 0$, respectively $\Delta\omega \gg 1$ but it is not very interesting, as $\Delta\omega$ varies continuously from approximately $-0.1\omega_s$ to $0.1\omega_s$. Another option could be to split the range spread by $\Delta\omega$ into several sub-intervals and obtain approximated equations over each interval using Taylor's series. Figures 6.2, 6.3 and 6.4 show the influence of $\Delta\omega$ on the coefficients α, β and γ. Only γ can be considered as constant over the normal ranges of $\Delta\omega$. The other two coefficients are hugely influenced by $\Delta\omega$.
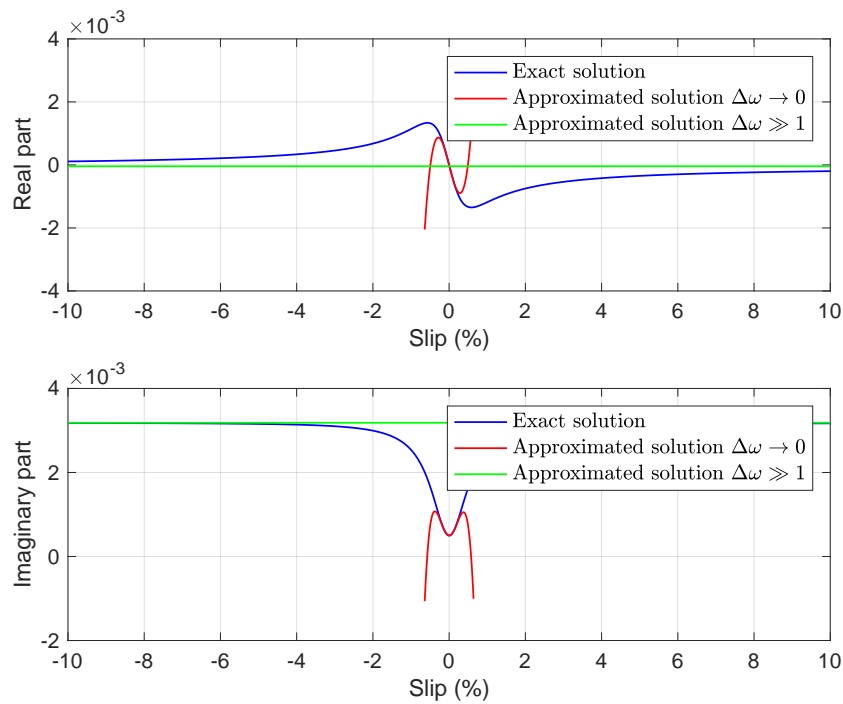
Figure 6.2 – α as function of the slip

$$\alpha_{\Delta\omega \gg 1} = -\frac{1}{1/T_\mathrm{s}' + j\omega_\mathrm{s}} \tag{6.34}$$

$$\alpha_{\Delta\omega \to 0} = -\frac{1}{1/T_\mathrm{s}' + j\omega_\mathrm{s}} \cdot$$
$$\cdot \left[\frac{T_\mathrm{r}'}{T_\mathrm{r}} + j\Delta\omega T_\mathrm{r}'\left(1 - \frac{T_\mathrm{r}'}{T_\mathrm{r}}\right) - \Delta\omega^2 T_\mathrm{r}'^2\left(\frac{T_\mathrm{r}'}{T_\mathrm{r}} + 1\right) + j\Delta\omega^3 T_\mathrm{r}'^3\left(\frac{T_\mathrm{r}'}{T_\mathrm{r}} - 1\right) - \Delta\omega^4 T_\mathrm{r}'^4 \right]. \tag{6.35}$$

The exact equation of α is

$$\alpha = -\frac{T_\mathrm{r}'/T_\mathrm{r} + j\Delta\omega T_\mathrm{r}'}{(1/T_\mathrm{s}' + j\omega_\mathrm{s})(1 + j\Delta\omega T_\mathrm{r}')}$$
$$= -\frac{T_\mathrm{r}'/T_\mathrm{r}}{1/T_\mathrm{s}' + j\omega_\mathrm{s}}\frac{1}{1 + j\Delta\omega T_\mathrm{r}'} - \frac{j\Delta\omega T_\mathrm{r}'}{1/T_\mathrm{s}' + j\omega_\mathrm{s}}\frac{1}{1 + j\Delta\omega T_\mathrm{r}'}$$
$$= -\frac{1}{1/T_\mathrm{s}' + j\omega_\mathrm{s}}\frac{1}{1 + j\Delta\omega T_\mathrm{r}'}\left(T_\mathrm{r}'/T_\mathrm{r} - j\Delta\omega T_\mathrm{r}'\right). \tag{6.36}$$

To obtain the approximation for $\Delta\omega \to 0$, the term $\frac{1}{1 + j\Delta\omega T_\mathrm{r}'}$ is approximated using a Taylor's series around 0 leading to

$$\alpha_{\Delta\omega \to 0} = -\frac{1}{1/T_\mathrm{s}' + j\omega_\mathrm{s}}\left[1 - j\Delta\omega T_\mathrm{r}' - \Delta\omega^2 T_\mathrm{r}'^2 + j\Delta\omega^3 T_\mathrm{r}'^3 + O(\Delta\omega^4)\right](T_\mathrm{r}'/T_\mathrm{r} + j\Delta\omega T_\mathrm{r}'). \tag{6.37}$$

Reorganising the terms in power of $\Delta\omega$ gives finally equation 6.35. For the approximation $\Delta\omega \gg 1$, the equation can be obtained starting from

$$\alpha_{\Delta\omega \gg 1} = -\frac{T_\mathrm{r}'/T_\mathrm{r}}{1/T_\mathrm{s}' + j\omega_\mathrm{s}}\frac{1}{1 + j\Delta\omega T_\mathrm{r}'} - \frac{1}{1/T_\mathrm{s}' + j\omega_\mathrm{s}}\frac{j\Delta\omega T_\mathrm{r}'}{1 + j\Delta\omega T_\mathrm{r}'}$$
$$= -\frac{T_\mathrm{r}'/T_\mathrm{r}}{1/T_\mathrm{s}' + j\omega_\mathrm{s}}0 - \frac{1}{1/T_\mathrm{s}' + j\omega_\mathrm{s}}1 = -\frac{1}{1/T_\mathrm{s}' + j\omega_\mathrm{s}}. \tag{6.38}$$
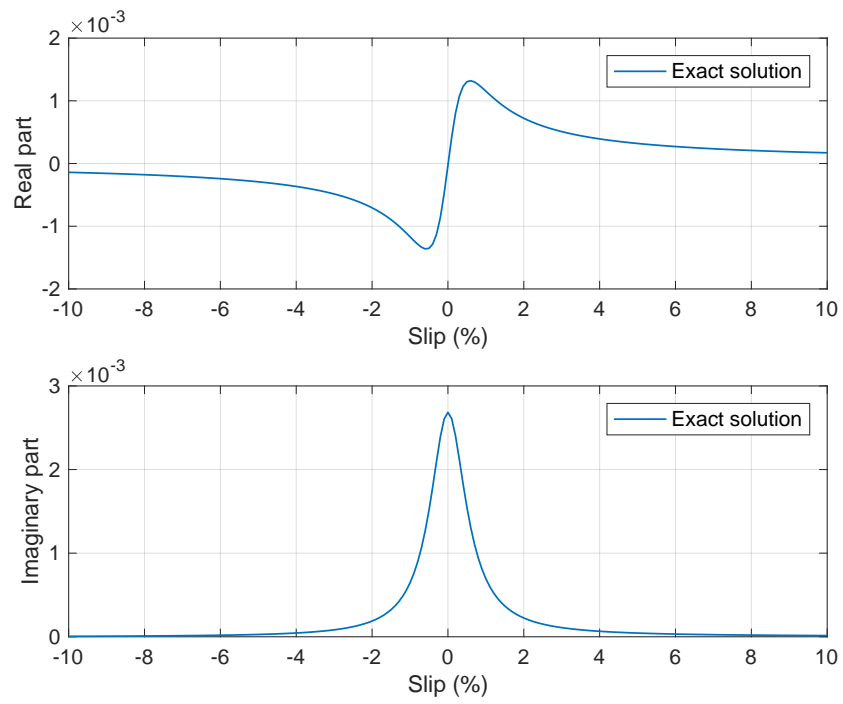
Figure 6.3 – β as function of the slip
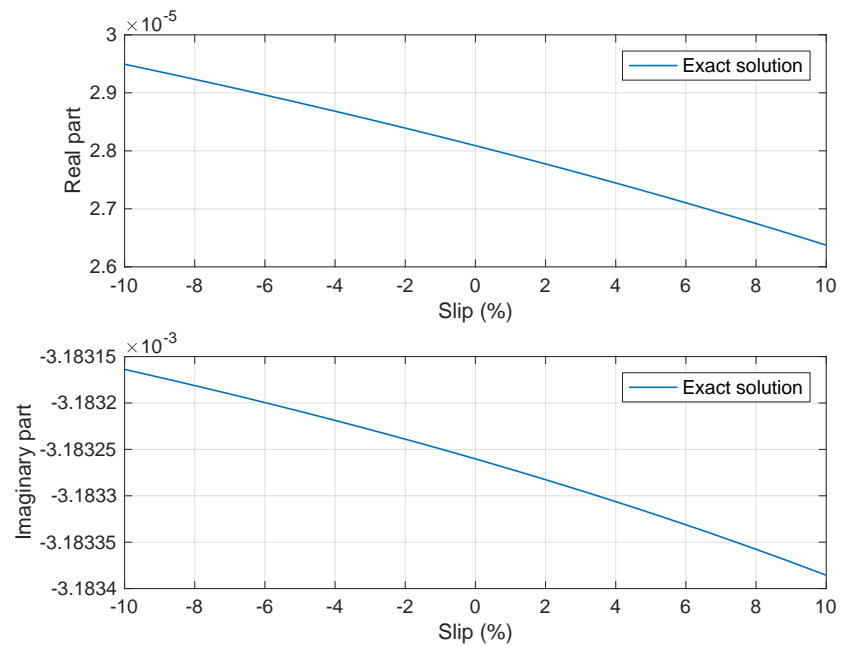
Figure 6.4 – γ as function of the slip

As it can be seen, in the case of a DFIG no simplified equation can be derived, only the complete equations can be used to compute the short-circuit current.

6.2.4 Transient equation for the stator flux

Starting from the voltage equations and using the flux instead of the current leads to

$$u_s = r_s i_s + (p + j\omega_s)\psi_s \tag{6.39}$$

$$u_r = r_r i_r + (p + j\Delta\omega)\psi_r. \tag{6.40}$$

with

$$\psi_s = x_s i_s + x_h i_r \tag{6.41}$$

$$\psi_r = x_r i_r + x_h i_s. \tag{6.42}$$

To obtain an equation for the stator flux, the stator current must be cancelled from equations 6.41 and 6.42. The rotor flux could also be calculated, but this is not the purpose of this calculation focussed on the stator flux to obtain finally the air-gap torque. Rewriting the flux equations in matrix-form leads to

$$\begin{bmatrix} \psi_s \\ \psi_r \end{bmatrix} = \begin{pmatrix} x_s & x_h \\ x_h & x_r \end{pmatrix} \begin{bmatrix} i_s \\ i_r \end{bmatrix} \tag{6.43}$$

Inverting the matrix will provide equation of the currents in function of the fluxes. After inverting one obtains

$$\begin{bmatrix} i_s \\ i_r \end{bmatrix} = \frac{1}{x_s x_r - x_h^2} \begin{pmatrix} x_r & -x_h \\ -x_h & x_s \end{pmatrix} \begin{bmatrix} \psi_s \\ \psi_r \end{bmatrix} \tag{6.44}$$

or

$$i_s = \frac{1}{x_s'}\psi_s - \frac{x_h}{x_s' x_r}\psi_r$$

$$i_s = \alpha\psi_s + \beta\psi_r \tag{6.45}$$

and for the rotor flux

$$i_r = -\frac{x_h}{x_s' x_r}\psi_s + \frac{1}{x_r'}\psi_r$$

$$i_r = \gamma\psi_s + \delta\psi_r \tag{6.46}$$

where

$$x_s' = \frac{x_s x_r - x_h^2}{x_r} \tag{6.47}$$

and

$$x'_r = \frac{x_s x_r - x_h^2}{x_s}. \tag{6.48}$$

Note that $\beta = \gamma$, but it was more convenient to define two variables (to keep the "matrix" thinking in the equations). Injecting these results into the rotor voltage equation leads to

$$
\begin{aligned}
u_r &= r_r i_r + (p + j\Delta\omega)\psi_r \\
&= r_r(\gamma\psi_s + \delta\psi_r) + (p + j\Delta\omega)\psi_r \\
&= r_r\gamma\psi_s + (r_r\delta + (p + j\Delta\omega))\psi_r.
\end{aligned}
\tag{6.49}
$$

Solving for ψ_r gives then

$$\psi_r = \frac{u_r - r_r\gamma\psi_s}{r_r\delta + (p + j\Delta\omega)}. \tag{6.50}$$

Putting this result in the stator voltage equation

$$
\begin{aligned}
u_s &= r_s i_s + (p + j\omega_s)\psi_s \\
&= r_s(\alpha\psi_s + \beta\psi_r) + (p + j\omega_s)\psi_s \\
&= (r_s\alpha + (p + j\omega_s))\psi_s + r_s\beta\psi_r \\
&= (r_s\alpha + (p + j\omega_s))\psi_s + r_s\beta\frac{u_r - r_r\gamma\psi_s}{r_r\delta + (p + j\Delta\omega)} \\
&= \frac{((r_s\alpha + (p + j\omega_s))(r_r\delta + (p + j\Delta\omega)) - r_s r_r\beta\gamma)\psi_s + r_s\beta u_r}{r_r\delta + (p + j\Delta\omega)}.
\end{aligned}
\tag{6.51}
$$

Solving this equation for ψ_s gives

$$
\begin{aligned}
\psi_s &= \frac{(r_r\delta + (p + j\Delta\omega))u_s - r_s\beta u_r}{(r_s\alpha + (p + j\omega_s))(r_r\delta + (p + j\Delta\omega)) - r_s r_r\beta\gamma} \\
&= \frac{(r_r\delta + (p + j\Delta\omega))}{(r_s\alpha + (p + j\omega_s))(r_r\delta + (p + j\Delta\omega)) - r_s r_r\beta\gamma}u_s \\
&\quad - \frac{r_s\beta}{(r_s\alpha + (p + j\omega_s))(r_r\delta + (p + j\Delta\omega)) - r_s r_r\beta\gamma}u_r
\end{aligned}
\tag{6.52}
$$

$$= G_{\psi u_s}(p)u_s + G_{\psi u_r}(p)u_r. \tag{6.53}$$

6.2.5 Transient equation for the rotor current

Recalling the voltage equations leads to

$$u_s = r_s i_s + (p + j\omega_s)\psi_s \tag{6.54}$$

$$u_r = r_r i_r + (p + j\Delta\omega)\psi_r \tag{6.55}$$

where the fluxes are given by

$$\psi_s = x_s i_s + x_h i_r \tag{6.56}$$

$$\psi_r = x_h i_s + x_r i_r. \tag{6.57}$$

The stator voltage equation is solved to obtain i_s which will be injected into the rotor voltage equation which will be solved to obtain the desired transfer function. Solving the stator voltage equation leads to

$$i_s = \frac{u_s - (p + j\omega_s) x_h i_r}{r_s(1 + (p + j\omega_s) T_s)}. \tag{6.58}$$

Injecting the result in the rotor voltage equation gives

$$
\begin{aligned}
u_r &= r_r(1 + (p + j\Delta\omega) T_r) i_r + (p + j\Delta\omega) x_h i_s \\
&= r_r(1 + (p + j\Delta\omega) T_r) i_r + (p + j\Delta\omega) x_h \frac{u_s - (p + j\omega_s) x_h i_r}{r_s(1 + (p + j\omega_s) T_s)} \\
&= \frac{r_r r_s(1 + (p + j\Delta\omega) T_r)(1 + (p + j\omega_s) T_s) - (p + j\Delta\omega)(p + j\omega_s) x_h^2}{r_s(1 + (p + j\omega_s) T_s)} i_r \tag{6.59} \\
&\quad + \frac{(p + j\Delta\omega) x_h}{r_s(1 + (p + j\omega_s) T_s)} u_s. \tag{6.60}
\end{aligned}
$$

Solving for i_r leads to

$$
\begin{aligned}
i_r &= \frac{r_s(1 + (p + j\omega_s) T_s)}{r_r r_s(1 + (p + j\Delta\omega) T_r)(1 + (p + j\omega_s) T_s) - (p + j\Delta\omega)(p + j\omega_s) x_h^2} u_r \\
&\quad - \frac{(p + j\Delta\omega) x_h}{r_r r_s(1 + (p + j\Delta\omega) T_r)(1 + (p + j\omega_s) T_s) - (p + j\Delta\omega)(p + j\omega_s) x_h^2} u_s \tag{6.61} \\
&= G_{i_s u_r}(p) u_r - G_{i_s u_s}(p) u_s. \tag{6.62}
\end{aligned}
$$

6.2.6 Simplification of the poles of the transfer function

Recalling the numerator of equation 6.23 leads to

$$p^2 + p\left[\frac{T_s + T_r}{T_s' + T_r'} + j(\omega_s + \Delta\omega)\right] + \frac{1}{T_s \cdot T_r'}[1 + j\Delta\omega T_r + j\omega_s T_s(1 + j\Delta\omega T_r')] = 0. \tag{6.63}$$

In the field of high power electrical machines, the following inequalities can be considered as fulfilled (refer to [28])

$$T_r > T_s \gg T_r' \gg T_s' \gg 1/\omega_s \tag{6.64}$$

or

$$\omega_s \gg 1/T_s' > 1/T_r' \gg 1/T_s > 1/T_r. \tag{6.65}$$

The inequalities are also called the "high power machines approximation". $\Delta\omega$ was deliberately not used in the inequalities as it can change in the range $-0.1\omega_s$ to $0.1\omega_s$. This will help us to simplify the equation of the poles and demonstrate that the poles (p_1 and p_2) can be expressed by

$$p_1 = -1/T_s' - j\omega_s \tag{6.66}$$

$$p_2 = -1/T_r' - j\Delta\omega \tag{6.67}$$

at leading order. Equation 6.63 is quadratic in p, so that the exact equation can be found for its solutions

$$
\begin{aligned}
p_{1/2} &= -\frac{1}{2}\left[\frac{T_s + T_r}{T_s \cdot T_r'} + j(\omega_s + \Delta\omega)\right] \\
&\quad \pm \frac{1}{2}\sqrt{\left(\frac{T_s + T_r}{T_s \cdot T_r'} + j(\omega_s + \Delta\omega)\right)^2 - \frac{4}{T_s T_r'}(1 + j\Delta\omega T_r + j\omega_s T_s(1 + j\Delta\omega T_r'))^2} \\
&= -\frac{1}{2}\zeta \pm \frac{1}{2}\sqrt{\eta - \nu}.
\end{aligned}
\tag{6.68}
$$

Let's first expand the term η and simplify it applying the inequalities

$$
\begin{aligned}
\eta &= \frac{T_s + T_r}{T_s \cdot T_r'}^2 - (\Delta\omega + \omega_s)^2 + 2j(\Delta\omega + \omega_s)\frac{T_s + T_r}{T_s \cdot T_r'} \\
&= -\omega_s^2\left[1 + 2\frac{\Delta\omega}{\omega_s} + \frac{\Delta\omega^2}{\omega_s^2} - \frac{1}{\omega_s^2}\left(\frac{T_s + T_r}{T_s \cdot T_r'}\right)^2 - 2j\frac{T_s + T_r}{T_s \cdot T_r'}\left(\frac{\Delta\omega}{\omega_s^2} + \frac{1}{\omega_s}\right)\right].
\end{aligned}
\tag{6.69}
$$

As η is in the square root it is very interesting to simplify the equation by taking $-\omega_s^2$ in evidence. The minus sign was used in order to get j after applying the square root. Neglecting the terms in $1/\omega_s^2$ leads to

$$
\begin{aligned}
\eta &\cong -\omega_s^2\left[1 + 2\frac{\Delta\omega}{\omega_s} + \frac{1}{\omega_s}\cdot\left(-2j\frac{T_s + T_r}{T_s \cdot T_r'}\right)\right] \\
&\cong -\omega_s^2\left(1 + \alpha\frac{\Delta\omega}{\omega_s} + \beta\frac{1}{\omega_s}\right).
\end{aligned}
\tag{6.70}
$$

Continuing with the simplification of ν

$$
\begin{aligned}
\nu &= -\frac{4}{T_s \cdot T_r'}(1 + j\Delta\omega T_r + j\omega_s T_s + j\omega_s T_s j\Delta\omega T_r') \\
&= -\omega_s^2\left(\frac{4}{\omega_s^2 T_s T_r'} + j\frac{\Delta\omega}{\omega_s^2}T_s\frac{4}{T_s \cdot T_r'} + j\frac{4}{\omega_s \cdot T_r'} + 4j^2\frac{\Delta\omega}{\omega_s}\right).
\end{aligned}
\tag{6.71}
$$

Neglecting once again the terms in $1/\omega_s^2$ leads to

$$\nu \cong -\omega_s^2\left(-4\frac{\Delta\omega}{\omega_s} + j\frac{4}{\omega_s \cdot T_r'}\right). \tag{6.72}$$

Calculating the term in the square root, ie making $\eta - \nu$ leads to

$$\eta - \nu = -\omega_s^2 (1 + 2\frac{\Delta\omega}{\omega_s} + \beta'\frac{1}{\omega_s}) \tag{6.73}$$

where β' is given by

$$\beta' = -2j\frac{T_s + T_r}{T_s \cdot T_r'} + \frac{4j}{T_r'}. \tag{6.74}$$

The equation under the square root becomes then

$$\sqrt{-\omega_s^2 (1 + 2\frac{\Delta\omega}{\omega_s} + \beta'\frac{1}{\omega_s})} \cong j\omega_s(1 - \frac{\Delta\omega}{\omega_s} + \frac{\beta'}{2}\frac{1}{\omega_s})$$

$$= j(\omega_s - \Delta\omega) + j\frac{\beta'}{2} = j(\omega_s - \Delta\omega) + \frac{T_s + T_r}{T_s \cdot T_r'} - \frac{2}{T_r'}. \tag{6.75}$$

The first solution of the equation p_1 becomes then

$$p_1 = -\frac{1}{2}\frac{T_s + T_r}{T_s \cdot T_r'} - \frac{j}{2}(\Delta\omega + \omega_s) - \frac{1}{2}j(\omega_s - \Delta\omega) - \frac{1}{2}\frac{T_s + T_r}{T_s \cdot T_r'} + \frac{1}{T_r'}$$

$$= -\frac{T_s + T_r}{T_s \cdot T_r'} + \frac{1}{T_r'} - j\omega_s = -\frac{1}{T_r'}(\frac{T_s + T_r}{T_s} - 1) - j\omega_s$$

$$= -\frac{T_r}{T_s \cdot T_r'} - j\omega_s = -\frac{1}{T_s'} - j\omega_s. \tag{6.76}$$

For the second solution p_2 one obtains

$$p_2 = -\frac{1}{2}\frac{T_s + T_r}{T_s \cdot T_r'} - \frac{1}{2}j(\Delta\omega + \omega_s) + \frac{1}{2}j(\omega_s - \Delta\omega) + \frac{1}{2}\frac{T_s + T_r}{T_s \cdot T_r'} - \frac{1}{T_r'}$$

$$= -\frac{1}{T_r'} - j\Delta\omega. \tag{6.77}$$

Figure 6.5 shows the evolution if the real part and imaginary part of p_1 and p_2 for different values of $\Delta\omega$. One can see that at leading order, the poles behave like the simplified equations predicts.

6.2.7 Torque harmonics for a 3-phase short-circuit, or 3-phase faulty synchronization

To exclude any excitation of a mechanical eigenmode of in the stator or rotor of the generator, one needs to determine the frequency of the torque harmonics. From equation 6.28 one can deduce that the stator current is given by

$$i_s = i_{s0} + i_{s1}\exp(-t/T_s')\sin(\omega_s t) + i_{s2}\exp(-t/T_r')\sin(\Delta\omega t) \tag{6.78}$$
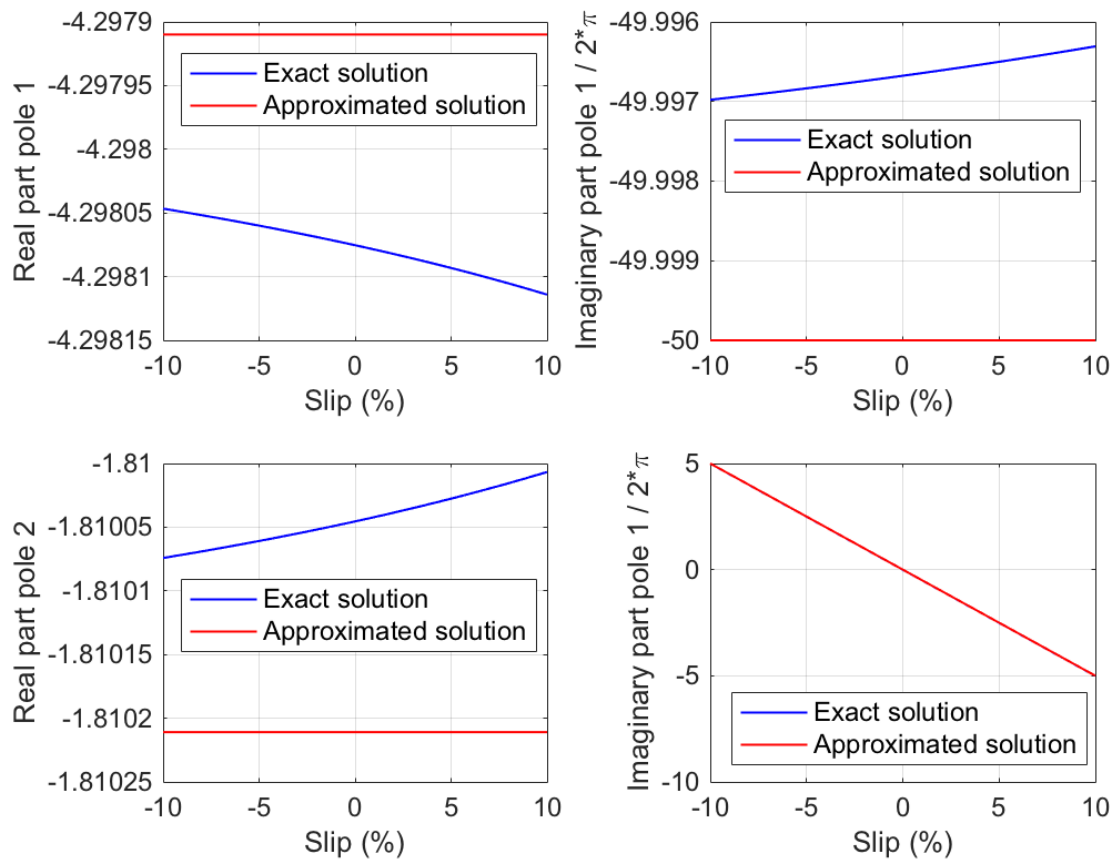
Figure 6.5 – Evolution of the poles p_1 and p_2 in function of $\Delta\omega$

where i_{s0}, i_{s1} and i_{s2} are obtained from the corresponding transfer function and the stator flux is obtained by a similar way a the stator current, starting from equation 6.53 and is given by

$$\psi_s = \psi_{s0} + \psi_{s1}\exp(-t/T_s')\sin(\omega_s t) + \psi_{s2}\exp(-t/T_r')\sin(\Delta\omega t) \tag{6.79}$$

where ψ_{s0}, ψ_{s1}, ψ_{s2} are obtained from the corresponding transfer function. The torque is given by

$$t_{em} = \frac{3}{2}\cdot p \cdot \mathbb{Im}\{\psi_s^* \cdot i_s\}. \tag{6.80}$$

The interested is mainly on the torque harmonics (to check if there could be any resonance between the mechanical system and the foundation), it is not mandatory to calculate each component but just its frequency dependence so that

$$
\begin{aligned}
t_{em} &\sim \sin(\omega_s t)^2 + \sin(\omega_s t) + \sin(\Delta\omega t)\sin(\omega_s t) + \sin(\Delta\omega t)^2 \\
&\sim \cos(0\cdot t) + \sin(\omega_s t) + \cos(2\omega_s t) + \cos((\omega_s \pm \Delta\omega)t) + \cos(2\Delta\omega t)
\end{aligned} \tag{6.81}
$$

where the sign $\sim$ means "is linearly proportional to". The torque presents therefore the following frequencies during a 3-phase short-circuit or a 3-phase faulty synchronisation

$$f_1 = 2\Delta\omega \tag{6.82}$$
$$f_2 = \omega_s \pm \Delta\omega \tag{6.83}$$
$$f_3 = \omega_s \tag{6.84}$$
$$f_4 = 2\omega_s. \tag{6.85}$$

6.2.8 Modelling the 2-phase short-circuit

Until now, there was no exact analytical equations for the current or torque of a 2-phase short-circuit in the dq-rotating frame. Based on previous works on the DC-Decay tests (2-phase short-circuit) in a synchronous machine [98], which could be calculated exactly analytically, it has been decided to search for an analytical equation for the voltage step in the dq-frame, which is the only reference frame that would lead to analytical equations for a rotating machine [96], [97] and [98]. The 2-phase short-circuit is characterised by the following equation

$$u_a = u_b. \tag{6.86}$$

This equation means nothing else than, the fact that the two voltages will be the same after the short-circuit. Supposing in addition that the machine is star connected leads to the following equation

$$
\begin{aligned}
u_a + u_b + u_c &= 0 \\
2u_a + u_c &= 0.
\end{aligned} \tag{6.87}
$$

To define the voltages after the short-circuit, the reaction of the voltage on phase c must be known or supposed known after the short-circuit. Before the short-circuit the voltage on this phase is given neither by the machine (through the induced voltage) or by the grid. Just after the short-circuit (a few milliseconds after), the currents in the machine will not have any discontinuity (as the current as well as the fluxes are state variables), so that the voltage in the phase c will remain the same. The grid voltage, as the phase c is not affected by the short-circuit will also not change. As there is no change in the voltage of phase c at the beginning of the short-circuit, then there will be no other changes in this voltage during the whole short-circuit. Mathematically speaking the phase voltage equation is of the following form

$$u_i = r_i i_i + \sum_j \frac{d\psi_{ij}}{dt} \tag{6.88}$$

To change the voltage u_i one should change instantaneously the flux ψ_{ik} which is not possible as it is a continuous state-variable. The current will not change instantaneously as the current is a linear combination of fluxes. Therefore,

$$u_c = u_s \tag{6.89}$$

where u_s is the stator voltage phasor **before** the short-circuit. In this case, it is interesting to keep Park's reference frame aligned with the stator voltage in order to get a real number. Knowing this, the stator voltage in the abc-frame is known before and after the short-circuit, where its given by

$$u_a = -u_c/2 \tag{6.90}$$
$$u_b = -u_c/2 \tag{6.91}$$
$$u_c = u_c. \tag{6.92}$$

To get the voltage in the dq-frame it is sufficient to take Park's transformation of this voltage. After some trivial trigonometric operation, one can find the voltage in the rotating frame which is given by

$$u_d = -\frac{u}{2}\sin(2\omega_s t) \tag{6.93}$$
$$u_q = -\frac{u}{2}(1 + \cos(2\omega_s t)), \tag{6.94}$$

which is an original contribution of this work. With these voltages, it is straightforward to obtain the Laplace-transformation of them to calculate the short-circuit currents. Let's see in the following paragraph how valid are these hypothesis regarding the voltage of phase c before and after the short-circuit, comparing simulation results with measurements done on a 110MVA motor.

Figure 6.6 shows the simulated voltage for a phase-to-phase short-circuit that occured in a

synchronous machine. One can notice that the voltage of the healthy phase remains constant as stated, while the voltage of the 2 other phases becomes identical. If one analysis very conscientiously the curves, one will see that the amplitude decreases. This decrease is due to the fact that the simulated machine is a pump. So that, when a short-circuit occurs, the machine will automatically slow-down and the induced voltage will be reduced. Please note that the voltage u_a and u_b are not null, because the handled case is a phase-to-phase short-circuit and not a 2-phase to neutral or ground short-circuit.
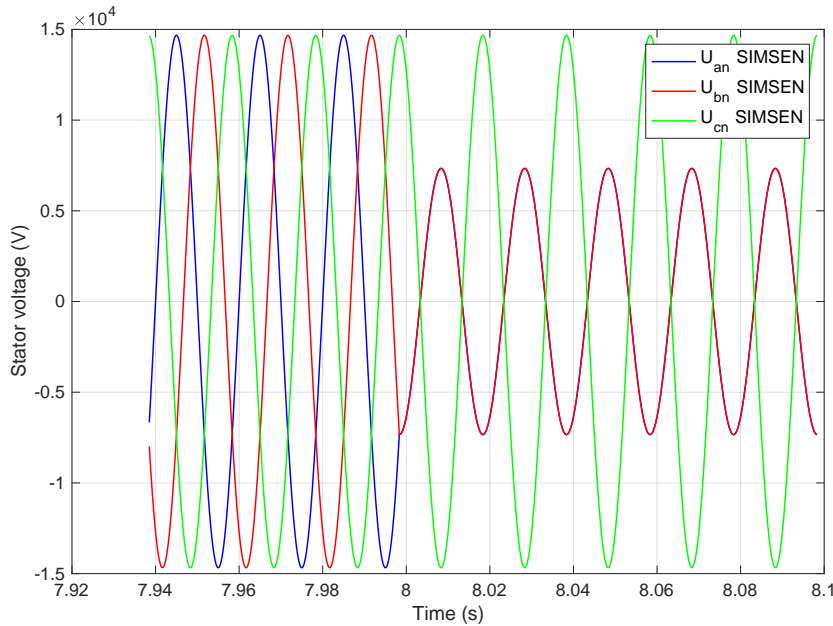
Figure 6.6 – Phase-to-phase short-circuit on a synchronous machine, simulated with SIMSEN

Figure 6.7 presents the measured voltages at the terminals of the machine during the short-circuit. It can be seen that the voltage of the phase c is not constant, but has also a step. The voltage of the phase a and b becomes identical as stated, but not symmetrical regarding the zero-volt axis. One must also notice that is this particular case, the short-circuit occurred not at the terminals of the machine, but in the machine itself. This could perhaps explain the discrepancy observed for the phase c between figures 6.6 and 6.7. Figure 6.6 shows the simulated voltage form for a phase-to-phase short-circuit. The stator voltage behaves as stated in the hypothesis, confirming that this hypothesis holds. At any rate the difference between the stated voltage on phase c and the measured one doesn't lead to a significant difference on the currents as one can see in figures 6.8 and 6.9.

As for the voltage of the phase c, one can also see a little discrepancy between the simulated and measured values. It remains unclear whether the errors can be put down to the fact that the short-circuit does not occur at the terminals of the machine, but in the machine. Nevertheless, the modelling of the 2-phase short-circuit can be considered as completed and successful.
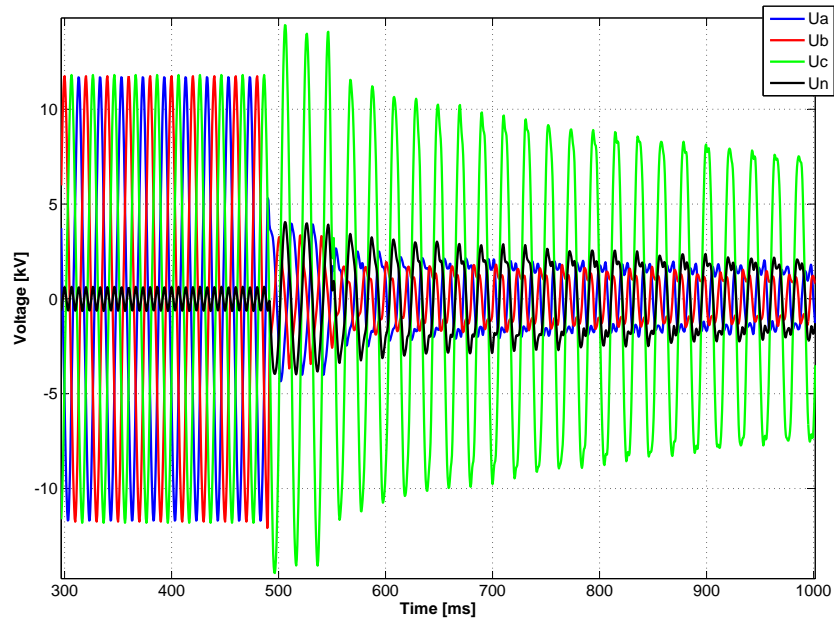
Figure 6.7 – Phase-to-phase short-circuit on a synchronous machine (110 MVA), measured values
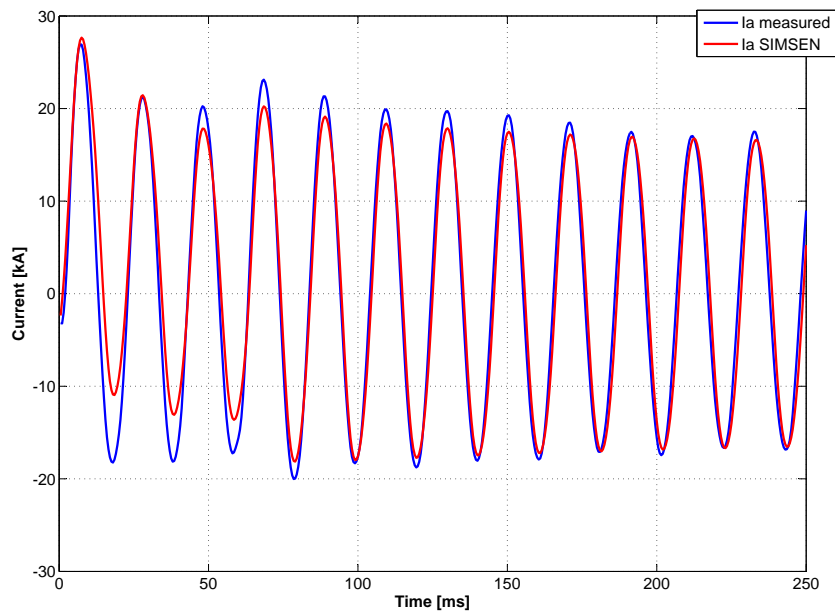
Figure 6.8 – Comparison of measured and simulated current (Phase a) for a phase-to-phase short-circuit
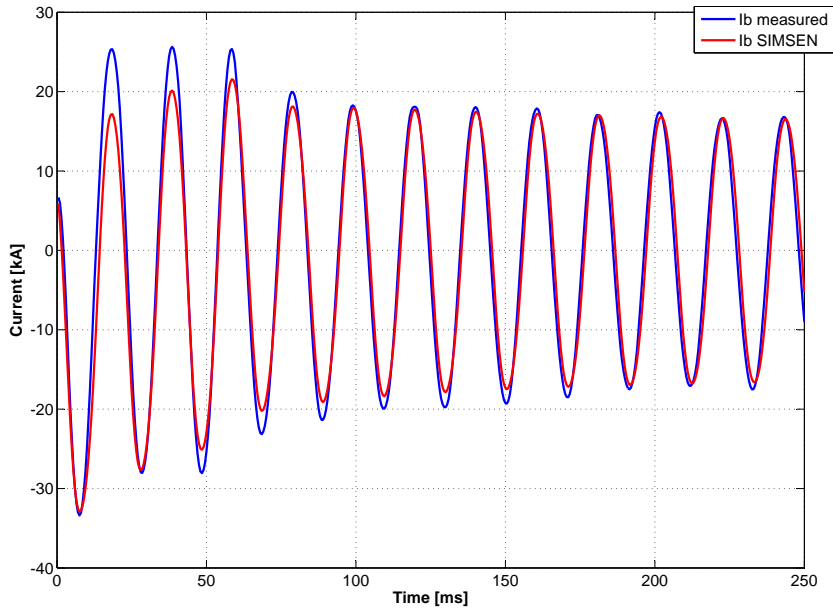
Figure 6.9 – Comparison of measured and simulated current (Phase b) for a phase-to-phase short-circuit

6.2.9 Faulty synchronization

The faulty synchronisation 2-phase as well as 3-phase can be treated on the same way as the short-circuit [28], with the only difference that the voltage step is not for example

$$-u_{\mathrm{s}} \tag{6.95}$$

but something like

$$u_{\mathrm{s}} \exp(j\phi) \tag{6.96}$$

where ϕ is the angle between the stator voltage and the grid voltage.

6.3 Validation of the analytical equations

This section presents the validation of the analytical equations developed above. The validation is done by a comparison with simulated curves using the software SIMSEN using the parameters defined in table 6.1. Figures 6.10, 6.11 and 6.12 present the air-gap curves for the ASM machine in three-phase and two-phase short-circuit and DFIG in the case of a three-phase short-circuit. All curves show a perfect agreement between the analytical equations and the simulated curves with SIMSEN. Additional information and curves can be found in A.6 mainly for the stator current and rotor current.
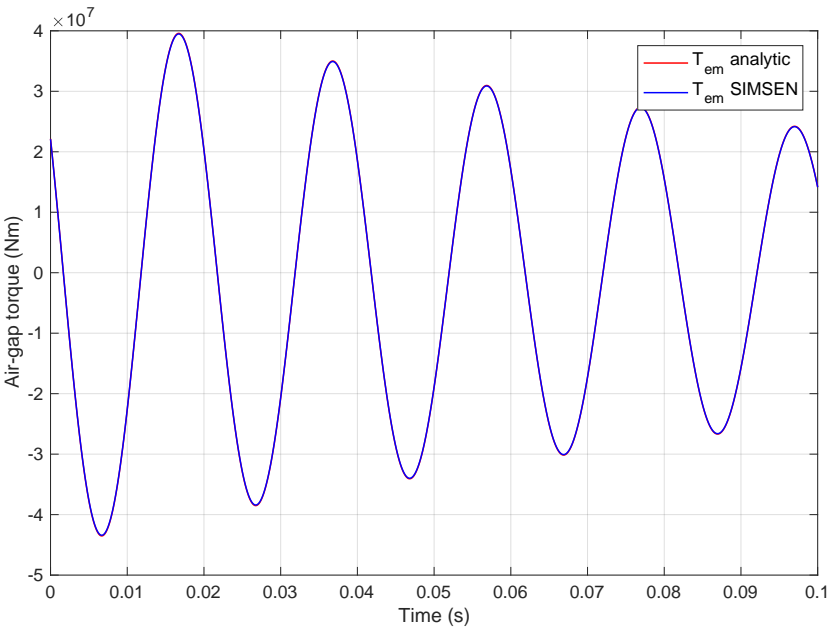
Figure 6.10 – Air-gap torque (ASM) three-phases short-circuit.
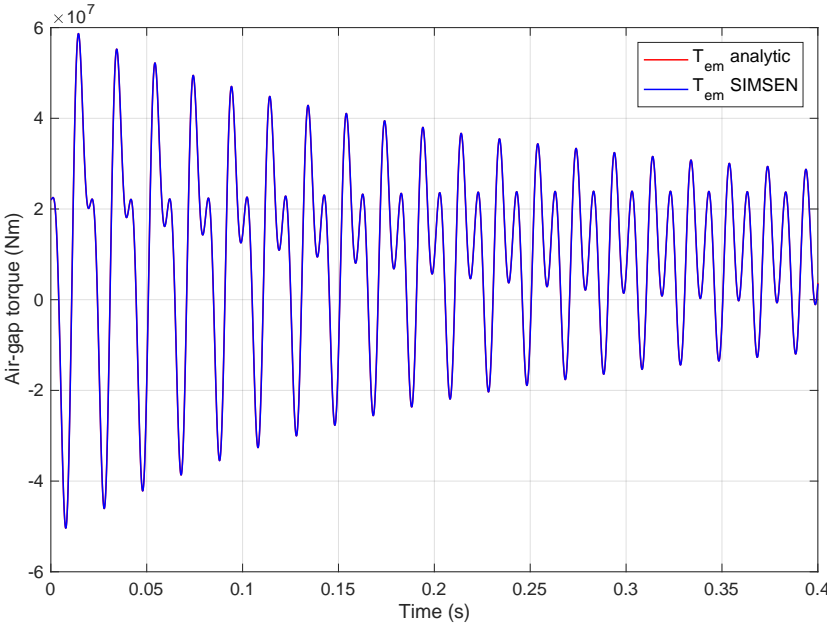
Figure 6.11 – Air-gap torque (ASM) two-phases short-circuit.
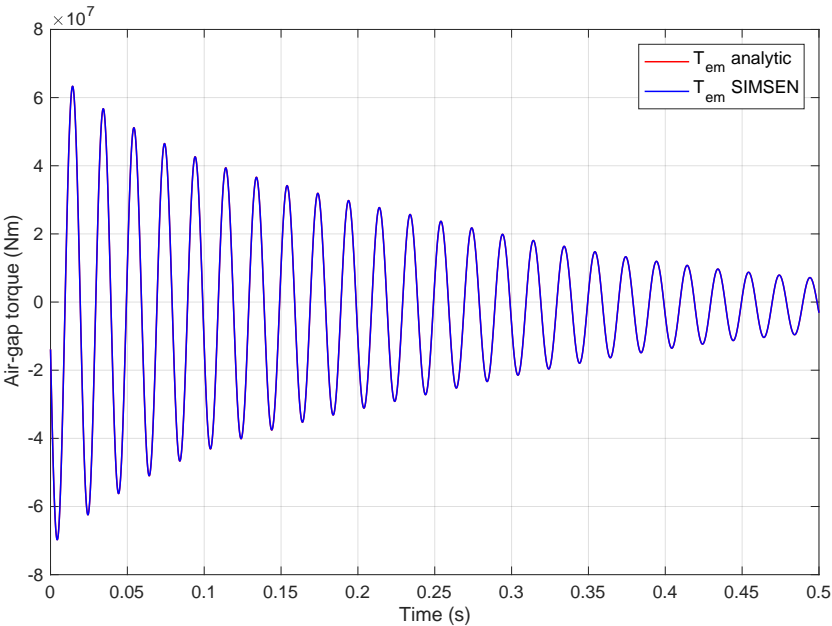
Figure 6.12 – Air-gap torque (DFIG) three-phases short-circuit.

7 Forces in the winding overhang

This chapter presents the force calculation in the winding overhang. The knowledge of these forces is very important as any high power electrical machine must withstand short-circuit stresses without any damages. In addition, the winding overhang is the mechanically weakest part of an electrical machine compared to other parts, as it is only composed of copper and insulation material which are both very weak materials. It is very difficult and expensive to build mechanical reinforcement in the overhang, this makes computation and optimisation of the forces in the winding overhang very interesting. Many authors published results on the force calculation in the end-winding of electrical machines, as for example [45]. They focussed mainly on the sudden short-circuit cases where the force amplitude is maximal. [45] studied the impact of the magnetic shaft and press-plates on the forces for a turbogenerator. Starting from the findings of this work, this study focusses itself on the origin of the magnetic field, respectively magnetic force. This can be used to reduce the magnetic forces in the overhang by adjusting the end-winding geometry, with the last step being out of the scope of this study.

This chapter starts with a comparison of the calculated forces using the equation developed in this work with an in-use integral force calculation tool. Then original contributions of the impact of the boundary (active part and rotor overhang), the calculation approximation and the operating point are presented. The study of the forces in the case of a large DFIG is in general a novel contribution as no publications have already shown any results regarding this new type of electrical machine in its large fashion. Some original plots of the winding overhang forces in a cylindrical coordinate system as well as in a spherical coordinate system give another point of view and insight about the force components and their interaction. There is also some original discussions about the origin of the force components, as the integral formulation utilised to obtain the magnetic field coming from current carrying conductors can easily provide this information. Original 3D-pictures and graphs show the magnetic field and forces.

This study is concentrated on the end-winding forces of the stator winding, especially on the end-winding forces of the top and bottom bar of slot #1, while the results are given in units of gravitational force (g) as this unit is intrinsically more understandable than kN/m.

In terms of construction, the stator winding is the same as for a hydro-generator: the bar is bent using the same bending machines as for an equivalent synchronous machine. The bar is bent over a conus. But as already mentioned and shown, the impact of the rotor on the winding overhang force will be much more significant. The turbogenerator has another winding overhang geometry, which will lead to a different winding overhang force layout [45].

7.1 Comparison of this work and another winding overhang calculation software
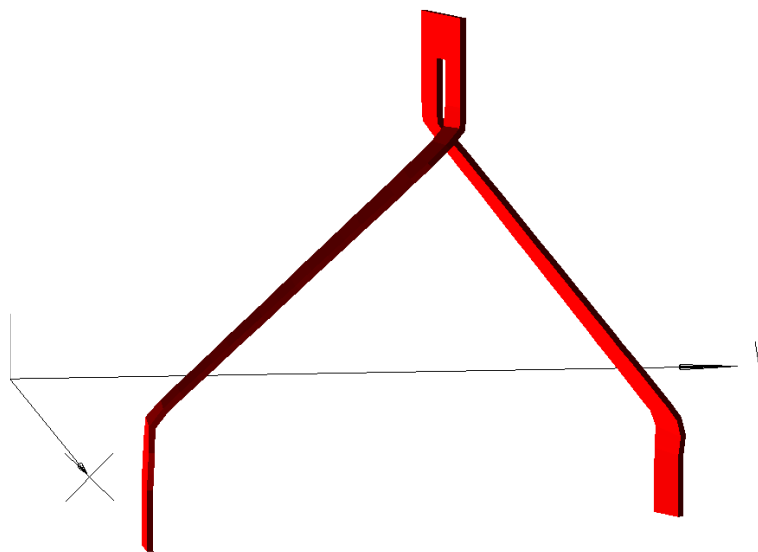
Figure 7.1 – Stator bar model in a in-use integral force calculation program.

Figure 7.1 shows the model of a top and bottom bar in a in-use integral force calculation program. The rotor bars can't be integrated in this software while the active part boundary is modelled using the mirror method.

Figures 7.2 and 7.3 present other views of the stator bar model. Comparing figures 7.2 and 7.3 with figures 5.12 and 5.14 one can see that the radial and tangential bendings of the bar are modelled differently: the in-use force calculation tool uses a straight line approximation with a current discontinuity between elements, while this study uses arc elements. In the in-use force calculation tool, the current can be spatially discontinuous between elements as the current is collinear to the straight abscissa. This current discontinuity can impact the calculated forces, but it is very difficult to quantify this effect. More generally speaking the shape of the overhang is not exactly the same, which will lead to some discrepancies between both forces calculation. It is difficult to predict them and therefore to give conclusive arguments for one or the other calculation tool.

Figure 7.2 – Another view of the stator bar model in a in-use integral force calculation program.
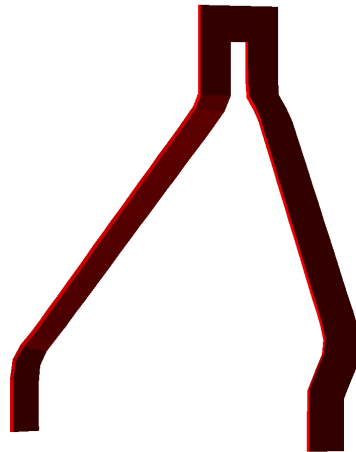
Figure 7.3 – Another view (2) of the stator bar model in a in-use integral force calculation program.

7.1.1 Comparison between the in-use calculation tool and this work

Figure 7.4 shows a comparison between the in-use software and this work where the results with the filament as well as the rectangular approximation are depicted. The curves match quite well considering the different geometries and hypotheses taken into account. The rectangular approximation exhibits the highest forces. The force components are monotone where the stator bar has not a lot of bendings, while the components show high variation when short radial and tangential bendings are present. When the stator bar is aligned with the machine axis, then the z-component of the force is null as expected.

Figure 7.5 presents the same comparison as depicted in figure 7.4 but for a top bar. The curves match also quite well and the rectangular approximation exhibits also the highest forces. The radial component of the force has a rather large discrepancy, which can not be fully explained due to the different geometries and hypotheses taken into account.

To conclude, the comparison shows that the force calculation of this work is in the same range than the force calculation of the in-use calculation tool considering the different hypotheses and geometries. The force calculation algorithm has been validated using Maxwell's filament (refer to section 5.9.3) so that it is a logical conclusion that the discrepancies are due to the different hypotheses and geometries. To have a strong conclusion, one should compare this work with a complete 3D-finite-element calculation, which is out of the range of this study.
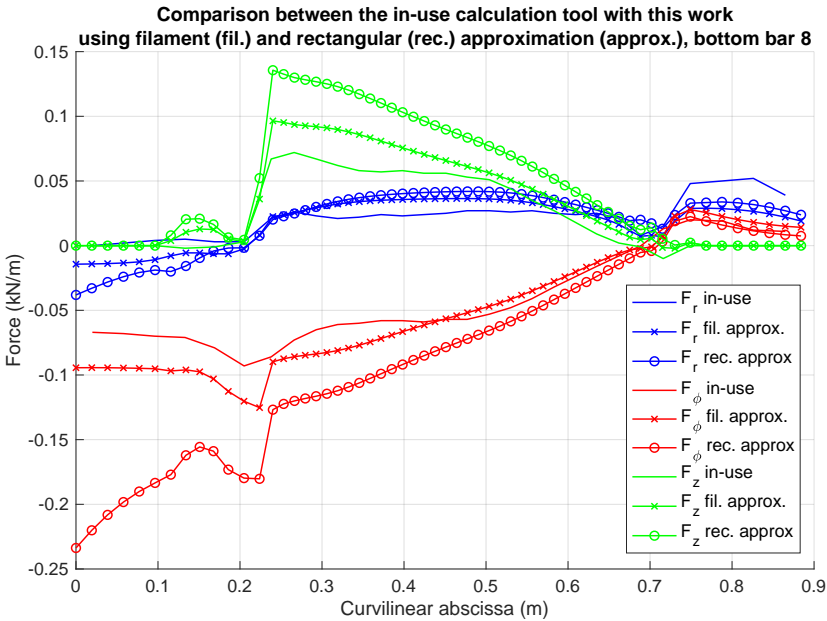
Figure 7.4 – Comparison between the in-use software and this work for a stator bottom bar (instantaneous values).
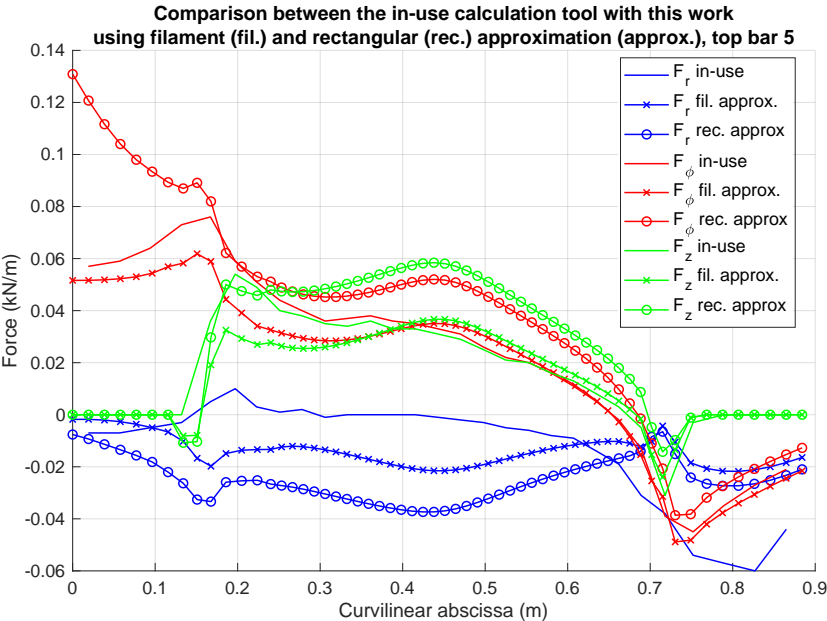
Figure 7.5 – Comparison between the in-use software and this work for a stator top bar (instantaneous values).

7.2   Definition of the calculated cases

Table 7.1 – Description of the simulation cases. OP stands for nominal operation point, while CC stands for stator short-circuit

Name	Boundary	Stator current	Rotor current
Case 1 (C1)	$\mu = 0$ (OP)	$I_s = I_s$	$I_r = I_r$
Case 2 (C2)	$\mu = 1$ (OP)	$I_s = I_s$	$I_r = 0$
Case 3 (C3)	$\mu = 1$ (OP)	$I_s = I_s$	$I_r = I_r$
Case 4 (C4)	$\mu = \inf$ (OP)	$I_s = I_s$	$I_r = I_r$
Case 5 (C5)	$\mu = \inf$ (OP) with air-gap conductor	$I_s = I_s$	$I_r = I_r$
Case 6 (C6)	Magnetic (OP)	$I_s = I_s$	$I_r = I_r$
Case 7 (C7)	Magnetic (CC)	$I_s = I_s$	$I_r = I_r$

Table 7.1 presents the simulated cases. For the different operation points, for the presented case it is chosen to have the stator current at its maximal value. The calculated cases are magneto-static cases, so that the force is given at a certain time. The cases have been chosen to highlight the impact of the boundary and operation point on the winding forces. In addition, the rotor current is put to zero to see the impact of the rotor on the forces. In cases 6 and 7, the magnetic rotor overhang is also added to take its effect into account. The forces are so-called Laplace forces with the total magnetic field (from current sources and magnetic sources) used in the cross-product. The forces are plotted in terms of gravity acceleration, as one can easily handle this value rather than a force in N/m or N/m3. As the focus of this study is on the impact of boundaries, elements of the model and operation point, there is no sudden short-circuit force calculation.

7.3   Influence of the boundaries on the magnetic forces

The aim of this section is to present original results that show the influence of the boundaries on the magnetic forces applying different permeabilities using the mirror method, applying or not the rotor current and including magnetised elements for the rotor overhang and last stack of the active part.

Figures 7.6 and 7.7 present the influence of different cases (only using the mirror method) on the winding force of the top of slot #1 located at the coordinate $y = 0$, therefore the x-component of the force coincides with the radial component of the force. The force is higher in the case of the rectangular approximation near the boundary of the active part. The force has progressively similar behaviour for both approximations the more the force points recede from the boundary. The boundary has a significative impact only on the first half of the overhang, where the impact of the boundary is about factor 2. As expected the force is maximal in the case of a zero-permeability boundary as the magnetic field lines are tangential to the boundary.
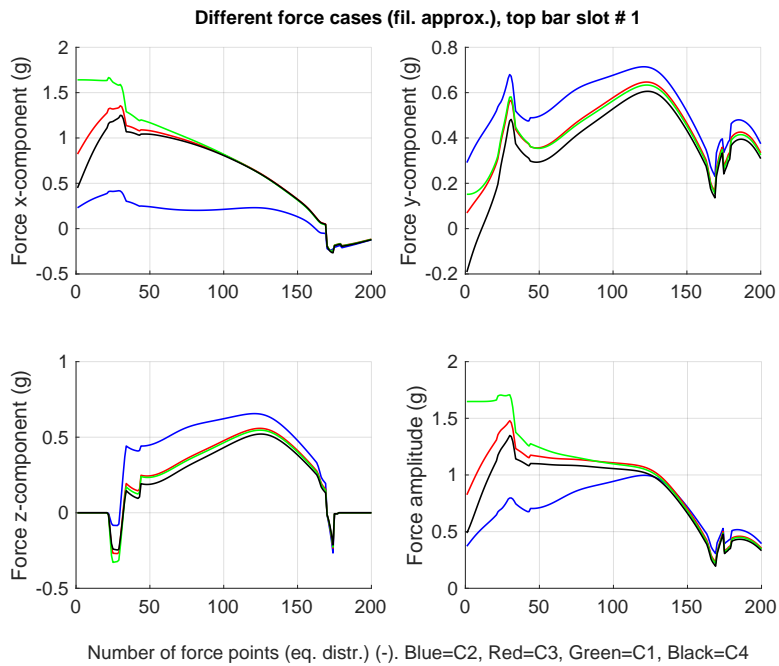
Figure 7.6 – Influence of the different cases on the magnetic force (equally distributed force points) on top bar slot #1, filament approximation. The results are plotted in cartesian coordinates.
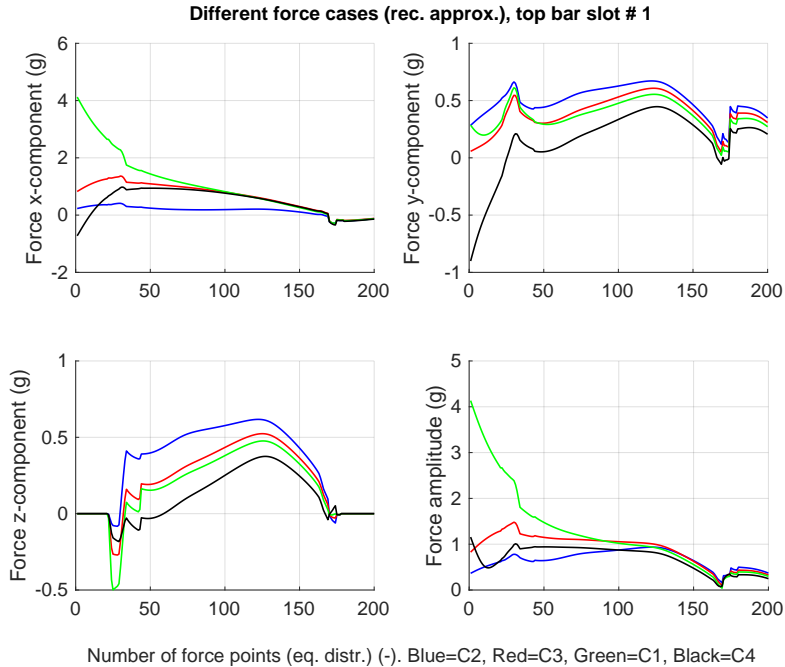
Figure 7.7 – Influence of the different cases on the magnetic force (equally distributed force points) on top bar slot #1, rectangular approximation. The results are plotted in cartesian coordinates.

The force component's curves are quite monotone which is positive for the winding. The amplitude is low as expected for normal operation of the electrical machine.

Different force cases (fil. approx.), bottom bar slot #1

Number of force points (ed) (-). Blue=C2, Red=C3, Green=C1, Black=C4, Cyan=C6*, Magenta=C7*
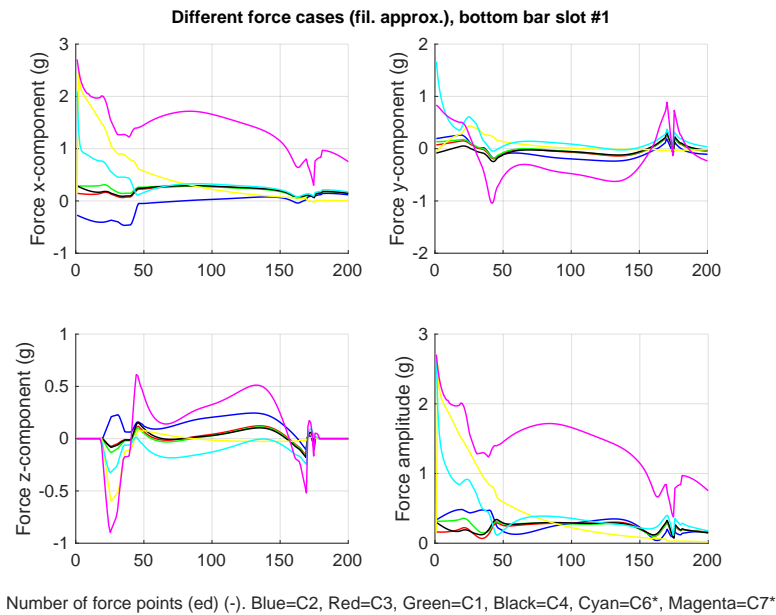
Figure 7.8 – Influence of the different cases on the magnetic force (equally distributed force points) on bottom bar slot #1, filament approximation. The results are plotted in cartesian coordinates.

Figures 7.8 and 7.9 present the influence of different cases on the winding force of the bottom of slot #1 located at the coordinate $y = 0$, therefore the x-component of the force coincides with the radial component of the force. In the short-circuit case, the force in the winding overhang is also significantly higher than for the nominal operation point. The force is also less monotone especially in the short-circuit case, where the average force amplitude reaches 2g. In normal operation, the force amplitude is in line with the values obtained for the cases using the mirror method. In the case of magnetic boundaries, the force is very similar for both approximations as the magnetic field is mainly due to the magnetic boundaries and not to the rotor and stator currents. The approximation doesn't influence the magnetic force significantly. Adding the air-gap conductor produced similar force behaviour near the air-gap as with the magnetic boundary, which is inline with the published literature [71] and [24].

The major impact on the force amplitude originates from the operation point, while the boundary has only a second order influence.

Different force cases (rec. approx.), bottom bar slot #1

Number of force points (ed) (-). Blue=C2, Red=C3, Green=C1, Black=C4, Cyan=C6*, Magenta=C7*
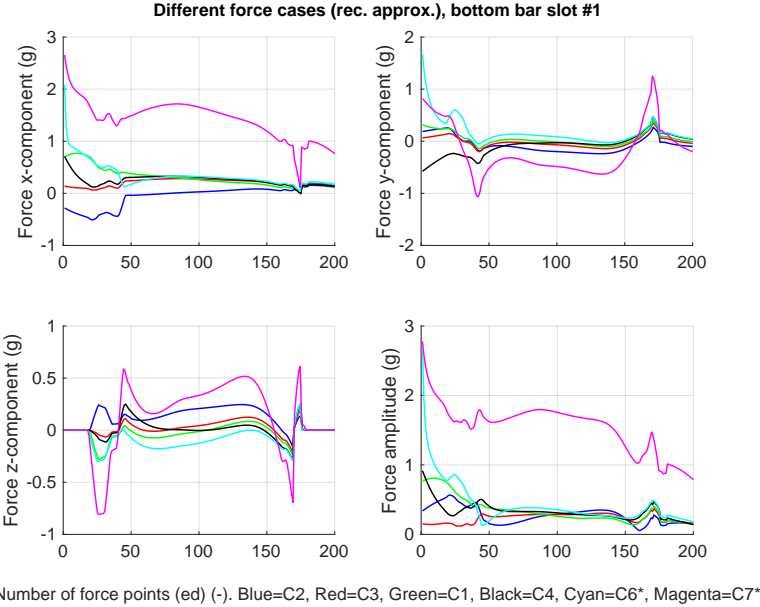
Figure 7.9 – Influence of the different cases on the magnetic force (equally distributed force points) on bottom bar slot #1, rectangular approximation. The results are plotted in cartesian coordinates.

7.4   Influence of the approximation on the magnetic forces

The purpose of this section is to analyse the influence of the approximation used on the winding force, which is an original contribution of this study. The choice of the approximation has not only an impact on the calculation precision but also on the calculation time. For instance, a calculation using the filament approximation takes 17s to be performed on a single processor, while this calculation takes 95s using the hybrid approximation and 3623s in the case of the rectangular approximation. The filament approximation uses the equations defined in section 5.1.1, the rectangular approximation uses the equations defined in section 5.1.2 and the hybrid approximation uses both approximations. Depending on the distance between the current carrying element and the force point the filament approximation is used in the "far-field" zone while the rectangular approximation is used in the "near-field" zone. The critical radius (refer to section 4.5) is set to 15 in this study.
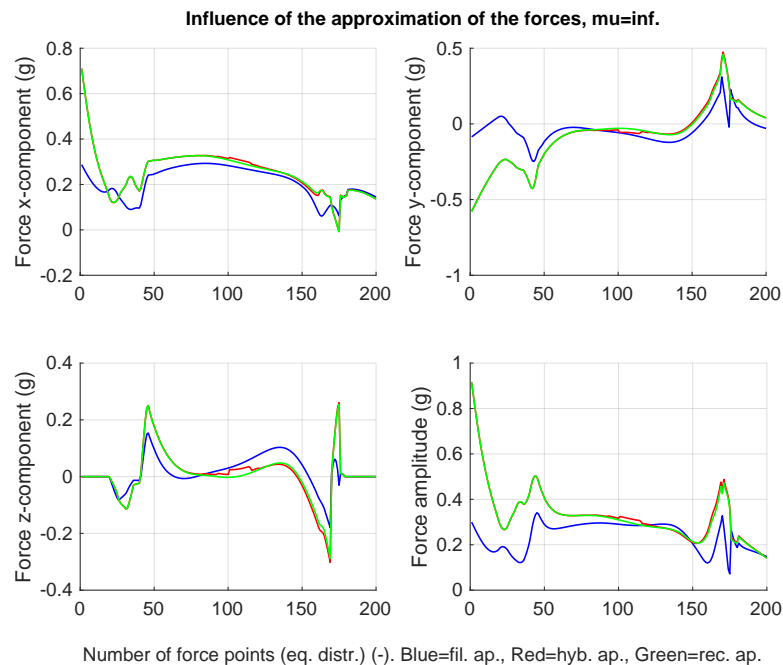
Figure 7.10 – Influence of the calculation approximation: filament approximation (fil. ap.), hybride approximation (hyb. ap.) and rectangular approximation (rec. ap.) of the magnetic force (equally distributed force points) with infinite-mirror on top bar slot #1. The results are plotted in cartesian coordinates, while the force is calculated in instantaneous values.

Figures 7.10, 7.11 and 7.12 show the influence of the approximations on the winding forces. All the approximations show very similar results independent of the calculated case. As expected, the hybrid approximation is very close to the rectangular approximation. The difference can be reduced when the critical radius is increased, but this will also increase the calculation time. The hybrid approximation presents a very good compromise between precision and calculation time and should be extensively used for practical applications. Figure 7.11 presents the winding forces calculated in spherical coordinates. The spherical coordinates represent an

interesting way of force presentation as the stator winding is bent over a conus, which equals to a sphere with constant θ-coordinate. The spherical coordinate representation shows that the phi-component of the magnetic force is constant over the straight part of the stator winding bar, while the two other components don't give any interesting additional information.

Influence of the approximation of the forces, mu=inf. (spherical coordinates)

Number of force points (eq. distr.) (-). Blue=fil. ap., Red=hyb. ap., Green=rec. ap.
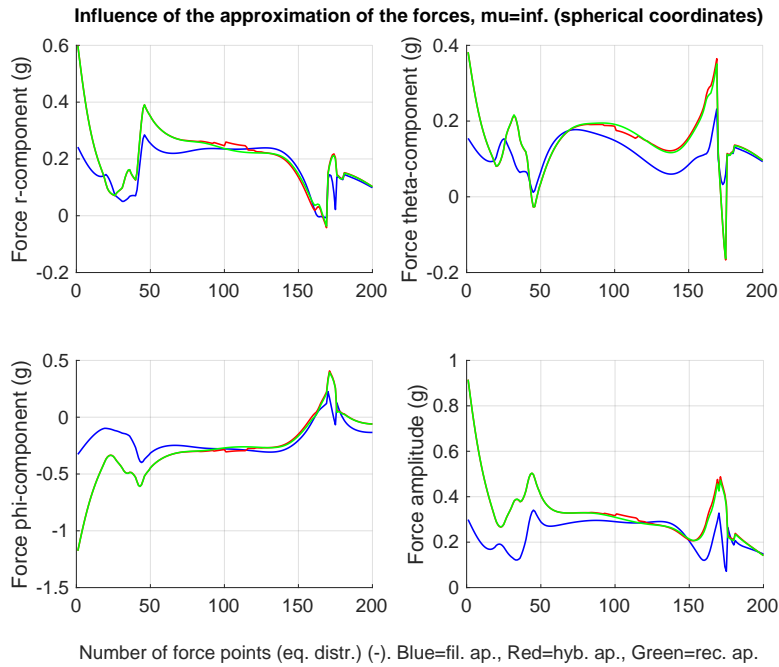
Figure 7.11 – Influence of the calculation approximation: filament approximation (fil. ap.), hybride approximation (hyb. ap.) and rectangular approximation (rec. ap.) of the magnetic force (equally distributed force points) with infinite-mirror on top bar slot #1. The results are plotted in spherical coordinates.
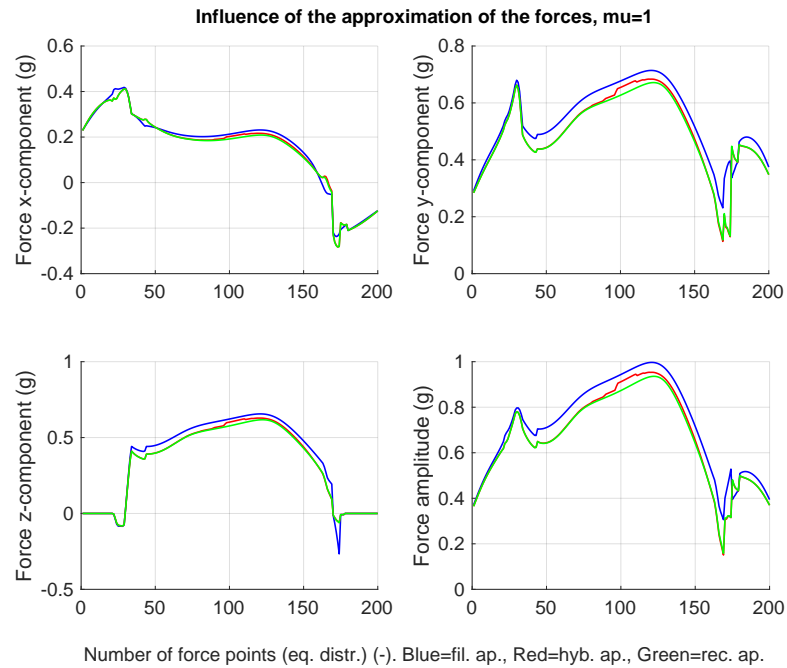
Figure 7.12 – Influence of the calculation approximation: filament approximation (fil. ap.), hybride approximation (hyb. ap.) and rectangular approximation (rec. ap.) of the magnetic force (equally distributed force points) without mirror on top bar slot #1. The results are plotted in cartesian coordinates.

7.5 Origin of the magnetic field

One of the main advantages of the integral numerical field calculation is the possibility to get to know the origin of the magnetic field, in other words which bar contributes how much to the magnetic field at a given location. To do so, the contribution of each bar is calculated for each force point and stored in a so-called interaction matrix. This matrix contains the values of each component of the magnetic field for each bar and each force point. Some original results are shown hereafter.
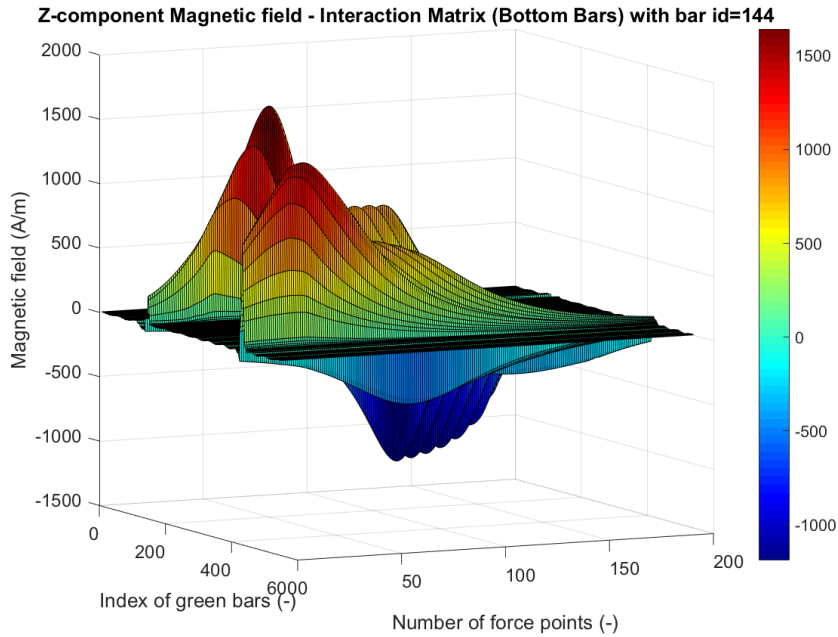
Figure 7.13 – Z-Component of the matrix field (Interaction Matrix) for bottom bars calculated on bar with id=144. The value 6000 at the intersection of the x-axis and y-axis is an artefact, which is due to the angle chosen for the representation of the 3D-plot. It must be understood as 600 on the y-axis and 0 on the x-axis.

Figure 7.13 presents the z-component of the magnetic field for the bottom bars only (stator and rotor winding). The results are shown for a force calculated applying the filament approximation on the stator top bar number 144 to have a more "centred" plot with respect to the index of the green bars. The z-component of the magnetic field is composed of 4 peaks located at the green bar index corresponding to the neighbouring bars. These peaks span over a few bars after which they tend towards zero, meaning that only the neighbouring bars contribute significantly to the magnetic field. Figure 7.14 presents a zoom for the bars with an id between 115 and 155. One can denote the small numbers of bars that contribute to the z-component of the magnetic field as well as the constant contribution of the bars with an id between 132 and 140. It is interesting to point out that the z-component of the magnetic field is negative before the calculated bar and positive after. The mirrored bars are not shown in this representation even if this representation has been calculated using the mirror method as the mirrored bars represent a boundary contribution and not a physical contribution.
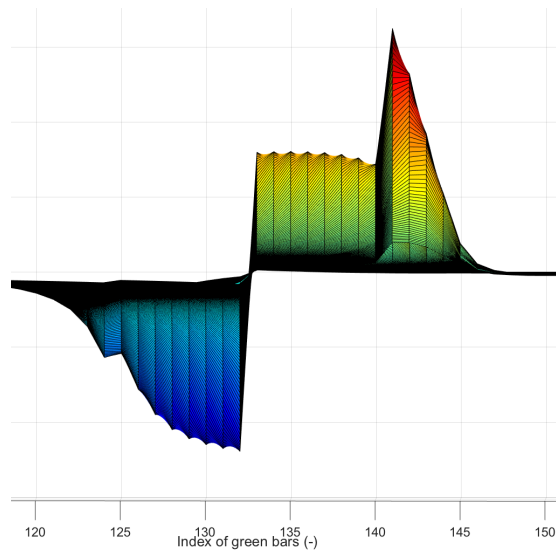
Figure 7.14 – Z-Component of the matrix field (Interaction Matrix) for bottom bars calculated on bar with id=144. Zoom on the bar with id between 115 and 155. The scale is the same as for figure 7.13.

Figure 7.15 shows the y-component of the magnetic field for the top bars (stator and rotor winding) only. The calculation methodology is the same as for figure 7.13 as well as the considerations for the mirrored bars. The y-component is composed of three peaks. Two peaks are due to the neighbouring bars of the stator winding, with the same sign property as for figure 7.13. The peak attributed to the rotor winding is positive. The peaks tend rapidly towards zero. A similar behaviour of the peaks as shown in figure 7.14 can be found.

As a conclusion, one can denote that the neighbouring bars contribution is the major part of the magnetic field, while the contribution of other bars tends rapidly towards zero. On a calculation point of view, this means that the preferred calculation method must be using the rectangular approximation or better the hybrid approximation to obtain a precise force calculation.
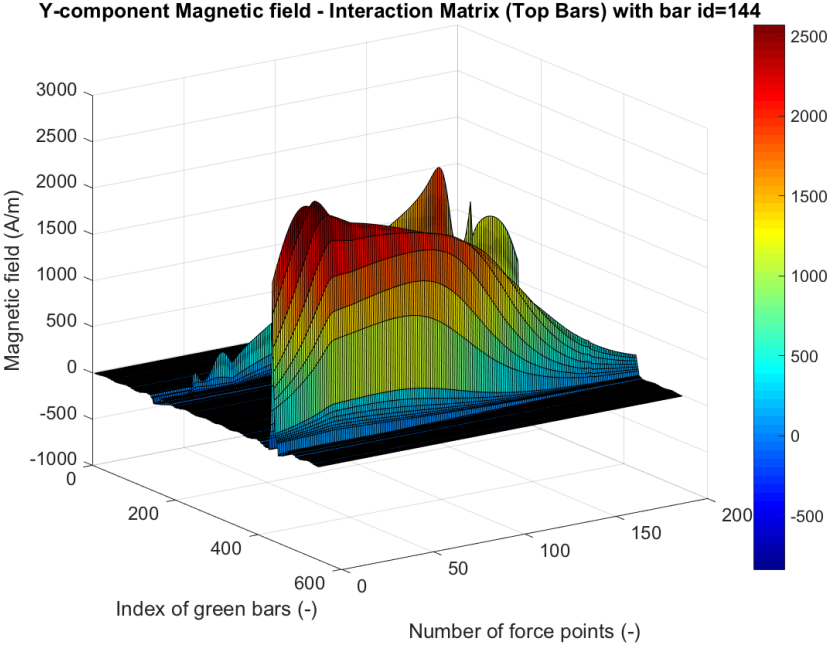
Figure 7.15 – Y-Component of the matrix field (Interaction Matrix) for top bars calculated on bar with id=144.

7.6 Origin of the magnetic force

With respect to the original results presented in the previous section, a next step forward is the determination of the force contribution of each bar. To do so, the magnetic field of the interaction matrix must be transformed into a force contribution. Using the Laplace-force equation with the local unitary current vector leads to the magnetic force contribution vector. These original results are plotted and discussed hereafter.
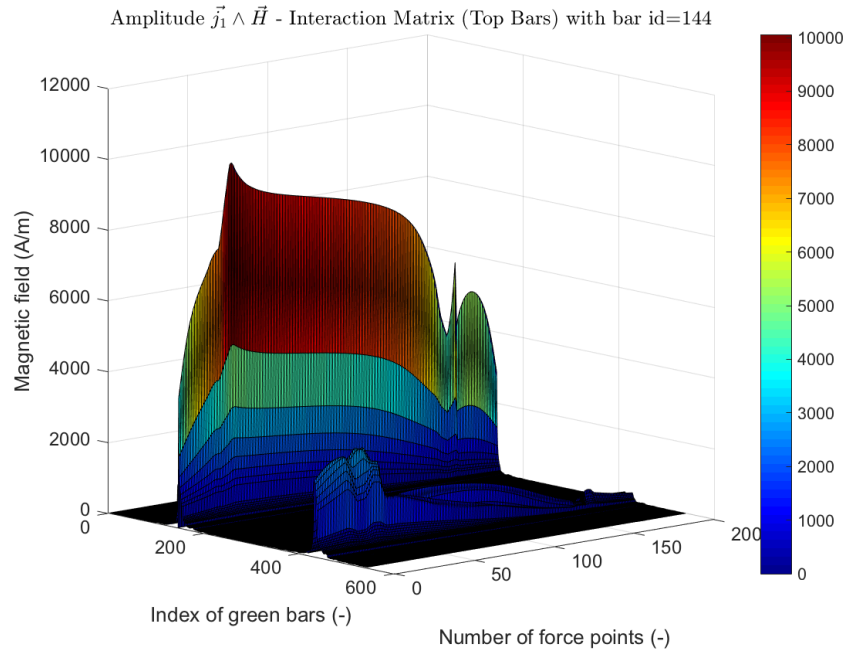
Figure 7.16 – Amplitude of $\vec{j}_1 \wedge \vec{H}$ (Interaction Matrix) for top bars calculated for bar with id=144, where $\vec{j}_1$ is the local unitary current vector.

Figure 7.16 shows the amplitude of the force contribution (Interaction Matrix) for only the top bars (stator and rotor winding). There are two peaks, one for the neighbouring stator bars and one for the rotor bars. As the representation is in amplitude of the contribution, the peak is wider than for the components of the magnetic field and spans over about 50 bars. The amplitude of the stator winding peak is about four times larger than the contribution of the rotor winding. The force contribution is maximal at the beginning of the bar and is slightly reduced until the end of the bar, this is due to the angle between the current vector and the magnetic field. The stator peak spans over the bars with an id between 142 and 148, while the rotor peak spans over the bars 429 to 435. The following criterion used to determine if a bar is inside or outside a peak is a force amplitude of 2'000 A/m.

Figure 7.17 shows the amplitude of the force contribution (Interaction Matrix) for only the bottom bars (stator and rotor winding). There are two peaks, one for the neighbouring stator bars and one for the rotor bars. As the representation is in amplitude of the contribution, the peak is wider than for the components of the magnetic field and spans over about 50 bars.
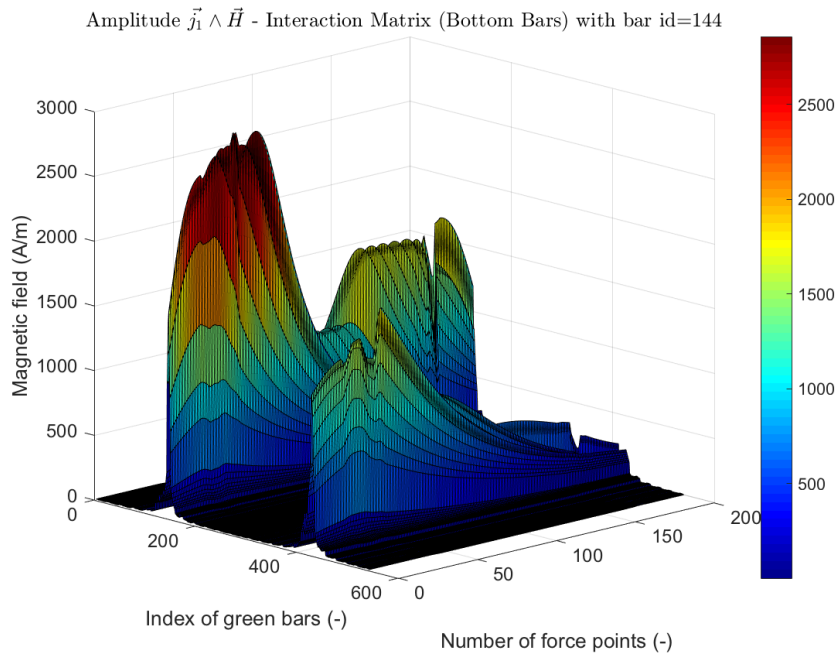
Figure 7.17 – Amplitude of $\vec{j}_1 \wedge \vec{H}$ (Interaction Matrix) for bottom bars calculated on bar with id=144, where $\vec{j}_1$ is the local unitary current vector.

The amplitude of the stator winding peak is about two times larger than the contribution of the rotor winding. The force contribution is maximal at the beginning of the bar, is lower in the middle part of the bar and increases again near the end of the bar. This is due to the angle between the current vector and the magnetic field. With a 2'000 A/m criterion for the peak, only the bars with an id spanning from 140 to 148 are inside the peak, lowering the peak-criterion to 500 A/m leads to a span from 120 to 148 and 415 to 423. Nevertheless, the peak is narrow and only the near neighbouring bars contribute significantly to the winding force.

7.7 3D-Results of the magnetic forces in the winding overhang

Some 3D-Views of the magnetic forces in the winding overhang are shown in this section. Figure 7.18 shows a 3D-view of the rotor and stator winding. Figure 7.19 shows the stator winding, while figure 7.20 presents a view of the rotor winding forces. For both windings, the behaviour of the force is similar. The force amplitude is maximal at the phase separation. When the the force amplitude is low, it is possible to see that the force vector is shaped like a wave. This is due to the geometry changes of the winding bar in the overhang. In the straight part of the winding overhang, the force is regular with a quasi constant amplitude.
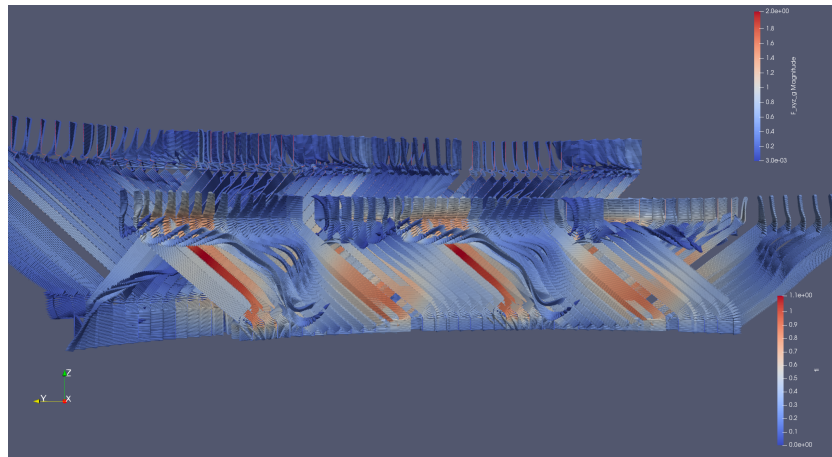
Figure 7.18 – 3D-View of the magnetic forces in the rotor and stator winding.
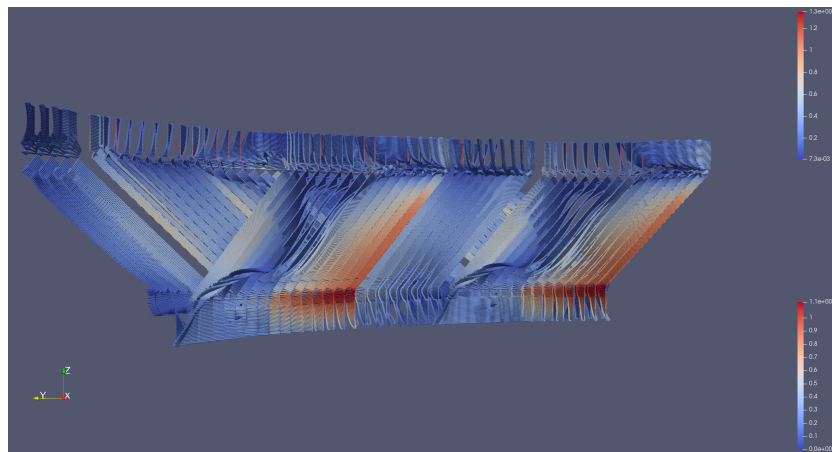
Figure 7.19 – 3D-View of the magnetic forces in the stator winding.
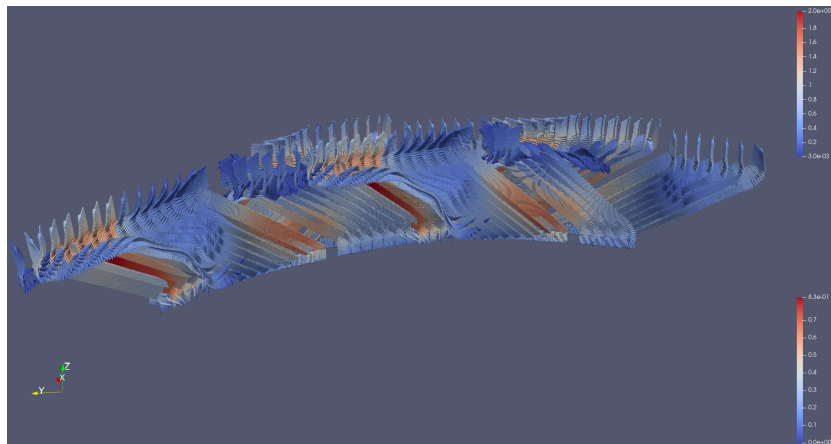
Figure 7.20 – 3D-View of the magnetic forces in the rotor winding.

7.8 Conclusion

This chapter presented the winding overhang force calculation and showed several original contributions to that topic. Using the hybrid formulation leads to the same results as using the rectangular approximation, while reducing the computational time by factor 36. It was possible to show the origin of the force, which can be used to optimise the design of the overhang regarding a possible minimisation of the end winding force. It was also possible to show the impact of the different boundaries on the force, whereas the magnetic boundary presents the most probable winding overhang forces even if it was not possible to validate these results against 3D finite-element due to limitation of computing capacities. The use of the mirror method, with or without air-gap conductor, can be suitable for "first-shot" computations but should not be used for force optimisations.

8 Circulating current calculation

This chapter is dedicated to the presentation of the original results of the circulating current calculation in the rotor and stator roebel bars of a DFIG under different operating conditions and applying different boundaries.

It starts with the explanation of the model used for each part of the circulating current calculation according to figure 1.11 to close the loop started in chapter 2. The composition of the chain-matrix in the active part is detailed afterwards. Some pictures of the induced flux in the winding overhang are shown to explain the origin of the induced voltage in the overhang.

After the practical description of the calculation method and models, this chapter continues with the presentation of the circulating current calculation:

- showing a lot of cases for both stator and rotor applying different boundaries of the active part,

- showing the impact of the stator and rotor winding on the circulating currents,

- detailing the impact of the operating point on the circulating currents,

- performing a comparison of the calculated value with an in-use software.

Then some results using special well-known transpositions are shown and well-known optimisations of the transposition are presented and their impact on the losses. Finally, the impact of the ventilation slits on the circulating currents is presented to discuss the impact of the hypothesis presented in [52] on DFIG. Basically, this chapter follows the same principle as the study presented in chapter 3. All the results presented in this chapter are original contributions of this work as no publications have already shown any results regarding this new type of electrical machine in its large fashion.

The strand numbering has been changed to the results presented in this chapter. Strand #1 and #n are located towards the air-gap, while strands #m and #m+1[1] are located towards the

---

[1] Refer to figure 3.1 for the explanation of the meaning of the variables n and m.

slot bottom.

8.1 Practical description of the calculation methods and models: different parts of the circulating current calculation

The slot inductance model used is the slot differential inductance model, which takes the coupling between the top and bottom bars into account (refer to section 4.6). There is no externally induced voltage in the active part taken into account. The impact of the neighbouring bars is also not taken into account in the modelling of the active part. The ventilation ducts are modelled using this approach. The inductances in the winding overhang as well as the externally induced voltage in the winding overhang are obtained using the model described in chapter 5. The inductances are calculated directly using the formulas for the vector potential created by a current conductor. For the induced voltage, the impact of the magnetised boundaries are taken into account depending on the simulated case. In some cases, the mirror method is applied with or without air-gap conductor.
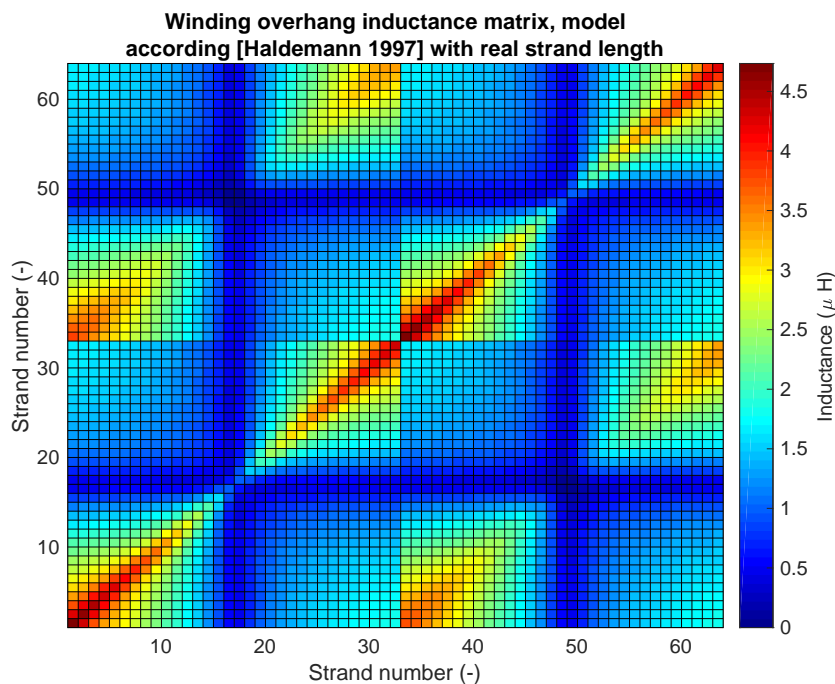
Figure 8.1 – Inductance matrix using the model described in [68] with the winding and bar parameters of the stator winding of the DFIG under study. There are no transpositions in the winding overhang and the return conductor is placed as described in [68].

Comparing figure 8.1 with figure 8.2 shows clearly the difference between the two inductance calculation models. As figure 8.2 uses the partial inductance concept, the main inductance is nearly constant as the vector potential is the same for each slot, while it is changing in figure 8.1 as the distance between the conductor and the return conductor is different for all strands.

Figure 8.2 – Partial inductance matrix of the stator winding overhang using the model of chapter 5 without an overhang transposition.
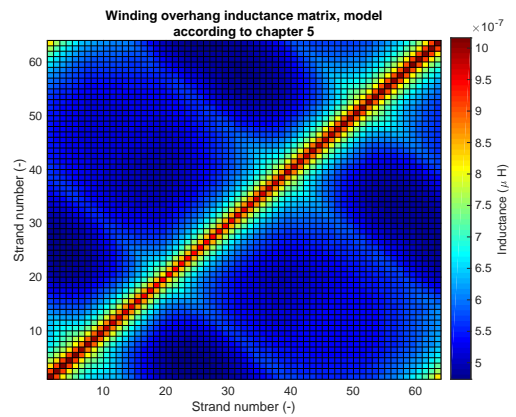
Figure 8.3 – Partial inductance matrix of the stator winding overhang using the model of chapter 5 with an overhang transposition of 180°.

It is important to note that the base hypothesis of both inductance calculation models are different: the calculation model of this work is based on an "partial-inductance" approach, while the inductance calculation model of figure 8.1 is obtained using a return-conductor model. The main impact on the winding overhang transposition on the inductances is to transform the inductance matrix into a diagonal matrix, with a very small coupling between the strands (constant inductance value). This effect will also tend to reduce the circulating current by equalising the impedance of each branch as one can see in figure 8.3.
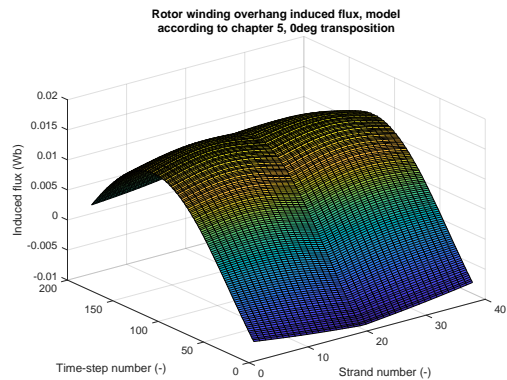
Figure 8.4 – Induced flux in the rotor winding overhang using the model of chapter 5 with 0°-transposition in the winding overhang.
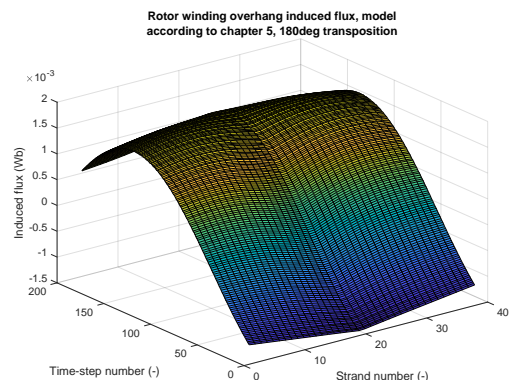
Figure 8.5 – Induced flux in the rotor winding overhang using the model of chapter 5 with 180°-transposition in the winding overhang.

Figures 8.4 and 8.5 show the impact of a overhang transposition on the induced flux. The amplitude is reduced by factor 10, which has an important impact on the circulating currents. The impact on the inductance is marginal so that the root cause of the circulating current reduction is due to the reduction of surface which induces a reduction of the induced flux.

The composition of the inductance matrix in the active part is done as follows. One knows the number and length of each core stack and ventilation duct. It is therefore possible to compute the equivalent inductance matrix taking the stack and ventilation ducts correctly into account. As the number of transpositions is also known, one can deduce the corresponding roebel pitch or roebel step. This step is used to decompose the equivalent inductance matrix into number of transpositions matrices. With the knowledge of the stack length and the exact location of the ventilation ducts, one can deduce exactly the transposition matrix which takes the ratio air/iron exactly into account.

8.2 Simulation cases

Table 8.1 shows the cases that will be used for the study on the circulating currents. These cases have been defined to highlight the impact of the rotor and stator winding and the boundaries on the circulating currents. The cases are always run with the currents for the nominal operation points and stator short-circuit operation.

Table 8.1 – Description of the simulation cases.

Name	Boundary	Stator current	Rotor current	Image current
Case 1	$\mu = \inf$	$I_s=0$	$I_r = I_r$	$I'_{s,r}{}^a = I_{s,r}$
Case 2	$\mu = \inf$	$I_s = I_s$	$I_r=0$	$I'_{s,r} = I_{s,r}$
Case 3	$\mu=1$	$I_s = I_s$	$I_r = I_r$	$I'_{s,r} = 0$
Case 4	$\mu=0$	$I_s = I_s$	$I_r = I_r$	$I'_{s,r} = -I_{s,r}$
Case 5	$\mu = \inf$ (no air-gap cond.)	$I_s = I_s$	$I_r = I_r$	$I'_{s,r} = I_{s,r}$
Case 6	Magnetic	$I_s = I_s$	$I_r = I_r$	No image current
Case 7	$\mu = \inf$ (air-gap cond.)	$I_s = I_s$	$I_r = I_r$	$I'_{s,r} = I_{s,r}$

---

[a]The prime denotes the mirror current.

8.3 Impact of the different cases on the circulating currents of a stator and rotor bar with a 360° transposition

Figure 8.6 presents the original stator circulating currents for different cases and operation points in the case of a 0/360/0-transposition. The fs-factor can be found in table 8.2. The curves show an expected behaviour. The case doesn't significantly influence the circulating currents except for the case without boundary ($\mu = 1$), transposing the fact that the boundary has some effect on the circulating currents. In the case of the magnetic boundary (case 6), the results are only presented for the case of the bottom bar. This is due to some numerical errors in the calculation of the induced voltage in the winding overhang that could not be diminished using reasonable computing power. But one can denote that the magnetic boundary as well as the different operation points significantly impact the results. The impact of the stator winding respectively rotor winding is marginal only. To obtain a reliable computation of the
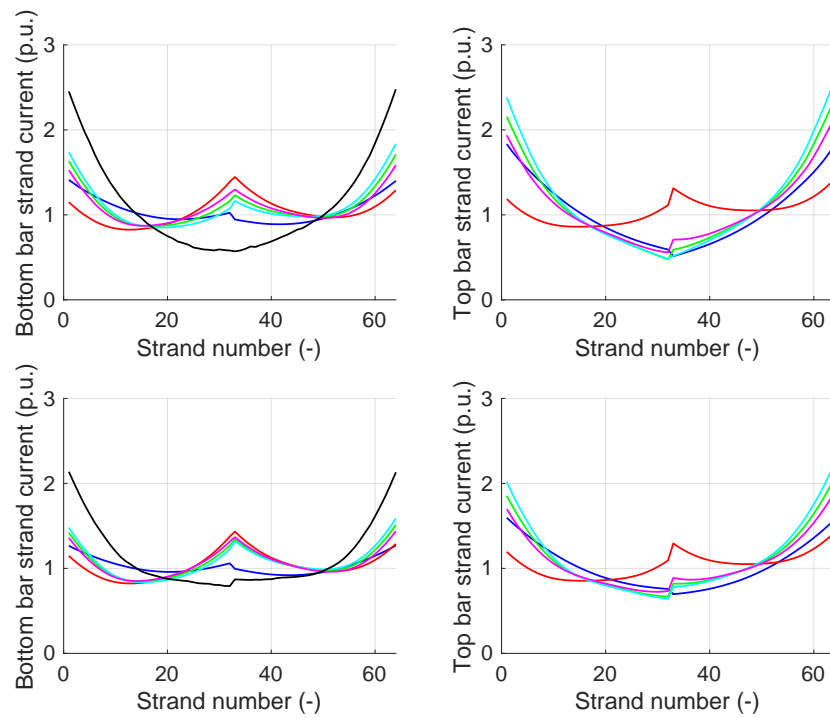
Figure 8.6 – Influence of the operation on the stator circulating currents. The top row of figures corresponds to the nominal operation point, the bottom row of figures corresponds to the stator short-circuit operation. The blue curve is related to case 1, the red one to case 2, the green one to case 3, the cyan one to case 4, the magenta one to case 5 and finally the black one to case 6.

circulating currents, one should therefore take the magnetic boundary as well as the operating point into account. The numerical value of the calculated fs-factor is higher for the bottom bar of the DFIG than the results shown in figure 3.2 for the turbogenerator, which can be explained by the high winding overhang to active length ratio, very small air-gap compared to the turbogenerator and presence of magnetisable iron on the total length of the winding overhang.
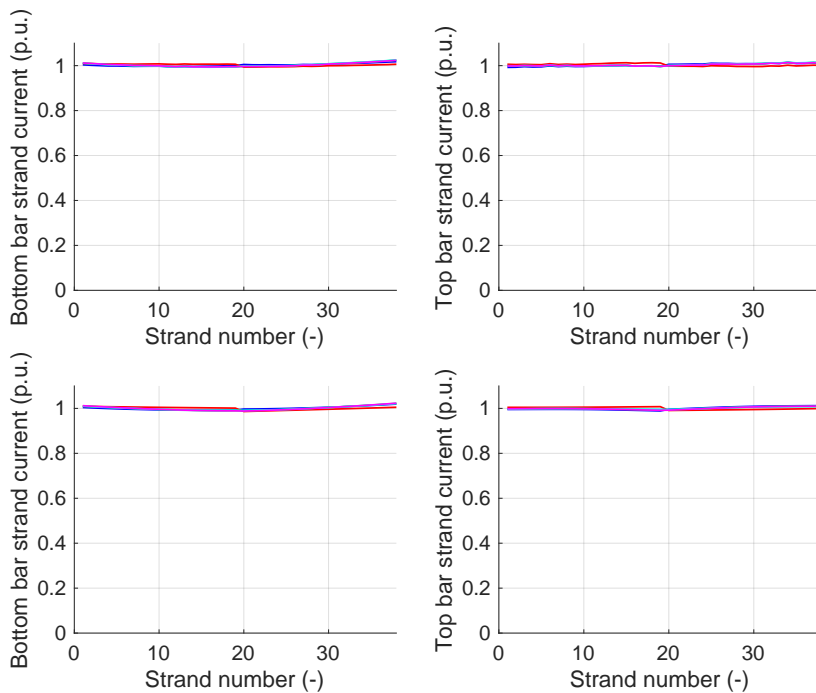
Figure 8.7 – Influence of the operation on the rotor circulating currents. The top row of figures corresponds to the nominal operation point, the bottom row of figures corresponds to the stator short-circuit operation. All quasi-superposed curves correspond to a specific case described in table 8.1.

The calculated circulating currents for the rotor are presented in figure 8.7. In all simulated cases, there is no circulating current. This is very positive, as it means that the roebel bar is already optimised regarding its current distribution. This is due to a positive combination of two facts: the first one is that the strands can be seen as resistive in the case of the low frequency, typically 1-5Hz, of the rotor currents, while the resistance of each strand is quasi the same, so that the currents will be split equally between all strands. The second one is that the rotor frequency is low, so the induced voltage will have a very small amplitude. Both factors are the root cause of the very low circulating currents, which is in-line with the known fact that the eddy current losses of the rotor winding are very low for the rotor of this type of machines. It is very important to point out that the amplitude of the induced flux is more or less the same for the stator winding as well as the rotor winding.

8.3. Impact of the different cases on the circulating currents of a stator and rotor bar with a 360° transposition

Table 8.2 – Fs-factor for the calculated windings (TB = top bar, BB = bottom bar) for the different cases defined in table 8.1 at varying operation points.

Name	Fs-factor stator TB	Fs-factor stator BB	Fs-factor rotor TB	Fs-factor rotor BB
Case 1 OP	1.1975	1.1106	1.0063	1.0061
Case 1 CC	1.1121	1.0619	1.0006	1.0006
Case 2 OP	1.1129	1.1143	1.0067	1.0058
Case 2 CC	1.1051	1.1037	1.0004	1.0003
Case 3 OP	1.4404	1.2244	1.0072	1.0067
Case 3 CC	1.2971	1.167	1.001	1.0009
Case 4 OP	1.6069	1.2542	1.0078	1.0067
Case 4 CC	1.4001	1.1812	1.0015	1.0011
Case 5 OP	1.3089	1.2012	1.0068	1.0066
Case 5 CC	1.215	1.1549	1.0007	1.0008
Case 6 OP	-	1.536	-	-
Case 6 CC	-	1.412	-	-
Case 7 OP	1.7960	1.2406	1.0102	1.0085
Case 7 CC	1.4922	1.1444	1.0035	1.0034

Table 8.2 presents the fs-factor for the calculated cases. It was possible to perform a comparison simulation with the in-use software developed for turbogenerators, with the stator bar geometry shown in figure 7.1 and no rotor winding. The slot inductance model is Model 1.0, the winding overhang inductances are calculated using the formulas developed in [68] for case 2 for the operation mode with an infinite permeability boundary and a zero permeability boundary.

Table 8.3 – Fs-factor for the calculated windings (TB = top bar, BB = bottom bar) comparison between this work (tw) and the in-use (iu) software.

Name	Fs-factor stator TB (tw)	Fs-factor stator TB (iu)	Fs-factor stator BB (tw)	Fs-factor stator BB (iu)
Case 2 OP /$\mu = 0$	1.1129	1.1203	1.1143	1.1125
Case 2 CC /$\mu = \inf$	1.1051	1.1172	1.1037	1.1129

Table 8.3 presents the obtained fs-factors for the stator winding with this work and the in-use software. It is very interesting to point out that the fs-factors has very similar values but in the in-use software the boundary has a much smaller impact than in this work. This difference is very small even though the models are fundamentally different by the degree of precision they take physics into account. It is very difficult to draw conclusions from this singular example, there should me more comparisons made to validate the hypothesis of very similar values between the two softwares. But it is a very positive sign that both softwares give quasi the

same result, as this shows that the fs-factor for DFIG is above the value normally obtained for hydrogenerators, which is another proof of the existence of non negligible circulating currents in DFIG.
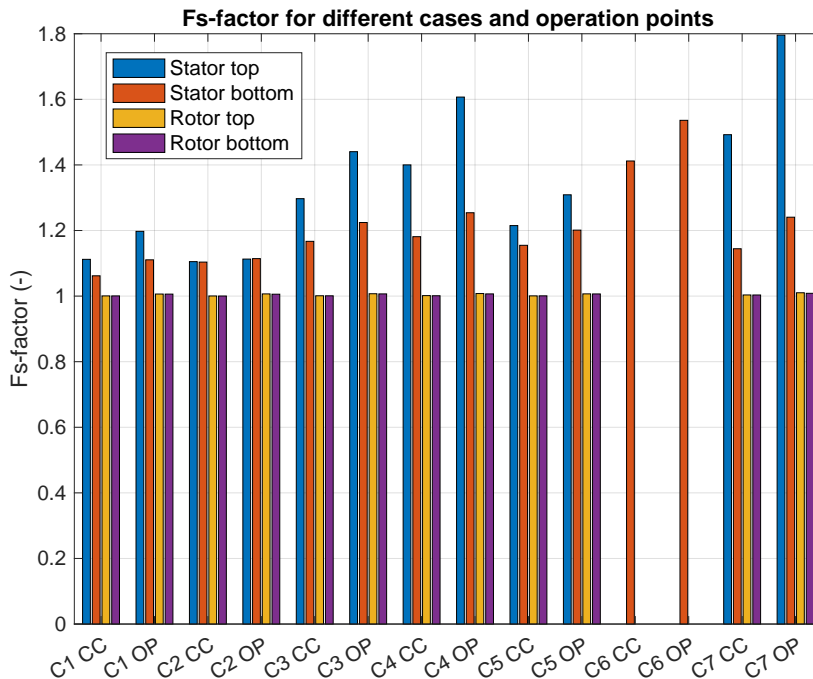
Figure 8.8 – Fs-factor for the calculated windings (TB = top bar, BB = bottom bar) for the different cases defined in table 8.1 under varying operation points.

Figure 8.8 presents the same results as table 8.2 in the form of a bar graph. The choice of the boundary has a significant impact on the fs-factor as well as the considered operation point.

For case 6, it was not possible to compute the circulating currents for the other cases as the induced voltage was not enough sinusoidal. This is certainly due to the coarse 3D-mesh that is used for the complete simulation model. Due to restrictions on the maximal queue time in the HPC is was not possible to increase the model size.

8.4 Impact of the temperature on the circulating currents of a stator bar with a 360° transposition

The copper temperature, which influences the copper resistance, can influence the circulating current losses as one can see in the original figure 8.9. The lower the temperature, the lower the resistance which tends to higher the circulating currents. This can be explained using the fact that a small resistance will create less circulating current damping as the induced voltage remains constant. This effect depends also on the ratio of inductance to resistance. The lower this ratio is, the more the circulating currents will depend on temperature changes.

Figure 8.9 – Influence of the stator copper temperature on the circulating currents in the case of a 0/360/0 transposition (case 3 CC).

8.5 Differences between a 360°, a 450° and a 540° transposition in the active part on the circulating currents of a stator bar

Figures 8.10 and 8.11 present an original result about the impact of a well-known special active part transposition (0/360/0 or 0/450/0 or 0/540/0), on the stator circulating currents with and without taking the ventilation slits into account. The curves show a very similar behaviour to the one presented in chapter 3. Taking the ventilation slits into account or not has only a very marginal impact on the circulating currents.

8.6 Impact of an overhang transposition on the circulating currents

Figures 8.12 and 8.13 show as another original result the impact of a known overhang roebelisation for a stator bottom and top bar. In the case of the bottom bar, the reduction of the circulating currents is very satisfying. The remaining circulating currents have a fs-factor of 1.5%, which can be considered as the target value when optimising the circulating current losses. For the top bar, the resulting circulating currents are higher with a fs-factor of around 10%. This is due to the long straight uncompensated end-winding portion at the end of the active part. This portion could be further optimised using the so-called extended transposition technique. This could help to further reduce the fs-factor for the top bars.
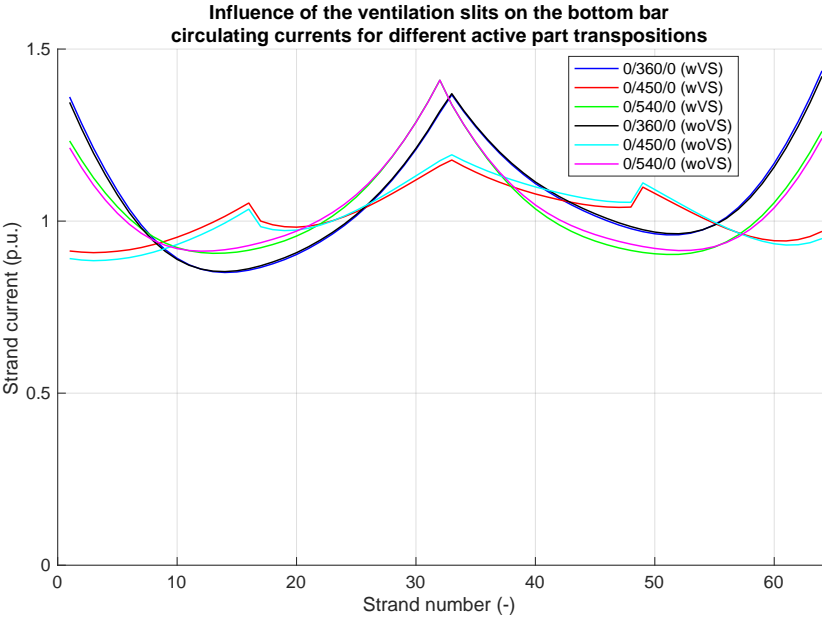
Figure 8.10 – Influence of the ventilation slits on the bottom bar circulating currents for different active part transpositions (case 3 CC).
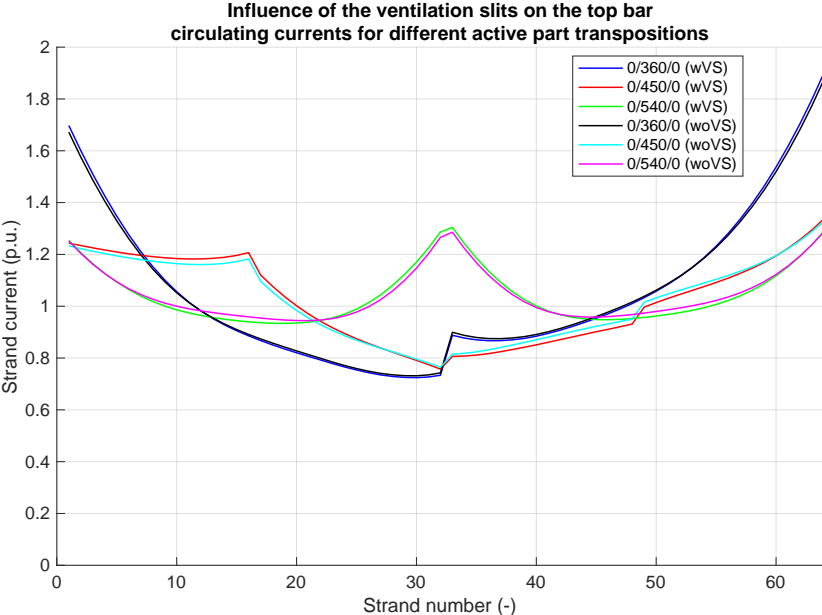
Figure 8.11 – Influence of the ventilation slits on the top bar circulating currents for different active part transpositions (case 3 CC).
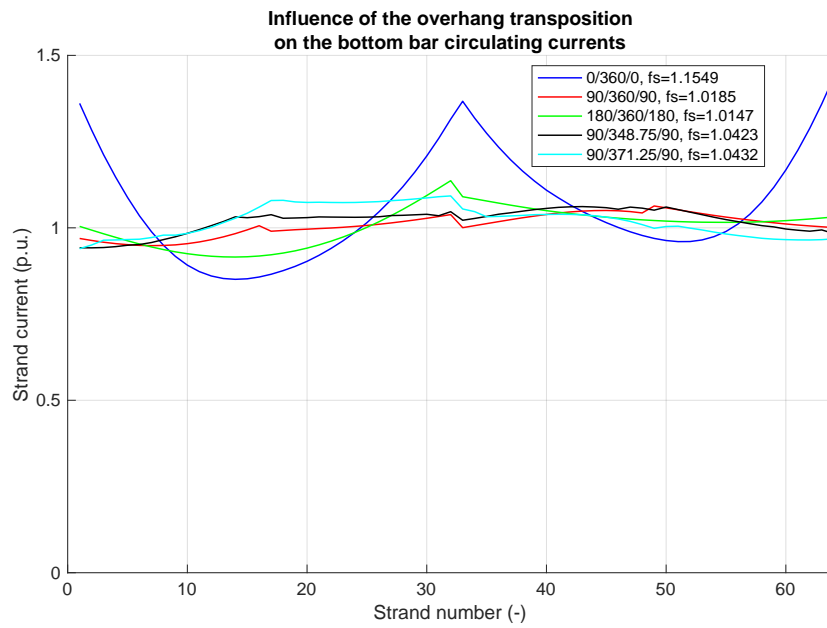
Figure 8.12 – Influence of winding overhang transposition on the bottom bar circulating currents (case 3 CC).
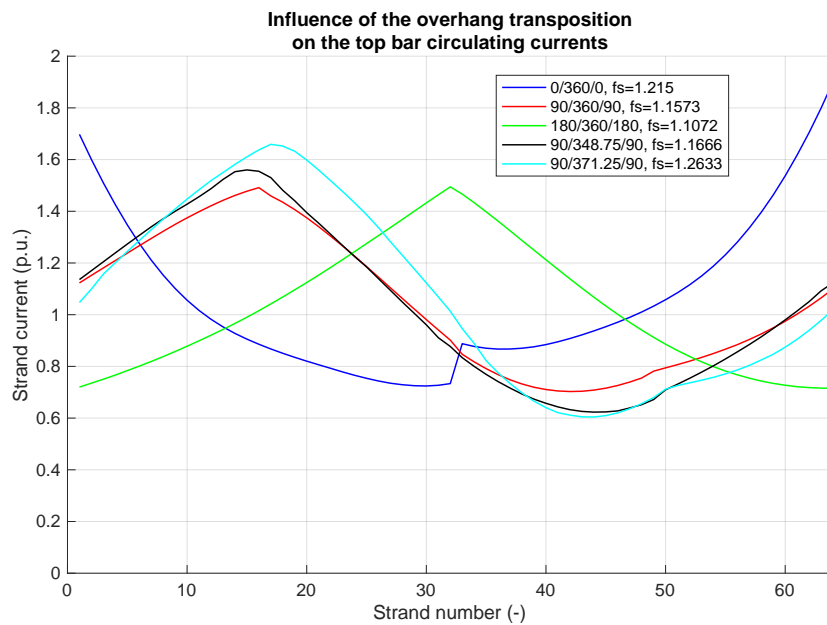
Figure 8.13 – Influence of winding overhang transposition on the top bar circulating currents (case 3 CC).

8.7 Impact of the ventilation slits with an under-roebelisation in the active part
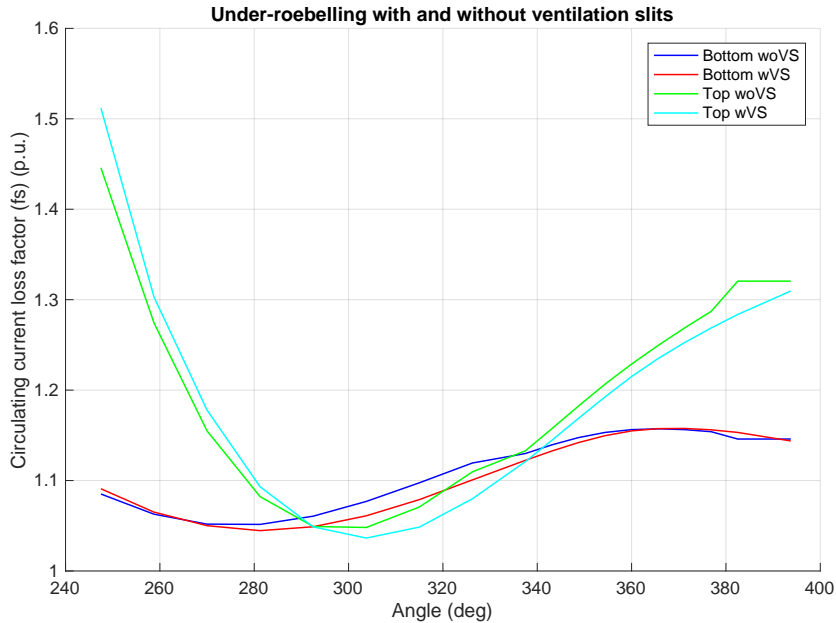
Figure 8.14 – Impact of the ventilation slits (present or not) in the case of an under-roebelisation in the active part (case 3 CC).

Figure 8.14 presents an original result the impact of the ventilation slits in the case of an under-roebelisation in the active part. This effect is well known in turbogenerators [52], but its impact to DFIG is an original contribution of this study. On can see that independent of the fact that the ventilation slits are taken into account or not, there is a reduction of the circulating current. The loss optimum is located at the same transposition with or without ventilation slits, which is very positive as it demonstrates the insensitivity of the ventilation to the location of the maximum, mathematically that the fact that the inductance of the iron active part contributes quasi the total of this compensation effect. It must be pointed out that the ventilation slits impact the amplitude of the circulating by inducing a small change of the branch impedance. The curves of figure 8.14 show a similar behaviour as the ones published in [52].

8.8 Impact of the variation of ventilation slits with special transposition in the active part

The last effect that has been studied is the impact of the distribution of the ventilation slits on the circulating currents for the 3 "classical" special transpositions in the active part. The DFIG under study has 54 ventilation slits with 8mm thickness, which are not equally distributed as the stacks are made of iron sheets of 0.5mm of thickness. The distribution is such that the

8.8. Impact of the variation of ventilation slits with special transposition in the active part
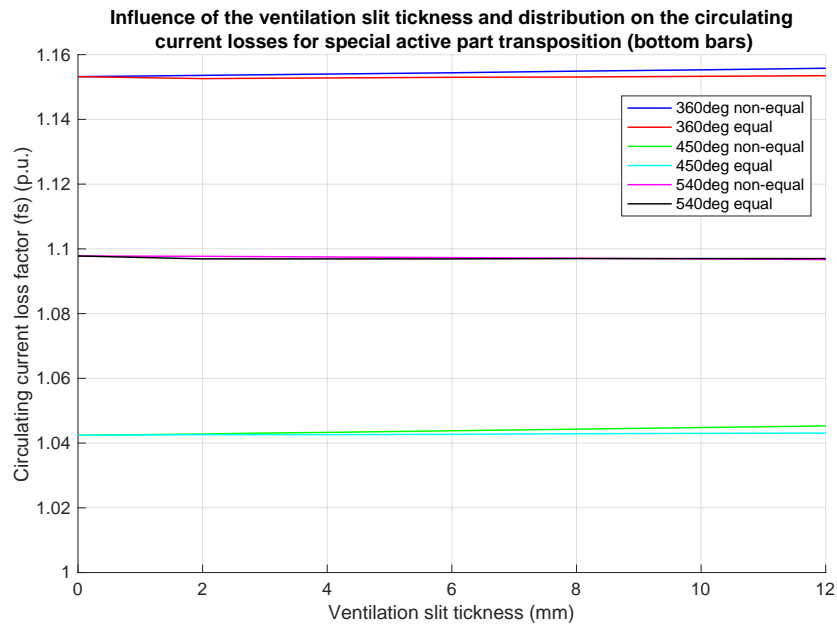
Figure 8.15 – Influence of the variation of the ventilation slits length and equal or non-equal distribution on the bottom bar circulating currents in the case of special transposition in the active part (case 3 CC).
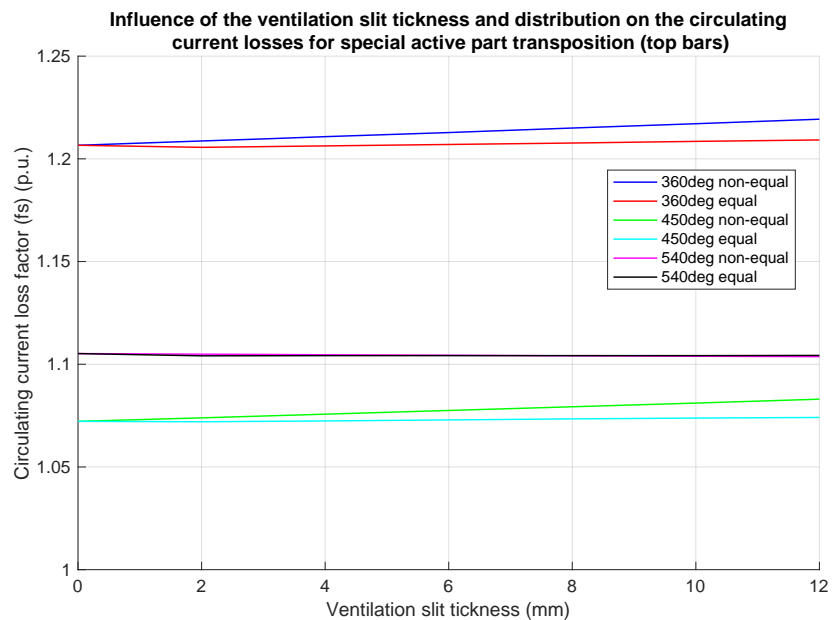
Figure 8.16 – Influence of the variation of the ventilation slits length and equal or non-equal distribution on the top bar circulating currents in the case of special transposition in the active part (case 3 CC).

stacking thickness is higher at the end of the active part and smaller in the middle. The number of ventilation slits is kept constant for this study. This effect has been studied numerically to analyse the impact of the hypothesis postulated in [52] to the DFIG, which constitutes an original contribution of this work. As one can see directly from figures 8.15 and 8.16, there is a marginal impact due to the ventilation slit thickness and distribution. This impact is higher for larger ventilation slits and higher for the top bar, mainly because the inductance is smaller for top bar strands than for bottom bar strands. The impact is the highest for the 0/360/0 transposition. The curves of figure 8.14 show a similar behaviour as the one published in [52] even if it was not possible to validate the formulas presented in [52] to the case of a DFIG.

8.9   Conclusion

The rotor winding of the DFIG has a very low fs-factor, while the stator winding has a quite high fs-factor. It can be very interesting from an efficiency point of view to reduce that factor, which will also bring a stator bar with more equilibrated losses in the winding overhang. For the stator winding, the loss reduction potential lies around 20% of the DC-copper losses, which is above the potential for hydrogenerators but below turbogenerators. Regarding the thermal footprint, it is difficult to give a quantitative loss reduction as the ventilation losses depend on all losses, so that the impact of a reduction of circulating losses must be compared to the total amount of losses and the air flow in the winding overhang. But a reduction of the circulating current losses will lead to a reduction of the ventilation losses via a reduction of the volume flow. The optimisation can be done using under-roebelling and / or winding overhang roebelling and it must be carried out for each machine design separately. The influence of the operation point on the fs-factor is not negligible, so that the circulating current calculation should be performed over all operation points of the machine taking into account how the losses will be measured: using the IEC-approach of segregated losses measurement or a non-normalized approach of total losses measurement for all the guaranteed efficiencies. The influence of the ventilation slits has also being studied in detail. It was possible to show that a non-equal ventilation slit distribution has a very small impact of the fs-factor, this impact is higher for top bars than for bottom bars. The ventilation slit thickness also has only a marginal impact on the fs-factor, even in the case of special active part transposition. When applying under-roebelling one should take into account the ventilation slits, as the curves are quite different with or without them, and could lead to wrong optimisation results which could lead to a damage of the stator winding.

9 Conclusion

The goal of this study is to calculate the circulating currents within a precision of 1%. Therefore, the developed models and methodology open the path to this precision by including all effects that could have an impact. The agreement between the developed models and finite-element simulation is excellent, transposing the precision of the developed models.

This work presented many original contributions and results which are briefly summarised hereafter. Chapter 2 is dedicated to the description of the published calculation methods and the choice of the calculation method used in this work, namely the inductance calculation method as well as the constituant parts of the calculation method and the equation system solved. Chapter 3 started with an extensive and comprehensive current situation of the circulating current calculation applied to salient pole synchronous machines including several original contributions. This study showed the loss optimisation potentials as well as the typical circulating current behaviour under different classical transpositions of the active part as well as in the winding overhang.

In chapter 4, this work continued with a deep analysis of the well-known slot inductance model, which helped to determine which parameter must be accurately taken into account in the slot inductance model. Starting from the model 1.0, 3 novel slot inductance models have been developed. This chapter ended with the presentation of the novel slot differential inductance model, which has been compared to measurements.

Chapter 5 was dedicated to the magnetic field in the winding overhang, where the analytical formulas developed by Urankar have been corrected and compared successfully to finite-element simulations. The mathematical treatment of the non-linear rotor overhang iron has been presented and validated afterwards. Finally the novel rotor overhang inductance model is compared to measurements, which showed that the novel inductance model is more precise than the existing one.

The original transient analytical expression used for the calculation of the two-phase short-circuit currents and torque as well as the expressions for the rotor current of a DFIG are the

highlight of the chapter 6 dedicated to the transient analytical calculation. Then some original results in the domain of the end winding force calculation (chapter 7) and finally, the original circulating current calculation in the rotor and stator winding of a DFIG is detailed in the last chapter (chapter 8).

The experimental validation could unfortunately not be performed with the requested precision. The precision level achieved for the experimental validation is 5 %, which is above the threshold, but the measurement precision could not be reduced below 5% with the equipment of the laboratory. One can conclude that the models are validated theoretically within the given precision, but today's experimental validation is above. The latter could be reduced using more precise laboratory equipment.

On a more industrial perspective, the novel models constitute a very important contribution to the design optimisation of DFIG, even if the current precision is 1% theoretically and 5% experimentally. With this precision, one can optimise the circulating currents in stator windings and obtain a loss reduction of around 20% of the DC-copper losses. In addition, the homogenisation of the current distribution creates an opportunity for a ventilation loss reduction. Finally, the DFIG has less circulating current losses than a turbogenerator because its bars are shorter and its overhangs smaller. But the DFIG has more circulating current losses than a hydrogenerator as the rotor winding has more or less the same axial length than the stator winding and there is a magnetic rotor overhang.

The main outlook of this study is to reduce the measurement precision to experimentally validate the developed models up to the targeted precision. Another important outlook is to validate the complete model with in-site measurements on a real DFIG.

Further improvements could be done in the domain of the end winding numerical field calculation, where the model could be implemented using CUDA instead of C++ to reduce the computational time by changing the processor architecture and move in direction of the future. One could implement some matrix memory optimisation to reduce the memory need. Another possibility would be to study if the magnetic field created by the current-carrying conductors or magnetisable elements could be approximated using cylindrical harmonics, which would lead to an important calculation time reduction as well as to a very precise control of the calculation precision. All these improvements can help to develop the 3D integral calculation tool, enhance its precision and help to broaden its application range keeping in mind that this tool could be the basis for the future of magnetic field computation as its kernel is intrinsically done for GPU-based highly parallelised computing architecture with low memory.

Regarding the transient phenomena a very interesting outlook would be to add the rotor crowbar to the analytical expressions as well as to compute the current and torque in the case of a 2-phase short-circuit for a synchronous machine, where exact analytical expressions are also lacking.

On a more practical point of view, the main outlook lies in a deep study of the boundaries and operating points to define precise rules to compute the circulating currents for a DFIG. Another very important outlook is to perform a deep and detailed sensitivity analysis of the models developed to manufacturing tolerances (BH-characteristics, stator winding tolerances, ...). In the force topic, an interesting outlook would be to study the winding overhang design changes that would reduce the winding overhang forces. Another outlook is to study more operating points to gain knowledge of the impact of the operating points on the circulating currents. It is also very important to continue the research on the simulation problem for the magnetic case in chapter 8, to be able to compute the circulating losses with magnetic boundaries.

A Appendix

A.5 Appendix to Chapter 5

A.5.1 Calculation of A_ϕ

This expression will be divided into 4 integrals, which will be integrated using integration by parts.

$$I_1 = \frac{1}{2} \int_{\rho_1}^{\rho_2} d\phi \quad \gamma D(\phi) \cos(\phi) \tag{A.1}$$

$$I_2 = \int_{\rho_1}^{\rho_2} d\phi \quad \gamma r \cos(\phi)^2 \operatorname{arcsinh} \beta_1(\phi) \tag{A.2}$$

$$I_3 = \frac{1}{2} \int_{\rho_1}^{\rho_2} d\phi \quad \left(r'^2 - r^2 \cos(2\phi)\right) \operatorname{arcsinh} \beta_2(\phi) \cos(\phi) \tag{A.3}$$

$$I_4 = -\frac{1}{2} \int_{\rho_1}^{\rho_2} d\phi \quad r^2 \sin(2\phi) \arctan \beta_3(\phi)) \cos(\phi). \tag{A.4}$$

The integral I_1 can be solved by transforming it into an elliptical integral

$$\begin{aligned}
I_1 =& \frac{1}{2} \int_{\rho_1}^{\rho_2} d\phi \quad \gamma D(\phi) \cos(\phi) \\
=& \gamma a \int_{\alpha_1}^{\alpha_2} d\alpha \quad \left(1 - 2\sin(\alpha)^2\right) \sqrt{1 - k^2 \sin(\alpha)^2} \\
=& \gamma a \Big(E(\alpha, k) + 2\gamma a \Big(\frac{1}{3} \big(\frac{1}{k^2} - 1\big) F(\alpha, k) + \frac{1}{3} \big(2 - \frac{1}{k^2}\big) E(\alpha, k) \\
& - \frac{1}{3} \sin(\alpha) \cos(\alpha) \sqrt{1 - k^2 \sin(\alpha^2)} \Big) \Big) \Big|_{\alpha=\alpha_1}^{\alpha=\alpha_2}
\end{aligned} \tag{A.5}$$

where $F(\alpha, k)$ is the first order elliptic integral and $E(\alpha, k)$ is the second order elliptic integral. Doing a similar transformation for the integral I_2 leads to

$$
\begin{aligned}
I_2 &= \int_{\rho_1}^{\rho_2} d\phi \quad \gamma r \cos(\phi)^2 \operatorname{arcsinh} \beta_1(\phi) \\
&= \frac{1}{2} \gamma r \int_{\rho_1}^{\rho_2} d\phi \quad \operatorname{arcsinh} \beta_1(\phi) + \frac{1}{2} \gamma r \int_{\rho_1}^{\rho_2} d\phi \quad \cos(2\phi) \operatorname{arcsinh} \beta_1(\phi).
\end{aligned}
\tag{A.6}
$$

The first integral (I_{2a}) will be solved numerically, as no analytical expression can be found for it. For the second one, using integration by parts leads to

$$
\begin{aligned}
I_{2b} &= \frac{1}{2} \gamma r \int_{\rho_1}^{\rho_2} d\phi \quad \cos(2\phi) \operatorname{arcsinh} \beta_1(\phi) \\
&= \frac{1}{4} \gamma r \sin(2\phi) \operatorname{arcsinh} \beta_1(\phi) \Big|_{\phi=\phi_1'}^{\phi=\phi_2'} \\
&\quad - \frac{1}{4} \gamma r \int_{\rho_1}^{\rho_2} d\phi \quad \sin(2\phi) \left(\frac{r \sin(\phi)}{D(\phi)} - r^2 \frac{\cos(\phi) \sin(\phi) r' - r \cos(\phi)^2 \sin(\phi)}{G(\phi) D(\phi)} \right).
\end{aligned}
\tag{A.7}
$$

To simplify, the integrals are divided into two parts

$$
\begin{aligned}
I_{2b1} &= -\frac{1}{4} \gamma r \int_{\rho_1}^{\rho_2} d\phi \quad \sin(2\phi) \frac{r \sin(\phi)}{D(\phi)} \\
&= \frac{1}{a} \gamma r^2 \int_{\alpha_1}^{\alpha_2} d\alpha \quad \frac{\sin(\alpha)^2 \cos(\alpha)^2 (1 - 2\sin(\alpha)^2)}{\sqrt{1 - k^2 \sin(\alpha^2)}} \\
&= \frac{1}{a} \gamma r^2 \int_{\alpha_1}^{\alpha_2} d\alpha \quad \frac{\sin(\alpha)^2 (1 - \sin(\alpha)^2)(1 - 2\sin(\alpha)^2)}{\sqrt{1 - k^2 \sin(\alpha^2)}} \\
&= \frac{1}{a} \gamma r^2 \int_{\alpha_1}^{\alpha_2} d\alpha \quad \frac{\alpha_0 + \alpha_2 \sin(\alpha)^2 + \alpha_4 \sin(\alpha)^4 + \alpha_6 \sin(\alpha)^6}{\sqrt{1 - k^2 \sin(\alpha^2)}} \\
I_{2b2} &= \frac{1}{4} \gamma r^3 \int_{\rho_1}^{\rho_2} d\phi \quad \sin(2\phi) \frac{\cos(\phi) \sin(\phi) r' - r \cos(\phi)^2 \sin(\phi)}{G(\phi) D(\phi)} \\
&= \frac{1}{2} \gamma r^3 \int_{\rho_1}^{\rho_2} d\phi \quad \frac{\cos(\phi)^2 \sin(\phi)^2 r' - r \cos(\phi)^3 \sin(\phi)^2}{G(\phi) D(\phi)} \\
&= -\frac{1}{2a} \gamma r^3 \int_{\alpha_1}^{\alpha_2} d\alpha \frac{(1 - 2\sin(\alpha))^2 4 \sin(\alpha)^2 (1 - \sin(\alpha)^2) r'}{G(\alpha) \sqrt{1 - k^2 \sin(\alpha^2)}} \\
&\quad + \frac{1}{2a} \gamma r^3 \int_{\alpha_1}^{\alpha_2} d\alpha \frac{r(1 - 2\sin(\alpha)^2)^3 4 \sin(\alpha)^2 (1 - \sin(\alpha)^2)}{G(\alpha) \sqrt{1 - k^2 \sin(\alpha^2)}} \\
&= -\frac{1}{2a} \gamma r^3 \int_{\alpha_1}^{\alpha_2} d\alpha \frac{\alpha_0 + \alpha_2 \sin(\alpha)^2 + \alpha_4 \sin(\alpha)^4 + \alpha_6 \sin(\alpha)^6 + \alpha_8 \sin(\alpha)^8 + \alpha_{10} \sin(\alpha)^{10}}{G(\alpha) \sqrt{1 - k^2 \sin(\alpha^2)}}
\end{aligned}
\tag{A.8}
$$

$$
\tag{A.9}
$$

The results for the integrals of equations (A.8) and (A.9) can be found in [22]. The third integral will be decomposed in two parts

$$
\begin{aligned}
I_{3b1} &= \frac{1}{2} r'^2 \int_{\rho_1}^{\rho_2} d\phi \quad \cos(\phi) \operatorname{arcsinh}(\beta_2(\phi)) \\
I_{3b2} &= -\frac{1}{2} r^2 \int_{\rho_1}^{\rho_2} d\phi \quad \cos(2\phi) \cos(\phi) \operatorname{arcsinh}(\beta_2(\phi)).
\end{aligned}
\tag{A.10}
$$

The integration will also be done using integration by parts leading to

$$
\begin{aligned}
I_{3b1} &= \frac{1}{2} r'^2 \int_{\rho_1}^{\rho_2} d\phi \quad \cos(\phi) \operatorname{arcsinh}(\beta_2(\phi)) \\
&= \frac{1}{2} r'^2 \sin(\phi) \operatorname{arcsinh}(\beta_2(\phi)) \\
&\quad + \frac{1}{2} r'^3 r \int_{\rho_1}^{\rho_2} d\phi \quad \frac{\sin(\phi)^2}{B^2(\phi) D(\phi)}
\end{aligned}
\tag{A.11}
$$

for I_{3b1}. This integral can be transformed into an elliptic integral

$$
\begin{aligned}
I &= -r'^3 r \int_{\rho_1}^{\rho_2} d\alpha \quad \frac{4 \sin(\alpha)^2 (1 - \sin(\alpha)^2)}{B^2(\alpha) D(\alpha)} \\
&= -r'^3 r \int_{\rho_1}^{\rho_2} d\alpha \quad \frac{4 \sin(\alpha)^2 (1 - \sin(\alpha)^2)}{B^2(\alpha) D(\alpha)} \\
&= -r'^3 r \int_{\rho_1}^{\rho_2} d\alpha \quad \frac{4 \sin(\alpha)^2 - 4 \sin(\alpha)^4}{B^2(\alpha) D(\alpha)}.
\end{aligned}
\tag{A.12}
$$

Doing the same procedure for the second integral I_{3b2} leads to

$$
\begin{aligned}
I_{3b2} &= -\frac{1}{2} r^2 \int_{\rho_1}^{\rho_2} d\phi \quad \cos(2\phi) \cos(\phi) \operatorname{arcsinh}(\beta_2(\phi)) \\
&= -\frac{1}{2} r^2 \int_{\rho_1}^{\rho_2} d\phi \quad (1 - 2 \sin(\phi)^2) \cos(\phi) \operatorname{arcsinh}(\beta_2(\phi)).
\end{aligned}
\tag{A.13}
$$

For the first part of the integral, please refer to the treatment of integral I_{3b1}. For the second part, using integration by parts leads to

$$
\begin{aligned}
I_{3b21} &= r^2 \int_{\rho_1}^{\rho_2} d\phi \quad \sin(\phi)^2 \cos(\phi) \operatorname{arcsinh}(\beta_2(\phi)) \\
&= \frac{r^2}{3} \sin(\phi)^3 \operatorname{arcsinh}(\beta_2(\phi)) \Big|_{\phi=\phi_1'}^{\phi=\phi_2'} - \frac{r^3 r' \gamma}{3} \int_{\rho_1}^{\rho_2} d\phi \quad \frac{\sin(\phi)^4}{B^2(\phi) D(\phi)}.
\end{aligned}
\tag{A.14}
$$

Appendix A. Appendix

The integral can be expressed in form of elliptic integrals

$$
I = -\frac{r^3 r' \gamma}{3} \int_{\rho_1}^{\rho_2} d\phi \quad \frac{\sin(\phi)^4}{B^2(\phi)D(\phi)} = \frac{2r^3 r' \gamma}{3a} \int_{\alpha_1}^{\alpha_2} d\alpha \quad \frac{(4\sin(\alpha)^2 - 4\sin(\alpha)^4)^4}{B^2(\alpha)\sqrt{1 - k^2 \sin(\alpha)^2}}
$$

$$
= \frac{2r^3 r' \gamma 4^4}{3a} \int_{\alpha_1}^{\alpha_2} d\alpha \quad \frac{\alpha_8 \sin(\alpha)^8 + \alpha_{10} \sin(\alpha)^{10} + \alpha_{12} \sin(\alpha)^{12} + \alpha_{14} \sin(\alpha)^{14} + \alpha_{16} \sin(\alpha)^{16}}{B^2(\alpha)\sqrt{1 - k^2 \sin(\alpha)^2}}
$$

$$(A.15)$$

which can be solved using the formulae given in [22]. For I_4 one obtains using integration by parts

$$
I_4 = -r^2 \int_{\rho_1}^{\rho_2} d\phi \quad \sin(\phi)\cos(\phi)^2 \arctan\beta_3(\phi) = +r^2 \frac{1}{3} \cos(\phi)^3 \arctan\beta_3(\phi) \Big|_{\phi=\phi_1'}^{\phi=\phi_2'}
$$

$$
+ r^2 \frac{1}{3} \int_{\rho_1}^{\rho_2} d\phi \quad \cos(\phi)^3 \left(\frac{\gamma r(r - r'\cos(\phi))}{D(\phi)B^2(\phi)} + \frac{\gamma r \cos(\phi)(r\cos(\phi) - r')}{D(\phi)G^2(\phi)} \right)
$$

$$(A.16)$$

The following integrals can be defined

$$
I_{41} = \frac{r^2}{3} \int_{\rho_1}^{\rho_2} d\phi \frac{\beta_3 \cos(\phi)^3 + \beta_4 \cos(\phi)^4}{D(\phi)B^2(\phi)}
$$

$$(A.17)$$

$$
I_{42} = \frac{r^2}{3} \int_{\rho_1}^{\rho_2} d\phi \frac{\beta_4' \cos(\phi)^4 + \beta_5' \cos(\phi)^5}{D(\phi)G^2(\phi)}.
$$

$$(A.18)$$

They can be transformed into elliptic integral using the fact that $\cos(\phi) = -(1 - 2\sin(\alpha)^2)$ into

$$
I_{41} = -\frac{2r^2}{3} \int_{\alpha_1}^{\alpha_2} d\alpha \frac{\alpha_0 + \alpha_2 \sin(\alpha)^2 + \alpha_4 \sin(\alpha)^4 + \alpha_6 \sin(\alpha)^6 + \alpha_8 \sin(\alpha)^8}{D(\alpha)B^2(\alpha)}
$$

$$(A.19)$$

$$
I_{42} = -\frac{2r^2}{3} \int_{\alpha_1}^{\alpha_2} d\alpha \frac{\alpha_0 + \alpha_2 \sin(\alpha)^2 + \alpha_4 \sin(\alpha)^4 + \alpha_6 \sin(\alpha)^6 + \alpha_8 \sin(\alpha)^8 + \alpha_{10} \sin(\alpha)^{10}}{D(\alpha)G^2(\alpha)}.
$$

$$(A.20)$$

A.5.2 Calculation of H_z

Starting with the expression for H_r leads to

$$
H_{r1} = \int_{\rho_1}^{\rho_2} d\phi \quad \cos(\phi)D(\phi)
$$

$$(A.21)$$

$$
H_{r2} = \int_{\rho_1}^{\rho_2} d\phi \quad r\cos(\phi)^2 \operatorname{arcsinh}\beta_1(\phi).
$$

$$(A.22)$$

The integration of the expression of H_{r1} is already done in expression I_1 for A_ϕ. For the integration of H_{r2}, refer to the integration of I_2. The integration for H_ϕ is done in a similar way

as for A_r. Integrating first over ϕ leads to

$$
\begin{aligned}
H_\phi &= \int_{\rho_1}^{\rho_2} d\phi \int_{r_1'}^{r_2'} dr' \int_{z_1'}^{z_2'} dz' \frac{-\gamma r' \sin(\phi)}{D(\phi)^3} \\
&= \frac{1}{r} \int_{r_1'}^{r_2'} dr' \int_{z_1'}^{z_2'} dz' \frac{\gamma}{D(\phi)} \bigg|_{\phi=\phi_1'}^{\phi=\phi_2'} \\
&= \frac{1}{r} \int_{r_1'}^{r_2'} dr' D(\phi) \bigg|_{\phi=\phi_1'}^{\phi=\phi_2'} \bigg|_{z'=z_1'}^{z'=z_2'} \\
&= \frac{1}{r} \bigg((\gamma^2 + r^2 \sin(\phi)^2) \operatorname{arcsinh}\left(\frac{r' - r\cos(\phi)}{\sqrt{\gamma^2 + r^2 \sin(\phi)^2}} \right) \\
&\quad + \frac{1}{2} (r' - r\cos(\phi)) D(\phi) \bigg) \bigg|_{r'=r_1'}^{r'=r_2'} \bigg|_{\phi=\phi_1'}^{\phi=\phi_2'} \bigg|_{z'=z_1'}^{z'=z_2'} .
\end{aligned}
\tag{A.23}
$$

For H_z the following integrals needs to be calculated

$$
H_{z1} = \int_{\rho_1}^{\rho_2} d\phi \quad \gamma \operatorname{arcsinh} \beta_1(\phi)
\tag{A.24}
$$

$$
H_{z2} = \int_{\rho_1}^{\rho_2} d\phi \quad -r\cos(\phi) \operatorname{arcsinh} \beta_2(\phi)
\tag{A.25}
$$

$$
H_{z3} = \int_{\rho_1}^{\rho_2} d\phi \quad -r\sin(\phi) \arctan \beta_3(\phi).
\tag{A.26}
$$

As the first integral (H_{z1}) has no analytical expression, it will be evaluated numerically. For H_{z2}, using integration by parts leads to

$$
\begin{aligned}
H_{z2} &= \int_{\rho_1}^{\rho_2} d\phi \quad -r\cos(\phi) \operatorname{arcsinh} \beta_2(\phi) \\
&= -r\sin(\phi) \operatorname{arcsinh}(\beta_2(\phi)) \bigg|_{\phi=\phi_1'}^{\phi=\phi_2'} - r^2 r' \gamma \int_{\rho_1}^{\rho_2} d\phi \quad \frac{\sin(\phi)}{B^2(\phi) D(\phi)}.
\end{aligned}
\tag{A.27}
$$

The remaining integral will be transformed into an elliptic integral

$$
\begin{aligned}
I &= -r^2 r' \gamma \int_{\rho_1}^{\rho_2} d\phi \quad \frac{\sin(\phi)}{B^2(\phi) D(\phi)} \\
&= \frac{8\gamma r^2 r'}{(r+r')^2 a} \int_{\alpha_1}^{\alpha_2} d\alpha \quad \frac{\sin(\alpha)^2 - \sin(\alpha)^4}{(1 - n^2 \sin(\alpha)^2)\sqrt{1 - k^2 \sin(\alpha)^2}}.
\end{aligned}
\tag{A.28}
$$

These elliptic integrals can be solved using the formulae of [22]. For H_{z3} one gets

$$
\begin{aligned}
H_{z3} &= \int_{\rho_1}^{\rho_2} d\phi \quad -r\sin(\phi) \arctan \beta_3(\phi) = r\cos(\phi) \arctan \beta_3(\phi) \bigg|_{\phi=\phi_1'}^{\phi=\phi_2'} \\
&\quad + \gamma r^2 \int_{\rho_1}^{\rho_2} d\phi \quad \cos(\phi) \left(\frac{r - r'\cos(\phi)}{D(\phi) B^2(\phi)} + \frac{\cos(\phi)(r\cos(\phi) - r')}{D(\phi) G^2(\phi)} \right).
\end{aligned}
\tag{A.29}
$$

Appendix A. Appendix

Defining two integrals (I_1 and I_2) that will be transformed into elliptic integrals gives

$$I_1 = \gamma r^2 \int_{\rho_1}^{\rho_2} d\phi \quad \cos(\phi) \frac{r - r' \cos(\phi)}{D(\phi) B^2(\phi)} \tag{A.30}$$

$$I_2 = \gamma r^2 \int_{\rho_1}^{\rho_2} d\phi \quad \cos(\phi) \frac{\cos(\phi)(r \cos(\phi) - r')}{D(\phi) G^2(\phi)}. \tag{A.31}$$

For I_1 one gets

$$\begin{aligned}
I_1 &= \frac{2r^2\gamma}{a(r+r')^2} \int_{\alpha_1}^{\alpha_2} d\alpha \quad (1 - 2\sin(\alpha)^2) \frac{r + r'(1 - 2\sin(\alpha)^2)}{(1 - n^2 \sin(\alpha)^2) \sqrt{1 - k^2 \sin(\alpha)^2}} \\
&= \frac{2r^2\gamma}{a(r+r')^2} \int_{\alpha_1}^{\alpha_2} d\alpha \quad \frac{\alpha_0 + \alpha_2 \sin(\alpha)^2 + \alpha_4 \sin(\alpha)^4}{(1 - n^2 \sin(\alpha)^2) \sqrt{1 - k^2 \sin(\alpha)^2}}.
\end{aligned} \tag{A.32}$$

These elliptic integrals can be solved using the formulae of [22]. For I_2 the transformation into elliptic integrals leads to

$$\begin{aligned}
I_2 &= -\frac{2r^2\gamma}{a} \int_{\alpha_1}^{\alpha_2} d\alpha \quad (1 - 2\sin(\alpha)^2)^2 \frac{r(1 - 2\sin(\alpha)^2) + r'}{G^2(\alpha) \sqrt{1 - k^2 \sin(\alpha)^2}} \\
&= -\frac{2r^2\gamma}{a} \int_{\alpha_1}^{\alpha_2} d\alpha \quad \frac{\alpha_0 + \alpha_2 \sin(\alpha)^2 + \alpha_4 \sin(\alpha)^4 + \alpha_6 \sin(\alpha)^6}{G^2(\alpha) \sqrt{1 - k^2 \sin(\alpha)^2}}.
\end{aligned} \tag{A.33}$$

These elliptic integrals can be solved using the formulae of [22]. In the case $r = 0$ the formulae for the vector potential and the magnetic field gets

$$\begin{aligned}
A_r &= \int_{\rho_1}^{\rho_2} d\phi \int_{r_1'}^{r_2'} dr' \int_{z_1'}^{z_2'} dz' \quad \frac{-r' \sin(\phi)}{(\gamma^2 + r'^2)^{1/2}} \\
&= \cos(\phi) \int_{z_1'}^{z_2'} dz' \quad \sqrt{\gamma^2 + r'^2} \Big|_{r'=r_1'}^{r'=r_2'} \Big|_{\phi=\phi_1'}^{\phi=\phi_2'} \\
&= \frac{1}{2} \cos(\phi) \left(r'^2 \operatorname{arcsinh}(\frac{\gamma}{|r'|}) + \gamma \sqrt{\gamma^2 + r'^2} \right) \Big|_{r'=r_1'}^{r'=r_2'} \Big|_{\phi=\phi_1'}^{\phi=\phi_2'} \Big|_{z'=z_1'}^{z'=z_2'}
\end{aligned} \tag{A.34}$$

$$\begin{aligned}
A_\phi &= \int_{\rho_1}^{\rho_2} d\phi \int_{r_1'}^{r_2'} dr' \int_{z_1'}^{z_2'} dz' \quad \frac{r' \cos(\phi)}{(\gamma^2 + r'^2)^{1/2}} \\
&= \sin(\phi) \int_{z_1'}^{z_2'} dz' \quad \sqrt{\gamma^2 + r'^2} \Big|_{r'=r_1'}^{r'=r_2'} \Big|_{\phi=\phi_1'}^{\phi=\phi_2'} \\
&= \frac{1}{2} \sin(\phi) \left(r'^2 \operatorname{arcsinh}(\frac{\gamma}{|r'|}) + \gamma \sqrt{\gamma^2 + r'^2} \right) \Big|_{r'=r_1'}^{r'=r_2'} \Big|_{\phi=\phi_1'}^{\phi=\phi_2'} \Big|_{z'=z_1'}^{z'=z_2'}
\end{aligned} \tag{A.35}$$

$$
\begin{aligned}
H_r &= \int_{\rho_1}^{\rho_2} d\phi \int_{r_1'}^{r_2'} dr' \int_{z_1'}^{z_2'} dz' \quad \frac{-\gamma r' \cos(\phi)}{(\gamma^2 + r'^2)^{3/2}} \\
&= \sin(\phi) \Big|_{\phi=\phi_1'}^{\phi=\phi_2'} \int_{z_1'}^{z_2'} dz' \quad \frac{\gamma}{\sqrt{\gamma^2 + r'^2}} \Big|_{r'=r_1'}^{r'=r_2'} \\
&= \sin(\phi) \sqrt{\gamma^2 + r'^2} \Big|_{r'=r_1'}^{r'=r_2'} \Big|_{\phi=\phi_1'}^{\phi=\phi_2'} \Big|_{z'=z_1'}^{z'=z_2'}
\end{aligned}
\tag{A.36}
$$

$$
\begin{aligned}
H_\phi &= \int_{\rho_1}^{\rho_2} d\phi \int_{r_1'}^{r_2'} dr' \int_{z_1'}^{z_2'} dz' \quad \frac{-\gamma r' \sin(\phi)}{(\gamma^2 + r'^2)^{3/2}} \\
&= -\cos(\phi) \Big|_{\phi=\phi_1'}^{\phi=\phi_2'} \int_{z_1'}^{z_2'} dz' \quad \frac{\gamma}{\sqrt{\gamma^2 + r'^2}} \Big|_{r'=r_1'}^{r'=r_2'} \\
&= -\cos(\phi) \sqrt{\gamma^2 + r'^2} \Big|_{r'=r_1'}^{r'=r_2'} \Big|_{\phi=\phi_1'}^{\phi=\phi_2'} \Big|_{z'=z_1'}^{z'=z_2'}
\end{aligned}
\tag{A.37}
$$

$$
\begin{aligned}
H_z &= \int_{\rho_1}^{\rho_2} d\phi \int_{r_1'}^{r_2'} dr' \int_{z_1'}^{z_2'} dz' \quad \frac{r'^2}{(\gamma^2 + r'^2)^{3/2}} \\
&= \phi \Big|_{\phi=\phi_1'}^{\phi=\phi_2'} \int_{z_1'}^{z_2'} dz' \quad \operatorname{arcsinh}(\frac{r'}{|\gamma|}) - \frac{r'}{\sqrt{\gamma^2 + r'^2}} \Big|_{r'=r_1'}^{r'=r_2'} \\
&= \phi \gamma \left(\operatorname{arcsinh}(\frac{r'}{|\gamma|}) - 1 \right) \Big|_{r'=r_1'}^{r'=r_2'} \Big|_{\phi=\phi_1'}^{\phi=\phi_2'} \Big|_{z'=z_1'}^{z'=z_2'}
\end{aligned}
\tag{A.38}
$$

A.5.3 Calculation of the tangential magnetisation

For the integral $\underline{A}_1$ one obtains

$$
\begin{aligned}
\underline{A}_1 &= \frac{\mu_0 J r' \underline{e}_z}{4\pi} \int_{\rho_1}^{\rho_2} d\phi \int_{z_1'}^{z_2'} dz' \frac{1}{D(\phi)} \Big|_{r'=r_1'}^{r'=r_2'} \\
&= \frac{\mu_0 J r' \underline{e}_z}{4\pi} \int_{\rho_1}^{\rho_2} d\phi \operatorname{arcsinh}(\frac{\gamma}{\sqrt{r^2 + r'^2 - 2r r' \cos(\phi)}}) \Big|_{r'=r_1'}^{r'=r_2'} \Big|_{z'=z_1'}^{z'=z_2'}.
\end{aligned}
\tag{A.39}
$$

Appendix A. Appendix

The integral along ϕ must be evaluated numerically as there exist no analytical formulation of it. The second integral ($\underline{A}_2$) will lead to a well-known analytical expression

$$
\begin{aligned}
\underline{A}_2 &= \frac{\mu_0 J \underline{e}_r}{4\pi} \int_{\rho_1}^{\rho_2} d\phi \int_{r_1'}^{r_2'} dr' \frac{r'}{D(\phi)} \Big|_{z'=z_1'}^{z'=z_2'} \\
&= \frac{\mu_0 J \underline{e}_r}{4\pi} \int_{\rho_1}^{\rho_2} d\phi D(\phi) + r\cos(\phi)\operatorname{arcsinh}(\frac{r'-r\cos(\phi)}{\sqrt{\gamma^2+r^2\sin(\phi)^2}}) \Big|_{r'=r_1'}^{r'=r_2'}\Big|_{z'=z_1'}^{z'=z_2'} \\
&= \frac{\mu_0 J \underline{e}_r}{4\pi} \int_{\rho_1}^{\rho_2} d\phi D(\phi) + r\cos(\phi)\operatorname{arcsinh}(\beta_1(\phi)) \Big|_{r'=r_1'}^{r'=r_2'}\Big|_{z'=z_1'}^{z'=z_2'} \\
&= -2a\frac{\mu_0 J \underline{e}_r}{4\pi}(E(\alpha_2,k)-E(\alpha_1,k)) \Big|_{r'=r_1'}^{r'=r_2'}\Big|_{z'=z_1'}^{z'=z_2'} \\
&\quad + \frac{\mu_0 J r \underline{e}_r}{4\pi} \int_{\rho_1}^{\rho_2} d\phi \cos(\phi)\operatorname{arcsinh}(\beta_1(\phi)) \Big|_{r'=r_1'}^{r'=r_2'}\Big|_{z'=z_1'}^{z'=z_2'}.
\end{aligned}
\tag{A.40}
$$

The last integral will be solved using integration by parts

$$
\begin{aligned}
I &= \int_{\rho_1}^{\rho_2} d\phi \cos(\phi)\operatorname{arcsinh}(\beta_1(\phi)) \\
&= \sin(\phi)\operatorname{arcsinh}(\beta_1(\phi))\Big|_{\phi'=\phi_1'}^{\phi'=\phi_2'} - \int_{\rho_1}^{\rho_2} d\phi \sin(\phi)(\frac{r\sin(\phi)}{D(\phi)} \\
&\quad - \frac{\cos(\phi)\sin(\phi)r^2(r'-r\cos(\phi))}{G^2(\phi)D(\phi)}).
\end{aligned}
\tag{A.41}
$$

The first integral can be transformed into an elliptical integral

$$
I_1 = \int_{\rho_1}^{\rho_2} d\phi r \frac{\sin(\phi)^2}{D(\phi)} = -2\frac{r}{a}\int_{\alpha_1}^{\alpha_2} d\alpha \frac{\alpha_2\sin(\alpha)^2+\alpha_4\sin(\alpha)^4}{\sqrt{1-k^2\sin(\alpha)^2}}.
\tag{A.42}
$$

For the second one one gets

$$
\begin{aligned}
I_2 &= r^2 \int_{\rho_1}^{\rho_2} d\phi \frac{\cos(\phi)\sin(\phi)^2(r'-r\cos(\phi))}{G^2(\phi)D(\phi)} \\
&= -2r^2 \int_{\alpha_1}^{\alpha_2} d\alpha \frac{\alpha_2\sin(\alpha)^2+\alpha_4\sin(\alpha)^4+\alpha_6\sin(\alpha)^6+\alpha_8\sin(\alpha)^8}{G^2(\alpha)D(\alpha)}.
\end{aligned}
\tag{A.43}
$$

The volume integral ($\underline{A}_3$) leads to

$$
\begin{aligned}
\underline{A}_3 &= \frac{\mu_0 J \underline{e}_z}{4\pi} \int_{\rho_1}^{\rho_2} d\phi \int_{r_1'}^{r_2'} dr' \int_{z_1'}^{z_2'} dz' \frac{1}{D(\phi)} \\
&= \frac{\mu_0 J \underline{e}_z}{4\pi} \int_{\rho_1}^{\rho_2} d\phi (r'-r\cos(\phi))\operatorname{arcsinh}(\beta_2(\phi)) \\
&\quad - r\sin(\phi)\arctan(\beta_3(\phi)) + \gamma\operatorname{arcsinh}(\beta_1(\phi))
\end{aligned}
\tag{A.44}
$$

which is composed by four integrals. The first and the last one must be calculated using numerical integration. The second one is already known and was calculated in expression

A.28 and the third one is given by equation A.26.

A.5.4 Case of the round edges rectangular coil - 3D finite elements versus analytical calculation

The selected coil has round edges and straight lines to integrate the two basic geometric elements (straight and arc) from which the analytical expressions for the magnetic field and the vector potential were derived in section 5.1. Figure A.1 shows the geometry of the coil used
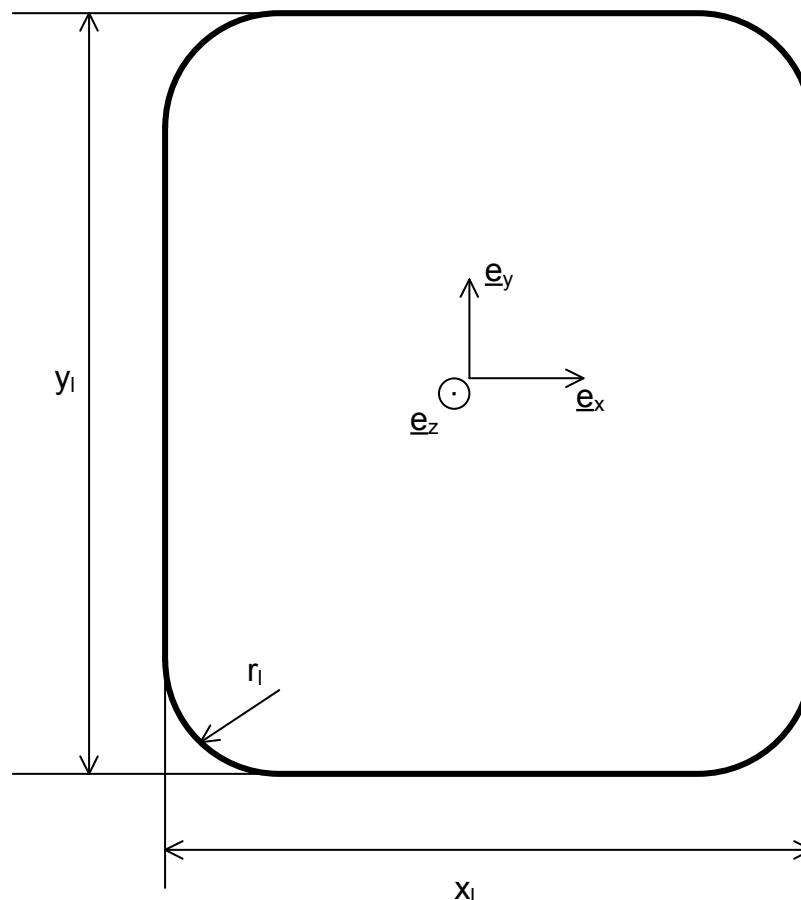
Figure A.1 – Schematic representation of the round edges rectangular coil.

for the validation. The edge radius (r_l) is 150mm, the length (y_l) is 2800mm and the width (x_l) is 1550mm. The coil is short-circuited with a current of 1MA. The validation consists in a comparison of the calculated analytical expression along 10 paths divided in 200, 400 or 600 points each with the results coming from the 3D finite element calculation evaluated at the same points. For the filament and the rectangular approximation only 4 curves are presented as the results are similar for the 10 paths evaluated. The ten path are given by the following expressions

$$Ox = \begin{cases} t & \text{with } t \in [-2, 2], \text{ 400 samples} \\ 0 \\ 0 \end{cases} \tag{A.45}$$

$$OxD = \begin{cases} t & \text{with } t \in [0.6, 1], \text{ 600 samples} \\ 0 \\ 0 \end{cases} \tag{A.46}$$

$$OxOy+ = \begin{cases} t & \text{with } t \in [-2, 2], \text{ 400 samples} \\ 1.75 \\ 0 \end{cases} \tag{A.47}$$

$$OxOz+ = \begin{cases} t & \text{with } t \in [-2, 2], \text{ 400 samples} \\ 0 \\ 1.25 \end{cases} \tag{A.48}$$

$$Oy = \begin{cases} 0 \\ t & \text{with } t \in [-2, 2], \text{ 400 samples} \\ 0 \end{cases} \tag{A.49}$$

$$OyOx- = \begin{cases} -1.75 \\ t & \text{with } t \in [-2, 2], \text{ 400 samples} \\ 0 \end{cases} \tag{A.50}$$

$$Oz = \begin{cases} 0 \\ 0 \\ t & \text{with } t \in [-1, 1], \text{ 200 samples} \end{cases} \tag{A.51}$$

$$Oz\text{-}Ox+Oy = \begin{cases} -0.5 \\ 0.5 \\ t & \text{with } t \in [-1, 1], \text{ 200 samples} \end{cases} \tag{A.52}$$

$$Oz+Ox+Oy = \begin{cases} 0.5 \\ 0.5 \\ t & \text{with } t \in [-1, 1], \text{ 200 samples} \end{cases} \tag{A.53}$$

$$Diag = \begin{cases} t & \text{with } t \in [-1, 1], \text{ 200 samples} \\ t & \text{idem} \\ t & \text{idem} \end{cases} . \tag{A.54}$$

Filament approximation

In the 3D-finite element software used (Flux3D), the filament can't be modelled with zero radius, but with 1mm. Figures A.3 and A.5 present the magnetic field and the difference between the analytical calculation and finite element calculation. As some field values are zero, it make no sense to calculate the relative error. For all points considered, the maximal value of the difference is below $1.1 \cdot 10^{-9}$ T traducing an excellent and quasi perfect agreement between both calculations methods. The maximal error due to the approximation of the elliptical integral is around 100ϵ[1] with Fukushima's algorithms. The remaining difference of around 4 order of magnitude is certainly also due to the mesh used in the finite element and some round-off errors in the finite-element code and in the analytical expressions. This assumption will be hardened when the analytical expressions of the filament are compared to the formulae of Maxwell's filament, where the difference is around 10ϵ. The non-zero conductor radius produces also a contribution to the difference seen.
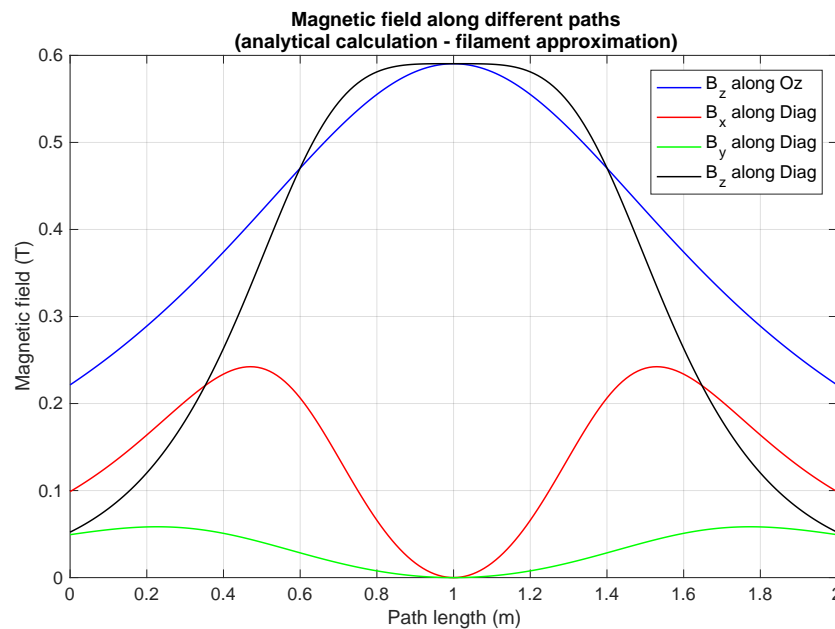
Figure A.2 – Magnetic field (filament approximation) along different paths.

Figure A.2 present the magnetic field along different paths. The curves are very smooth, which will considerably help for numerical integration. The maximal value of the magnetic field is about 0.6T in the center of the coil, which is inline with the expectations as the current is 1MA. The magnetic field tends to zero rapidly when leaving the coil, the decrease rate of the magnetic field is $1/r^2$. Figure A.3 shows the difference between the analytical expression and the 3D finite element computation along different paths. It is interesting to point out, that the difference is not smooth at all. The steps in the difference can be attributed to the mesh, while the error is very smooth for the path Oz. This fact could not be explained. The difference along

---

[1] ϵ is equal to $2.220446049250313 \cdot 10^{-16}$, which is the double machine precision.

Oz is constant (within an order of magnitude) for about 2/3 of the path length. The difference is symmetric which traduces the symmetry in the magnetic field expressions and shows also a very good accuracy of both calculation modes (analytic and finite-element).

Figure A.3 – Magnetic field (filament approximation) difference along different paths.

Figure A.4 exhibits the same behaviour as figure A.2. For the difference figure A.5, similar conclusion is obtained as for figure A.3.

Rectangular approximation

The coil has the same dimensions are the one used for the filament approximation (see figure A.1). The rectangular cross-section has the following dimensions $\Delta x'$=150mm, $\Delta y'$=125mm, $\Delta r'$=125mm, $\Delta z'$=150mm where x' and y' are used for the straight part and r' and z' for the arc part. The short-circuit current is again 1MA. The maximal value of the difference is slightly above 1e-6T traducing once again a very good precision of the integral expressions. Nevertheless, the error is 3 order of magnitude higher than for the filament approximation. This is mainly due to the approximation of the elliptic integral of the third kind, which has an error in the range of 1'000ϵ and 10'000ϵ with Fukushima's algorithms and to the numerical integration needed where the relative error used is around 1e-9. The mesh and the round-off errors add also their contributions to the increase of the error.

The curves of figure A.6 have a very similar shape as the one of figure A.2. Because of that, a comparison between both approximations have been conducted to see numerically the impact of the approximation in the far-field zone, as the results of section 4.5 focused on the near-field zone and the frontier between the near-field zone and the far-field zone.
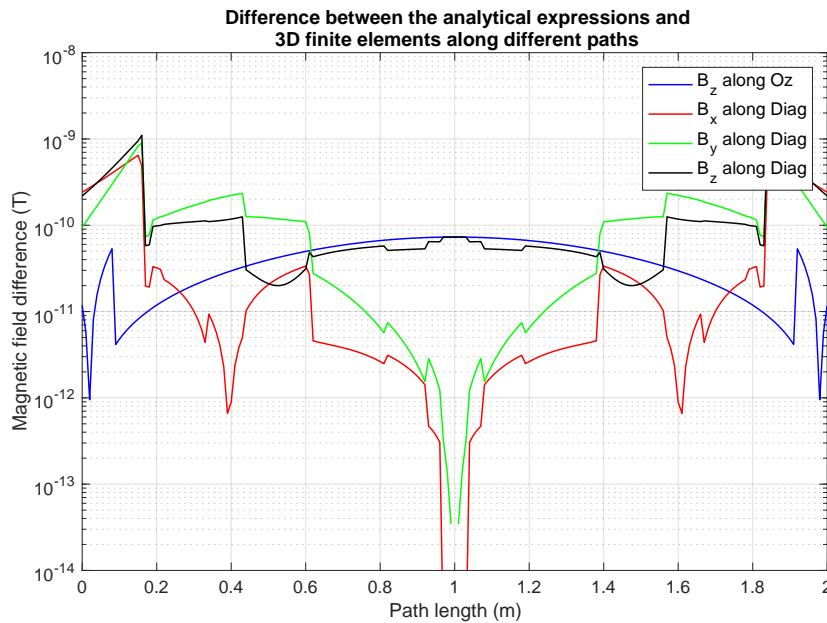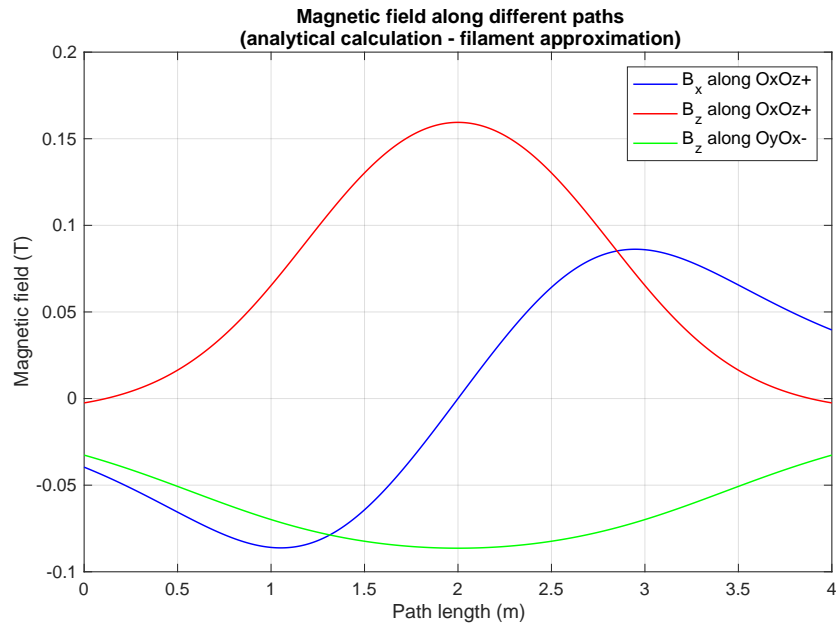
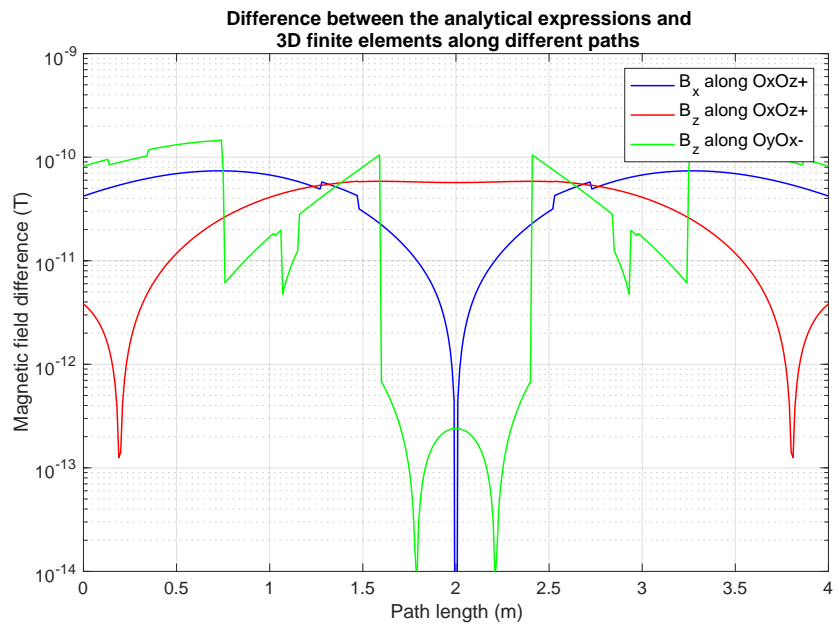Figure A.4 – Magnetic field (filament approximation) along different paths.

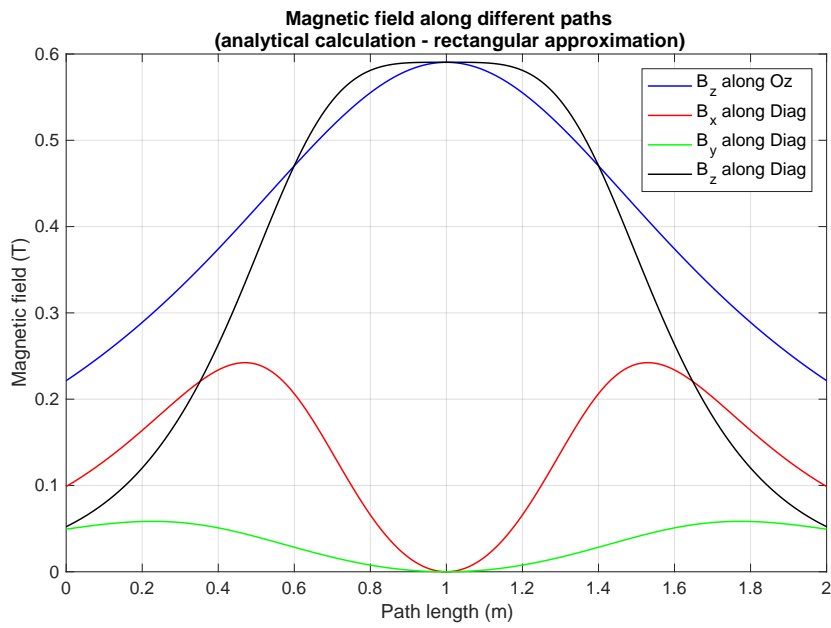Figure A.5 – Magnetic field (filament approximation) difference along different paths.

Figure A.6 – Magnetic field (rectangular approximation) along different paths.
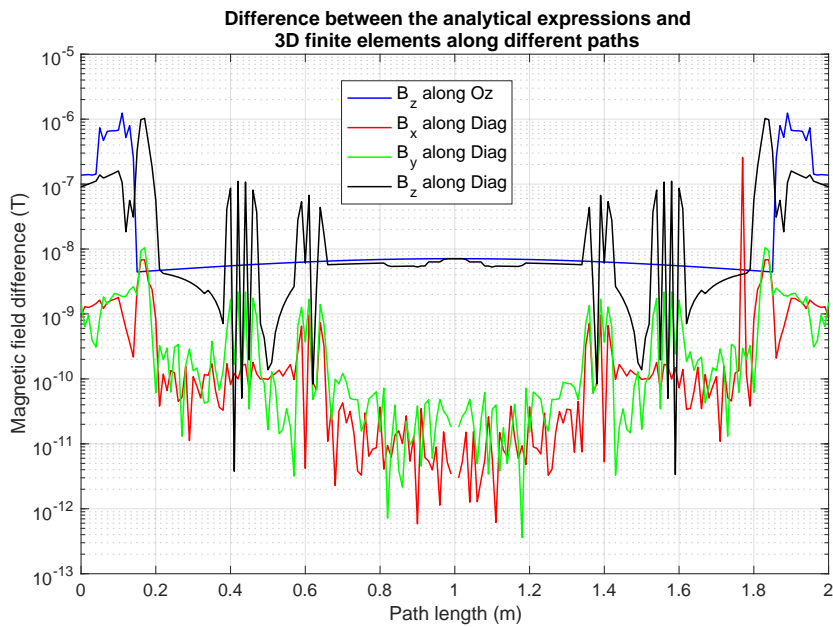

Figure A.7 – Magnetic field (rectangular approximation) difference along different paths.

Comparing figure A.7 and A.3 leads to the following conclusion: along the Diag-path, the error is not smooth at all for the rectangular approximation. In addition, the error is 3 order of magnitude higher than for the filament approximation. The error along the path Oz behaves the same as for the filament approximation.
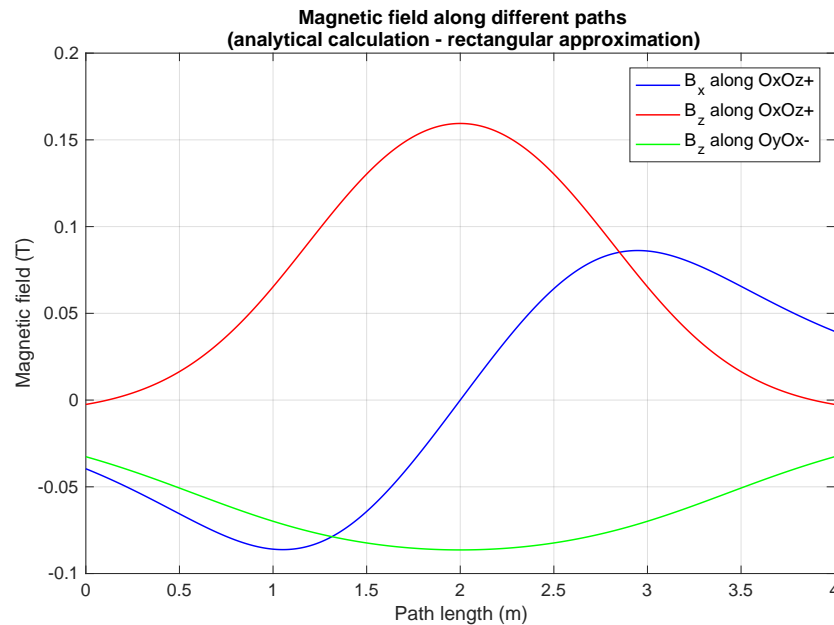

Figure A.8 – Magnetic field (rectangular approximation) along different paths.

The error for B_x along the path OxOz+ is significantly lower than the two others and is not smooth at all (see figure A.9). While the error for the other 2 curves is smooth with 2 steps for B_z along the path OyOx-. The errors are symmetric as the curves in figure A.7 and all the curves for the filament approximation. The glitches that occur in any figures can certainly be attributed to some mesh error or numerical issues in the numerical integration.

Comparison between the filament and rectangular approximation

As the curves of figures A.2 and A.4 for example have at a first glance a very similar shape, it is interesting to study the similarity more in details to gain knowledge about the far-field impact of the chosen approximation. Figures A.10 and A.11 show the difference between the filament and rectangular approximations (difference calculated using the 3D finite element simulation with rectangular cross-section as reference). The filament approximation has a significant higher difference (about 2 to 3 order of magnitude) than the rectangular approximation. It is interesting to point out, that at the considered distances, that the distance from the coil seems not to impact the difference, as one may expect. May be the considered distance was not big enough to show this effect. The curves of the filament approximation are very smooth compared to the one of the rectangular approximation. One could therefore conclude, that the source of the non-smoothness of the curves are due to the calculation way (elliptical integral
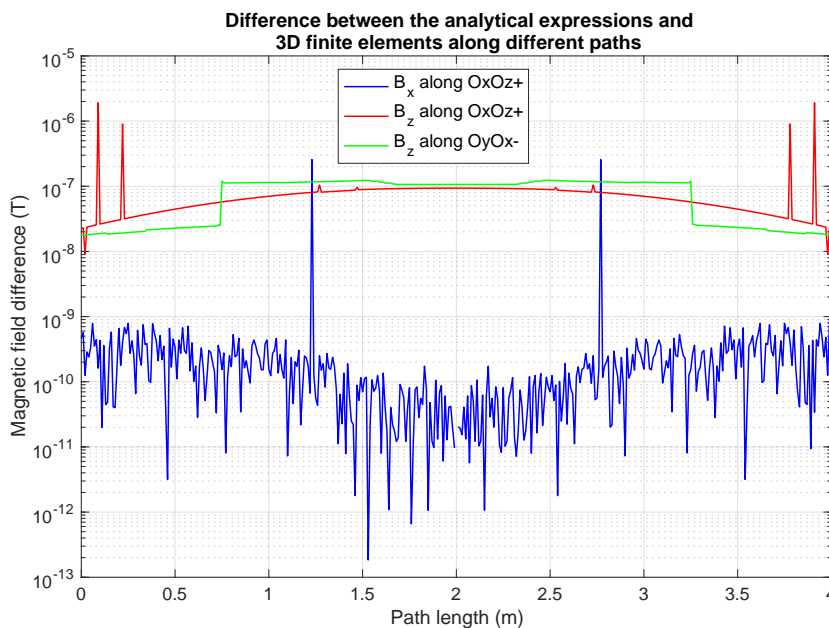
Figure A.9 – Magnetic field (filament approximation) difference along different paths.

of the third kind and numerical integration) used in the rectangular approximation. On the other hand, there are some curves (namely B_z along the path OxOz+ and B_z along the path OyOx-) where the error is very smooth.

If the analytical expression needs to be used for a very high precision magnetic field computation, then this problematic must be studied more in details and one should tend to obtain errors in the range 1e-14 to 1e-15. For the actual application of this work, namely double fed induction machines and more general electrical machines, the precision range achieved now is more than sufficient.

Table A.1 shows the mean value of the difference between the 3D finite element calculation and the analytical expression for both approximations. The advantage of the mean value is to cut the glitches and filter out a little bit the "noise" for the rectangular approximation. So that one can have comparable results for both approximations. The difference between both approximations is around 2 to 3 order of magnitude and the filament approximation is significantly worser than the rectangular approximation, which is expected.
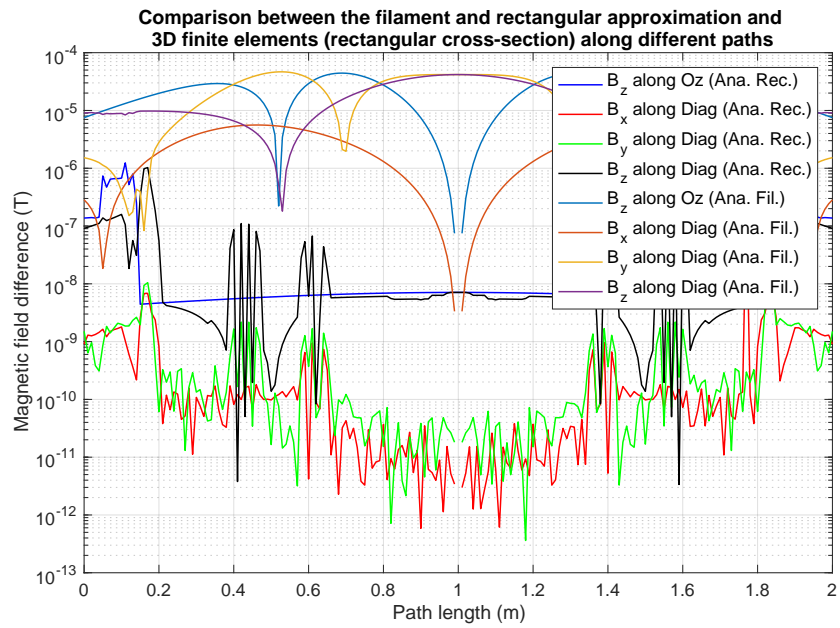
Figure A.10 – Magnetic field difference along different paths, comparison between the filament and rectangular approximation.
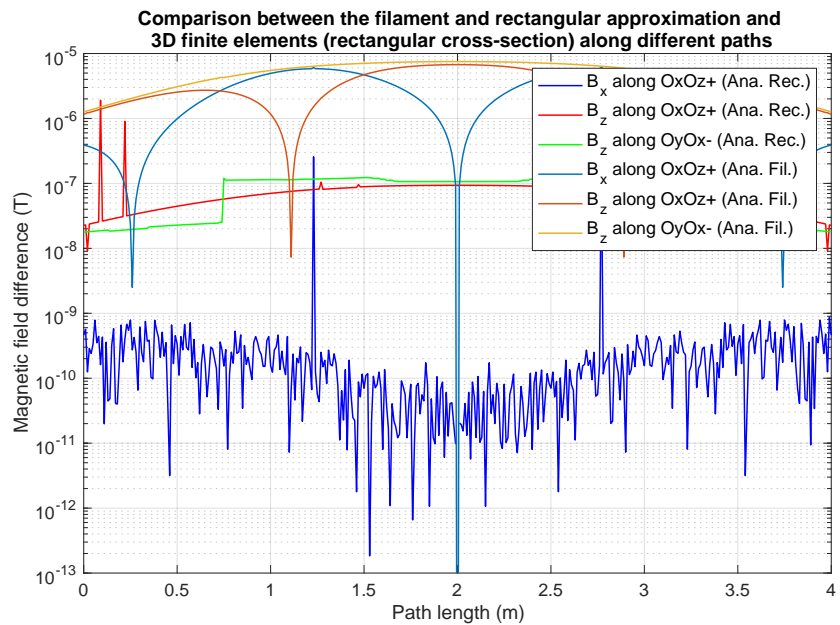
Figure A.11 – Magnetic field difference along different paths, comparison between the filament and rectangular approximation.

Table A.1 – Comparison between the filament and rectangular approximation against 3D finite elements (rectangular cross-section) along different paths.

Path	Filament approximation (T) mean value of the difference	Rectangular approximation (T) mean value of the difference
B_z along Oz	1.4988e-05	7.8334e-08
B_x along Diag	2.0599e-05	1.7510e-09
B_y along Diag	2.5755e-06	6.9299e-10
B_z along Diag	2.2549e-05	5.4944e-08
B_x along OxOz+	2.7652e-06	1.4778e-09
B_z along OxOz+	3.0858e-06	7.9363e-08
B_z along OyOx-	5.0184e-06	7.9247e-08

A.5.5 Magnetised bodies in cartesian coordinates - comparison between 3D finite-elements and analytical formulae

The validation of the 3-dimensional model is based on a comparison of the calculated results with 3-dimensional finite-element, as no published literature presented results that could be compared with a precision of around 10-100 A/m. The 3-dimensional finite-element simulations use the scalar approximation for the magnetic field, so that they have an impressive precision without a too coarse mesh. The analytical expressions have been eye-compared with some published results, before starting the validation using the finite-element simulation. The analytical calculation is considered as validated if there error is below 10-100 A/m for all simulated cases.

The comparison is done using a 10x10x10mm cube with a given magnetisation. The magnetic field is compared on seven paths which are given by the following expressions

$$\text{Ox} = \begin{cases} t & \text{with } t \in [-0.5, 0.5], \text{ 200 samples} \\ 0 & \\ 0 & \end{cases} \tag{A.55}$$

$$\text{OxD} = \begin{cases} t & \text{with } t \in [-0.5, 0.5], \text{ 400 samples} \\ 0.05 & \\ 0.065 & \end{cases} \tag{A.56}$$

$$\text{Oy} = \begin{cases} 0 & \\ t & \text{with } t \in [-0.5, 0.5], \text{ 200 samples} \\ 0 & \end{cases} \tag{A.57}$$

$$\text{OyD} = \begin{cases} 0.05 & \\ t & \text{with } t \in [-0.5, 0.5], \text{ 400 samples} \\ 0.065 & \end{cases} \tag{A.58}$$

$$\text{Oz} = \begin{cases} 0 & \\ 0 & \\ t & \text{with } t \in [-0.5, 0.5], \text{ 200 samples} \end{cases} \tag{A.59}$$

$$\text{OzD} = \begin{cases} 0.05 & \\ 0.065 & \\ t & \text{with } t \in [-0.5, 0.5], \text{ 400 samples} \end{cases} \tag{A.60}$$

$$\text{Diag} = \begin{cases} t & \text{with } t \in [-1, 1], \text{ 300 samples} \\ t & \text{idem} \\ t & \text{idem} \end{cases} . \tag{A.61}$$

$$\underline{M} = M\underline{e}_x$$

Figure A.12 – Comparison between analytical formulae and finite element calculation with a magnetisation along x-axis on different paths.

Figures A.12 and A.13 show the results of the comparison for the magnetic field calculation. The agreement is very good for all curves. The analytical formulae have some discrepancies in the diag path at the point singularity as expected. The treatment of this singularity is detailed in section 5.8. The curves (see figures A.14 and A.15) for the vector potential have a higher error due to the sparser mesh and vector potential formulation[2] used. The analytical expressions can still be considered as validated as the error is very small. The results are similar for the two other main axes so that they are not showed.

---

[2]As for the demonstration of the mirroring hypothesis, the finite element simulation in the vector potential formulation has a much lower precision than its counter-part in the scalar potential formulation.

Figure A.13 – Comparison between analytical formulae and finite element calculation with a magnetisation along x-axis on different paths (2nd).

Figure A.14 – Comparison between analytical formulae and finite element calculation with a magnetisation along x-axis on different paths (3rd).
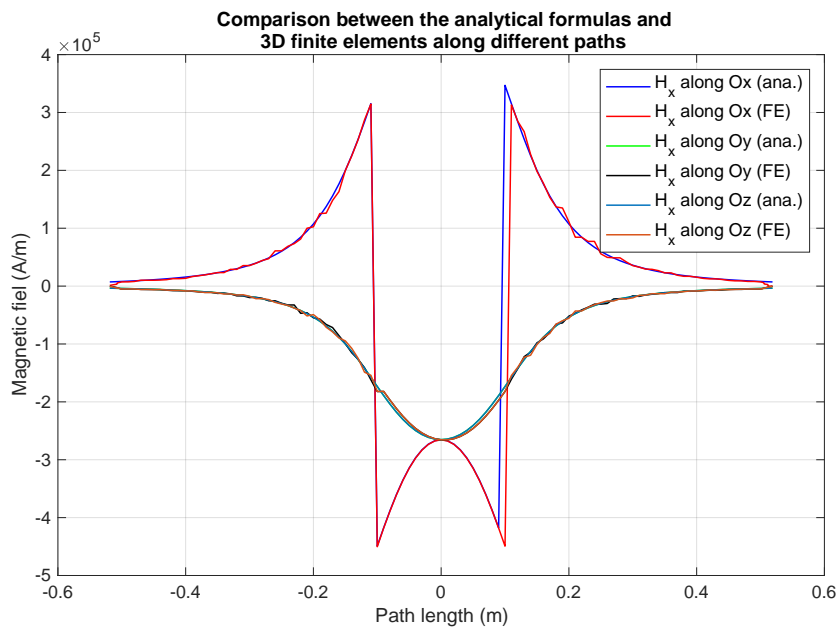
Figure A.15 – Comparison between analytical formulae and finite element calculation with a magnetisation along x-axis on different paths (4th).

A.5.6   Magnetised bodies in cylindrical coordinates - comparison between 3D finite-elements and analytical formulae

The comparison is done using a part of an arc-shaped with rectangular cross-section parallelepiped (see figure 5.4) with a given magnetisation. The parallelepiped has the following geometric parameters: $r'_1 = 0.35m$, $r'_2 = 0.65m$, $z'_1 = -0.25m$, $z'_2 = 0.25m$, $\theta'_1 = -\pi/4$ and $\theta'_2 = \pi/4$. The magnetic field is compared on ten paths which are given by the following expressions

$$\text{Ox} = \begin{cases} t & \text{with } t \in [-1,1],\ 200 \text{ samples} \\ 0 \\ 0 \end{cases} \tag{A.62}$$

$$\tag{A.63}$$

$$
\text{OxOy+} = \begin{cases} t & \text{with } t \in [-1, 1], \text{ 200 samples} \\ 1 \\ 0 \end{cases} \tag{A.64}
$$

$$
\text{Oy} = \begin{cases} 0 \\ t & \text{with } t \in [-1, 1], \text{ 200 samples} \\ 0 \end{cases} \tag{A.65}
$$

$$
\text{Oz} = \begin{cases} 0 \\ 0 \\ t & \text{with } t \in [-1, 1], \text{ 200 samples} \end{cases} \tag{A.66}
$$

$$
\text{OzD} = \begin{cases} -0.126 \\ 0.55 \\ t & \text{with } t \in [-1, 1], \text{ 400 samples} \end{cases} \tag{A.67}
$$

$$
\text{RD} = \begin{cases} t\cos(22.5\pi/180) \\ t\sin(22.5\pi/180) \\ 0.147 & \text{with } t \in [0, 1], \text{ 400 samples} \end{cases} \tag{A.68}
$$

$$
\text{Theta} = \begin{cases} 0.5\cos(t) \\ 0.5\sin(t) \\ 0 & \text{with } t \in [-\pi/2, \pi/2], \text{ 750 samples} \end{cases} \tag{A.69}
$$

$$
\text{ThetaBis} = \begin{cases} 0.5\cos(t) \\ 0.5\sin(t) \\ 0.125 & \text{with } t \in [-\pi/2, \pi/2], \text{ 750 samples} \end{cases} \tag{A.70}
$$

$$
\text{ThetaD} = \begin{cases} 0.5\cos(t) \\ 0.5\sin(t) \\ -0.206 & \text{with } t \in [-\pi/2, \pi/2], \text{ 750 samples} \end{cases} \tag{A.71}
$$

$$
\text{Diag} = \begin{cases} t & \text{with } t \in [-1, 1], \text{ 350 samples} \\ t & \text{idem} \\ t & \text{idem} \end{cases} . \tag{A.72}
$$

Radial magnetisation (Mr)

Figures A.16 and A.17 show the results of the comparison for the magnetic field calculation. The agreement is very good for all curves. The curves (see figures A.18 and A.19) for the vector potential has a higher error due to the sparser mesh used as for the magnetisation along the x-axis. The analytical expressions can still be considered as validated as the error is very small.

Figure A.16 – Comparison between analytical formulae and finite element calculation with a radial magnetisation on different paths.

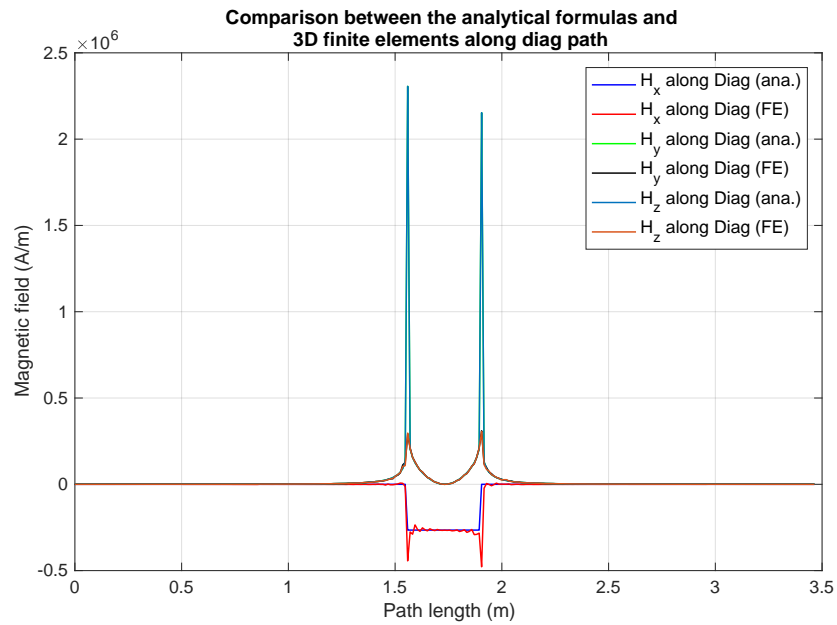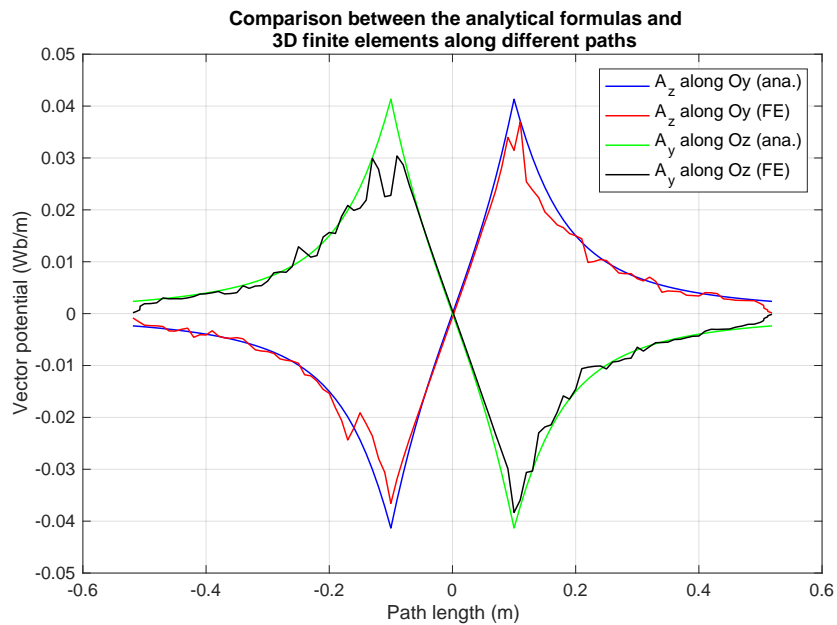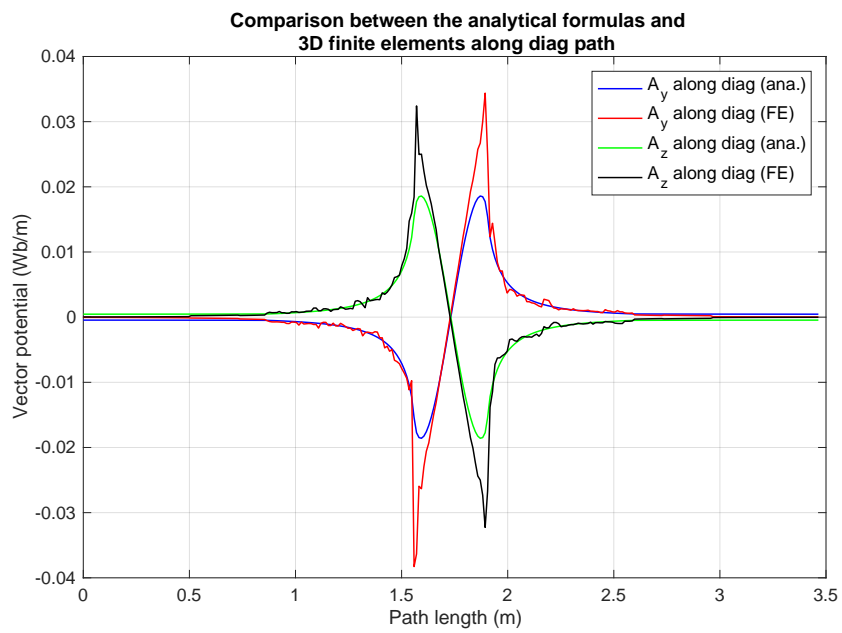

Figure A.17 – Comparison between analytical formulae and finite element calculation with a radial magnetisation on different paths (2nd).

Figure A.18 – Comparison between analytical formulae and finite element calculation with a radial magnetisation on different paths (3rd).

Figure A.19 – Comparison between analytical formulae and finite element calculation with a radial magnetisation on different paths (4th).

Tangential magnetisation (M_ϕ)

Figure A.20 – Comparison between analytical formulae and finite element calculation with a tangential magnetisation on different paths.

Figures A.20 and A.21 show the results of the comparison for the magnetic field calculation. The agreement is very good for all curves except for the diag-path. It was not possible to find the root cause of this discrepancy. It must be pointed out that only this path exhibits huge errors, for all remaining path the discrepancy is very small. The curves (see figures A.22 and A.23) for the vector potential has a higher error due to the sparser mesh used as for the magnetisation along the x-axis. The analytical expressions can still be considered as validated as the error is very small and despite the discrepancies observed on the curves of the diag-path.

Axial magnetisation (M_z)

Figures A.24 and A.25 show the results of the comparison for the magnetic field calculation. The agreement is very good for all curves. The curves (see figures A.22 and A.23) for the vector potential has a higher error due to the sparser mesh used as for the magnetisation along the x-axis. The analytical expressions can still be considered as validated as the error is very small.
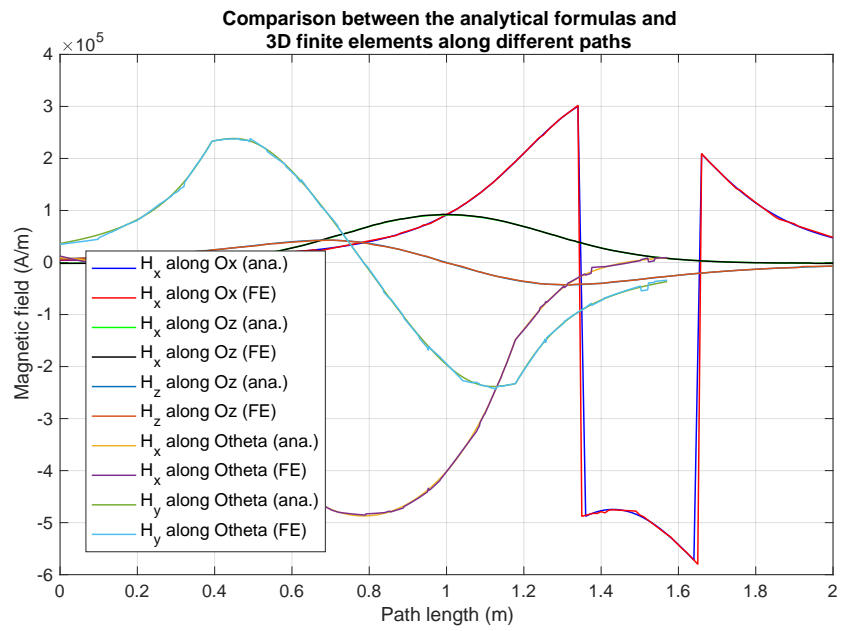
Figure A.21 – Comparison between analytical formulae and finite element calculation with a tangential magnetisation on different paths (2nd).
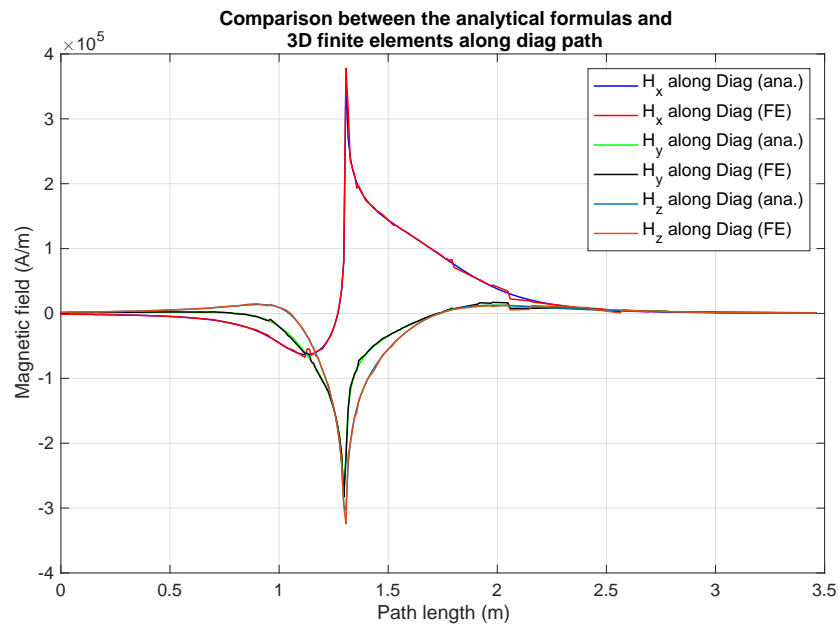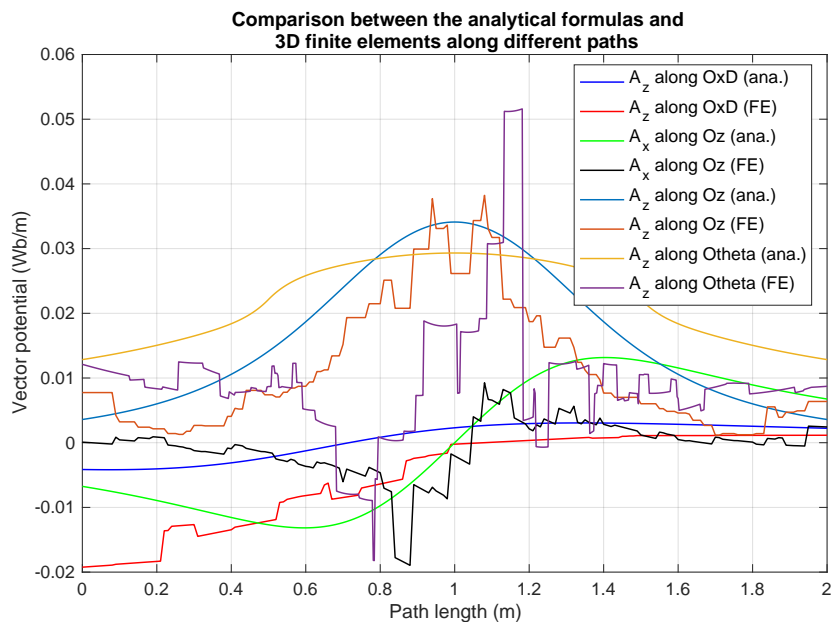

Figure A.22 – Comparison between analytical formulae and finite element calculation with a tangential magnetisation on different paths (3rd).
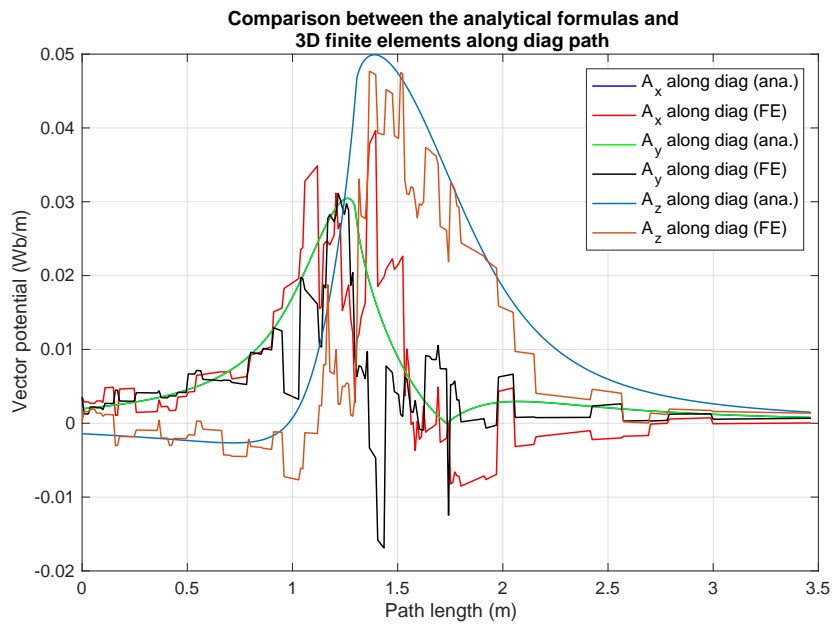
Figure A.23 – Comparison between analytical formulae and finite element calculation with a tangential magnetisation on different paths (4th).
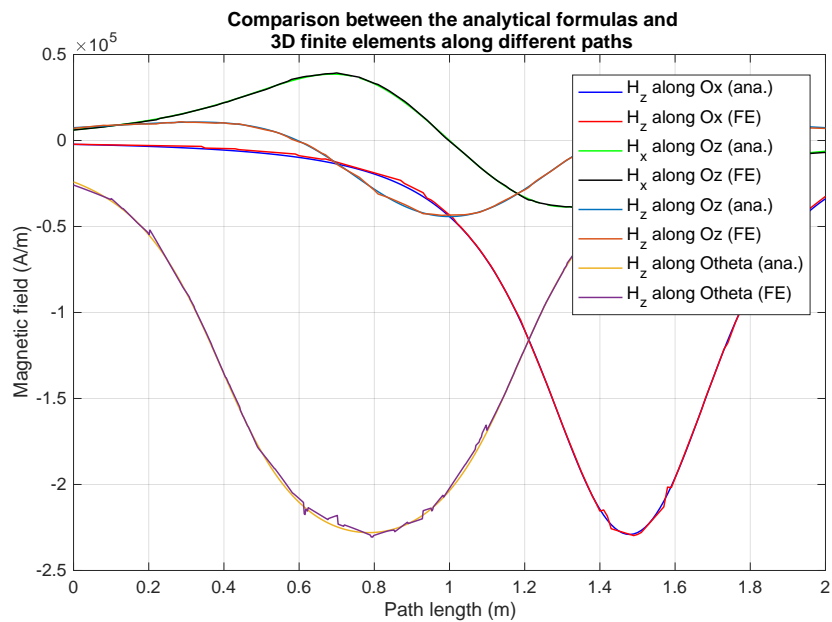
Figure A.24 – Comparison between analytical formulae and finite element calculation with an axial magnetisation on different paths.
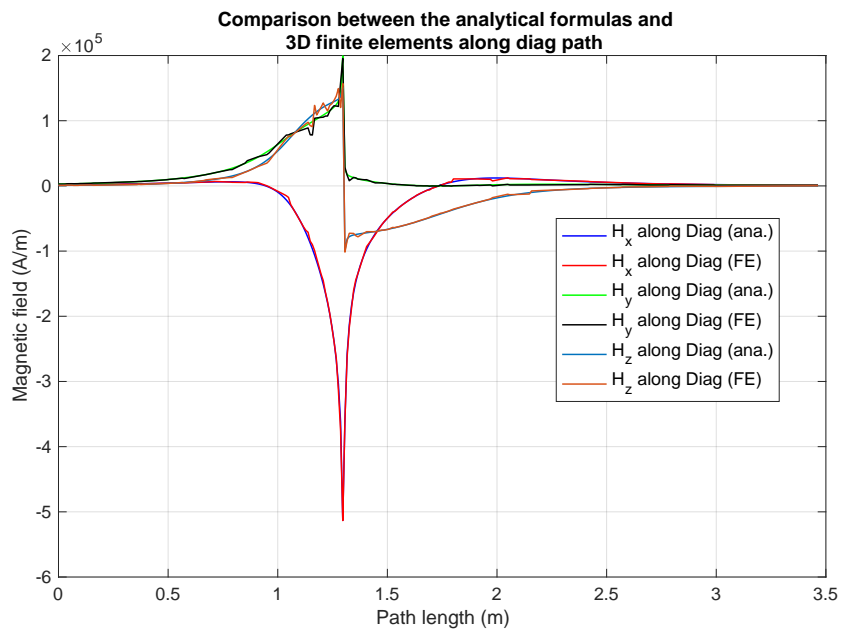
Figure A.25 – Comparison between analytical formulae and finite element calculation with an axial magnetisation on different paths (2nd).
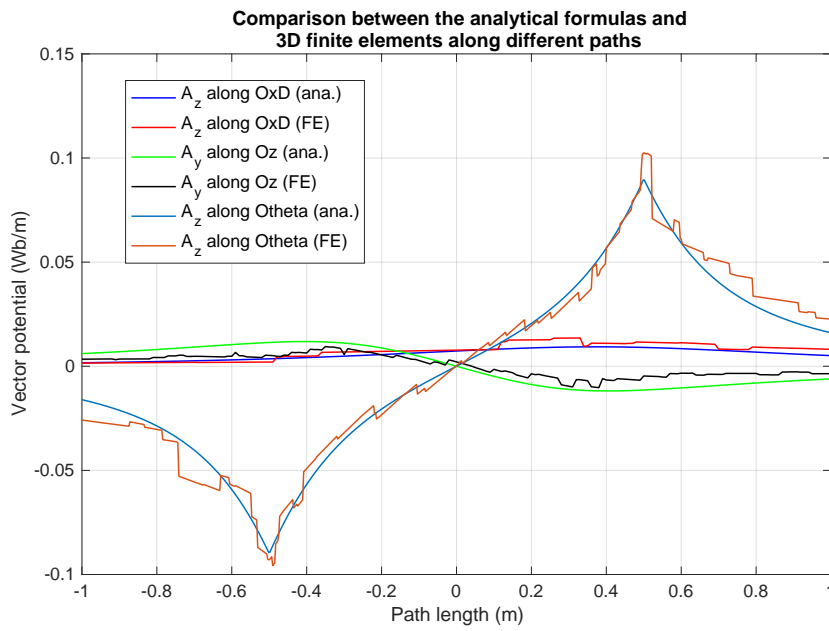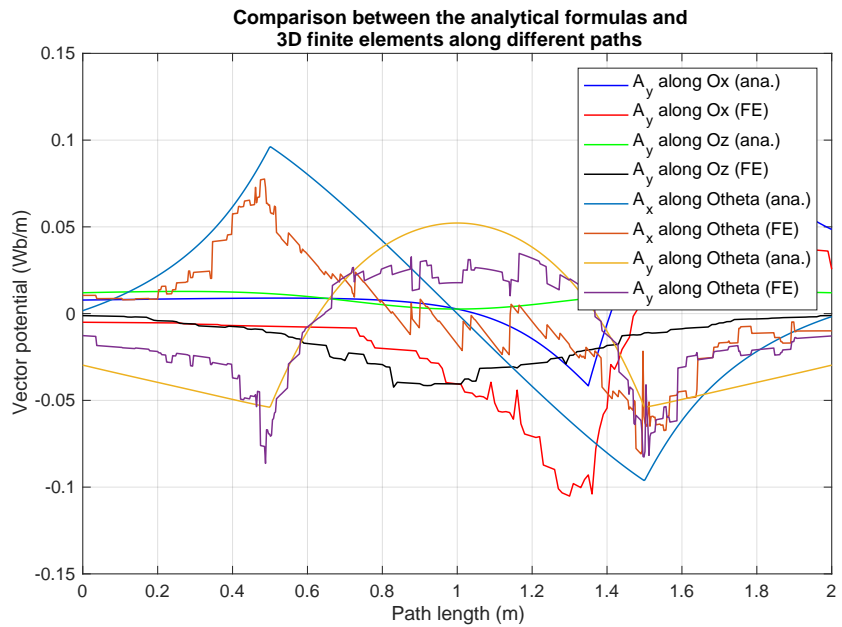

Figure A.26 – Comparison between analytical formulae and finite element calculation with an axial magnetisation on different paths (3rd).
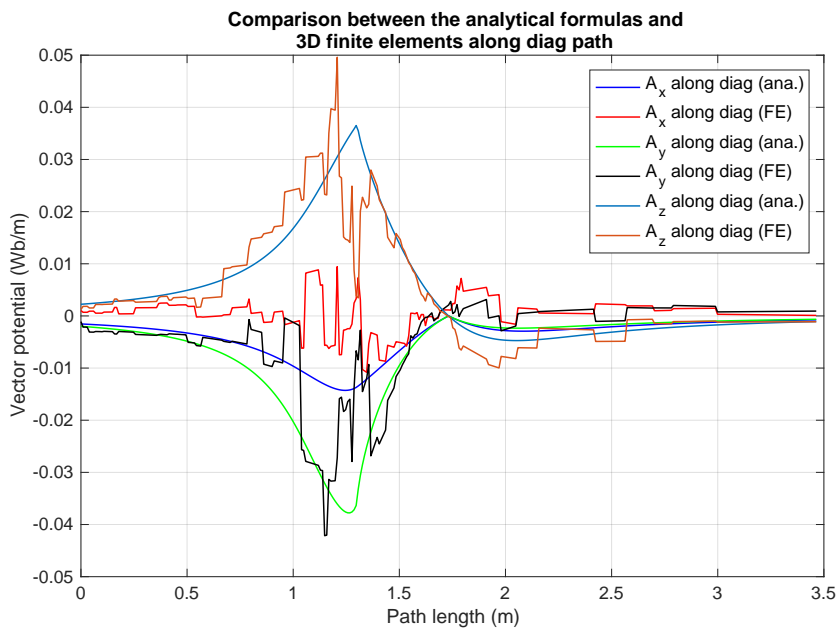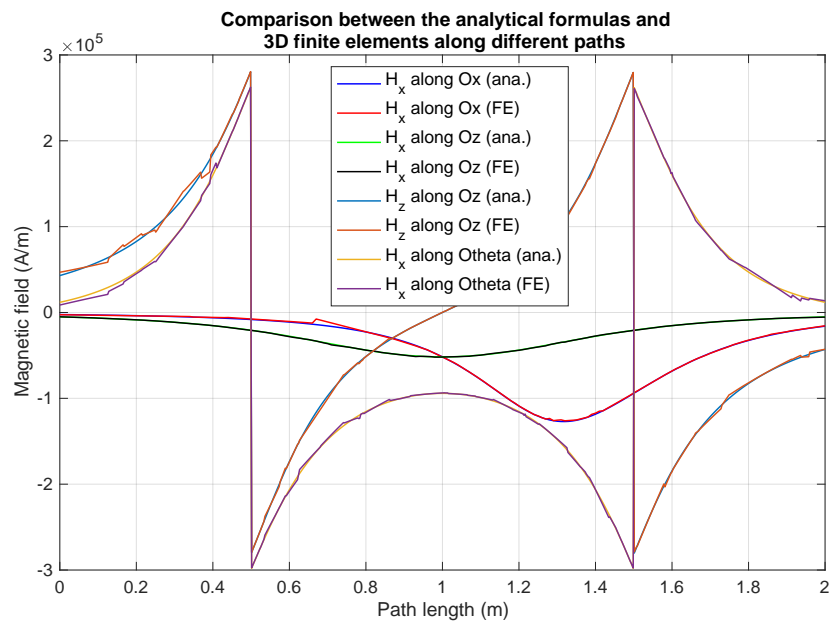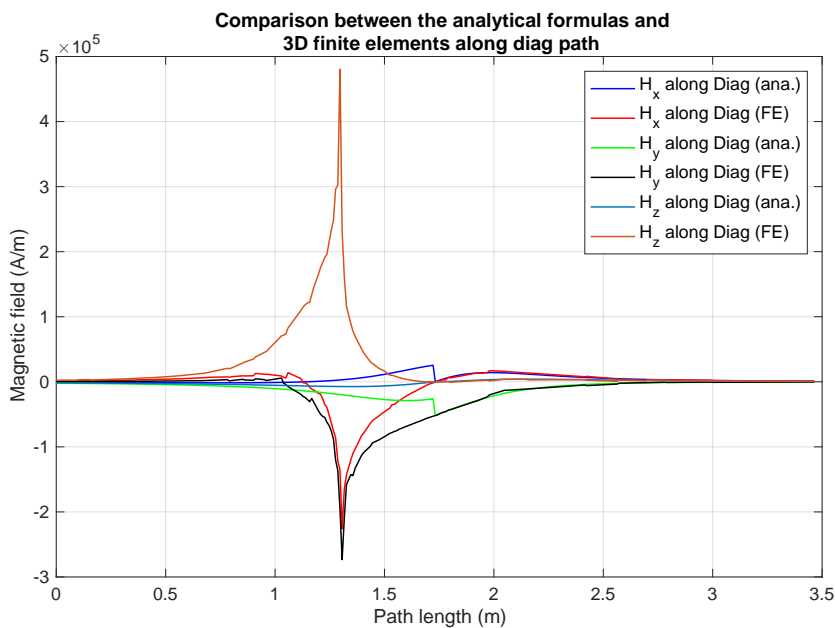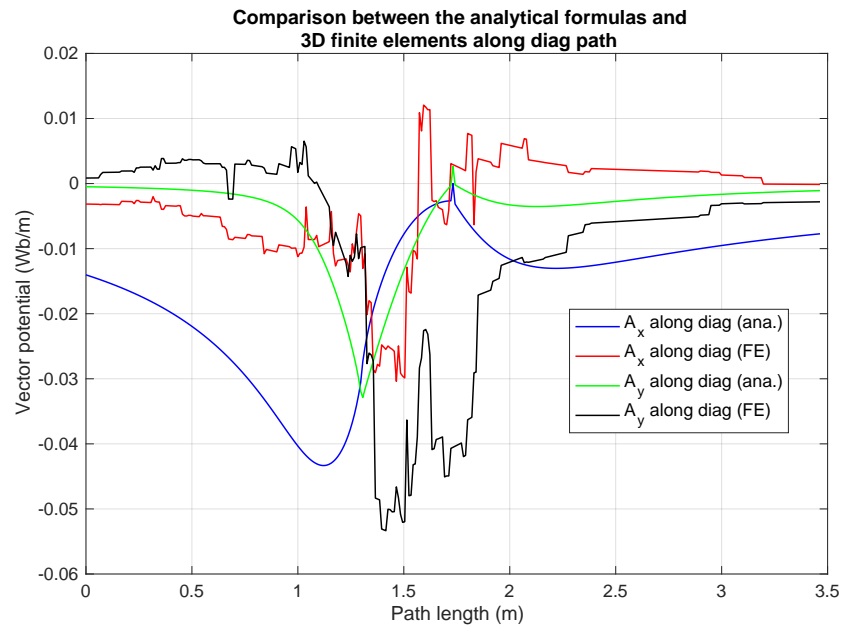
Figure A.27 – Comparison between analytical formulae and finite element calculation with an axial magnetisation on different paths (4th).

A.6 Appendix to Chapter 6

A.6.1 3-Phase short-circuit in a asynchronous motor

Figures A.28, A.29 and A.30 show the comparison between the analytical expressions and simulated curves. The agreement is perfect which enables to validate the analytical expressions for the 3-phase short-circuit in the case $u_r = 0$ (equations for the asynchronous motor).

A.6.2 2-Phase short-circuit in a asynchronous motor

Figures A.31, A.32 and A.33 show the comparison between the analytical expressions and simulated curves. The agreement is perfect which enables to validate the analytical expressions for the 2-phase short-circuit in the case $u_r = 0$ (equations for the asynchronous motor).

A.6.3 3-Phase short-circuit (stator and rotor) in a DASM machine

Figures A.34, A.35, A.36, A.37 and A.38 show the comparison between the analytical expressions and simulated curves. The agreement is perfect which enables to validate the analytical expressions for the 3-phase short-circuit in the case $u_r = cste$ (equations for the DASM machine).
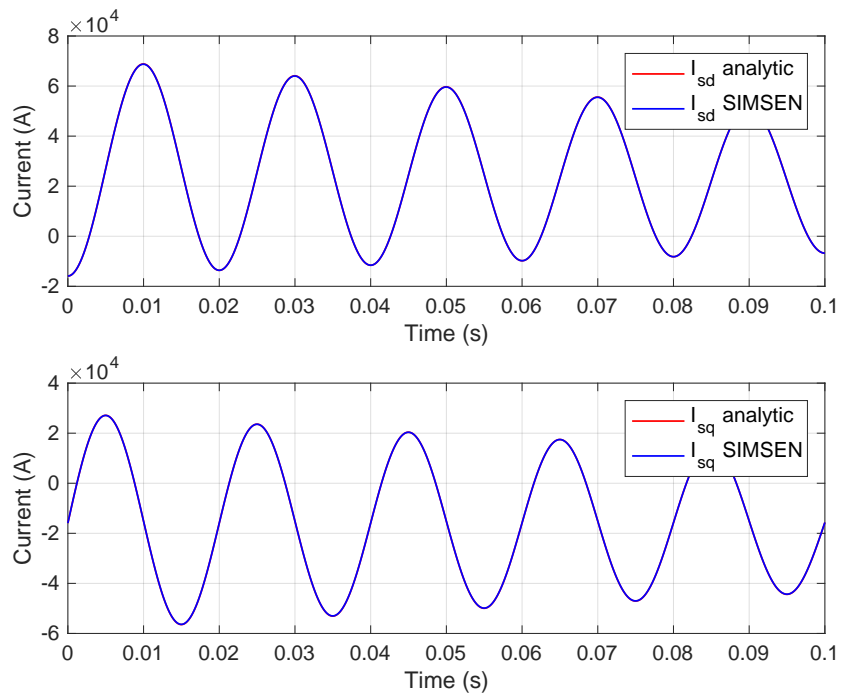
Figure A.28 – Stator currents in the rotating dq-frame
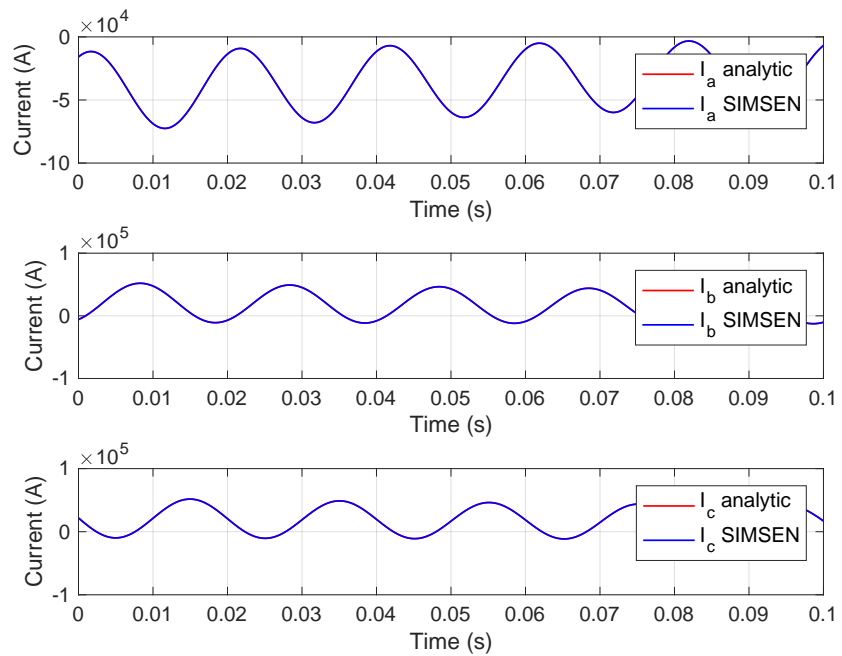
Figure A.29 – Stator currents in the fixed abc-frame
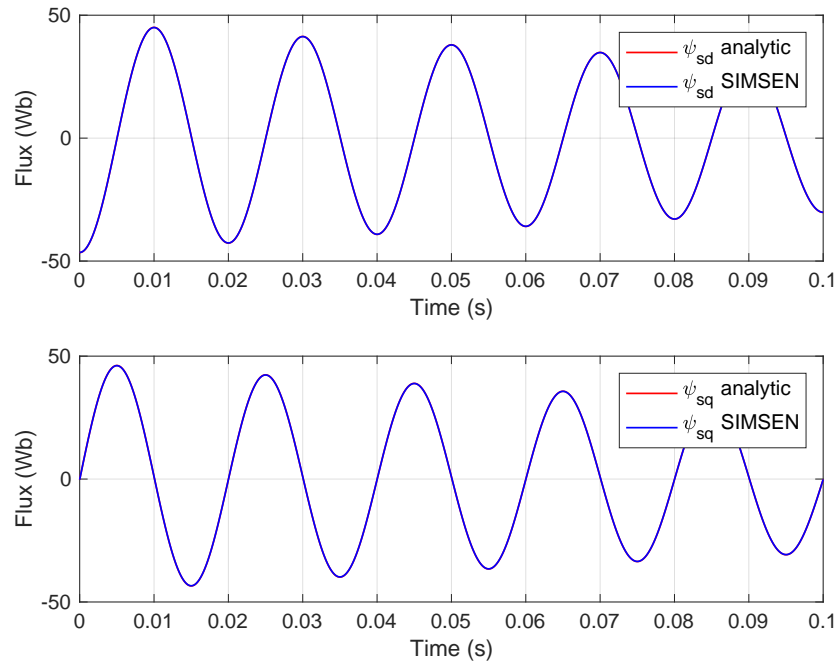
Figure A.30 – Stator fluxes in the rotating dq-frame
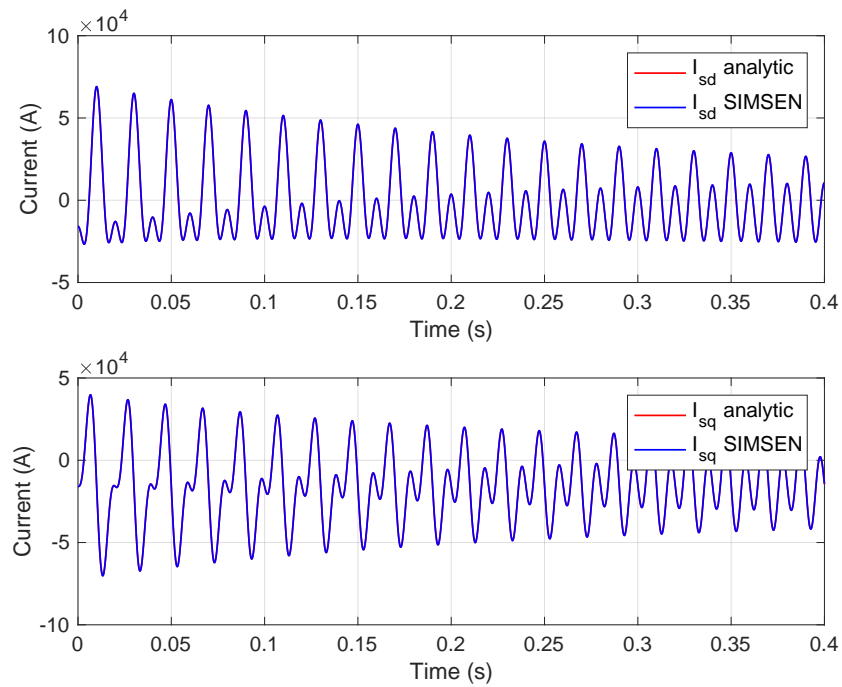
Figure A.31 – Stator currents in the rotating dq-frame
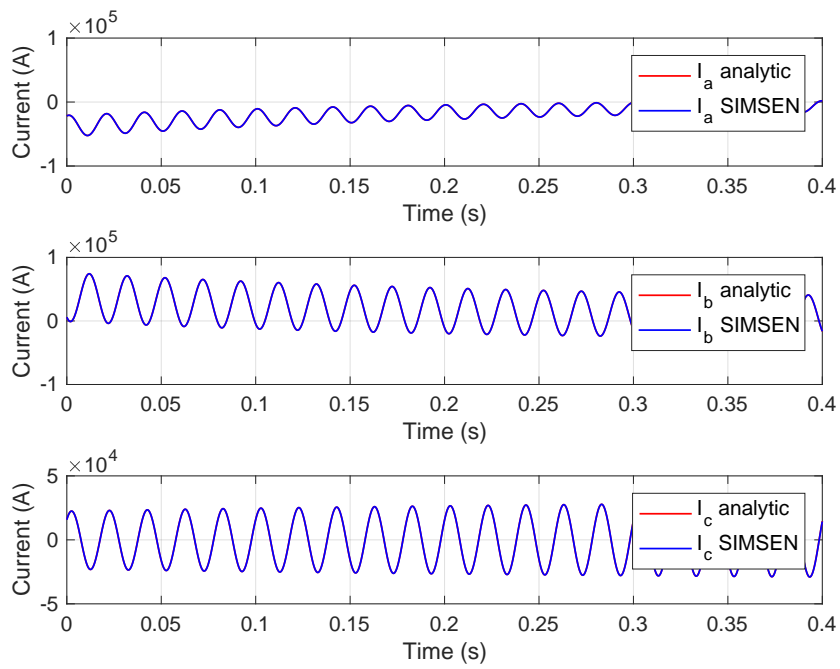
Figure A.32 – Stator currents in the fixed abc-frame
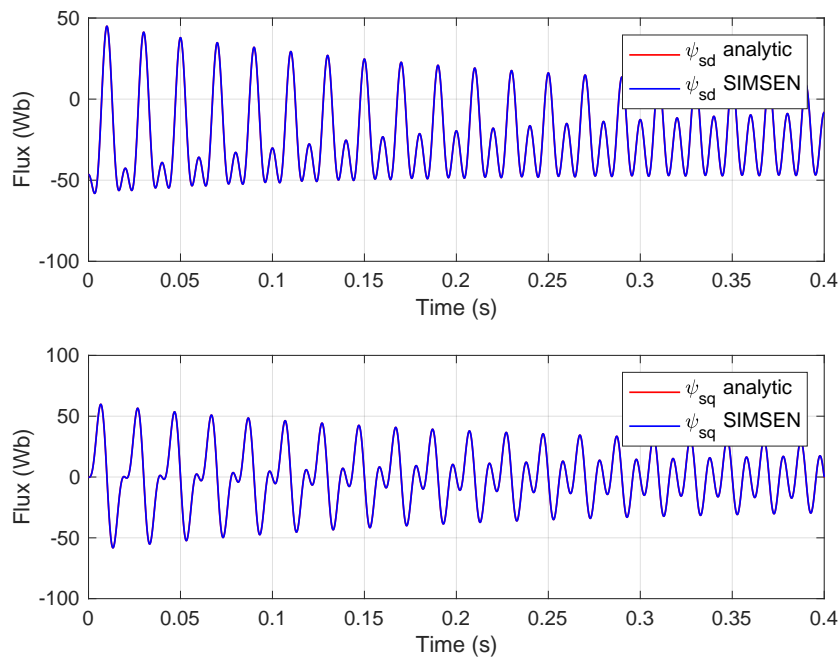
Figure A.33 – Stator fluxes in the rotating dq-frame
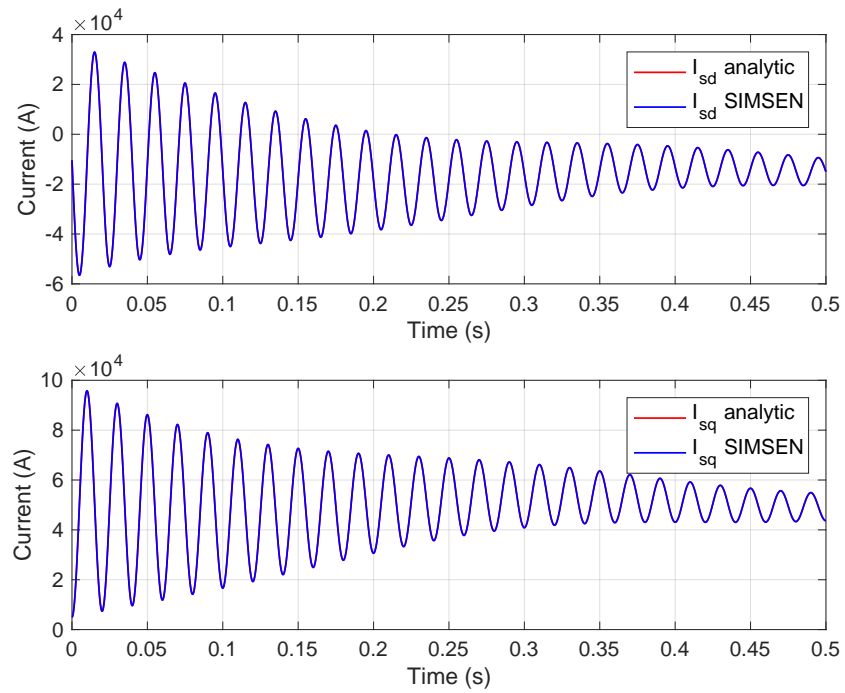
Figure A.34 – Stator currents in the rotating dq-frame
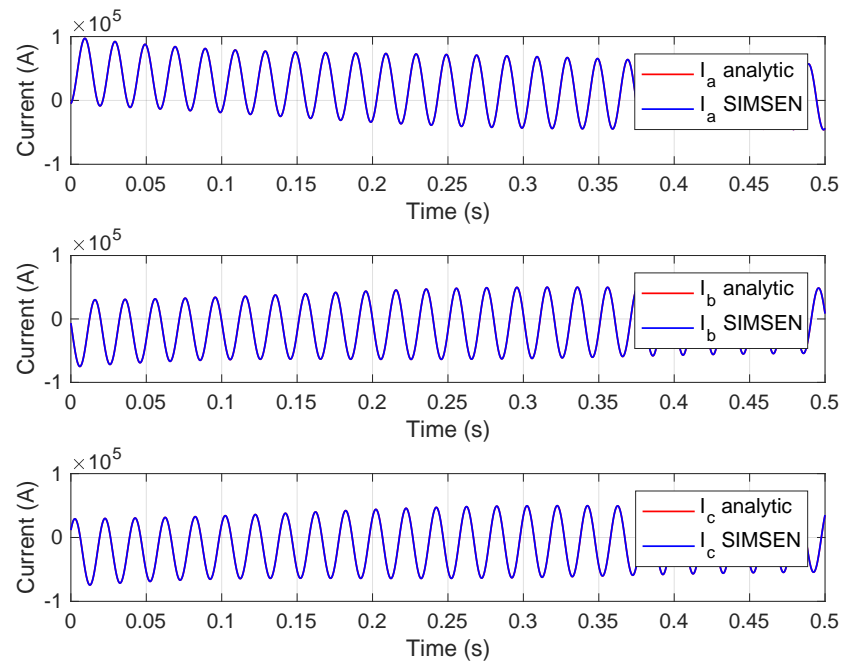
Figure A.35 – Stator currents in the fixed abc-frame
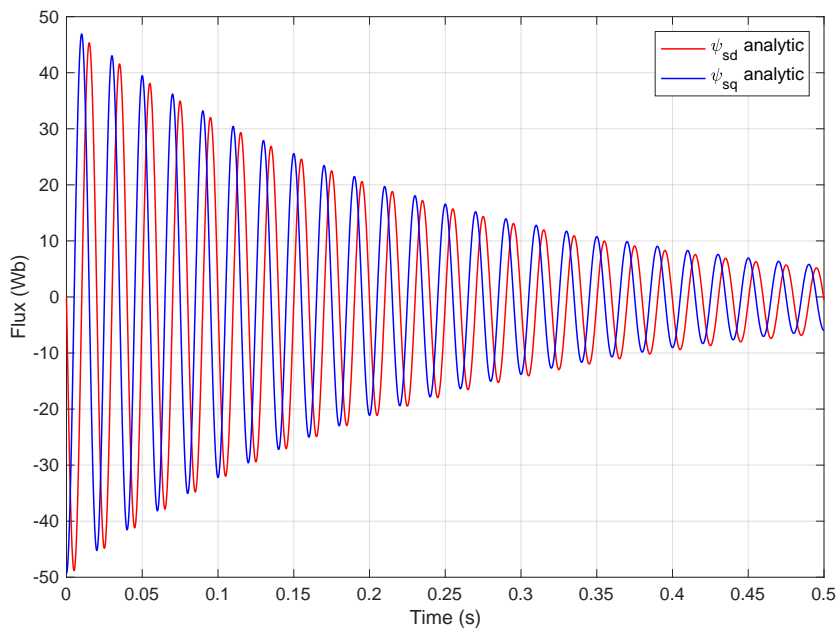
Figure A.36 – Stator fluxes in the rotating dq-frame
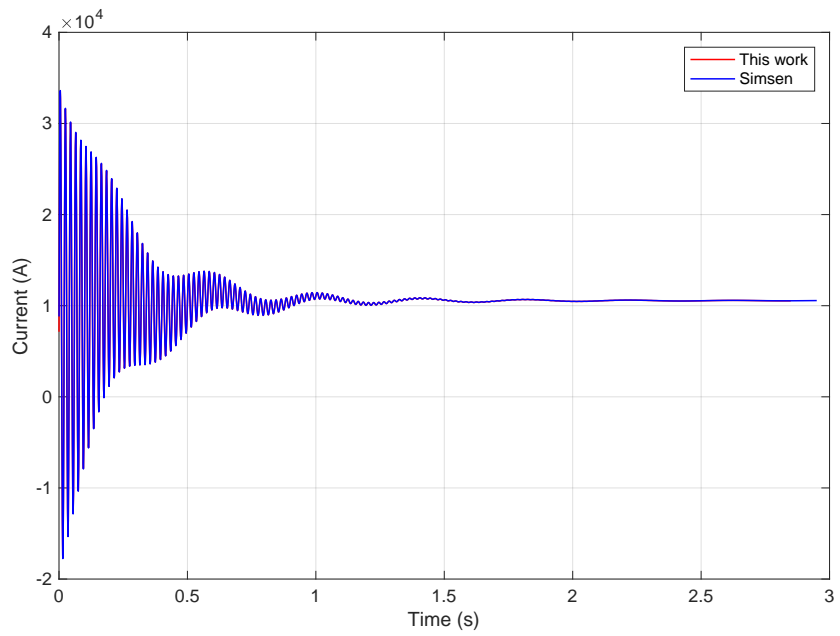
Figure A.37 – Rotor current (d-axis) in the rotating dq-frame
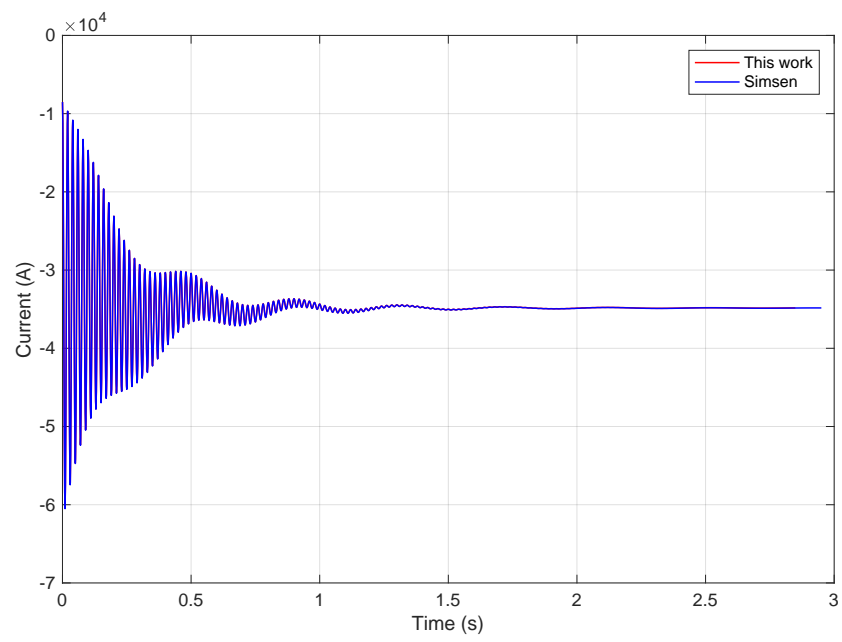
Figure A.38 – Rotor current (q-axis) in the rotating dq-frame

Bibliography

[1] A. Pramanik A.B.J. Reece. Calculation of the end-region field of a.c. machines. *PROC. IEEE*, 1965.

[2] Hubert Anton Aebischer and Beat Aebischer. Improved Formulae for the Inductance of Straight Wires. *Advanced Electromagnetics*, 3(1):31–43, 2014.

[3] International Energy Agency. World Energy Outlook 2014, 2014.

[4] et al. Decio Bispo, Luciano Martins Neto. A New Strategy for Induction Machine MModeling taking Into Acoount the Magnetic Saturation. *Advanced Electromagnetics*, 3(1):31–43, 2014.

[5] et al Guillermo Bossio, Cristian De Angelo. A 2D-Model of the Induction Motor: An Extension of the Modified Winding Function Approach. *IEEE*, 2002.

[6] A.G. Armstrong, C. J. Collie, N. J. Diserens, and M. J. Newman. New developments in the magnet design computer program GFUN. *RL-75-066*, March 1975.

[7] A.G. Armstrong, C. J. Collie, J Simkin, and C. W. Trowbridge. The solution of 3D magnetostatic problems using scalar potentials. *Compumag 78*, 1(Conference on the Computation of Magnetic Field), 1978.

[8] Bruno Azzerboni, Ermanno Cardelli, Marco Raugi, Andrea Tellini, and Giuseppe Tina. Analytic expressions for magnetic field from finite curved conductors. *Magnetics, IEEE Transactions on*, 27(2):750–757, 1991.

[9] S.I. Babic and C. Akyel. New Analytic-Numerical Solutions for the Mutual Inductance of Two Coaxial Circular Coils With Rectangular Cross Section in Air. *IEEE Transactions on Magnetics*, 42(6):1661–1669, June 2006.

[10] Slobodan Babic and Cevdet Akyel. New Formulas for Mutual Inductance and Axial Magnetic Force Between Magnetically Coupled Coils: Thick Circular Coil of the Rectangular Cross-Section-Thin Disk Coil (Pancake). *IEEE Transactions on Magnetics*, 49(2):860–868, February 2013.

Bibliography

[11] Slobodan I. Babic and Cevdet Akyel. Improvement in the analytical calculation of the magnetic field produced by permanent magnet rings. *Progress In Electromagnetics Research C*, 5:71–82, 2008.

[12] G. A. Bànyai. *Advanced Model for Multiphase Generators*. PhD thesis, EPFL, n° 5121, 2011.

[13] C.S. Cross B.C. Mecrow, A.G. Jack. Electromagnetic design of turbogenerator stator end regions. *IEE Proceedings*, 1989.

[14] F.-J. Biehl. Variregions Principles and Natural Boundary Conditions. *Unknown*, 1993.

[15] K.J. Binns, P.J. Lawrenson, and C.W. Trowbridge. *The Analytical and Numerical Solution of Eletric and Magnetic Fields*. Wiley, 1992.

[16] A. Bossavit. Magnetostatic problems in multiply connected regions: Some properties of the curl operator. *IEE Proceedings*, 1988.

[17] A. Bossavit. Whitney forms: A class of finite elements for three-dimensional computations in electromagnetism. *IEE Proceedings*, 135(8):493–500, November 1988.

[18] A. Bossavit. Simplicial Finite Elements for Scattering Problems in Electromagnetism. *Computer Methods in Applied Mechanics and Engineering*, 76:299–316, 1989.

[19] BP. BP Statistical Review of World Energy June 2017, June 2017.

[20] James H. Bramble and Joseph E. Pasciak. A New Computation Approach For the Linearized Scalar Potential Formulation of the magnetic field problem. *IEEE Transactions on Magnetics*, 18(2):357–361, March 1982.

[21] Roland Bulrisch. Numerical Calculation of Elliptic Integrals and Elliptic Functions*. *Numerische Mathematik*, 7:78–90, 1965.

[22] P.F. Byrd and M.D. Friedman. *Handbook of Elliptic Integrals for Engineers and Scientists*. Springer-Verlag Berlin Heidelberg New York, second edition, revised edition, 1971.

[23] B.C. Carlon. Computing elliptic integrals by duplication. *Numerische Mathematik*, 33(1):1–16, March 1979.

[24] C. J. Carpenter. The application of the Method of Images to Machine End-Winding Field. *The Institution of Electrical Engineers*, 1960.

[25] Anthony Carpentier. *Formulation intégrale de volume magnétostatique et calcul des densités de force magnétique : Application au couplage magnéto-mécanique*. PhD thesis, Université de Grenoble, Grenoble, December 2013.

[26] Andrea Cavagnino. On the Accuracy of the Slot Leakage Inductance Analytical Computation. *Electrical Machines (ICEM), 2016XXII International Conference on*, 2016.

[27] Liuchen Chang. An Improved FE Inductance Calculation for Electrical Machines. *IEEE Transactions on Magnetics*, 1996.

[28] Jean Chatelain. *Machines électriques*, volume X of *Traité d'électricité*. PPUR, Lausanne, ppur edition, 2013.

[29] I. R. Ciric. Scalar Potential Formulations for Magnetic Field Problems. *Unkown*, 1983.

[30] I. R. Ciric. New Models for Current Distributions and Scalar Potential Formulations of Magnetic Field Problems. *Journal of Applied Physics*, 1987.

[31] I. R. Ciric. Simple analytical Expressions for the Magnetic Field of Current Coils. *IEEE Transactions on Magnetics*, 1991.

[32] I. R. Ciric. New Model for the Computation of Quasi-Stationary FField Due to Arbitrary Distributions of magnetic Dipoles. *IEEE Transactions on Magnetics*, 2000.

[33] C. J. Collie. Magnetic field and potentials of linearly varying current or magnetisation in a plane-bounded region. *RL-76-037*, April 1976.

[34] P. Cordovil and I.E. Chabu. Analytical calculation of slot leakage inductance in multiphase electrical machines. *Electrical Machines (ICEM), 2016XXII International Conference on*, 4-7 Sept. 2016.

[35] V. I. Danilov and M. Ianovici. Magnetic Field of DC Coils of Cyélindrical Configuration. *Nuclear Instruments and Methods*, 79:29–42, 1970.

[36] V. I. Danilov and M. Ianovici. Magnetic field of thick finite dc solenoids. *Nuclear Instruments and Methods*, 94(3):541–550, 1971.

[37] G. Darrieus. Unterteilter Leiterstab mit verringerten Verlusten fèr elektrische Maschinen, 1963.

[38] G. Darrieus. Détermachines et Tracà des champs a trois dimensions application aux têtes de bobines, notamment des turbo-alternateurs. *Revue G*, 1967.

[39] P. Hammond D.S. Ashworth. The Calculation of the Magnetic Field of Rotating Machines. *The Institution of Electrical Engineers*, 1961.

[40] Tadashi Tokumasu et al. Kaoru Ito. Simulation for Design Purposes of Magnetic Fields in Turbine-Driven Generator End Region. *IEEE Transactions on Power Apparatus and Systems*, 1980.

[41] Yuta Watanade et al Katsumi Yamazaki. A Method of Eddy Current Calculation for Stator core Ends of turbine Generators. *Unknown*, 2006.

[42] Poopak Roshanfekr Fard. *Roebel Windings for Hydro Generators*. PhD thesis, Chalmers University of Technology, 2007.

Bibliography

[43] A. B. Field. Eddy Currents in Large Slot-wound Conductors. *AIEE*, 1905.

[44] Marzia Fontana. Integration methods for the calculation of the magnetostatic field due to coils, 2001.

[45] Barbara Frei-Spreiter. *Ein Beitrag Zur Berechnung Der Kräfte Im Wickelkopfbereich Grosser Synchromaschinen.* PhD thesis, ETH Zürich, 1998.

[46] Mark J. Friedman. Mathematical Study of the nonlinear singular integral magnetic field equation. I*. *SIAM J. APPL. MATH.*, 39(1):14–20, August 1980.

[47] Mark J. Friedman. Mathematical Study of the nonlinear singular integral magnetic field equation. II*. *SIAM J. NUMER. ANAL.*, 18(4):644–653, August 1981.

[48] Mark J. Friedman. Mathematical Study of the nonlinear singular integral magnetic field equation. III*. *SIAM J. MATH. ANAL.*, 12(4):536–540, July 1981.

[49] Mark J. Friedman. Finite Element Formulation of the General Magnetostatic Problem in the Space of Solenoidal Vector Functions. *Mathematics of Computation*, 43(168):415–431, October 1984.

[50] Mark J. Friedman and Joseph E. Pasciak. Spectral Properties for the Magnetization Integral Operator. *Mathematics of Computation*, 43(168):447–453, October 1984.

[51] Masafumi Fujita, Tadashi Tokumasu, Yasuo Kabata, Masanori Arata, Mikio Kakiuchi, and Susumu Nagano. Rotary electro-dynamic machine and armature winding thereof, April 2006.

[52] Masafumi Fujita, Tadashi Tokumasu, Yasuo Kabata, Masanori Arata, Mikio Kakiuchi, and Susumu Nagano. Rotary electro-dynamic machine and armature winding thereof, December 2007. U.S. Classification 310/216.106, 310/209, 310/213; International Classification H02K1/00; Cooperative Classification H02K1/20, H02K1/16, Y02E10/725, H02K3/14; European Classification H02K3/14.

[53] Masafumi Fujita, Tadashi Tokumasu, and Mikio Kakiuchi. Armature winding of electric rotating machine, stator of electric rotating machine and electric rotating machine, October 2010. U.S. Classification 310/213, 310/201, 310/179, 310/260; International Classification H02K3/14; Cooperative Classification H02K1/16, H02K3/14; European Classification H02K3/14.

[54] Toshio Fukushima. Fast computation of complete elliptic integrals and Jacobian elliptic functions. *Celestial Mechanics and Dynamical Astronomy*, 105(4):305–328, December 2009.

[55] Toshio Fukushima. Fast computation of Jacobian elliptic functions and incomplete elliptic integrals for constant values of elliptic parameter and elliptic characteristic. *Celestial Mechanics and Dynamical Astronomy*, 105(1-3):245–260, November 2009.

[56] Toshio Fukushima. Fast computation of incomplete elliptic integral of first kind by half argument transformation. *Numerische Mathematik*, 116(4):687–719, October 2010.

[57] Toshio Fukushima. Precise and fast computation of a general incomplete elliptic integral of second kind by half and double argument transformations. *Journal of Computational and Applied Mathematics*, 235(14):4140–4148, May 2011.

[58] Toshio Fukushima. Precise and fast computation of the general complete elliptic integral of the second kind. *Mathematics of Computation*, 80(275):1725–1743, 2011.

[59] Toshio Fukushima. Precise and fast computation of a general incomplete elliptic integral of third kind by half and double argument transformations. *Journal of Computational and Applied Mathematics*, 236(7):1961–1975, January 2012.

[60] Toshio Fukushima. Fast computation of a general coplete elliptic integral of the third kind by half and double argument transformation. *Journal of Computational and Applied Mathematics*, 253:142–157, 2013.

[61] E. P. Furlani, S. Reznik, and A. Kroll. A three-dimensional field solution for radially polarized cylinders. *IEEE transactions on magnetics*, 31(1):844–851, 1995.

[62] Fred Gardiol. *Traité d'électricité - Electromagnétisme*. PPUR, ppur edition, 2004.

[63] J.Milimonfared H. Akbari, H. Meshgin-Kelk. Extension of winding Function Theory for Radial and Axial Non-uniform Air Gap in salient Pole synchronous machines. *Progress In Electromagnetics Research*, 2011.

[64] J. Haldemann and F. Maurer. *Wicklung Für Eine Elektrische Maschine*. Google Patents, August 2016.

[65] Johan Haldemann. Berechnung der Schling- und Wirbelstromfaktoren die für Hydro-generatoren Itaipul, Karakaya, XanMenXia, Sarelli, Houay Ho, Silz. Internal ABB-Report, 1997.

[66] Johan Haldemann. Spezialversuche: StatoStator mit Sonderverdrillung. Internal Report ABB, 1997.

[67] Johan Haldemann. Teilleiterstrombestimmung während des Laufversuches durch nutquerfeld-Messung. Internal ABB-Report, 1997.

[68] Johan Haldemann. *Untersuchung Verschiedener Verdrillungsarten in Statorwicklungen Grosser Synchronmaschinen, Deren Wirkung Auf Strom- Und Temperaturverteilung Und Zusatzverluste in Verschiedenen Betriebszuständen*. PhD thesis, ETHZ, 1997.

[69] Johan Haldemann. History of the Roebel Bar and its Mechanisms of Annihilating Eddy Currents - In Memory of the Invention of Ludwig Roebel in 1912. *Unpublished*, 2018.

[70] Henry Hämäläinen. *Indentification of Some Additional Loss Components in High-Power Low-Voltage Permanent Magnet Generators*. PhD thesis, Lappeenranta University of Technology, 2013.

[71] P. Hammond. Electric and magnetic images. *Proc. IEE*, 107:306, 1960.

[72] P. Hammond. Electric and Magnetic Images. *The Institution of Electrical Engineers*, 1960.

[73] C. S. Harrold. Cutting Multiply Connected Domains. *IEEE Transactions on Magnetics*, 1985.

[74] D.F. Hofsommer and R.P. Van de Riet. On the Numerical Calculation of Elliptic Integrals of the first and second kind and the Elliptic Functions of Jacobi *. *Numerische Mathematik*, 5:291–302, 1963.

[75] Slobodan I. Babic and Cevdet Akyel. An improvement in the calculation of the magnetic field for an arbitrary geometry coil with rectangular cross section. *International Journal of Numerical Modelling: Electronic Networks, Devices and Fields*, 18(6):493–504, November 2005.

[76] M. Idemen. Universal Boundary Conditions and Cauchy Data for the Electromagnetic Field. *Unknown*, 1993.

[77] Markus Albrecht Iseli. *Zusatzverluste in Statorwicklung Grosser Synchronmaschinen Unter Berücksichtigung Der Verdrillung Und Der Stirnraumfelder*. PhD thesis, ETH Zürich, 1991.

[78] C.W. Trowbridge J. Simkin. Three-Dimensional Nonlinear Electromagnetic field CComputation, Using Scalar Potential. *IEE Proceedings*, 1980.

[79] Linni Jian and Kwok-Tong Chau. Analytical calculation of magnetic field distribution in coaxial magnetic gears. *Progress In Electromagnetics Research*, 92:1–16, 2009.

[80] Marcel Jufer. *Traité d'électricité - Electromécanique*, volume 9. PPUR, ppur edition, 2004.

[81] M. Sato K. Takahashi, M. Takahashi. Calculation Method for Strand Current Distributions in Armature Winding of a Trubine Generator. *Electrical Engineering in Japan*, 2003.

[82] K. W. Kanelis. Analytical equations of the induction machine. In *Electrical Machines (ICEM), 2016 XXII International Conference On*, pages 2854–2860. IEEE, 2016.

[83] Michel Kant. Etude du champ mangétique de la partie frontale d'un turbo-alternateur. *Revue Générale de l'électricité*, 1966.

[84] S. Keller. *Large Low Speed Hydrogenerators - UMP and Additional Damper Losses in Eccentricity Conditions*. PhD thesis, EPFL, n° 3773, 2007.

[85] Lauri Kettunen and Kimmo Forsman. Volume Integral equations in non-linear 3-D Magnetostatics. *Internation Journal for Numerical Methods in Engineering*, 38:2655–2675, 1995.

[86] Lauri Kettunen, Kimmo Forsman, David Levine, and William Gropp. Solutions of TEAM Problems 13 and 20 Using a Volume Integral Formulation. *Unkown*, XX:NA, 1995.

[87] Lauri Kettunen, Kimmo Forsman, David Levine, and William Gropp. Volume Intergral Euqations in Nonlinear 3D Magnetostatics. *PER 259*, 38:2655–2675, 1995.

[88] Lauri Kettunen and Larry R. Turner. A Volume INtegral Formulation for Nonlinear Magnetostatics and Eddy Currents Using Edge Elements. *IEEE Transactions on Magnetics*, 28(2):1639–1642, March 1992.

[89] P. R. Kotiuga. On making cuts for magnetic scalar potential in multiply connected regions. *Journal of Applied Physics*, 1987.

[90] P. Cruz-Romero L. Serrano-Iribarnegaray and A. Gomez-Exposito. Critical Review of the modified winding Function Theory. *Progress In Electromagnetics Research*, 2013.

[91] P.J. Lawrenson. Forces on turbogenerator end windings. *Proceedings IEE*, 112(6):1144–1158, June 1965.

[92] Christoph Lehmann. *Einfluss Der Sättigung Des Eisens Der Zähne Und Des Joches Auf Die Stromverdrägung Im Nutbereich Elektrischer Maschinen*. PhD thesis, Universität Duisburg, 1984.

[93] D. C. Macdonald. Loss in Roebel bars: Effect of slot portion on circulating currents. *Proceedings IEE*, 1970.

[94] D. C. Macdonald. Circulating-current loss wiwith Roebel-bar stator windings in hydro-electric alternators. *Proceedings IEE*, 1971.

[95] Touma Holmberg Marguerite. *Three-Dimensional Finite Element Computation of Eddy Currents in Synchronous Machines*. PhD thesis, Chalmers University of Technology, Göteborg, Sweden, December 1998.

[96] F. Maurer, M. T. Xuan, and J. Simond. Two novel methods for parameter identification of synchronous machine using DC-decay test with rotor in arbitrary position. In *2016 XXII International Conference on Electrical Machines (ICEM)*, pages 633–639, September 2016.

[97] F. Maurer, M. T. Xuan, and J. Simond. Two Full Parameter Identification Methods for Synchronous Machine Applying DC-Decay Tests for a Rotor in Arbitrary Position. *IEEE Transactions on Industry Applications*, 53(4):3505–3518, July 2017.

[98] Frederic Maurer. *Détermination des paramètres de la machine synchrone par essais "DC-Decay"*. Master thesis, EPFL, January 2009.

[99] D. Bruce Montgomery. *Calcul et Construction de Bobines Solenoidales Permettant d'obtenir Des Champs Magnétiques Élevés.* PhD thesis, EPFL (thèse n° 75), 1969.

[100] A.A. Arkadan N.A. Demerdash, T.M. Hijaki. Computation of winding iinductance of permanent magnet brushless DC motors with damper windings by energy perturbation. *IEEE Transactions on Energy Conversion*, 1988.

[101] Neidhöfer. Stromverdraegung in Maschinenwicklung. *TH Darmstadt*, 1966.

[102] G. Neidhöfer. Innenkühlung von Roebelstäben und Massnahmen zur Verminderung der zusatzverluste. *Scientia Electrica*, 1968.

[103] Jacques Neirynck, Martin Hasler, Catherine Dehollain, and Hervé Dedieu. *Filtres électriques (TE volume XIX)*, volume 19. PPUR, Lausanne, 1st edition edition, 1996.

[104] Wolf-Rainer Novender. *Dreidimensionale Nichtlineare Magnetfeld-Berechnung Für Synchron-Turbogeneratoren Zur Bestimmung Der Schlingstromverteilung in Roebelstäben.* PhD thesis, TH Darmstadt, 1984.

[105] K. Oberretl. Dreidimensionale Berechnung des Linearmotors mit Berücksichtigung der Endeffekte und der Wicklungsverteilung. *Archiv für Elektrotechnik*, 1973.

[106] Vlado Ostovic. A Method for Evaluation of Transient and Steady State Performance in Saturated squirrel cage induction machines. *IEEE Transactions on Energy Conversion*, 1986.

[107] Joseph E. Pasciak. An Iterative Algorithm for the volume integral method for magnetostatics problems, November 1980.

[108] Joseph E. Pasciak. An Iterative Algorithm for the volume integral method for magnetostatics problems. *Comp. & Maths. with Appls.*, 8(4):283–290, 1982.

[109] Joseph E. Pasciak. The H-Gradient method for magnetostatic field computations. *IEEE Transactions on Magnetics*, 19(6):2344–2347, November 1983.

[110] Joseph E. Pasciak. A New Scalar Potential Formulation of the Magnetostatic Field Problem. *Mathematics of Computation*, 43(168):433–445, October 1984.

[111] Clayton R. Paul. What Is "Partical Inductance" ?, 2008.

[112] Clayton R. Paul and G. A. Macon. Partial Inductance. In *2008 IEEE International Symposium on Electromagnetic Compatibility*, 2010.

[113] H. L. Rakotoarison, J.-P. Yonnet, and B. Delinchant. Using Coulombian Approach for Modeling Scalar Potential and Magnetic Field of a Permanent Magnet With Radial Polarization. *IEEE Transactions on Magnetics*, 43(4):1261–1264, April 2007.

[114] Carlos Ramirez. *Plate-forme numérique d'essais pour machines électriques de puissance.* PhD thesis, EPFL, Lausanne, 2003.

[115] R. Ravaud, G. Lemarquand, and V. Lemarquand. Magnetic Field Created by Tile Permanent Magnets. *IEEE Transactions on Magnetics*, 45(7):2920–2926, July 2009.

[116] R. Ravaud, G. Lemarquand, V. Lemarquand, and C. Depollier. Permanent Magnet Couplings: Field and Torque Three-Dimensional Expressions Based on the Coulombian Model. *IEEE Transactions on Magnetics*, 45(4):1950–1958, April 2009.

[117] Romain Ravaud and Guy Lemarquand. Analytical expression of the magnetic field created by tile permanent magnets tangentially magnetized and radial currents in massive disks. *Progress In Electromagnetics Research B*, 13:309–328, 2009.

[118] Romain Ravaud and Guy Lemarquand. Comparison of the coulombian and amperian current models for calculating the magnetic field produced by radially magnetized arc-shaped permanent magnets. *Progress In Electromagnetics Research*, 95:309, 2009.

[119] Romain Ravaud and Guy Lemarquand. Magnetic field produced by a parallelepipedic magnet of various and uniform polarization. *Progress In Electromagnetics Research*, 98:207–219, 2009.

[120] Romain Ravaud and Guy Lemarquand. Synthesis about Analytical Approaches for Calculating the Magnetic Field Produced by Permanent Magnets of Various Topologies. *PIERS Proceedings*, 1(Cambridge USA, July 5-8):154–158, 2010.

[121] Romain Ravaud, Guy Lemarquand, Valerie Lemarquand, and Claude Depollier. Analytical Calculation of the Magnetic Field Created by Permanent-Magnet Rings. *IEEE Transactions on Magnetics*, 44(8):1982–1989, August 2008.

[122] Romain Ravaud, Guy Lemarquand, Valérie Lemarquand, and Claude Depollier. The three exact components of the magnetic field created by a radially magentized tile permanent magnet. *Progress In Electromagnetics Research*, PIER 88:307–319, 2008.

[123] Romain Ravaud, Guy Lemarquand, Valerie Lemarquand, and Claude Depollier. Discussion about the analytical calculation of the magnetic field created by permanent magnets. *Progress In Electromagnetics Research B*, 11:281–297, 2009.

[124] Albert Ruehli. Inductance Computations Using Partial Inductance Concepts, 2007.

[125] Jerry P. Selvaggi, Sheppard Salon, O.-Mun Kwon, and M. V. K. Chari. Computation of the Three-Dimensional Magnetic Field From Solid Permanent-Magnet Bipolar Cylinders By Employing Toroidal Harmonics. *IEEE Transactions on Magnetics*, 43(10):3833–3839, October 2007.

[126] Jerry P. Selvaggi, Sheppard Salon, O.-Mun Kwon, M. V. K. Chari, and Mark DeBortoli. Computation of the External Magnetic Field, Near-Field or Far-Field, From a Circular Cylindrical Magnetic Source Using Toroidal Functions. *IEEE Transactions on Magnetics*, 43(4):1153–1156, April 2007.

Bibliography

[127] J Simkin and C.W. Trowbridge. On the use of the total scalar potential in the numerical solution of field problems in electromagnetics. *International Journal for Numerical Methods in Engineering*, 14:423–440, 1979.

[128] J Simkin and C.W. Trowbridge. Three Dimensional Computer Program (TOSCA) for Non-Linear Electromagnetic Fields, December 1979.

[129] M.Liese St. Kunckel, G. Klaus. Calculation of Eddy Current LoLoss and Temperature Rises at the Stator End Portion of Hydro Generators. *Unknown.*

[130] K. Ito T. Tokumasu, S. Doi and M. Yamamoto. An electric vector potential method approach for 3-D eletrcomagnetic field in turbine generator stator core end. *IEEE Transactions on Power Apparatus and Systems*, 1984.

[131] Susumu Maeda Tasuei Nomura. Analysis of Magnetic Flux in Stator End Windings of Large Turbine Generators Using Fourier Expansion. *IEEE Transactions on Magnetics*, 1990.

[132] Gheorghe Madescu Toma Dordea, Victor Proca and et al. Roebel Bar Model for Additional Loss Estimation in High Power Hydrogenerators. *3rd International Symposium on Electrical Engineering and Energy Converters*, 2009.

[133] L. Urankar. Vector potential and magnetic field of current-carrying finite arc segment in analytical form, Part I: Filament approximation. *IEEE Transactions on Magnetics*, 16(5):1283–1288, September 1980.

[134] L. Urankar. Vector potential and magnetic field of current-carrying finite arc segment in analytical form, Part III: Exact computation for rectangular cross section. *IEEE Transactions on Magnetics*, 18(6):1860–1867, November 1982.

[135] L. Urankar. Vector potential and magnetic field of current-carying finite arc segment in analytical form, part II: Thin sheet approximation. *IEEE Transactions on Magnetics*, 18(3):911–917, May 1982.

[136] L. Urankar. Vector potential and magnetic field of current-carrying finite arc segment in analytical form, part IV: General three-dimensional current density. *IEEE Transactions on Magnetics*, 20(6):2145–2150, November 1984.

[137] L. Urankar. Common compact analytical formulas for computation of geometry integrals on a basic conic sub-domain in boundary and volume integral methods. *Engineering Analysis with Boundary Elements*, 7(3):124–129, 1990.

[138] L. Urankar. Common compact analytical formulas for computation of geometry integrals on a basic conic sub-domain in boundary and volume integral methods. *Archiv für Elektrotechnik*, 73:97–107, 1990.

[139] L. Urankar, P. Henninger, and F. S. Nestel. Compact Extended Algorithms for Elliptic Integrals in Electromagnetic Field and Potential Computations Part II: Elliptic Integral of the thirs Kind with Extended Integration Range. *IEEE Transactions on Magnetics*, 30(3):1236–1241, May 1994.

[140] L. K. Urankar. High Accuracy Field Computation of Magnetized Bodies. *IEEE Transactions on Magnetics*, Mag. 21(6):2169–2172, 1985.

[141] L. K. Urankar and P. Henninger. Compact Extended Algorithms for Elliptic Integrals in Electromagnetic Field and Potential Computations Part I: Elliptic Integrals of the First and Second Kind with Extended Integration Range. *IEEE Transactions on Magnetics*, 27(5):4338–4342, September 1991.

[142] Eva Varga and Adalbert Beyer. Magnetic field of a uniformly magnetized hollow cylinder. *IEEE transactions on magnetics*, 34(3):613–618, 1998.

[143] M. Ianovici V.I. Danilov. Magnetic Field of Thick Finite DC Solenoids. *Nuclear Instruments and Methods*, 1971.

[144] N. Wavre. *Etude Harmonique Tridimensionnelle Des Moteurs Linéaires Asynchrones à Bobinages Polyphasés Quelconques*. PhD thesis, EPFL, n° 219, 1975.

[145] John P. Wikswo, Jr. Swinney, and Kenneth R. Swinney. Scalar multipole expansions and their dipole equivalents. *Journal of Applied Physics*, 57(9):4301–4308, 1985.

Frédéric Maurer

Schillingstrasse 3
CH-3005 Bern
M +41 79 744 46 44
frederic.maurer@icloud.com
http://www.linkedin.com/in/
fmmaurer

Profile

Eight years' experience in hydrogenerators. Negotiation and technical exchange with different customers on several continents. People- and project leading while working in an international environment.

Effective team-player, open persuasive and assertive communicator and negotiator with strong work ethics. Flexibility, ability to improvise and quick learning. Good in crisis. Positive minded and self-motivated person.

Experience

GE Renewable Energy (former ALSTOM Power), Technical Project Manager - Linthal 2015 (4x250MW); Birr – 2014-present
Technical leader for the motor-generator and technical support in the construction phase. Managing engineering activities and budget.

Working fast across different functions and businesses at different organisation levels from R&D to Site.

Rapid change management and crisis management. Technical exchange and negotiation with the customer.

Coordination and integration of punctual engagement of around 35 different persons located in different countries and of several nationalities.

GE Renewable Energy (former ALSTOM Power), Lead Electrical design Engineer - special calculations; Birr — 2011-present
Technical exchange and negotiation with various customers around the world as well as trainings and technical exchanges with other locations. Participation to design reviews and support of other functions.

More than 30 technical tenders (electrical design) based on WTO-rules of a very large spectrum of synchronous units of different types from 5MVA to 400MVA.

Special electrical calculations with analytical and numerical methods. Diagnosis and troubleshooting on-site during operation as well as during commissioning.

ALSTOM Schweiz AG, R&D Engineer; Birr — 2009-2011
Development of a calculation tool for VARSPEED units. Investigations on wave-windings and stator vibration.

Laboratory of Electrical Machines EPFL, Trainee; Lausanne — 07.2008-08.2008
Contribution to the automation of a numerical test bench for salient pole synchronous machines. Application of functional programming to get automated finite element simulations using Flux2D and Python.

Digger Demining Technologies, Trainee; Tavannes — 08.2006-09.2006
Development of an automated test bench for the embedded machine electronics to be used for in-field troubleshooting using LabView and self-developed electronic circuits.

Education	**EPFL, Lausanne — PhD, 2013-On-going**
	"Electrical effects in windings of large electrical AC machines – application to advanced large size DFIG". Development of an integral 3D-magnetostatic program for very high accuracy field calculation using modern programming methods to achieve low computation time. Experimental validation of the developed software.
	EPFL, Lausanne — 3rd year of BSc of physics (5.27/6 grade), 2010-2011
	Quantum physics I&II, Solid state physics I&II, Optics, Nuclear Physics, Laboratory III&IV (metrology), Hydrodynamics, Statistical physics, Plasma physics, Material physics, Mathematical methods for physics.
	EPFL, Lausanne — MSc in electrical engineering (5.83/6 grade), 2004-2009
	Master thesis : "Determination of the parameters of the equivalent diagram of a synchronous machine using DC-Decay method".
Academic Awards	Prix LEM, Prix IM Maggia, Prix Anna Barbara Reinhard, Prix de la Société des ingénieurs et des architectes, section vaudoise.
Patents & Publications	1 patent application, 2 patent disclosures. 1 journal paper. 3 conference papers - 3 oral presentations. 1 award for the best technical paper in Hydrovision 2013.
Technical skills	Softwares: SIMSEN, Simulink, Flux3D, MatLab, Mathematica, LabView, LaTeX, MS Office, Windows and Mac OS X.
	Programming: C#, C++, C, Python, Delphi, PHP and MySQL.
	Engineering: Product definition, Design reviews, design validation.
	Scientific: Statistical data analysis (up to 10 GB), Measurements and validation, Multi-physics simulations, Analytical calculations.
Languages	French: mother tongue. German: C1. English: C1.
Interests	Rugby (LNB and 5 selections in the national team U17, U18), Travelling around the world, Reading magazines (GEO) and newspapers (The Economist, Le monde diplomatique) as well as books about international relations and swiss politics.
	Licence software (development and support) of the Swiss Rugby Union since 2004. Director of sports Rugby Club Bern.
Personal details	Swiss citizen, 31 years old, non married, category B driving licence, Lt in the civil protection (Kantonale Formation Bern).